Building Power Grid Resilience to Extreme Wildfire Risks with Distributed Energy Resources

Weijia Yang

Keble College

University of Oxford

A thesis submitted for the degree of

Doctor of Philosophy

Trinity 2024

Acknowledgements

I would like to express my sincere gratitude and appreciation to the many wonderful people who have supported and helped me throughout my DPhil journey.

First and foremost, I would like to thank my supervisors, Professor David Wallom and Professor Sarah Sparrow, for their outstanding guidance and unwavering support. I feel truly honoured and fortunate to have been part of the inaugural cohort of the MSc in Energy Systems at Oxford. This programme has not only provided me with a comprehensive understanding of energy systems but also introduced me to lifelong friends with shared interests. Most importantly, it strengthened my determination to pursue DPhil research in the interdisciplinary fields of energy and climate under the supervision of David and Sarah.

The four years of my DPhil study have been both rewarding and challenging. I would like to express my heartfelt appreciation to my family for their unconditional love and care, especially to my parents, who have always comforted and encouraged me during difficult times. They are my role models, exemplifying dedication to work, kindness to others, and a graceful attitude towards life.

I would also like to express my deep gratitude to my partner, Ouya. Despite his own PhD commitments in London, Ouya has always made time to come to Oxford and care for me. I have lost count of the number of late nights we have spent studying together. Whenever I have felt discouraged or lacked confidence, it has been Ouya who brought light and reassurance into my life. I believe it is a beautiful destiny that we have met and grown together.

In addition, I would like to thank my master's supervisor, Professor Thomas Morstyn, who sparked my interest in studying the power grid under wildfire risks. With his kind supervision and support, I was able to publish my first journal paper, which was a follow-up outcome of my master's dissertation.

I am grateful to my colleagues in our lab, especially the postdocs in the Energy Environmental Informatics Lab and the Energy and Power Group. I extend my thanks to Dr Weiqi Hua, Dr Devki Nandan Jha, Dr Masaō Ashtine, Dr Maomao Hu, Dr Dongjiao Ge, Dr Pu Yang, Dr Elnaz Azizi, and Dr Iago Perez for their generous guidance and support.

Furthermore, I have had the pleasure of meeting some wonderful DPhil students at Holywell House, and I have greatly enjoyed the friendly atmosphere there. I would like to thank Dr Hankun Ren, Dr Sara Abdelaziz, Katya Soegiharto, Rohan Agrawal, Laurence Peinturier, and Maitha Al Shimmari. I look forward to continuing to explore the field of energy and the environment with such great colleagues.

There are so many more people to whom I owe thanks for their support throughout my DPhil journey. I will always treasure the time spent and the wonderful people I have met in Oxford, and these memories will remain close to my heart forever.

Publication List

1. **Yang, W.**, Sparrow, S., Ashtine, M., Wallom, D., and Morstyn, T. (2022) Resilient by design: Preventing wildfires and blackouts with microgrids. Applied Energy, 313, 118793. [1]

2. **Yang, W.**, Sparrow, S., and Wallom, D. (2023) Optimising multi-factor assistance in a deep learning-based electricity forecasting model with climate resilience: an Australian case study. IEEE PES Innovative Smart Grid Technologies Europe Conference. [2]

3. **Yang, W.**, Sparrow, S., and Wallom, D. (2024) A Comparative Climate-Resilient Energy Design: Wildfire Resilient Load Forecasting Model Using Multi-Factor Deep Learning Methods. Applied Energy, 368, 123365. [3]

4. **Yang, W.**, Yang P., and Hirmer, S. (2025) Building the resilience of local power systems against climate change. In: W. Hua, X. Zhang and D. Wallom, eds., Digitalisation of Local Energy Systems. Springer Nature. [4]

As all papers are co-authored, detailed work allocation for Papers 1-3 are provided in Chapters 3 and 4 since they contribute to the two main phases of this DPhil study. The 4^{th} publication (working book chapter) is a thorough review of grid resilience study under extreme climate events. The book chapter is building significantly on Chapter 2 (Literature Review). Detailed author contribution is listed here. Weijia Yang: Methodology, Conceptualization, Writing – original draft, Writing – review & editing. Pu Yang: Writing – original draft, Conceptualization. Stephanie Hirmer: Writing – review & editing, Supervision.

Abstract

Climate change is a crucial issue for sustainable development in the 21^{st} century. To mitigate and adapt to global warming, the Paris Agreement targets limiting global temperature rise to 2°C above pre-industrial levels. Since energy production is responsible for three-quarters of global carbon emissions, a sustainable energy transition is vital to achieving Net Zero and addressing climate change. Green electrification is central to this transition but also involves challenges, including the effects of extreme weather, ageing infrastructure, and the inherent intermittency of renewable generation on energy system optimisation. This DPhil study addresses these challenges by developing a resilient and sustainable power system model to withstand extreme weather risks, explicitly focusing on wildfires. The study is structured into four phases. Phase I developed a prototype Wildfire Energy Model (WEM) based on worst-case scenario simulations of the power grid in Victoria, Australia, during wildfire seasons. In Phase II, a Wildfire Resilient Load Forecasting Model (WRLFM) was constructed using deep learning techniques and multiple climate factors to predict energy consumption. Phase III extended the WEM to a dynamic time-series version, based on a modified IEEE 24-bus Reliability Test System, to generalise the model. In Phase IV, the time-series WEM was further developed using real-world data from Victoria to assess grid performance during the 2019-2020 wildfire season. Throughout the four phases, the study evaluates grid resilience from technical, economic, and environmental perspectives. The WRLFM was employed to account for system-wide uncertainties and calculate the probabilistic power reserve required during wildfire events in the generalised WEM. The results demonstrate that distributed energy sources are effective strategies for preventing blackouts and managing wildfire risks. This research proves the feasibility of building a resilient and sustainable grid that ensures safe operation, cost-efficiency, and decarbonisation in the face of extreme climate events.

Contents

List of Figures

List of Tables

List of Abbreviations

ACOPF	Alternating Current Optimal Power Flow
AEMC	Australian Energy Market Commission
AEMO	Australian Energy Market Operator
AER	Australian Energy Regulator
AI	Artificial Intelligence
AMR	Average Mitigating Rate
ARIMA	Autoregressive Integrated Moving Average
BI	Burning Index
CAIDI	Customer Average Interruption Duration Index
CFFDRS	Canadian Forest Fire Danger Rating System
CNN	Convolutional Neural Network
DBN	Deep Belief Network
DCNN	Deep Convolutional Neural Network
DCOPF	Direct Current Optimal Power Flow
DER	Distributed Energy Resource
DF	Drought Factor
DG	Distributed Generation
ECMWF	European Centre for Medium-Range Weather Forecasts
ENSO	El Niño-Southern Oscillation
ENTSO-E	European Network of Transmission System Operators for Electricity
ESM	Exponential Smoothing Models
ESS	Energy Storage Systems
EUE	Expected Unserved Energy
EURE	Expected Unserved Ramping Energy

FFDI	Forest Fire Danger Index
FWI	Fire Weather Index
GRU	Gated Recurrent Unit
HRE-MG	Hybrid Renewable Energy-based Microgrid
IEEE	Institute of Electrical and Electronics Engineers
IRRE	Insufficient Ramping Resource Expectation
LCOE	Levelised Cost of Electricity
LIBSVM	Library for Support Vector Machines
LOLE	Loss of Load Expectation
LOLP	Loss of Load Probability
LSTM	Long Short-Term Memory
LTS	Long-Term Scheduling
MILP	Mixed Integer Linear Programming
ML	Machine Learning
MLP	Multilayer Perceptron
MMSDM	Market Management System Data Model
MPC	Market Price Cap
NFDRS	National Fire-Danger Rating System
NN	Neural Network
NTNDP	National Transmission Network Development Plan
OPF	Optimal Power Flow
PDF	Probability Density Function
PSPS	Public Safety Power Shutoff
RES	Renewable Energy Source
RF	Random Forest
RNN	Recurrent Neural Network
RSC	Reserve Scarcity Prices
RTS	Reliability Test System
SAIDI	System Average Interruption Duration Index
SAIFI	System Average Interruption Frequency Index
SAM	Semi-parametric Additive Models

SARIMAX	Seasonal Autoregressive Integrated Moving Average with Exogenous Regressors
SRMC	Short-Run Marginal Cost
SVM	Support Vector Machine
TCN	Temporal Convolutional Network
VoLL	Value of Lost Load
WEM	Wildfire-Energy Nexus Model
MLR	Multiple Linear Regression
WRLFM	Wildfire Resilient Load Forecasting Model
XGB	Extreme Gradient Boosting

1

Introduction

Contents

In the era of electrification and decarbonisation, electricity is at the heart of modern economies. In 2023, electricity accounted for 20.6% of global final energy consumption, reflecting a 3% increase since 2010 [5]. This share has remained relatively stable since 2020. However, the International Energy Agency (IEA) projects that electricity's share of final energy consumption will exceed 50% by 2050 in the Net Zero Emissions 2050 Scenario, as electricity becomes increasingly central to the decarbonisation of end-use sectors [6].

With increasing dependence on electricity, the resilience and reliability of power grid operations have become increasingly critical topics. Ageing electricity infrastructure, the integration of low-inertia renewable energy generation, the long-term impacts of climate change, and the short-term effects of extreme weather events all exacerbate the challenge of building a resilient and sustainable energy system capable of withstanding extreme climate risks [7]. This thesis aims to investigate the interaction between the power grid and extreme weather risks, developing a generalised tool to simulate and enhance grid resilience during extreme weather events. The model will evolve through four phases, transitioning from a static worst-case scenario to a dynamic, high-resolution, and probabilistic scenario.

Chapter 1 provides a review of the study's background, outlining the motivations behind it. The chapter then discusses the research questions and the challenges associated with developing a resilient grid model under extreme weather risks. Research objectives are defined to clarify how the main research question will be addressed step-by-step. To facilitate case studies on real power networks, suitable use cases are identified, focusing on a specific type of extreme weather chosen for this DPhil study: wildfires. The final section of the chapter presents the structure of the thesis.

1.1 Background and motivation

Most electricity transmission networks, distribution infrastructures, and conventional power stations are ageing and part of the networks will soon reach the end of their expected lifespans. According to a technical report from Ofgem [8], the current weighted age and the estimated weighted average technical life of the electricity transmission network are 35 years and 55 years in the UK, respectively. In Europe, decommissioning data indicate that the average technical lifetimes of coal, oil, and gas power stations are 40 years, 34 years, and 34 years, respectively. Based on historical trends, 100% of the currently operational oil and gas power plants in Europe will have reached the end of their expected lifetimes by 2050 [9]. The risk of faults in energy systems will increase as these infrastructures continue to operate beyond their intended lifespans. Moreover, the frequency and severity of extreme weather events are rising due to climate change. For example, a 1°C increase in autumn temperatures and a 30% decrease in autumn precipitation in California have doubled the likelihood of extreme wildfires in the state since the early 1980s [10]. The risk of power outages will grow significantly as ageing infrastructure faces more frequent extreme weather events [11].

Different types of extreme weather events can impact power systems in diverse ways, each exhibiting distinct characteristics in the resulting electrical faults. According to a summary report from the U.S. Department of Energy, comparatively little attention has been paid to research on grid issues under high wildfire risk, in contrast to other types of extreme weather, such as extreme temperatures, wind, and flooding [12]. For this reason, wildfires have been selected as the specific focus of extreme weather in this DPhil research.

Wildfire-related damage to power grids has become a global concern in recent years. For example, the 2019-2020 Australian wildfire season was unprecedentedly devastating, resulting in the destruction of 46 million acres of land, 34 fatalities, and the loss of at least 3,500 homes [13]. As the region most severely affected by wildfire risk, approximately 20,000 customers in New South Wales were left without power at the peak of the fires during the New Year period [14]. Similarly, California has also faced significant wildfire disasters. Pacific Gas and Electric (PG&E), California's largest energy utility, operates a service area covering 70,000 square miles [15]. One of the most devastating wildfires, the 2018 Camp Fire, was caused by the failure of a suspension hook holding up an insulator string in PG&E's transmission network, leading to the deaths of 85 people and disrupting the power supply to millions of customers [16]. PG&E was forced to declare bankruptcy due to $13.5 billion in property damage [17]. Consequently, smart technologies to mitigate the wildfire impact on power grids and reduce the risk of electrically-triggered wildfires are of considerable practical significance.

To reinforce the ageing power grid in the face of increasing extreme events, the transition to a resilient and green grid has become a top priority for many countries. The concept of resilience refers to a system's ability to resist, adapt to, and recover from contingencies (e.g., low-probability, high-risk events) [18]. Various reinforcement methods like upgrading pole material, undergrounding lines, and increasing the frequency of vegetation management can be implemented before such events rather than relying solely on reactive measures following devastating disasters. The specific metrics for assessing grid resilience, along with methods for enhancement, will be reviewed in Sections 2.1.3 and 2.3.3, as these are the primary tools for evaluating grid performance and preventing blackouts and wildfires in this study.

The Paris Agreement aims to limit the global temperature increase to below 2°C above pre-industrial levels, with efforts to further restrict it to 1.5°C [19]. In recent years, the global energy sector has steadily transitioned towards renewable energy. Clean energy surged in 2023, with 50% more renewable capacity added to energy systems worldwide compared to the previous year. In total, 507 GW of additional renewable electricity capacity were installed in 2023, with solar PV accounting for three-quarters of the global additions [20]. By the end of 2023, 84 countries had agreed to phase out coal or halt the development of new unabated coal power plants, collectively accounting for approximately 30% of current coal consumption for electricity generation [21]. Consequently, distributed generation (DG) and microgrids with renewable and green energy resources are being prioritised in our work to address grid resilience issues in the face of extreme weather risks. DG is a way to produce electricity close to where it is used, while a microgrid is a small, localised energy system that can operate independently. Both DG and microgrids are considered potential solutions to improve system resilience at emergent events and facilitate the decarbonisation goal in this thesis. Furthermore, renewable generation technologies are intermittent and significantly affected by extreme weather, highlighting the necessity of developing a climate-resilient grid-weather model incorporating renewable technologies.

1.2 Research questions and challenges

Climate resilience studies for power grids are still at an early stage, particularly with regard to power grid resilience under extreme wildfire risks, a field that has seen relatively little research. Motivated by current issues surrounding climate change, increasing wildfire risks, ageing grid infrastructure, the energy transition, and the research gap in this area, this DPhil project has been developed. The anticipated outcomes of this research are: (1) to improve the resilience of power systems under extreme wildfire risks using distributed generation in a sustainable way, and (2) to learn the interplay between wildfire risks and power systems using data-driven methods, enabling grid operators to optimise the short-term dispatch and long-term planning. This section introduces the primary research questions to be addressed to develop a generalised Wildfire Energy Model (WEM) in this DPhil study while also discussing the challenges involved in its implementation.

1.2.1 Research questions

In this section, the main research question of the DPhil study is clarified first. Three sub-research questions are then proposed and discussed one by one, which will be addressed through the main chapters of this thesis.

The main research question for the DPhil study

Wildfire risks can affect power grid operation directly by damaging equipment through burning and indirectly through heat and smoke, which may cause line sagging and alter the dielectric properties of the surrounding air, leading to arcing faults. Consequently, it is essential to evaluate grid resilience under wildfire risks and develop effective strategies to enhance resilience against escalating fire threats. The main research question for this DPhil study is: **How can power system**

resilience be assessed and enhanced under extreme wildfire risks?

I. How is grid resilience affected by wildfire risks under selected peak fire conditions?

To investigate the impact of wildfires on power system resilience, several worst-case scenarios under selected daily peak fire conditions are analysed as a foundational step. This research question is addressed in Chapter 3, using real grid operational data from days with various fire risks.

II. How can electricity demand be accurately predicted during wildfire seasons?

To enhance power system resilience under wildfire risks, it is essential to understand how electricity demand varies and is affected during wildfire seasons. More accurate demand forecasting enables system operators to optimise power dispatch and implement grid reconfiguration to mitigate the impact of wildfires on the grid, such as preventing unintentional blackouts.

III. How can the resilience of wildfire-affected power grids be continuously assessed and enhanced in both theoretical and real-world case studies?

While the first research question addresses worst-case scenarios under peak fire conditions, this question focuses on the continuous simulation, assessment and enhancement of wildfire-affected power systems. The objective is to model and reinforce both theoretical and real-world grids, providing practical and generalisable solutions for power utilities.

1.2.2 Main challenges

The main challenges in addressing the aforementioned research questions are discussed in this section. While these challenges are broad and high-level, specific research gaps will be explained in Section 2.5 following a review of existing related works.

I. Dataset availability

Both the datasets for the power grid and wildfire risk distribution are essential for constructing the integrated WEM. Most global wildfire risk indices are available from independent intergovernmental organisations and some national meteorological organisations, such as the European Centre for Medium-Range Weather Forecasts (ECMWF) [22] and the Bureau of Meteorology (BoM) [23], or can be calculated directly from standard meteorological variables, including surface temperature, wind, and humidity [24]. However, the availability of datasets for power system components depends on the target region. Technical, economic, and spatial datasets are typically sourced and collated from various providers for a specific regional grid. In some cases, grid information may not be publicly accessible, necessitating contact with official organisations to request further details.

II. Temporal and spatial resolution

The WEM should be dynamic and flexible to closely simulate real operating conditions. To achieve this, the temporal and spatial resolutions of both the wildfire risk distribution and the power grid should be selected at appropriate levels. The temporal and spatial resolutions of wildfire risks are determined based on the resolution of the selected index. Wildfire risk indices from ECMWF are set by the resolution of the model used in the reanalysis, where observational data are assimilated into the forecast model. In most power grid studies, the temporal resolution is hourly or half-hourly. Therefore, the resolutions of the grid model and wildfire risk indices should be adjusted accordingly to ensure model consistency.

III. Forecasting tools with climate resilience

As discussed in Research Question II, accurate load forecasting with climate resilience is crucial for safe grid operation under extreme weather risks. Innovations in both model structures and multiple factors in the model input should be pursued to develop an energy forecasting tool that is still reliable under extreme weather conditions. State-of-the-art model structures should be reviewed and compared. Regarding multiple factors, most existing studies test various factors' contributions to forecasting performance without examining the relationships between them. It would be more effective to explore the relationships between energy patterns and selected climate factors before incorporating specific factors into the input of the forecasting model.

IV. Adaptability

While some countries are densely populated and rely on conventional large transmission networks, others are sparsely populated and make extensive use of distributed generation systems. The WEM should be tested across various case studies to ensure its adaptability and generalisation across a range of population densities and network distribution scenarios.

V. Relationships between wildfire risk and grid operational constraints

Limited existing literature has begun to explore the enhancement of power grid resilience using smart measures. For example, Rhodes et al. attempted to improve system resilience during wildfire seasons by employing power shut-off methods to sustain the operation of critical load delivery as much as possible [25]. However, they provided no clear justification for the power shut-off procedure. The relationship between wildfire risks and deficiencies in grid operation requires further study. For instance, what should be the appropriate threshold to trigger precautionary or protective actions? Under what circumstances should the line be switched off, and subsequent smart measures adopted? Can we establish a theoretical relationship between wildfire risk and grid control strategy?

1.3 Research goals

The ultimate research goal is to develop a generalised Wildfire Energy Model (WEM) capable of assessing and enhancing grid resilience under extreme wildfire risks through the application of distributed generation. To address the three sub research questions, the WEM is constructed in four phases, as outlined in detail in Chapters 3, 4, 5, and 6 (Research question III is addressed in Chapters 5 and 6). Figure 1.1 illustrates the sub-research goal for each phase of the DPhil study.

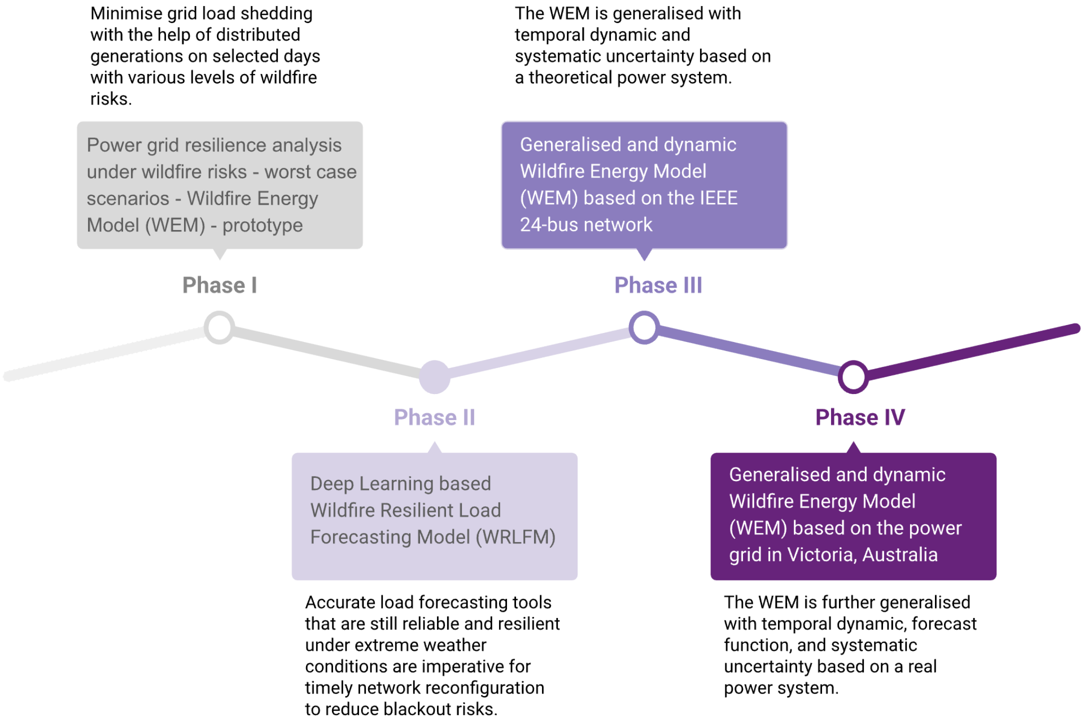

Figure 1.1: Research goals through four main phases of the DPhil study

In Phase I, the prototype WEM is developed to simulate grid performance under wildfire risks in worst-case scenarios based on real grid data from Victoria, Australia. As the fire risk index is provided in the format of a daily peak, the worst-case scenarios are tested on selected days with varying levels of wildfire risk. Distributed energy resources are employed to minimise load shedding and maximise system cost benefits. In Phase II, the Wildfire Resilient Load Forecasting

Model (WRLFM) is developed by applying comparative deep learning methods and incorporating multiple factors into the model inputs. With accurate load forecasting tools, grid operators can reconfigure system structures to manage variability caused by extreme weather risks in time. In Phase III, the prototype WEM is upgraded into a generalised and dynamic model, based on a theoretical grid case study. While the prototype WEM remains static for worst-case scenarios, the generalised WEM is simulated hourly with high-resolution grid and wildfire risk models. System-wide uncertainty is managed through probabilistic power reserve analyses. In Phase IV, the main research goal is achieved by applying and validating the generalised and dynamic WEM in a real grid day-ahead case: the Victoria's power system during the 2019-2020 wildfire season. The robust forecasting model developed in Phase II is embedded into the final phase, enabling the operators to determine proper grid resilience enhancement methods in advance during high wildfire risk periods. The WEM is proven to be an adaptable and universal model capable of evaluating and enhancing grid resilience under extreme wildfire risks, with technical, economic, and environmental benefits.

1.4 Use cases

As discussed in Section 1.1, California and Australia experience catastrophic wildfire seasons annually. The spatial, technical, economic, and historical dispatch data for the Australian grid is relatively accessible. Therefore, regions in Australia have been selected for test cases, facilitating the generalisation and refinement of the prototype WEM. Victoria, being one of the Australian states most affected by wildfire risks, has been chosen as the study area for this DPhil research.

To illustrate the detailed methodology for forming an optimal power flow model, theoretical IEEE grid cases are tested and studied as paradigms. In Phase III, the generalised WEM is developed based on the IEEE 24-Bus Reliability Test System (RTS) [26], demonstrating a standardised process for implementing dynamic power modelling and integrating wildfire risk information into the grid operational model.

1.5 Thesis arrangement

The first chapter outlines the motivation and background for this DPhil study, as well as the research questions, challenges, and objectives. Following this, a comprehensive literature review is presented in Chapter 2, covering energy systems, wildfire risk calculations, weather-affected grid analysis, and energy forecasting techniques. Based on this review, specific research gaps are identified, and potential innovative solutions are proposed.

Chapters 3, 4, 5, and 6 comprise the core methodology and analysis of the DPhil study. Each chapter reviews the main methodologies used in each phase, provides detailed references for the data used in the case studies, and offers comprehensive discussions of the results. Chapter 3 presents the prototype WEM analysis based on worst-case scenarios. This chapter is mainly based on publication, since a journal paper has been published for Phase I. Chapter 4 covers the development of the WRLFM, employing comparative deep learning structures and incorporating multiple factors. This chapter is also publication-based, with one journal paper and one conference paper generated from Phase II. Chapter 5 focuses on the primary methodology for forming a generalised and dynamic WEM using the IEEE theoretical grid case. Detailed steps are provided to develop a high-resolution grid model and calculate high-resolution fire risk models from fundamental climate variables. Chapter 6 further generalises the WEM by applying it to the real Victoria grid. To emphasise the practical relevance of the generalised WEM, the forecasting model developed in Phase II is integrated into the WEM in Phase IV to implement a day-ahead grid reserve assessment under wildfire risks. The generalised WEM is validated across multiple dimensions, demonstrating its advantages from technical, economic, and environmental perspectives. The main research question is addressed in Chapter 6 using the generalised and dynamic WEM.

Chapter 7 summarises the key findings from each phase of the study. A cross-phase discussion follows, synthesising the model development logic and overall results. The main contributions of this thesis are summarised to answer research questions raised in Chapter 1. Finally, the limitations of the study and suggestions for future development are discussed.

2

Literature review

Contents

In Chapter 2, fundamental concepts and relevant literature are reviewed. Section 2.1 and Section 2.2 provide an overview of power systems and wildfire risks. Basic concepts and related methodologies are discussed to enhance understanding of power system modelling and wildfire risk calculation. In Section 2.3, literature on weather-affected power systems is reviewed to summarise contemporary methods for assessing power system resilience under extreme weather conditions, with a particular focus on wildfire-affected power grid analysis. Additionally, proposed solutions to mitigate the impact of wildfires on grid operations are reviewed, encompassing both practical applications in grid operations and academic research methodologies. Section 2.4 examines state-of-the-art techniques for electricity forecasting. Existing methods that consider climate impact in electricity forecasting are analysed. As multiple sources contribute to uncertainty in forecasts, both conventional and probabilistic grid reserve analysis methods are discussed to determine appropriate grid reserve capacity, thereby enhancing grid resilience.

Regarding wildfires, the simulation is more complex due to the presence of numerous uncertain anthropogenic factors, unlike other more common extreme events such as winds and storms. Few studies have comprehensively examined grid resilience in the context of wildfires. Consequently, Section 2.5 identifies the research gaps and proposes potential solutions.

2.1 Overview of power systems

2.1.1 The structure and characteristics of power system

Power grids are deployed to deliver electricity from the generation site (power stations) to the demand side (households, industries, etc.). As shown in Figure 2.1, most power grids in the world are currently operating in a traditional one-way system. Centralised power plants generate electricity that travels through high-voltage transmission networks (red lines), arrives in distribution networks (black lines), and is finally delivered to a large number of end-users [27].

The power balance between load and supply is essential for maintaining stable grid operation. In addition, power grids are topologically interconnected, and a

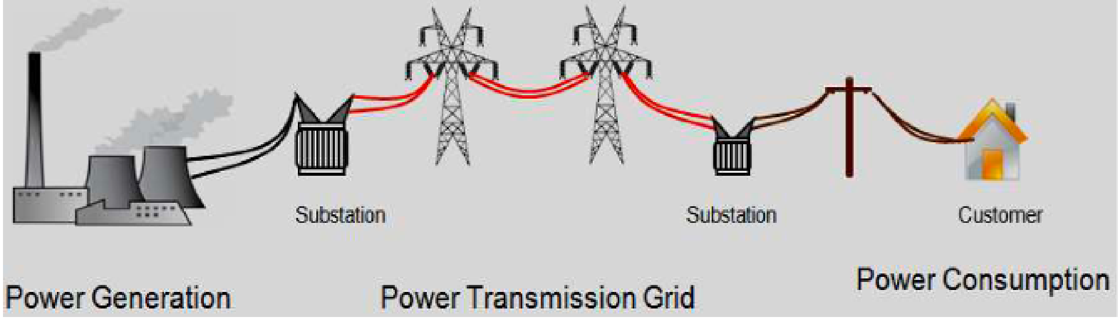

Figure 2.1: Traditional one-way power grid structure [28]

series of machines operate synchronously at a fixed frequency. For example, as described in Swing Equation [29], once a disturbance occurs in the grid, the rotor of generators will accelerate or decelerate accordingly to maintain grid stability. Therefore, timely measures should be implemented for each minor disturbance under extreme weather conditions to prevent large-scale outages.

2.1.2 Renewable energy and microgrids

Renewable Energy Sources (RESs), such as solar, hydropower, wind, and biomass are considered a cost-effective and viable means to accelerate the global energy transition towards net zero [30]. Despite the impact of the pandemic, RESs were the only energy source that increased in 2020, demonstrating their resilience to extreme events such as COVID-19 lockdown measures [31]. Beyond mitigating global warming, RESs can also foster long-term socio-economic development. The International Renewable Energy Agency (IRENA) has projected that the rapid expansion of RESs will increase social income by 15% and create approximately 19 million new employment opportunities by 2050 [32].

While the benefits of RESs have been highlighted, there are still some drawbacks to consider when applying these technologies in real grid operations. The power output from natural resources varies annually, seasonally, and even diurnally, resulting in the inherent intermittency and uncertainty of RESs [33]. To mitigate these issues, Energy Storage Systems (ESS) or microgrids incorporating multiple RESs can be utilised. For instance, excess electricity generated by wind farms around midnight can be stored in ESS and utilised later during peak demand periods. The integration of diverse generation sources also contributes to system balance, as different types of DGs have distinct power output patterns. For example, solar power is generated during the daytime, wind energy is typically abundant at night, and biomass provides a relatively controllable source to address shortages on cloudy, windless days. Bahramara et al. [34] have demonstrated the economic and environmental feasibility of a Hybrid Renewable Energy-based Microgrid (HRE-MG) system—comprising solar, wind, hydro, fuel cells, diesel generators, and ESS—in either on-grid or off-grid modes.

According to the U.S. Department of Energy, a microgrid is a localised grid that connects to the main grid but can also disconnect and operate autonomously when the main grid is down [35]. Microgrids are composed of various distributed energy sources, such as wind turbines. They can enhance grid resilience by providing a faster system response to mitigate grid disturbances, functioning as a flexible energy source. Therefore, this DPhil research aims to explore appropriate operational strategies for green microgrids to protect grids from extreme wildfire conditions.

2.1.3 Power system resilience and reliability

In Bie et al. [18], power system resilience is defined as the ability to anticipate, resist, adapt to, and promptly recover from disruptions, e.g., extreme weather attacks and electrical faults. Reliability is a traditional concept in power grids used to evaluate the quality and quantity of electricity delivered to meet demand [36]. Both concepts are crucial for assessing power grid performance, albeit with different focuses. While grid resilience emphasises the capacity to resist and recover from rare and extreme events, grid reliability indicates the consistency of normal system operations. Commonly used reliability metrics include the Customer Average Interruption Duration Index (CAIDI), the System Average Interruption Duration Index (SAIDI), and the System Average Interruption Frequency Index (SAIFI), which generally exclude outages caused by extreme events [37]. Commonly used resilience metrics include the time-to-restoration, the degree of resilience deterioration and so on [38, 39].

A highly resilient system is not necessarily reliable, and vice versa. For instance, rolling brownouts may be acceptable in a resilient power system as long as the power supply can be quickly restored [36]. Given that extreme wildfires are a critical condition for our research, grid resilience will be the primary criterion for assessing grid performance under extreme conditions as the traditional concept, reliability, is analysed during normal operational conditions. Nonetheless, reliability remains an essential parameter as it reflects the consistency of safe grid operation. Common metrics for assessing grid reliability and resilience are reviewed in Table 2.1 and Table 2.2 [18]. These metrics provide a standardised approach to measuring grid resilience and reliability in various case studies. Such quantitative metrics are helpful in evaluating the effectiveness of measures and comparing the resilience levels among different power networks.

Table 2.1: Common metrics of grid reliability

Name	**Equation**	**Definition & comments**
System Average Interruption Duration Index (SAIDI) [40]	$SAIDI = \frac{\sum U_i N_i}{N_T}$ (Hour)	Average annual total duration of outages per customer. i: the location, U_i: the annual outage time, N_i: the customer numbers at the i^{th} location, N_T: the total number of the customers served
Loss Of Load Expectation (LOLE) [41]	$\sum_{i=1}^{N} P[C_i < L_i]$ (Hour)	Expected number of days/hours in a pre-defined period that demand is not met by supply. N: the number of days/hours, P: the probability function, C_i: the available capacity on the i^{th} day/hour, L_i: the daily/hourly peak demand [42]

System Average Interruption Frequency Index (SAIFI) [43]	$SAIFI = \frac{\sum N_{ci}}{\sum N}$	Average annual total number of outages per customer. N_{ci}: the total number of customer interruptions, N: the total number of served customers
Customer Average Interruption Duration Index (CAIDI) [43]	$CAIDI = \frac{\sum U_iN_i}{l_iN_i}$ (Hour)	Average time to recover once an outage occurs for a specific customer. U_i: yearly outage time, N_i: the number of customers, l_i: failure rate, i: the location
Customer Average Interruption Frequency Index (CAIFI) [44]	$CAIFI = \frac{\sum N_{ci}}{\sum N_{dc}}$	Frequency of power supply interruption for customers who have at least experience one power outage. N_{ci}: the total number of customer interruptions, N_{dc}: the number of distinct customers interrupted (customers who experience at least one power outage)
Customer Total Average Interruption Duration Index (CTAIDI) [44]	$CTAIDI = \frac{\sum U_iN_i}{N_{io}}$ (Hour)	Cumulative average interruption duration for customers who have at least experience one power outage. i: the location, U_i: yearly outage time, N_i: the number of customers, N_{io}: the customer number that were interrupted
Average Service Availability Index (ASAI) [45]	$ASAI = \frac{\sum N_i \times 8760 - \sum U_iN_i}{\sum N_i \times 8760}$	Ratio between total available customer hours and demanded hours. i: the location, U_i: yearly outage (hours), N_i: the number of customers
Average Service Unavailability Index (ASUI) [44]	$ASUI = \frac{\sum U_iN_i}{\sum N_i \times 8760} = 1 - ASAI$	Ratio between total unavailable customer hours and demanded hours. i: the location, U_i: yearly outage (hours), N_i: the number of customers

Momentary Average Interruption Frequency Index (MAIFI) [44]	$MAIFI = \frac{\sum N_{ci}}{\sum N_c}$	Cumulative interruption amount experienced by a customer in a defined period. N_{ci}: the total number of customer interruptions (momentary - less than a specific time), N_c: the total number of customers served

Table 2.2: Common metrics of grid resilience

Name	Equation	Definition & comments
Resilience triangle (resilience impact) [46]	$I = \int_{t_E}^{t_R} [Q_N - Q(t)]dt$	I is the quantified resilience impact. t^R: time of restoration completion, t_E: starting time of the event, Q_N: grid normal functionality, $Q(t)$: grid functionality at time t
Availability based Resilience Index [47]	$\rho = \frac{A_1}{nln(t1)} \sum_{i=1}^{n} \frac{A_2^i A_3^i}{ln(t_3^i - t_2^i)}$	ρ is the ultimate availability-based resilience index. A_1, A_2, A_3: the availability at the steady-state, the after-shock transient state and the new balance state. t_1: steady-state time. $t_3 - t_2$: measured static post shock time. $i \in [1, n]$, n is the number of shocks
Resilience trapezoid [38]	$FLEP(\Phi \Lambda E \Pi)$ $\Phi = \frac{R_{pdo} - R_{0_o}}{t_{ee} - t_{oe}}$ (MW/hour) $\Lambda = R_{0_o} - R_{pdo}$ (MW) $E = t_{or} - t_{ee}$ (hour) $\Pi = \frac{R_{0_o} - R_{pdo}}{T_{or} - t_{or}}$ (MW/hour)	A group of resilience metrics to measure the system performance during various phases of the trapezoid. $R_{0_o} - R_{pdo}$: the degree of resilience deterioration. $t_{ee} - t_{oe}$: period of disaster. $t_{or} - t_{ee}$: period of the post-threat degraded state. $T_{or} - t_{or}$: period of the restoration state

The power ratio between targeted and real performance [48]	$P_\omega = \frac{\sum_{m=1}^{M} \frac{1}{N} \sum_{n=1}^{N} P_d(m,n)}{\sum_{m=1}^{M} P_{(m)}} \times 100\%$ (%)	P_ω: percentage of power supply. $m \in M$: the area of services. $n \in N$: simulation numbers. $P_d(m,n)$: power output of the area m under the n^{th} simulation. $P_{(m)}$: power output of the area m under normal condition
Topological resiliency [49]	$G = (N, E, W)$ $D = \frac{2\|E\|}{\|N\|(\|N-1\|)}$ $l_G = \frac{\sum_{i \neq j} d(n_i,n_j)}{N(N-1)}$ $C_n = \frac{2e_n}{k_n(k_n-1)}$	Graph G comprises of a set of nodes N and edges E. W: weights (power flow of each section). D: graph diameter. l_G: average path length of the graph G. $d(n_i, n_j)$: distance between the node i and j. C_n: clustering coefficient. e_n: number of connected pairs between all neighbours of a node n. k_n: number of neighbours of node n
Network resiliency probability [50]	$R_\alpha = \sum_\beta P(\phi(x) \geq d \| \alpha, \beta) P_\beta$	R_α: expected resiliency in the presence of α failure. β: unique non-repeating combination. d: network performance requirement. $\phi(x)$: network capacity under system state vector x
Time-to-restoration [39]	N/A	Based on historical outage and recovery records

As summarised in Table 2.2, several studies evaluate grid resilience; however, most focus on grid deterioration during disturbance events or on the restoration process. Few address fault prevention at the pre-disturbance stage, indicating a need for further research into preventive resilience measures. Moreover, existing methods typically employ technical metrics — such as restoration time and functionality loss — while economic, social and environmental dimensions remain under-explored. Therefore, more comprehensive resilience metrics are required to establish a systematic evaluation framework for power utilities.

In Bie et al. [18], methods for enhancing grid resiliency were comprehensively reviewed and primarily classified into two categories: system hardening and operational resilience strategies (also referred to as hard resilience and soft resilience). Hard resilience strategies encompass measures such as undergrounding lines, upgrading poles with more robust materials, adding grid redundancy, tree trimming, and elevating substations. These strategies enhance the durability of transmission and distribution networks. For instance, during a snowstorm that struck Southern China in 2008, there were 129 line faults, leading to power loss for 14.66 million households [51]. Subsequently, higher ice-resistant transmission lines and towers, as well as ice-melting equipment, have been widely adopted to improve grid resilience in areas prone to snowstorms [18].

System hardening strategies are often costly and typically suited to a single type of extreme events. Therefore, soft strategy, such as emerging smart grid technologies, must also be integrated with hard measures, e.g., microgrid islanding operation, demand side management, fault location, isolation, restoration, etc. Bie et al. proposed the Distribution System Resilient Load Restoration Framework as a soft grid resilience strategy, utilising reconfiguration and DG islanding [18]. Further information on optimising distribution system performance through DG and load reconfiguration can be found in [52], [53], [54], [55], and [56]. More discussion on solutions to enhance grid resilience against extreme wildfire risks will be provided in Section 2.3.3.

2.1.4 Electrical faults and wildfire ignitions

As discussed in Chapter 1, global ageing energy infrastructures are becoming increasingly vulnerable to the rising intensity and frequency of extreme wildfire conditions, resulting in significant economic and social losses. Most devastating wildfires are initiated by electrical faults [57]. In California, power line fires accounted for 8% of all ignitions in 2015, but they were responsible for 51% of the total wildfire burnt area (approximately 150,000 acres) [58]. Similarly, in Australia, power line fires cause 10% of wildfire ignitions yet represent 90% of fatal wildfires [57]. Southern Californian power utilities and fire agencies have identified the reasons for the correlation between electrical faults and catastrophic wildfires [59]. Electrical faults are more likely to occur under hot, dry, and windy conditions. For example, line overloading is more prevalent during peak fire seasons, increasing thermal stress and leading to a higher probability of line sagging and flashovers [60]. Additionally, strong winds elevate the likelihood of conductor slap faults, where the ejection of hot materials from electrical faults ignites wildland fuels. The weather conditions increase the risk of electrical faults and ignition probability simultaneously, contributing to the rapid spread of wildfire. Consequently, electrically-induced wildfires tend to be larger than those caused by other means.

Most electrical faults related to wildfire disasters occur in transmission and distribution networks. Large fires can cause physical damage to grid-supporting structures, such as poles and towers, resulting in the collapse of power lines. However, even without direct physical damage, the heat, smoke, and particulate matter from a wildfire can disrupt normal grid operations [12]. For instance, soot accumulation on insulation can create a conductive path for leakage currents, leading to line shutdowns. Additionally, smoke may alter the dielectric properties of the surrounding air, causing line-to-line or line-to-ground arcing [61]. Fire retardants dropped from firefighting aircraft can also affect line capacity. Even if not overloaded, the line sagging caused by high fire temperatures may violate safety clearance between lines and surrounding vegetation, increasing the risk of contact faults and arcing [62].

While high wildfire risk conditions can lead to grid outages and losses, electrical faults can sometimes cause wildfire ignitions. For instance, in the summer of 2020, a transformer explosion in Utah Valley triggered a wildfire, resulting in utility property damage and large-scale evacuation [63]. Muhs et al. [60] characterised the probability of wildfires ignited in a power distribution network using a sensitivity analysis that included factors such as wind speed, line congestion, and grid protection and reclosing. The study demonstrated that mid-range wind speeds, line overloading, and extended arc duration due to inadequate protection could increase the likelihood of line-induced wildfires. However, this research was based on the IEEE 33-bus distribution system and 24-hour weather observation data from a region near Paradise, California, in 2018. A case study based on a real grid in fire-prone areas with a more extended simulation period could be implemented in the WEM for a more comprehensive and convincing discussion.

2.2 Overview of wildfire risk calculation

This section discusses and analyses the distribution of global fire risks and their primary causes for several typical fire-prone regions. Wildfire risk indices and calculation methods are reviewed and categorised to understand the dynamics and principles underlying each index. These indices are compared to select the most appropriate one for the following WEM-related studies.

2.2.1 Current global fire risk distribution and pattern

According to the NASA Earth Observatory, the average fire size across the globe from 2003 to 2016 is displayed in Figure 2.2, illustrating the recent global distribution of wildfires [64]. Large fires tend to occur in grasslands and steppes in Africa, Kazakhstan, and Russia. Wildfires in boreal forests in North America (Canada and the western United States) and Siberia are also likely to be widespread.

In 2020, the global direct cost of wildfires amounted to approximately $17 billion, making it the fifth costliest year on record for wildfire losses. This was primarily due to extreme wildfire activities in Australia, the western United States, Brazil, and the Arctic. Despite the high costs, 2020 experienced below-average wildfire activity, as several commonly fire-prone regions had a notably low level of wildfires that year [65]. According to the Copernicus Atmosphere Monitoring Service, tropical Africa

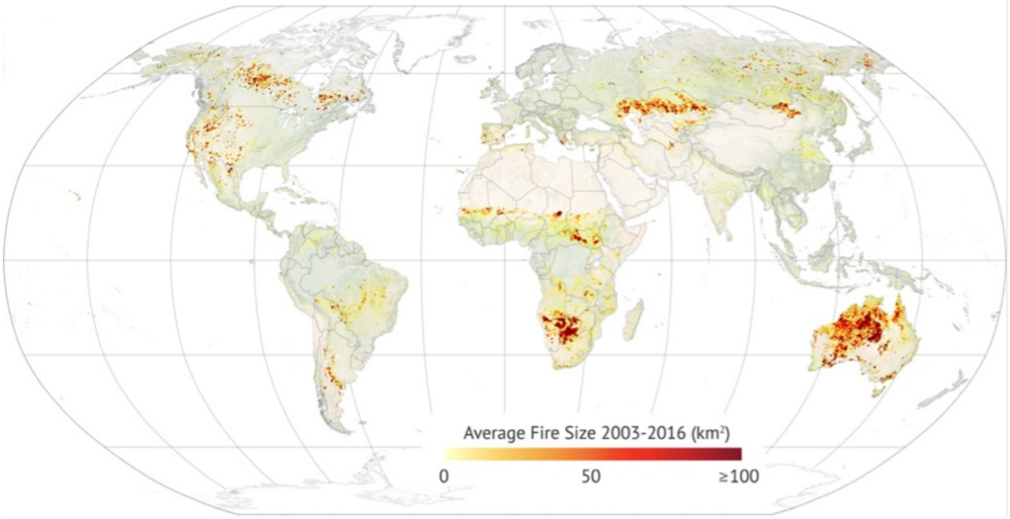

Figure 2.2: The Global Average Fire Size, ranging from Zero (White) to 100 km^2 (Red) [64]

and Canada had deficient wildfire activities in 2020 compared to previous records [66].

Regarding global wildfire distribution, a specialised discipline known as pyrogeography examines the past, present, and future of spatiotemporal fire distributions through multi-factor analysis. Krawchuk et al. [67] identified three main factors contributing to the distribution and spread of wildfires: flammable vegetation resources, environmental conditions conducive to combustion, and ignition. In addition to these natural conditions, many previously fire-free areas now experience wildfires due to increasing anthropogenic pressures, such as uncontrolled land clearing, campfires left unattended, negligently discarded cigarettes, malfunctions of equipment use, and intentional acts of arson [68]. Thus, it is essential to assess these factors and understand the primary causes of wildfires when examining a fire-prone region. Major ignition sources in typical fire-prone areas are illustrated in Figure 2.3 [69], [70], [71], [72], [73], [74], [75], [76]. It is noteworthy that certain levels of wildfire are crucial for ecosystems in fire-adapted biomes, making the complete elimination of fires undesirable. For instance, chaparral vegetation is well adapted to wildfires and can regenerate rapidly after burning. This shrub-dominated, evergreen vegetation is common at mid-elevations in California, covering

3.4 million hectares [77]. Therefore, it is imperative to ensure the optimal operation of the electricity network under such conditions.

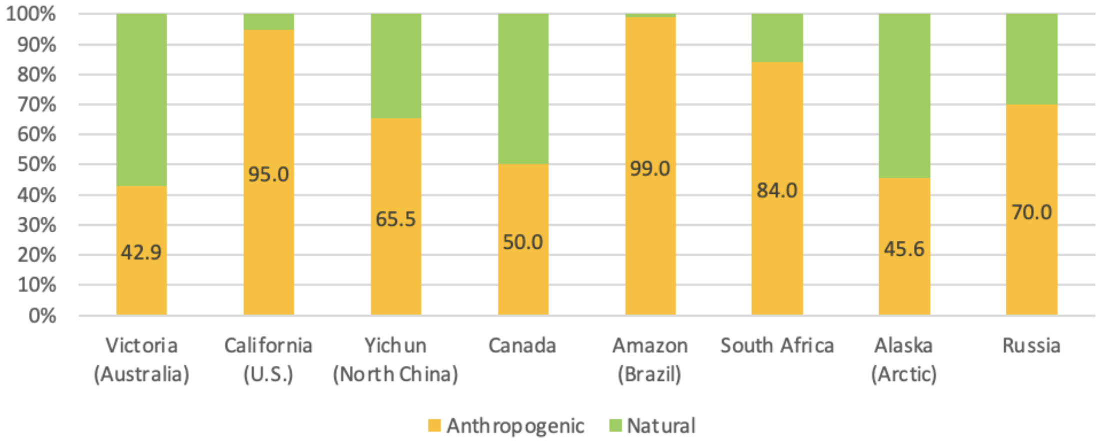

Figure 2.3: Wildfire ignition sources in fire-prone regions

2.2.2 Overview and characteristics of up-to-date fire rating systems

i. The Canadian Forest Service Fire Weather Index Rating System (FWI)

The Fire Weather Index (FWI) System was first developed in 1970 as part of the Canadian Forest Fire Danger Rating System (CFFDRS). The FWI System aims to quantify the effects of weather on forest fires and fuels by using measurements of temperature, relative humidity, wind speed, and 24-hour precipitation taken at noon Local Standard Time (LST). The daily FWI value is then calculated to predict the peak burning conditions of the day, around 4 pm LST. As illustrated in Figure 2.4, the FWI System comprises six main components, including three fuel moisture codes and three fire behaviour indices [78].

ii. The Australian McArthur Rating Systems (Mark 5)

McArthur's Forest Fire Danger Rating Systems were initially developed to assess wildfire severity across Eastern Australia. Under the Mark 5 Rating Scheme, the McArthur Forest Fire Danger Index (FFDI) is designed to calculate the probability of fire initiation, intensity, spread rate, and suppression difficulty (developed in 1980). Similar to the FWI, the calculation process of the FFDI also considers

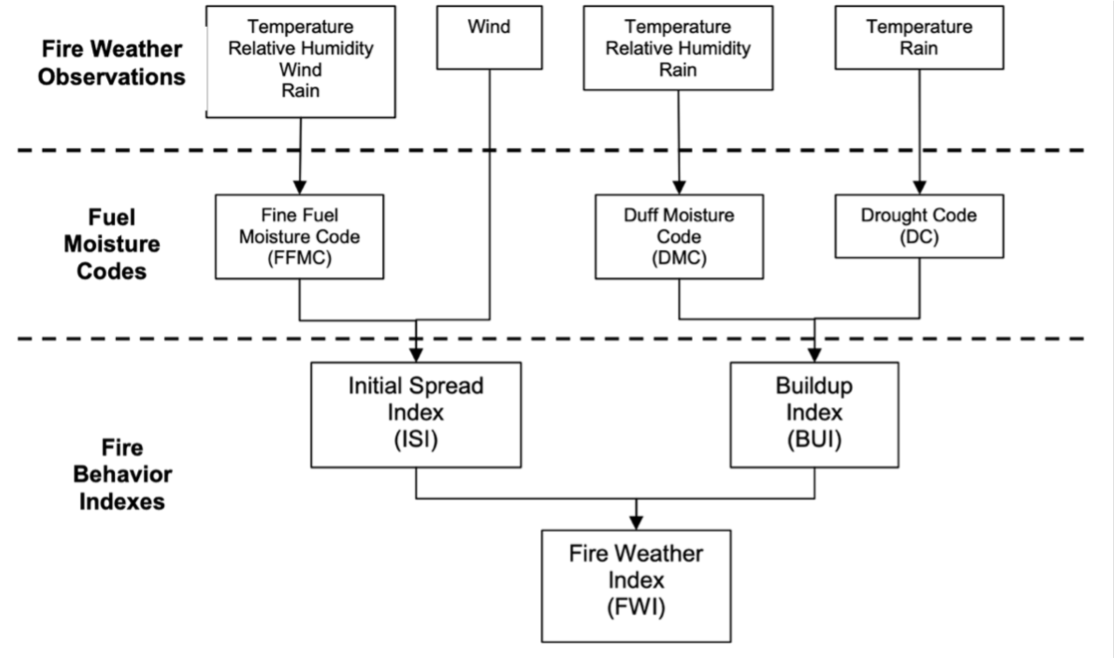

Figure 2.4: Structure of the Canadian Forest Service Fire Weather Index Rating System (FWI)

temperature, relative humidity, and wind speed. However, the primary difference is that the FFDI utilises the Drought Factor (DF) instead of the 24-hour precipitation used in the FWI to represent the effects of both long-term and short-term droughts [79].

iii. The U.S. Forest Service National Fire-Danger Rating System (NFDRS)

The NFDRS was first introduced in 1972 to describe fire danger in the United States. It combines fuel, weather and topography factors to quantify the risk of ignition [80]. To be more specific, fuel information includes fuel type and fuel moisture. Weather-related inputs include temperature, relative humidity, and wind speed. Topographic factors like slope and elevation are considered risk calculation inputs. Within the NFDRS framework, the Burning Index (BI) is derived from a combination of the Energy Release Component (which represents the energy contained in the fuel) and the Spread Component (which indicates the rate of spread). Related to flame length, BI represents the level of effort required to contain a fire. The indices and components of the NFDRS are linear, as changes in their values directly correspond to changes in risk levels (e.g., a BI of 60 indicates twice the difficulty in fire suppression compared to a BI of 30) [79].

2.2.3 Wildfire risk index comparison and selection

The FWI, FFDI, and BI are all crucial indices for fire risk assessments globally. Each index originates from different developmental environments, emphasising various factors resulting in different sensitivities and performances. The strengths, descriptions, and limitations of these indices are summarised in Table 2.3. As the foremost goal of this DPhil research is to develop a generalised and universal model, it is essential to focus initially on one index to ensure consistency across case studies. The development of the WEM is intended to be versatile and flexible, allowing for improvements and adjustments to the index or enabling the output to be directly integrated with alternative fire forecast models.

Table 2.3: Summary of fire indices

Index	**Strength**	**Description**	**Limitation**
FWI	The most widely used index for public information about fire dangers	Numerical rating of fire intensity	Cannot be expressed in a single equation as simply as the FFDI case
FFDI	Can be expressed in a single formula. It has an explicit standardised set of classification for risk dangers	Numerical rating related to the chance of ignition, rate of spread, intensity, and suppression difficulty	Indicates less severe conditions than FWI where the climatological index is relatively low
BI	Intuitional (rate directly related to risk)	Metrics of flame length in feet of the fire head	Only consider the intensity and spread after the fire start rather than the risk of initiating a fire

Overall, FWI has been selected as the most appropriate index for the initial assessment of wildfire risks in the WEM. The performance of the FWI System has been validated in case studies across various regions on top of Canada [81], [82]. Additionally, FWI has demonstrated superior performance in comparative studies of different fire indices [83]. Compared to the FFDI System, originally developed in Australia, the FWI System performance has also proven effective when tested in Australian contexts [84]. Moreover, many developed wildfire indices chose to build on the FWI System. For example, the England and Wales Fire Severity Index (FSI) utilises the FWI structure to predict wildfire risks, with the Met Office claiming that the FWI is the most effective index for identifying high-fire risk periods in England and Wales [85]. Thus, the FWI has been selected as the primary rating index for simulating wildfire conditions in this DPhil study, aiming for universality and generalisation. The utilisation of this index is intended to be flexible, allowing for the incorporation of improved indices or alternative forecast products as appropriate.

2.3 Weather-affected grid model

In this section, we begin by reviewing the impacts of various types of extreme weather on power network operations. We then focus specifically on existing work about power grid analyses under high wildfire risk, as wildfires are the selected extreme weather type for this DPhil research. Research gaps are identified based on a comprehensive literature review concerning the assessment and enhancement of power grid resilience in the face of wildfire risks.

2.3.1 Various weather risk impact on power grid operation

This section examines the effects of extreme weather on energy systems from the perspectives of generation, transmission, distribution, and demand behaviour. Furthermore, while emissions from the energy sector exacerbate climate change in the long term, some electrical faults can also trigger extreme weather events. The bidirectional impact between energy systems and extreme weather is discussed in this section.

Extreme weather events can damage various parts of the power grid. In addition to physical damage, generation characteristics and demand behaviours can also be indirectly affected, increasing the complexity of power system dispatch. According to a U.S. based study [86], 62.1% of outages lasting over 8 hours co-occur with extreme weather events, particularly heavy precipitation, anomalous heat, and cyclones. Conversely, some electrically-caused faults can initiate extreme weather events, resulting in high economic and social costs.

Typical extreme weather events that weaken the safety of power grid operations include floods, ice storms, cyclones (wind), heatwaves, droughts, wildfires, and so on [10]. Each type of weather event impacts different aspects of the power system. The major concerns for each are summarised in Table 2.4.

Table 2.4: Main impacts on power grid due to various extreme weather events

Extreme weather type	**Major concerns**	**Example**
Flood	Inundated substation	A four-day power cut in Lancaster, UK due to an inundated substation in 2016. More than 100,000 people affected [87]
Extratropical cyclone (wind)	High-voltage/ extra high-voltage transmission network (e.g., lines contact failure & pole collapse)	Storm Arwen & Eunice hit the UK in 2021 & 2022: over one million customers' power connections got disrupted [88]
Ice storms	Frozen generators Surging demand Freezing rain on lines	Taxa's Power Failure due to the winter storm in 2021 [89]
Heatwaves	Reduced line capacity surging demand	The worst heatwave clipped 80% of power generation capacity in Sichuan Province, China in 2022 [90]

Droughts	Hydro power shortage, additional transboundary fossil fuel generation needed	Drought-induced power shortage led to 65% more fossil-fuel based electricity consumed in the Western U.S., which was imported from other regions [91]
Wildfires	Direct damage on grid equipment & indirect damage: heat, smoke, and particle matter related faults	2019-2020 devastating wildfire seasons, resulting in over 20,000 household disconnections in Victoria, Australia [14]

2.3.2 Literature review on power grid analysis under high fire risks

Integrated simulations of power grids and wildfire risks are still in their early stages, with most research papers published after 2015. Various methods have been implemented in both distribution and transmission networks to calculate the probability of grid-related wildfire ignitions and the effects of wildfires on grids.

This paragraph reviews and discusses studies on wildfires in distribution networks. In 2015, Ansari et al. developed a two-stage stochastic optimisation model to find the most economic solution based on an IEEE 123-bus test distribution network using a heuristic qualitative wildfire risk approach [92], [93]. The two stages considered the reserve purchased by the utility in advance and then the power dispatch during the fire event. However, their model was only theoretical and not applied to a real power grid. More practical models could be developed by incorporating detailed spatiotemporal fire risk variations rather than relying on stochastic wildfire distributions [92]. In 2018, Trakas et al. established an optimal model to minimise grid load shedding during a wildfire emergency, considering the uncertainty from DGs and wildfire spread (including solar radiation, wind speed, and wind direction). This method was implemented on a modified IEEE 33-bus distribution network, considering the progression of the wildfire with some assumed probability distribution curves. It could be further applied to real power grids with historical risk data [94]. In 2020, Muhs et al. [60] determined the probability of electrically-caused wildfire ignition risks in distribution networks by combining the probability of a line fault with the probability of initiating a sustained ignition of vegetation near a line. Their model considered environmental conditions, power line protections, and power flow congestion and was tested on a 33-bus distribution system using historical wildfire data from a fire-prone area in California. Testing this model on an actual distribution network in California could provide more practical insights. In 2020, Teng [95] developed a stochastic mixed-integer linear program (MILP) wildfire-grid model based on a 33-bus distribution network, primarily considering the thermal effects of wildfires on power lines. A sensitivity analysis studied how the number of lines affected by wildfires and the availability of DG sources influenced grid resilience under wildfire risks. Teng's model considered the impact of radiative heat on dynamic line rating constraints. However, the methods to assess fire impact with uncertainty were based on assumed probability curves. The real historical risk index can be considered to enhance the model's practicality in the future. In 2021, Zhao and Barati proposed a real-time deep learning model to classify and localise electrical faults and then estimated the fault-related ignition probability in a rural distribution network [96]. The likelihood of wildfire ignition due to faults was evaluated based on the fault type and the corresponding released incident energy. The model's accuracy could be enhanced by incorporating more feature vectors beyond the single observability characteristic in the current algorithm [96]. In 2023, Bayani and Manshadi [97] proposed optimal long-term resilient expansion planning strategies for power distribution networks under prolonged wildfire risks, encompassing the addition of new lines, modification of existing lines, and installation of distributed energy resources. However, their study was conducted on the IEEE 118-bus test system rather than on real-world grids.

The previous paragraph focuses on issues in distribution networks, where most faults occur. However, some papers examine the situation in transmission networks, where the consequences of fires tend to be more severe than in distribution networks [98]. As illustrated in Equation (2.1), Rhodes et al. [25] calculated the wildfire risks of a transmission network by summing the risks from different components.

$$R_{Fire} = \sum_{d \in D} x_d R_d + \sum_{g \in G} z_g R_g + \sum_{l \in L} z_l R_l + \sum_{i \in I} z_i R_i \tag{2.1}$$

Where D, G, L and I stand for the set of demands, generators, transmission lines and buses; R represents the total risk from each component; z_g, z_l, z_i are the binary operational variables for generators, lines and buses, denoting the components are either energised or de-energised; $x_d \in [0, 1]$ indicates the fraction of active load (based on the operational mode of distribution networks). Rhodes et al. [25] devised intentional power shut-off methods to mitigate load shedding. However, the method was not sustainable due to the absence of DGs in the test system. In 2021, Tapia et al. [99] proposed a robust decision-support method to simulate and enhance the resilience of highly renewable transmission networks in Chile, considering the joint uncertainty of wildfire trajectories and intermittent renewable generation. Although the grid model was based on a practical transmission network in Chile, wildfire risk scenarios were generated using stochastic programming. In future studies, the wildfire model should refer to local historical wildfire data, as wildfire patterns differ regionally. Sathaye et al. [61] were the first to assess how long-term climate change impacts affect the risks to transmission lines attributed to wildfires in California. They overlaid Westerling's wildfire projection grid onto Californian electricity transmission networks. Westerling's wildfire projection dataset, developed by Westerling and colleagues [100], estimates the future probability of wildfire in California for three 30-year periods relative to a historical 30-year base period centred on 1975. Their results indicated a significant increase in the number and length of transmission lines exposed to wildfire risks over time. However, it is important to note that their findings are limited by the three 30-year period projections in Westerling's dataset, which confines the forecast to this simulation period. The results were presented as the accumulated values for each 30-year period [101], analysing the long-term but discrete trend of lines exposed to wildfire risks. Further analysis to learn how long-term climate change impacts fire-line risks should be upgraded by applying continuous climate change models. Dale et al. assessed current and future wildfire impacts on California's transmission and distribution networks by estimating regional wildfire risk using historical data of wildfires ignited near selected lines [102]. They proposed a comprehensive five-level classification of wildfire impacts on transmission networks, defining risk levels based on line voltages and potential damage extents. This classification is beneficial as it assigns corresponding economic losses in the generation and transmission of electricity based on different impact levels, which can be considered in power dispatch optimisation. However, their research mainly focused on assessing wildfire impacts rather than mitigation methods, targeting 40 selected transmission lines and seven urban "fringe" distribution systems in California [102]. Similar evaluation systems could be applied to a broader region for model generalisation with possible mitigation methods in future studies. In 2024, Yang et al. [103] proposed a two-stage stochastic programme for planning pre-emptive de-energisation using the RTS-GLMC test case for southern California, solved via an enhanced Lagrangian cut decomposition algorithm. However, the wildfire events were modelled merely as stochastic disruptions with random magnitude and timing. To improve model fidelity, it is recommended to integrate real grid information and actual fire-risk data into the fire-affected power system model.

2.3.3 Mitigation solutions for line induced wildfires and wildfire related power outages

Various mitigation strategies have been designed and applied to power grids in fire-prone regions. Common mitigation methods used by utilities include overhead line reinforcement, line undergrounding, more aggressive inspections, more frequent vegetation management, more accurate forecasting models for extreme weather risks, and community preparedness projects [25], [60], [104]. However, methods related to system structural upgrades, management, and forecast models are long-term plans that need to be implemented over years and are cost-prohibitive on a large scale. For example, a study by the Edison Electrical Institute (EEI) demonstrated that complete line undergrounding for an entire state's grid would be prohibitively expensive, costing billions of dollars [105]. To be more specific, it is estimated that it will take over $100 billion for PG&E to underground all its high voltage lines across their entire network (2/3 of California). Besides the significant expense, there is concern about the environmental effects of undergrounding in bio-diverse regions [106]. Although line undergrounding is one of the most effective ways to reduce the frequency of electrical outages, the restoration time for faults in underground cables increases due to the difficulty in detecting underground lines, especially in the event of flooding [104].

In addition to long-term planning strategies, some short-term day-to-day mitigations have been employed by energy suppliers to manage disruptive emergencies promptly. One such short-term solution is reducing or disabling automatic reclosing to prevent multiple arcing events at fault points [60]. However, this strategy neither prevents damage from the initial ignition nor addresses high-impedance faults (e.g., contact with road surfaces or trees) [107]. The only method to eliminate the risk entirely is to switch off the line, as de-energised components cannot initiate fires. Some Californian utilities, such as PG&E, began implementing intentional power shutoffs following devastating electrically-caused wildfires in 2017-2018. Utilities adopted more controlled "Public Safety Power Shutoff" (PSPS) strategies to prevent cascading outages and widespread wildfires. From 2013 to 2020, PSPS caused over nine billion customer outages, with an average outage duration of two days [108]. The effectiveness of PSPS in mitigating wildfires and outages has been demonstrated. However, for critical infrastructure such as water treatment plants and medically vulnerable populations who depend on electricity, microgrids should be integrated nearby to enable these communities to operate independently until power is restored.

2.4 Electricity forecast with multiple uncertain sources

Towards the pathway to NetZero, the power system faces significantly growing uncertainty due to generation diversification and demand electrification. Meanwhile, increasing extreme weather poses substantial challenges to reliable and resilient energy system operation, even resulting in unintentional power blackouts. Therefore, it is essential to develop intelligent and climate-resilient load forecasting tools to properly dispatch power in advance.

This section first reviews methods for forecasting energy demand using both traditional statistical techniques and state-of-the-art Machine Learning (ML) approaches. Subsequently, multiple factors that enhance forecast accuracy are discussed, with particular emphasis on incorporating climate resilience into the load forecasting model. Finally, methods for estimating sufficient power capacity for grid reserves are examined. Grid redundancy is critical, as load forecasts cannot achieve 100% accuracy in an environment with increasing uncertainty. Both conventional "N-1" methods and advanced probabilistic approaches are reviewed and compared.

2.4.1 State-of-the-art load forecasting: statistical and machine-learning based methods

Regarding the model for load forecasting, there are two primary approaches: traditional statistical methods based on time series analysis and Artificial Intelligence (AI)-based methods [109]. In [110] and [111], several widely used statistical forecasting techniques are discussed, including Multiple Linear Regression (MLR), Semi-parametric Additive Models (SAM), Autoregressive Integrated Moving Average (ARIMA), and Exponential Smoothing Models (ESM). Statistical forecasting methods are currently the most frequently employed tools. However, these methods may struggle to capture demand fluctuations caused by extreme weather events due to their implicit non-linear characteristics. These demand changes are not proportional because (1) once demand reaches a certain threshold, additional stress on infrastructure can amplify consumption patterns (fans used alongside AC if too hot), (2) Extreme weather impacts different regions and populations unevenly, and (3) High demand under extreme weather may trigger grid performance drop, i.e., voltage drop and outage, indirectly leading to the irregularity of electricity required.

To address non-linearity, data-driven methods such as shallow Machine Learning (ML) and Deep Learning (DL) have emerged in recent research. Common shallow ML methods encompass Support Vector Machine (SVM), Random Forest (RF) and Extreme Gradient Boosting (XGB) [112]. A Multilayer Perceptron (MLP) is the fundamental structure of DL methods to tackle classification and regression tasks [113]. DL methods have further evolved in two main directions: Recurrent Neural Network (RNN) specialised in handling sequential data and Convolutional Neural Network (CNN) proficient in capturing spatial data features, such as image recognition [114], [109].

Traditional RNNs face challenges in capturing long-range dependencies due to the vanishing or exploding gradient problem. More advanced architectures, such as Long Short-Term Memory (LSTM) networks and Gated Recurrent Unit (GRU) networks, have been introduced to address these issues. These architectures incorporate gating mechanisms that help control the flow of information through the network, allowing for more effective handling of long sequences and mitigating gradient-related problems. In [115], daily enterprise electricity consumption was predicted using RNNs and their two variants: LSTM and GRU. The results demonstrated that GRU outperformed the other two methods in forecasting accuracy. Similarly, [116] proposed a well-calibrated GRU model design to forecast day-ahead load based on the European Network of Transmission System Operators for Electricity (ENTSO-E). It was proven that the GRU-based method contributes to better forecast performance than both an ARIMA-based model and the day-ahead load forecast model used by ENTSO-E.

When employing RNN-based methods for time-series forecasting, it is important to address gradient issues. Gradient vanishing occurs when gradients become extremely small—especially in deep time dependencies—so that repeated multiplications drive them toward zero, preventing weight updates and halting learning. Gradient explosion arises when gradients grow through successive multiplications, leading to excessively large updates. Common remedies include appropriate weight initialisation, gradient clipping, layer normalisation, shorter sequence lengths, and learning-rate adjustment. Compared to traditional RNNs and LSTMs, the more recent GRU architecture mitigates gradient problems via its update and reset gates. These gates enable additive rather than purely multiplicative gradient flows, reducing the risk of vanishing or exploding gradients. Moreover, the GRU's simpler structure enhances numerical stability.

Although CNN-related methods were originally developed to process image data, they can be adapted to tackle sequential tasks with spatial information. For example, an LSTM-CNN-Autoencoder-based model was proposed in [117] to predict load for an energy distributor in Brazil. The model considered input with unequal lengths of time series, trained simultaneously by leveraging the specific structures. It outperformed statistical methods such as the Seasonal Autoregressive Integrated Moving Average with Exogenous Regressors (SARIMAX) and Prophet, as well as the Temporal Convolutional Network (TCN) model. In [118], a CNN-GRU-transfer-learning-based model was developed to predict multi-energy use in a data-deficient scenario. The model's performance was compared with ARIMA, GRU, LIBSVM (Library for Support Vector Machines), and DBN (Deep Belief Network), demonstrating its superiority.

Figure 2.5 outlines the main categories of recent trending load forecasting methods. The mechanisms for each forecasting method will be discussed in detail in Chapter 4, and therefore, will not be expanded upon here. Although many studies have proposed novel load forecasting methods, most existing research has only selected a few methods as comparison groups. Few studies have conducted comprehensive comparative analyses across a wide range of existing load forecasting techniques alongside their newly proposed methods, with systematic review and classification. When proposing a new load forecasting method, it is recommended to compare it with a broader range of load forecasting approaches.

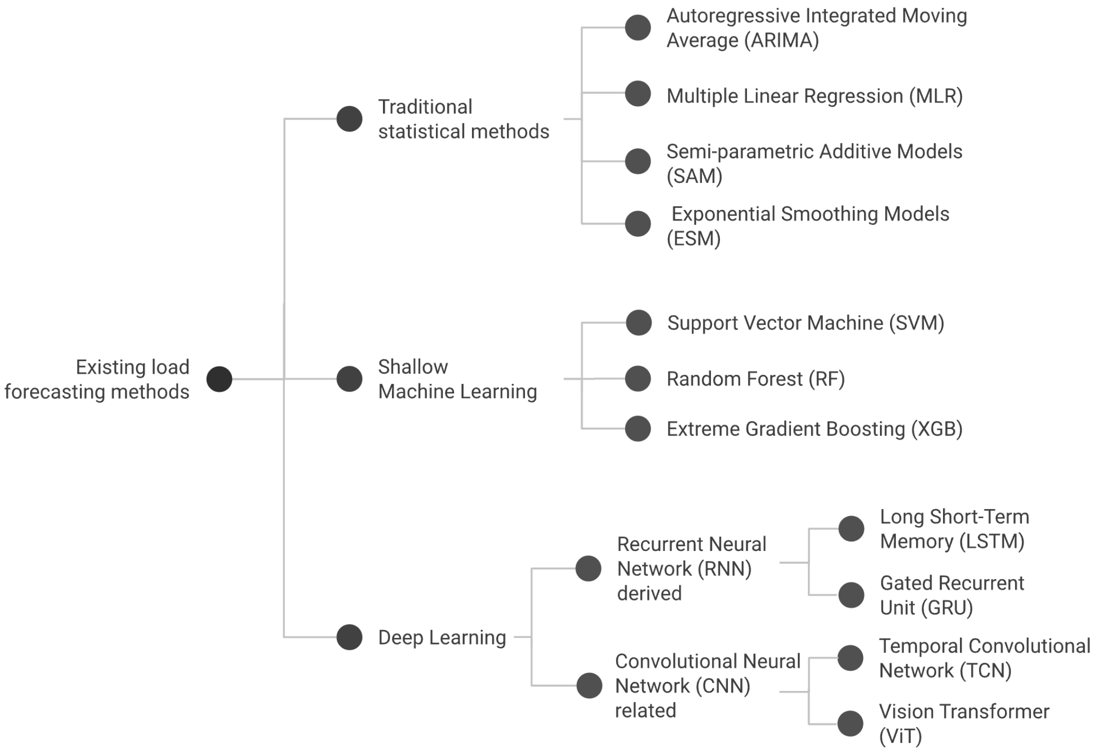

Figure 2.5: State-of-the-art load forecasting methods by categories

2.4.2 Incorporating climate resilience into energy forecasting

In addition to the novelty in model structures, the inclusion of multiple factors is crucial for enhancing forecast accuracy. Few studies have investigated the internal relationships between various factors and load behaviours before incorporating them as model inputs. For example, prior studies [119] and [120] typically used 24-hour ahead load data as the only default input due to its daily periodicity but had yet to explore the optimised design of input structures. Calendar effects have been applied to load forecasting studies in various ways, such as the classification of working and non-working days in [121]. While most studies adopt a specific method for handling calendar effects, there is still room to explore and compare different approaches. Moreover, multiple climate-related factors, such as temperature, humidity, wind speed, and precipitation, have been previously considered. Daily mean or instantaneous temperature has been commonly used [122], [123], [124], [125]. However, the relationship between load and temperature varies by region, necessitating a thorough investigation into the efficient utilisation of temperature and its temporal dynamics. It is important to consider the relationship between factors and load before incorporating them into load forecasting models in the future.

Weather data have been integrated into electricity forecasting models by power system operators in many countries. For example, the Australian Energy Market Operator (AEMO) incorporates weather variables such as extreme temperature, solar radiation, and wind patterns into demand forecasting. This is particularly critical in summer, when heatwaves drive peak demand. AEMO draws on global satellite feeds, multiple demand and weather forecast providers, and over 515 weather stations nationwide [126]. In France, RTE (Réseau de Transport d'Électricité) integrates meteorological data, particularly temperature, into day-ahead forecasts, as French demand is highly sensitive to winter heating loads [127]. In the United Kingdom, the National Energy System Operator (NESO) uses weather data (temperature, wind, solar radiation, cloud cover, etc.) for short- and medium-term demand forecasts. National Grid Electricity Distribution (NGED) employs an industry-specific weather forecasting service providing daily and short-term forecasts across its network to assist with load prediction. This system uses a red–amber–green (RAG) framework to highlight risk levels. Daily forecasts advise NGED control centres on temperature, lightning, gales, rainfall, and snow, including line-icing risks. For example, temperature warnings are triggered at 28 °C to ensure appropriate fault response arrangements are in place [128].

Although weather datasets are widely used in electricity forecasting tools, most operators still rely on traditional statistical methods such as Multiple Linear Regression (MLR) and time-series models like Autoregressive Integrated Moving Average (ARIMA). However, load forecasting is becoming increasingly challenging due to extreme climate and weather risks. Few studies have explicitly addressed the specific risks posed by extreme weather events in load forecasting models. Consequently, there remains significant scope to develop practical weather-informed forecasting approaches using more advanced machine learning methods.

2.4.3 Systematic grid reserve analysis: deterministic & probabilistic estimation methods

Estimating power grid reserve capacity is critical for ensuring the reliability and resilience of electricity supply, especially in the face of uncertainties like demand fluctuations, generation variability, and extreme weather events. State-of-the-art methods for estimating power grid reserve capacity involve advanced techniques that account for these uncertainties, as well as evolving grid dynamics due to the increasing penetration of renewable energy sources. There are two main streams of grid reserve methods: deterministic "N-1" criteria and probabilistic estimation.

The "N-1" and "N-1-1" criteria are traditional deterministic standards used by grid operators. The "N-1" criterion ensures that the grid can withstand the failure of any single component without leading to widespread outages. The "N-1-1" criterion extends this to withstand the failure of a second component following the first failure. For instance, the "N-1-1" criterion is adopted by the UK National Grid to assist in grid dispatch [129]. In Australian power networks, the "N-1-50MW" criterion was proposed to enhance system reliability and resilience by Powerlink Queensland (one of the biggest energy operators in Australia) [130]. A novel "N-1" contingency test method based on topological approximation was developed using a German power network, demonstrating superior performance compared to traditional "N-1" contingency tests. The estimation results were accurate, while the computational cost was significantly lower than that of the conventional "N-1" method [131]. In [132], the traditional "N-1" criterion was enhanced to an "N-1-1" reliable solution by incorporating transmission switching methods, illustrating its benefits to grid reliability.

On the other hand, power reserves can be estimated by probabilistic methods that consider the nature of multi-source uncertainties in grids. The most typical way to integrate uncertainty in reserve analysis is to use Monte Carlo simulation. There are five main steps to assess grid reserve using Monte Carlo methods:
(1) Form probabilistic distributions: Fit probabilistic distributions for uncertain sources, i.e., renewable generation and load.
(2) Generate scenarios: Generate scenarios based on the probabilistic distributions (ideally over 10,000).
(3) Run power flow: Run the power flow analysis to see if the grid can be balanced, or else calculate the shortfall.
(4) Determine reserves: identify the power reserve needed for each probabilistically-generated scenario.
(5) Demonstrate results with probability: aggregate the results to find the reserve required to meet the reliability goals, e.g., ensuring 95% of scenarios do not have energy deficiency.

In [133], the Monte Carlo method was applied to the IEEE 118-bus system to calculate blackout risk by accounting for cascading outages due to overloading lines and hidden protection system failures. An integrated software, "Long-Term Scheduling (LTS)", was utilised to assess long-term power system resource adequacy in Greece from 2018 to 2027 [134]. Specific probabilistic indicators were employed in the LTS to evaluate grid flexibility, such as Loss of Load Expectation (LOLE), Expected Unserved Energy (EUE), Insufficient Ramping Resource Expectation (IRRE), and Expected Unserved Ramping Energy (EURE). It has been demonstrated that thermal energy and its dispatch flexibility are crucial for long-term resilient grid operation, especially as more renewable energy is integrated into power networks on the pathway to Net Zero. While Monte Carlo methods can simulate uncertainty from multiple sources, they are computationally intensive due to the need for repeated calculations. In [135], the traditional Monte Carlo method was enhanced with an unsupervised clustering approach, specifically k-means clustering, to reduce the computational burden. The generated scenarios were partitioned into several groups using k-means clustering, with the centroid case representing the patterns for each cluster. Subsequent optimal power flow analyses were conducted based on the selected representative scenarios to assess grid performance and the reserve needed to avoid energy shortfalls.

In recent years, several studies have started developing grid reserve analysis methods that combine the traditional "N-1" criterion with probabilistic approaches. For instance, an "N-1" static security assessment method based on a Deep Convolutional Neural Network (DCNN) was proposed in [136] for grids with high proportions of renewable energy penetration. The DCNN-aided "N-1" method was tested using the IEEE 14-bus, 30-bus, and 118-bus test systems, demonstrating its effectiveness compared to conventional methods. Notably, the integrated approach was up to 300 times faster than traditional Monte Carlo methods while still producing reliable results. There remains significant potential to develop efficient and reliable grid reserve calculation tools by leveraging the strengths of the deterministic "N-1" criterion, probabilistic estimation methods, and machine learning-based techniques.

2.5 Research gaps and innovation inspirations

Although research on grid resilience under fire risks has been gaining momentum in recent years, there remain gaps that can be addressed to develop more comprehensive and innovative models with practical significance. This section summarises these research gaps based on a review of the existing literature. In line with the research questions outlined in Section 1.2.1, this section identifies four key research gaps, which will be addressed in the following four main chapters.

1. Simulating and assessing a wildfire-affected power system using real fire data rather than hypothesised risks

Most existing models generate fire risks based on stochastic processes. However, wildfire risks should be modelled using historical datasets, as wildfire patterns vary significantly across regions [99]. Additionally, numerical fire risk indices should be employed instead of coarse, simplified wildfire risk maps that provide only a limited number of risk classifications [25].

2. Forecasting electricity demand under extreme wildfire conditions by incorporating relevant factors

Few studies have looked at electricity forecasting under extreme events. Given the uncertainties associated with renewable generation, end-user behaviour, ageing transmission infrastructure, and climate change, a climate-resilient load forecasting tool is essential. Accurate and robust forecasts enable system operators to efficiently pre-dispatch energy and restore power outages promptly. Developing such a tool requires advancements in two key areas: innovations in forecasting model structures, including statistical and machine learning-based approaches, and the integration of multiple influencing factors, such as climate variables and calendar information.

3. Enhancing grid resilience under wildfire risks through the sustainable deployment of renewable distributed generation

Some studies have optimised grid reconfiguration to maximise energy delivery during Public Safety Power Shutoffs (PSPS). However, prolonged intentional blackouts may compromise social security, particularly when they affect critical infrastructure such as water treatment facilities and hospitals. Therefore, further research is needed to explore how the deployment of renewable distributed generation can maintain a resilient electricity supply in a cost-effective manner.

4. Evaluating grid reserve requirements under extreme weather conditions using probabilistic, deterministic, and machine learning methods

Grid reserve analysis is crucial for assessing power system vulnerability and contingency planning. The traditional "N-1" method identifies critical grid components but may be insufficient to safeguard the system against increasing uncertainties under extreme wildfire conditions. Probabilistic, deterministic, and Machine Learning (ML) methods should be further explored and refined to develop robust grid reserve analysis tools capable of effectively managing power networks under extreme events.

In Chapters 3, 4, 5, and 6, the aforementioned research gaps are systematically addressed. Chapter 3 outlines the methodologies used to construct a static WEM for worst-case scenarios during the 2019-2020 wildfire seasons in Victoria, Australia. In Chapter 4, state-of-the-art load forecasting methods are reviewed and further developed to create a wildfire-resilient load forecasting tool for grids under high wildfire risks. Chapters 5 and 6 integrate the findings from the first two phases and enhance the static WEM into a dynamic and probabilistic WEM, applying it to both an IEEE theoretical case study and the actual Australian power networks.

3

Phase I: Power network resilience analysis under wildfire risks - worst case scenarios

Contents

This chapter presents the first phase of the entire DPhil research through the published journal paper titled "Resilient by design: Preventing wildfires and blackouts with microgrids". The paper, with extended results and updated methods, is discussed, while some relevant literature review has been relocated to Chapter 2. This chapter develops a prototype Wildfire Energy Model (WEM) by assessing worst-case grid resilience scenarios on selected days during the 2019-2020 wildfire season in Victoria, Australia. The integrated model evaluates grid performance from technical, economic, and environmental perspectives, exploring methods to improve grid resilience and manage wildfire risks using distributed generations in a sustainable manner.

As this is a co-authored paper, a detailed description of each author's contribution should be provided. Weijia Yang: Methodology, Software, Writing – original draft, Writing – review & editing. Sarah Sparrow: Writing – review & editing, Methodology, Supervision. Masaō Ashtine: Writing – review & editing, Supervision. David Wallom: Conceptualization, Writing – review & editing, Supervision. Thomas Morstyn: Conceptualization, Methodology, Writing – review & editing, Supervision.

3.1 Introduction

This chapter models and evaluates grid operation under peak fire conditions on selected days for the transmission network in Victoria, Australia. In the first scenario, transmission lines exposed to fire risk are disconnected based on varying fire risk thresholds. The impact of these thresholds on grid resilience is analysed using two representative high-risk days. In the second scenario, distributed generators of varying capacities are installed at nodes experiencing load shedding to mitigate blackouts. In response to regional wildfire threats, portions of the transmission network are deactivated, and local demand is supported by distributed generation to minimise load shedding. Transmission lines in unaffected "fire-free" areas maintain power flow between nodal demand and central grid generation. In this context, nodal demand is met partially by the main grid and partially by local distributed generation, depending on economic considerations such as real-time electricity pricing. This chapter aims to evaluate and enhance grid performance during peak fire conditions through the strategic use of renewable distributed generation. A cost-benefit analysis is conducted to assess the viability of the proposed distributed generation approach.

In terms of the selection of DG sources, solar photovoltaic power is not a recommended local DG source in fire-prone regions since the wildfire smoke negatively affects the power generation – the overall daily reduction in electricity generation is 7%, with the peak power shedding of 27% in a fire-burn case study in Canberra [137]. Similar phenomena have been found in California and Malaysia – a 30% reduction in daily electricity generation in California during September 2020 [138] and 0.43 W power reduction per increment of 1 point Air Pollution Index (API) for a 1 kWp PV in Malaysia in 2014 [139]. In comparison, wind generation is generally a more appropriate DG source during fire seasons, as the risk of fire is positively correlated with wind within a range (when the wind speed is lower than the cut-off speed for wind generation). A commonly used rule of thumb, the 10% Wind Speed Rule, estimates a wildfire's forward spread rate. For instance, with an open wind speed of 30 km/h, the estimated spread rate during severe burning conditions would be approximately 3 km/h [140]. Therefore, wind generation is selected as the DG technology to mitigate load shed in this chapter.

As an extensively validated measure of fire potential, the Canadian Forest Service Fire Weather Index Rating System (FWI) is innovatively utilised to describe the wildfire risk distribution over a power grid. The previous study [25] utilised a static wildfire risk distribution model that was spatially partitioned into only three levels based on loosely assembled data from [141]. In comparison, in our study the wildfire risk is measured daily and regionally with exact 'Danger Ratings' to achieve a higher accuracy. The method in our chapter is adaptable and can be applied to protect power networks in other fire-prone areas. The Wildfire Energy System (hereafter the Test System) represents an example case of our model based on a practical grid scenario of Victoria, Australia, in the 2019-2020 wildfire season.

Section 3.2 outlines the methodology used to construct the Test System incorporating geographical data. Section 3.3 presents an overview of the scenario designs and their data sources, with the aim of examining how FWI-based line disconnection thresholds and DG deployments affect grid resilience. Section 3.4 provides a comprehensive analysis of resilience performance, considering factors such as line loading, load shedding, system operating costs, and carbon emission intensity. The cost-benefit analysis of DG solutions is also addressed. Finally, Section 3.5 summarises the key findings and offers recommendations for potential future developments of the Test System.

3.2 Methodology

This section describes the methodology to build the WEM with DG support. The Wildfire Index calculation and the Grid Model construction are first explained in Sections 3.2.1 and 3.2.2. A spatial analysis technique is then described to match the Grid Model with the Wildfire Index using the coordinates of transmission lines (as explained in Section 3.2.3). In this study, DG solutions are utilised to share regional demand when bulk supply is significantly reduced due to wildfires. Designs of DGs and automatic line control strategies are also discussed in this section (as explained in Section 3.2.4).

Furthermore, the simulation methods used to assess system resilience are described as the critical analysis of this chapter in Section 3.2.5. Direct Current Optimal Power Flow (DCOPF) has been implemented as the main simulation to calculate the optimal grid solution under system safety conditions, producing various performance indices. Figure 3.1 shows the main components and the main steps to obtain grid resilience under fire risks in this chapter.

3.2.1 The wildfire index

The simulation of the wildfire risk distribution is one of the critical parts for the Test System design. Wildfire risk levels can have substantial simultaneous differences

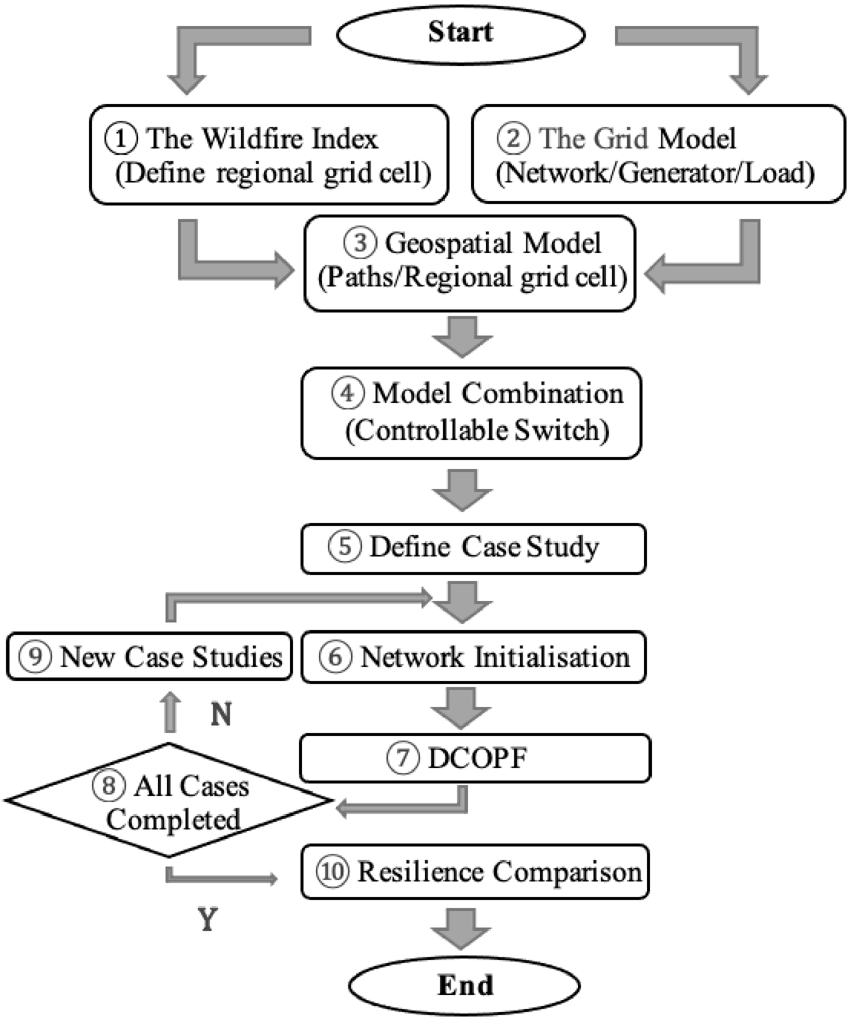

Figure 3.1: Main components and construction steps flow chart for the Wildfire Energy System

within a large country. Therefore, a better temporal and spatial accuracy of the wildfire risk severity is crucial to model the Test System better.

A weather-dependent risk index was utilised in our study to simulate the wildfire risk distribution during the 2019-2020 wildfire season. The FWI is a meteorological index that is used to evaluate the risk of wildfires [142]. The FWI ingests meteorological parameters such as temperature, wind speed, relative humidity and 24-hr precipitation [143]. The FWI Danger Rating (DR) is classified into six levels, and the relationship with FWI is described in Table 3.1.

Table 3.1: FWI Danger Rating classification adapted from [143] (upper bound excluded)

Fire Danger	FWI ranges
Very low	(0, 5.2)
Low	(5.2, 11.2)
Moderate	(11.2, 21.3)
High	(21.3, 38.0)
Very high	(38.0, 50.0)
Extreme	$(50.0, +\infty)$

The FWI of each microclimate region is available from the Copernicus Climate Data Store [79] in Network Common Data Format (netCDF) files [144]. A microclimate is defined as a region with specific climate conditions and topographic locations [145]. This chapter describes a microclimate as a region with a different wildfire risk feature from neighbouring regions. For the case study area, the whole studied region was divided into $0.25°\times0.25°$ grid cells in line with the spatial resolution of the wildfire risk distribution data. As the geographical coverage of the data is on a global scale, the FWI distribution can be calculated for other regions using the same method [146]. As an example of wildfire risk distribution, Figure 3.2 shows the Australian FWI on 30thDecember 2019, highlighting the wildfire risk danger level.

In previous studies, such as [146], [147] and [148], FWI is used as a measure of fire risk irrespective of ignition sources. Determining the actual risk of powerline ignition at a particular FWI value is beyond the scope of this chapter as we are unable to quantify the likely occurrence of all possible ignition sources at all locations. In this chapter, the FWI serves as a general guide, indicating the relative intensity of fire impact on transmission lines across the entire study region. In future, data-driven methods may be used to assess actual electrical fault-related fire risks for grids in different regions. This is especially true given a number of ignition sources that are the direct result of human behaviour. In França et al., FWI was utilised as one of the three main elements to assess the fire-risk-breakdown of the power lines in Northern Brazil [149]. Thus, the FWI was regarded as a reference

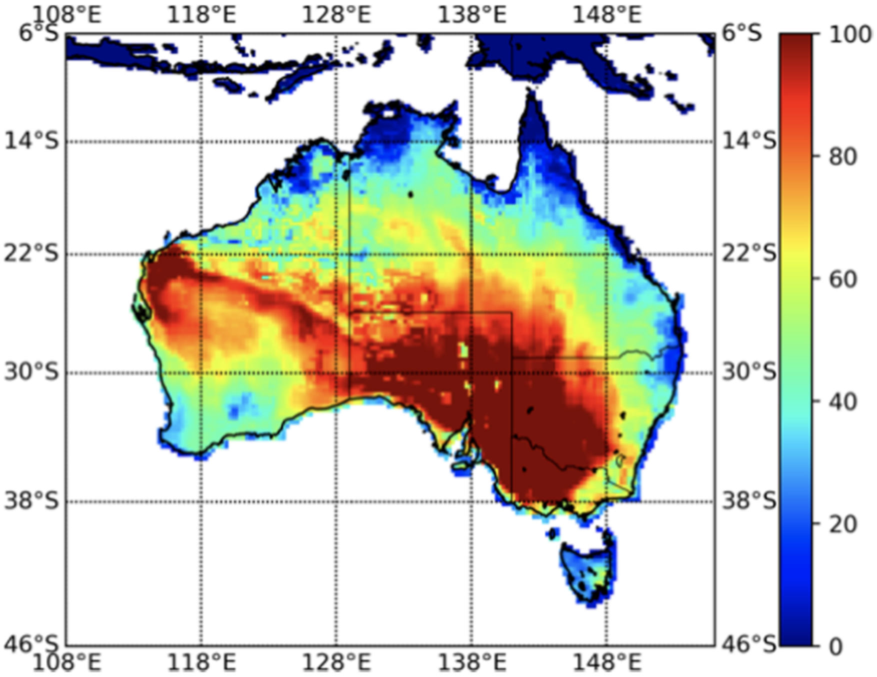

Figure 3.2: Australia FWI colour map on 30th Dec 2019

index here to help determine the proper operating mode of the grid component within the Grid Model to avoid a larger scale outage. In real operation, the grid operators should design a fire prevention plan considering both the regional FWI and possible ignition sources nearby.

3.2.2 The grid model

Three main steps to construct the Grid Model are explained in detail in this section. The power network was set up within the Grid Model in Step 1, the power generation information was added in Step 2, and the energy demand distribution was obtained in Step 3. The detailed construction procedures and data sources specific to the Victoria Case study are discussed in detail in Section 3.3.

It is notable that our model focuses on grid formation and static power dispatch rather than dynamic energy dispatch. Our grid resilience analytical parameters are obtained for the worst-case scenario (when the grid is operating at peak load). The current work is assessed with dynamic wildfire risk simulations and grid at peak demand. We only consider instantaneous wind generation at selected fire peak times. However, future work could consider more detailed modelling of local microgrid load profiles, which would allow us to investigate the value of battery storage.

Step 1: Network assembly

A Keyhole Markup Language (KML) file is a file format to display geographic data containing pinpoint locations and image overlays [150]. As input, raw KML data were downloaded to obtain the geographical and electrical information about transmission lines, substations, and power stations [151]. State and boundary data were imported in the format of shapefiles [152]. The Statistical Area Level 2 (SA2) population dataset [153] was obtained to estimate the regional demand distribution by the Voronoi tessellation method [154]. Then, the operational grid components belonging to National Electricity Market (NEM) zones were sorted based on the information from energy market operators [155]. As an example, the operational grid and the demand proportion served by each node within the state of Victoria are shown in Figure 3.3.

Step 2: Generator dataset

While the power station positions were given in Step 1, technical and economic parameters were assigned to generation information. The technical data of generators were collated, including fuel types and registered capacities. The operational cost of each generator was calculated as the product of fuel cost and heat rate, plus operation and maintenance (O&M) expenses [156]. The heat rate (GJ/kWh) measures a plant's efficiency in converting fuel energy into electricity: a lower heat rate indicates higher efficiency, since less fuel is required per unit of output. Fuel cost is the cost of one unit of energy fuel, with the unit of £/GJ. Databases containing the unit technical parameters and operating costs were imported to supplement the information in this step. After filtering generators that did not satisfy the system conditions (e.g., standing exemption of small-scale DGs according

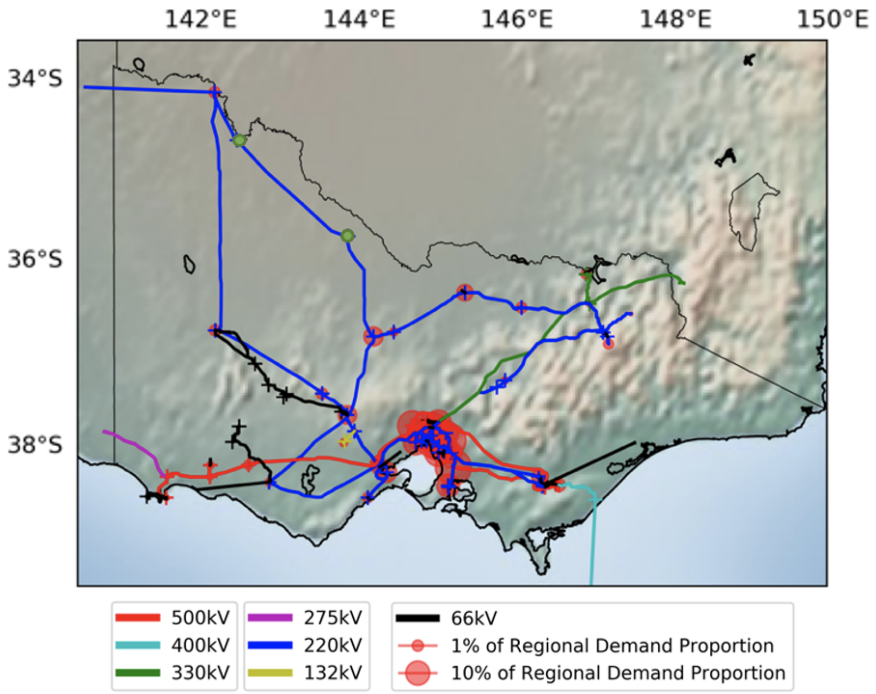

Figure 3.3: High voltage transmission network in Victoria, Australia, where "+" represents substations, the size of red circles represents regional energy demand proportion, the two green spots indicate a 220 kV transmission line from Red Cliffs to Kerang, which will be discussed as an example in Section 3.2.4

to the local authority), a comprehensive dataset that contained all the necessary generation information was obtained.

Step 3: Historical load and dispatch

Historical load signals were required to provide the actual demand for the power flow simulation in DCOPF. However, most of the public load dispatch data were regional rather than nodal demands divided into smaller clusters. The nodal demand distribution was obtained using the aforementioned method of Voronoi tessellation, which can divide a given space into regions based on the distance to a set of points [154]. Finally, the nodal demand was attained by multiplying the total demand by the nodal proportion.

Distributed generation solutions

In the DG scenario, wind generators were installed at selected nodes of the Grid Model to facilitate flexible transitions between grid-connected and islanded modes.

Table 3.2: Evaluation metrics to assess grid resilient performance

Categories	**Metrics**	**Definition**	**Unit**
Technical	LL_{grid}^{ave}	Ave line loading of the whole grid	%
	LL_{grid}^{max}	Max line loading of the whole grid	%
	LS_{grid}	Total system load shed	MWh
	$LS_{grid}^{percent}$	The ratio between the total load shed and the system demand	%
Economic	C_{grid}	Total system operational cost	$
Economic	C_{grid}^{ave}	Unit operational cost	$\$/MWh$
Environmental	E_{grid}	Total system carbon emission	kg
	E_{grid}^{ave}	Unit carbon emission	kgCO_{2eq}/MWh
Vulnerable	Selected	Lines that have loadings over 70%	N/A

Different proportions of nodal demands were served with additional DG integrations to recover the load shed due to fire risks in the second scenario. To be more specific, wind DGs were initially installed at nodes experiencing load curtailment, with capacities matching the shed load. The wind generation capacities were then incrementally increased until full load recovery was achieved at the selected nodes. Finally, the whole system performance was assessed by comparing the result of resilience parameters (Table 3.2). A cost-benefit analysis was conducted to seek a better trade-off between load-shedding costs and DG installation expenditures.

3.2.3 Geospatial modeling

The length and the trajectory of transmission lines are essential for the Test System, primarily because some electrical parameters (e.g., resistance) are closely related to the line length. Another reason is that knowing the exact path of lines (rather than only start points and end points) is essential for accurate wildfire risk detection of lines that cross multiple microclimates. To complement the Grid Model with network line geographical information, KML files containing multiple coordinates were utilised to describe the line paths with a higher accuracy. To be more specific, the coordinates in the Australian transmission line KML files are with a fine spatial resolution of 2.5 m [157]. Thus, KML files were chosen here due to their availability and human readability. In addition to KML, SHP and GeoJSON are also common data formats for processing geographical information. SHP is not human-readable (binary vector format) but is ideal for processing with GIS tools. GeoJSON is suited for web mapping and modern apps. These alternatives could be considered in the future if relevant datasets for other regions become available.

In terms of spatial information within the Wildfire Index, the original netCDF4 data of FWI were calculated for discontinuous grid cell vertices. To overlay the value over the entire region, each sampling point was first selected as the centre of one grid cell. Then the FWI of this grid region was assumed to have the average FWI of the four surrounding vertices.

3.2.4 Combining wildfire and grid information

In combining the Wildfire Index with the Grid Model, methods to assess and determine the operational status of grid components are essential. As in most networks, transmission lines, especially high voltage lines, are geographically extended over a large area [158]; long transmission lines may cross different regions with separate and different wildfire risk conditions due to their microclimates. For instance, Victoria has a major transmission line (from Red Cliffs to Kerang), traversing different microclimates as shown and marked with green dots in Figure 3.3. Long-extending transmission lines result in difficulties in making well-justified operational decisions as various line segments may have different failure probabilities.

Two main methods have been proposed to define the failure probability of system components that span multiple microclimate regions. The first utilised the weighted-average method: an incremental multiplier of failure rate (IMFR) can obtain the overall failure rate by adding the point-specific failure rates along each line segmentation according to their respective microclimate regions [159]. In the second category, the failure rate for the entire transmission line was determined by the highest failure rate along with any one single point of a line [41]. The choice between using the average line risk or the maximum risk to determine a line's operational status depends on the parameter under consideration. When resistance is the primary factor, the average line risk is appropriate. Conversely, for fault or sag-related risks, the maximum line risk should be used to represent the overall risk under fire conditions.

According to the Australian government, lines with a voltage greater than 66 kV are defined as transmission lines. Those at lower voltages are classified into the distribution level [160]. Thus, only transmission lines with voltage levels over 66 kV were considered in this chapter. The focus was given to cases in which transmission lines cross various microclimate regions. As the fire risk is calculated for each 0.25° × 0.25° grid cell, a microclimate region is defined as a 0.25° × 0.25° cell in our study. As shown in Figure 3.3, most lines crossed different microclimates with different failure rates during the wildfire season. As minor failures can instantaneously have a great impact on the wider high-voltage transmission lines, this chapter assumed that the worst failure rate along the line was selected to judge the whole line's failure and following operational modes.

The Test System operated according to simulated information from both the Wildfire Index and the Grid Model. The operation method here is similar to the real-world solution: transmission lines have reclosers installed which can be automatically disconnected if a fault or overload occurs [161]. To isolate the section of the power network under high fire risks and avoid a larger-scale outage, a controllable line-bus switch was set on each transmission line in the Test System [162]. While the worst line failure rate (depending on the worst fire risk exerting on the line) was available, the line operational mode was then controlled by line switches. When any part of the transmission line crossed an area exceeding the preset risk threshold, the switch on the line was automatically disconnected.

In the line disconnection decision process, the sampling accuracy can be changed according to the resolution of the data. For instance, since the grid cell length was 0.25° in Victoria, the coordinates along each line were extracted in steps of 0.01° latitude to achieve good spatial accuracy (corresponding longitudes were obtained according to the coordinates recorded in the KML files). After obtaining the transmission line coordinates, the corresponding FWI grid cell covering each line sampling point was identified. As the FWI of each regional cell had been computed, each coordinate along the line was assigned with a value of FWI.

Finally, the maximum FWI value was selected along each line and compared with the preset FWI threshold under different fire control conditions. A switch was opened within the Grid Model if the maximum FWI along a line exceeded the limit. Similarly, in practice, lines are disconnected to prevent wildfires, followed by customers being disconnected if no other connected path can serve the load to ensure the power grid is not overloaded [163].

3.2.5 Simulation methods - objective, constraints, and variables

Grid performances (Table 3.2) were obtained from an optimal power flow model incorporating wildfire risk distributions. The Optimal Power Flow (OPF) is the best operating situation of power stations to meet the grid demand, determined by network variables, constraints, and the specific objective of the OPF model utilised. The most common objective for OPF is to minimise operating costs [164]. OPF can be classified into Alternating Current OPF (ACOPF) and Direct Current OPF (DCOPF). ACOPF problems are typically approximated and solved by DCOPF that focuses exclusively on active power constraints due to its linearity [165].

To optimise the grid dispatch, a Mixed Integer Linear Programming (MILP) model is formulated with variables, constraints, and objective functions. MILP is a mathematical optimisation technique used to solve problems involving both discrete and continuous decision variables [166]. In a MILP problem, the objective function and the constraints are linear, but some decision variables are required to take integer values. In power grid operation scenarios, certain variables are constrained to integers, such as the operational status of a generator. Therefore, MILP is an appropriate method for solving the optimal power flow problem.

To solve MILP problems, several well-developed solvers can compute global optimal or near-optimal results with efficient and reliable computational quality, including Gurobi, CPLEX, and SCIP [167]. Equipped with advanced algorithms and heuristics, Gurobi was selected as the solver to tackle the large-scale MILP problem efficiently in this chapter.

For transmission network-level analysis, DCOPF is more commonly used to evaluate grid operation for several reasons: **(1) Reduced Computational Complexity**: In DCOPF, reactive power and losses are neglected, resulting in a linear and convex optimisation problem. In contrast, ACOPF considers the non-linear relationship between active and reactive power, requiring more complex and computationally intensive resources. **(2) Convexity**: The convexity characteristic of DCOPF ensures that the global optimal result can be found efficiently and reliably using solvers. However, finding the global optimum in a non-convex ACOPF problem is more challenging. **(3) Reasonable Accuracy and Computational Cost**: Despite being an approximation, it has been widely demonstrated that DCOPF can provide reasonably accurate and reliable optimisation results [168]. Therefore, DCOPF is suitably chosen as the OPF calculation method for our proposed study, which looks at large-scale transmission networks. Further details on simplifying ACOPF into DCOPF can be found in [165] and [164].

To formulate the DCOPF model, the objective function, constraints and decision variables are defined with detailed explanations.

Objective Function

DCOPF aims to achieve the minimum operational cost while satisfying all safety constraints. As displayed in (3.1), the total grid operational cost comprises the generation cost, wind cost, storage cost (considered in temporally continuous cases in Chapters 5 and 6), and the penalty for wind power curtailment. Value of Lost Load (VoLL) represents the cost associated with disconnected customers, estimating the economic and social losses due to power outages [169]. As VoLL may vary significantly according to the customer types, operational seasons, and time of the day, VoLL is not included in the system cost objective function, instead, VoLL will be considered in the cost-benefit analysis.

$$\begin{aligned} OF = \sum_{g,t} a_g(P_{g,t}^2) + b_g P_{g,t} + c_g + \sum_{i,t} P_{i,t}^w \times LRMC_w + \sum_{i,t} VWC \times P_{i,t}^W C \\ + \sum_{i,t} P_{i,t}^c \times LRMC_s + \sum_{i,t} P_{i,t}^d \times LRMC_s \\ s.t. \sum_{g \in \Omega_G^i} P_{g,t} + LS_{i,t} + P_{i,t}^w - L_{i,t} - P_{i,t}^c + P_{i,t}^d = \sum_{j \in \Omega_l^i} P_{ij,t} \\ P_{ij,t} = \frac{\delta_{i,t} - \delta_{j,t}}{X_{ij}} \end{aligned} \tag{3.1}$$

OF represents the Objective Function (total system operational cost), $P_{g,t}$ denotes the power generation for the g^{th} generator at the t^{th} time point, a_g, b_g, and c_g are the cost coefficients for the g^{th} generator, $VOLL$ is the Value of Lost Load, $LS_{i,t}$ is the load shed for the i^{th} bus at the t^{th} time point, VWC is the value of wind curtailment, and the $P_{i,t}^W C$ is the wind power curtailment for the i^{th} bus at the t^{th} time point, $P_{i,t}^w$ is the wind power output for the i^{th} bus at the t^{th} time point, $LRMC_w$ is the long run marginal cost for wind generation, $P_{i,t}^c$ and $P_{i,t}^d$ refer to the power charging and discharging for the i^{th} node at the t^{th} time point, respectively, $LRMC_s$ is the long run marginal cost for the storage. Wind curtailment penalty is considered in the objective function to encourage more renewable power production.

Storage related terms are only considered in the continuous operating cases in Chapters 5 and 6.

The second line of the Equation (3.1) is the power balance equation. The difference between the power flowing out of a node and the power flowing into a node is equal to the sum of net power flow to all nodes j that are connected to the node i. $L_{i,t}$ represents the power demand for the i^{th} bus at the t^{th} time point. $P_{ij,t}$ denotes the power flow transmitted from the i^{th} node to the j^{th} node at time t, where i & j are the connecting nodes for lines belonging to the transmission line set (l) of the grid. The final row of Equation (3.1) illustrates the relationship among the phase angles of voltage at bus i and bus j ($\delta_{i,t}$ & $\delta_{j,t}$), line reactance X_{ij} and the line power $P_{ij,t}$ [165].

Operational constraints

Constraints that guarantee safe grid operations are discussed in this section. Equation (3.2) states that load shedding should be less than or equal to the total load at each bus across all operational times.

$$0 \leq LS_{i,t} \leq L_{i,t} \tag{3.2}$$

The real-time line power is constrained by the defined maximum line capacity. Since energy can flow in both directions, the line constraints are expressed by Equation (3.3).

$$-P_{ij}^{max} \leq P_{ij,t} \leq P_{ij}^{max} \tag{3.3}$$

As shown in Equations (3.4), (3.5), and (3.6), operational constraints for power generators include limitations on power output, ramp-up rate, and ramp-down rate. RU_g and RD_g represent the ramp-up and ramp-down rates of the g^{th} generator.

$$P_g^{min} \leq P_{g,t} \leq P_g^{max} \tag{3.4}$$

$$P_{g,t} - P_{g,t-1} \leq RU_g \tag{3.5}$$

$$P_{g,t-1} - P_{g,t} \leq RD_g \tag{3.6}$$

While the original case does not include renewable generation, renewable generators can be installed in subsequent operating cases to ensure safe and sufficient system operations when some lines are disconnected due to high weather-related risks. The operational constraints for wind power are provided in Equations (3.7) and (3.8), where $w_{i,t}$ denotes the available wind power source, and Λ_i^w is the capacity factor of the wind power for the i^{th} node at time t.

$$P_{i,t}^{W}C = w_{i,t}\Lambda_i^w - P_{i,t}^w \tag{3.7}$$

$$0 \leq P_{i,t}^w \leq w_{i,t}\Lambda_i^w \tag{3.8}$$

Due to the inherent intermittency of renewable generation, adequate energy storage capacities are required to store surplus electricity and discharge energy during peak demand periods. Operational constraints for energy storage are discussed in Equations (3.9), (3.10), (3.11), and (3.12). $SOC_{i,t}$ represents the state of charge for the storage at the i^{th} bus at time t, indicating the remaining charge in the battery (ranging from 0% to 100%) [170]. η_c and η_d are the efficiency parameters for charging and discharging. $P_{i,t}^c$ denotes the charging power of the battery, which varies between the minimum charging power $P_{i,min}^c$ and the maximum charging rate $P_{i,max}^c$. Similarly, $P_{i,t}^d$ denotes the discharging power of the battery, limited within the minimum and maximum discharging power, $P_{i,min}^d$ and $P_{i,max}^d$.

$$SOC_{i,t} = SOC_{i,t-1} + (P_{i,t}^c\eta_c - P_{i,t}^d/\eta_d) \times \Delta t \tag{3.9}$$

$$P_{i,min}^c \leq P_{i,t}^c \leq P_{i,max}^c \tag{3.10}$$

$$P^d_{i,min} \leq P^d_{i,t} \leq P^d_{i,max} \tag{3.11}$$

$$SOC_{i,min} \leq SOC_{i,t} \leq SOC_{i,max} \tag{3.12}$$

Equations (3.13) and (3.14) define the efficiency of charging and discharging. E_{bat} represents the energy measured or calculated at the battery terminal. ΔE denotes the energy loss within the battery [171].

$$\eta_c = \frac{E_{bat} - \Delta E}{E_{bat}} \tag{3.13}$$

$$\eta_d = \frac{E_{bat}}{E_{bat} + \Delta E} \tag{3.14}$$

3.3 Case study

In this section, the Test System prototype in Victoria, Australia, is first introduced, followed by a detailed description of two scenarios used to analyse grid resilience performance. The first scenario examines how preset FWI-based line disconnection thresholds affect grid resilience, while the second investigates how distributed generation can effectively enhance resilience under fire conditions. Both scenarios are applied to two representative days (3^{rd} & 12^{th} December 2019) with varying fire risk levels to improve the generalisability of the proposed model.

3.3.1 The Test System overview

To better apply the proposed methods to real-world network operations, a real power grid was selected in this chapter. As mentioned in Section 1, Australia was attacked by a devastating wildfire from December 2019 to February 2020. Compared to other states in Australia, Victoria has some factors that make it suitable for a case study, such as large transmission networks, highly varying wildfire risks and good data availability. Thus, ‘Victoria, Australia’ (hereafter ‘Victoria’) in December

2019 has been selected as the research region of our case study.

Following the three steps explained in Section 3.2.2, the grid model for Victoria was built. In terms of the input for Step 1, 'Network Assembly', raw KML data from Geoscience Australia were utilised to obtain the electrical and geographical information on transmission lines [157], substations [172], and power stations [173]. State and boundary data in the format of shapefiles were accessed from the Australian Statistical Geography Standard in the Australian Bureau of Statistics [152]. According to the Regional Population Growth Module in the Australian Bureau of Statistics [153], the SA2 population datasets were obtained to estimate the regional demand distribution. The NEM supplies approximately 90% of Australia's population but is not connected to Western Australia or the Northern Territory. As our research focuses on the NEM operational region, we utilised its geographical coverage to extract NEM network data from Australia's broader network information. Specifically, the NEM zone information was sourced from the Australian Energy Market Operator (AEMO) [155], the independent energy market and system operator, as well as the system planner for the NEM and Western Australia's Wholesale Electricity Market.

Then we moved to Step 2, 'Generator Dataset', the technical data of generators were collated from the Market Management System Data Model (MMSDM) [174]. The National Transmission Network Development Plan (NTNDP) database also contained information about the unit technical parameters and the operating costs [175]. The technical and economic generator dataset was constructed in Step 2.

As for Step 3, 'Historical Demand and Dispatch', the nodal demand proportion was obtained using the Voronoi tessellation method. The nodal demand was calculated by multiplying the nodal proportion by the total demand [174].

Main grid components and parameters

In this chapter, the Victoria network was filtered so that only high voltage lines were retained. Thus, only lines with voltage levels over 66 kV were kept to focus on the high voltage system. Power stations with less than 5 MW ratings were also filtered as AEMO allowed standing exemptions for these small plants, which should not be categorised as generators [176]. There were 201 transmission lines within the NEM operational region in Victoria before the filter procedures. The information on the remaining system components is provided in the following paragraph.

Figure 3.4 illustrates the geographical information for the Victoria case study, including generators, substations, transmission lines, and demand points. In this Victoria network, 72 buses, 122 transmission lines, and 84 power generators are distributed across networks with voltage levels of 66kV, 132kV, 220kV, 275kV, 330kV, 400kV, and 500kV.

Dynamic wildfire risk maps

To assess the impact of wildfire risk on the power grid, it is essential to extract the spatial features of wildfires. Figure 3.5 illustrates the climate variable maps used to generate the FWI risk map for Victoria at 4 pm on 3^{rd} December 2019. The methodology for calculating hourly FWI using climate variables from the ERA5 datasets will be detailed in Figure 4.8, which is used to compute the hourly FWI for the energy forecasting model in the second phase of this DPhil work. Climate variables to calculate FWI include hourly datasets of temperatures at 2m, wind speed, relative humidity, and total precipitation in the previous 24 hours [177], [178]. The resulting FWI risk heat map, including transmission line trajectories, is shown in Figure 3.6. Figure 3.6a displays the standard FWI risk heat map for Victoria at 4 pm on 3^{rd} December 2019. The FWI risk distribution is classified according to various risk boundaries, as depicted in Figure 3.6b, based on the danger rating classifications mentioned in Table 3.1. Similarly, the climate and FWI maps are plotted in Figures 3.7 and 3.8 for the 4 pm condition on 12^{th} Dec 2019, as all

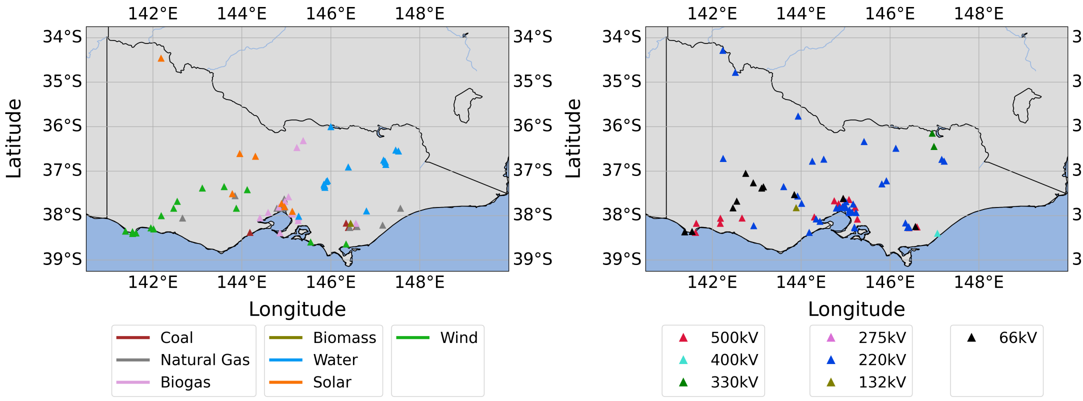

(a) Generators **(b)** Substations

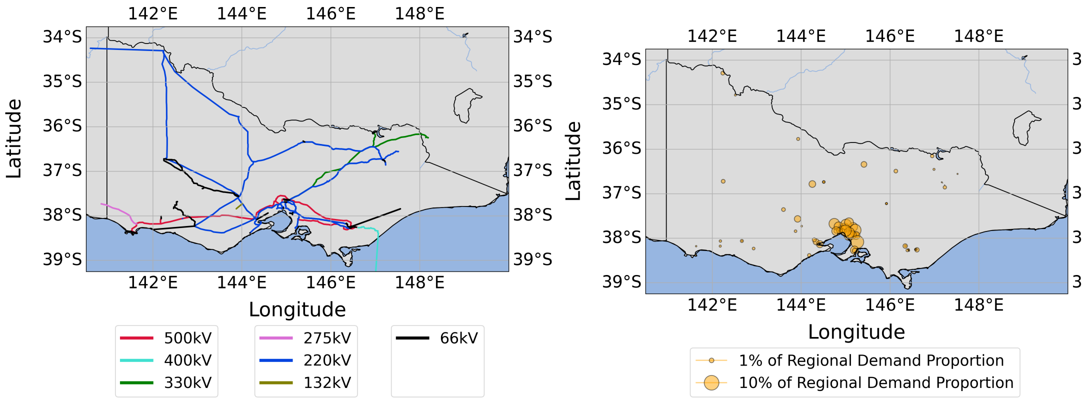

(c) Transmission lines **(d)** Demand

Figure 3.4: Main NEM grid components in Victoria, Australia. (a) shows the location and types of generators. (b) displays the locations and voltage levels of substations. (c) demonstrates the trajectories and voltage levels of transmission lines. (d) represents the demand proportions with locations

scenarios will be applied to these two representative days. It is notable that the 12^{th} case has higher fire risks at the fire peak time (4 pm).

The Test System geographical coverage

A geographical rectangle region that could contain the entire Victoria territory was selected with the latitude range of [-39.25°, -33.75°] and the longitude range of [140.50°, 150.00°]. Since the resolution of FWI reanalysis data was 0.25°×0.25°, the length and width of each grid cell were both 0.25°. Thus, there were 836 grid cells in the selected research region in our model. It is noticeable that one degree represents different distances at different latitudes [179] (e.g., 0.25° denote 28 km at 0°, whereas 22 km at 36°S in Victoria). As the latitude range of Victoria

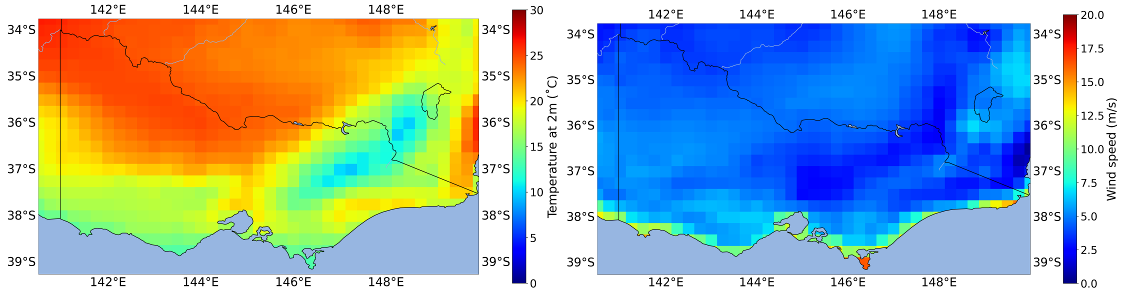

(a) Temperature at 2m [177]

(b) Wind speed [177]

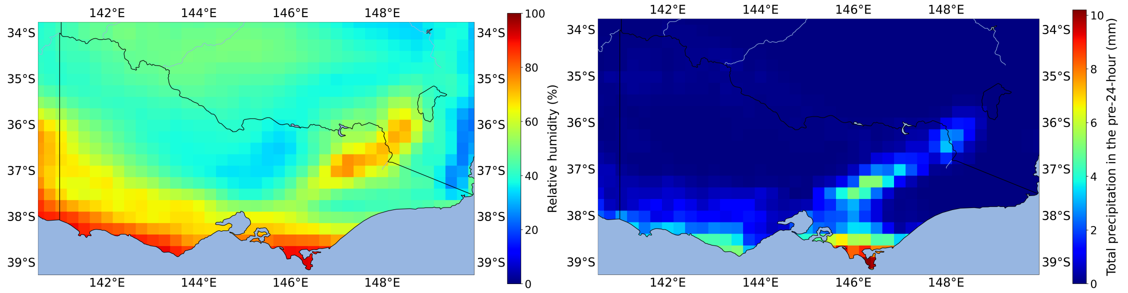

(c) Relative humidity [178]

(d) Total precipitation in the pre-24-h [177]

Figure 3.5: Climate variable heat maps at 4 pm on the 3^{rd} Dec 2019 in Victoria, Australia

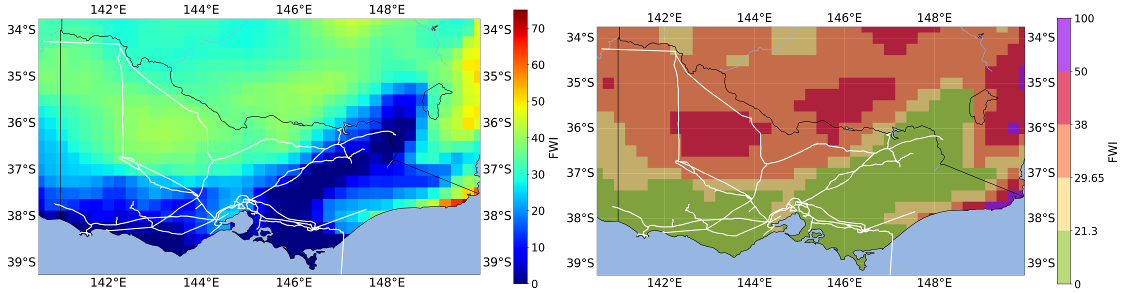

(a) FWI heat map with lines

(b) FWI risk levels with lines

Figure 3.6: FWI heat maps at 4 pm on the 3^{rd} Dec 2019 in Victoria, Australia, using different classification methods (transmission lines are shown in white)

is not too wide, the side length of one grid cell can be regarded consistently as 22 km.

3.3.2 Scenario overview

Figure 3.9 demonstrates the scenarios designed for this chapter. Two scenarios are assessed based on the fire risk conditions in Victoria, Australia, on 3rd and 12th December 2019. The setting of FWI line disconnection thresholds may affect the

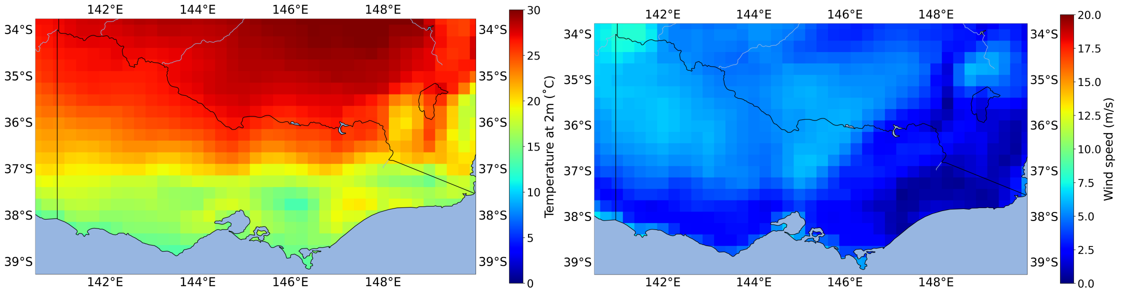

(a) Temperature at 2m [177]

(b) Wind speed [177]

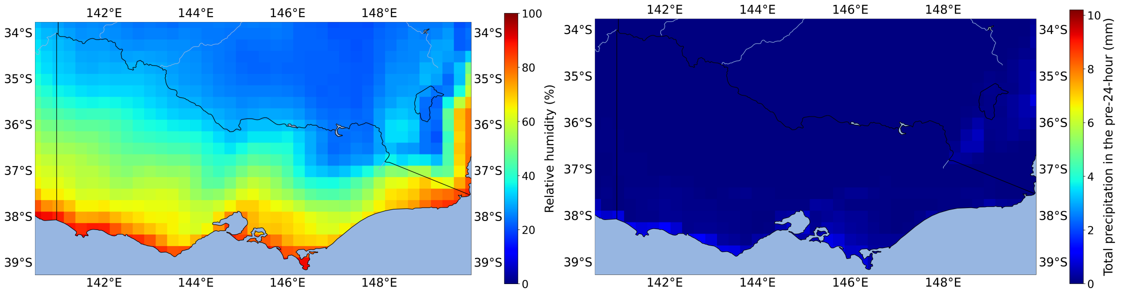

(c) Relative humidity [178]

(d) Total precipitation in the pre-24-h [177]

Figure 3.7: Climate variable heat maps at 4 pm on the 12^{th} Dec 2019 in Victoria, Australia

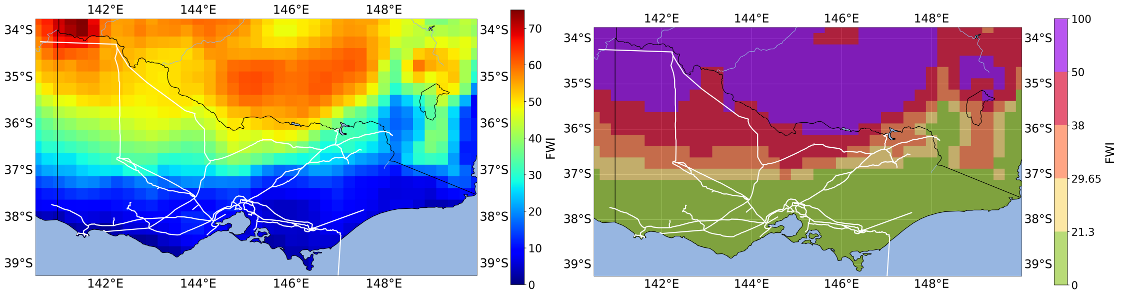

(a) FWI heat map with lines

(b) FWI risk levels with lines

Figure 3.8: FWI heat maps at 4 pm on the 12^{th} Dec 2019 in Victoria, Australia, using different classification methods (transmission lines are shown in white)

system operation's safety and effectiveness. To be more specific, each transmission line has a calculated FWI value, and more lines will be disconnected as the FWI disconnection threshold is set at a lower value. A lower FWI line disconnection threshold means achieving a stricter fire risk control circumstance. Scenario 1 explored the impact of varying FWI disconnection thresholds on grid resilience under different fire control conditions. Three thresholds were selected: 50.0 (extreme), 38.0 (very high), and 21.3 (high), in accordance with the danger rating table (Table

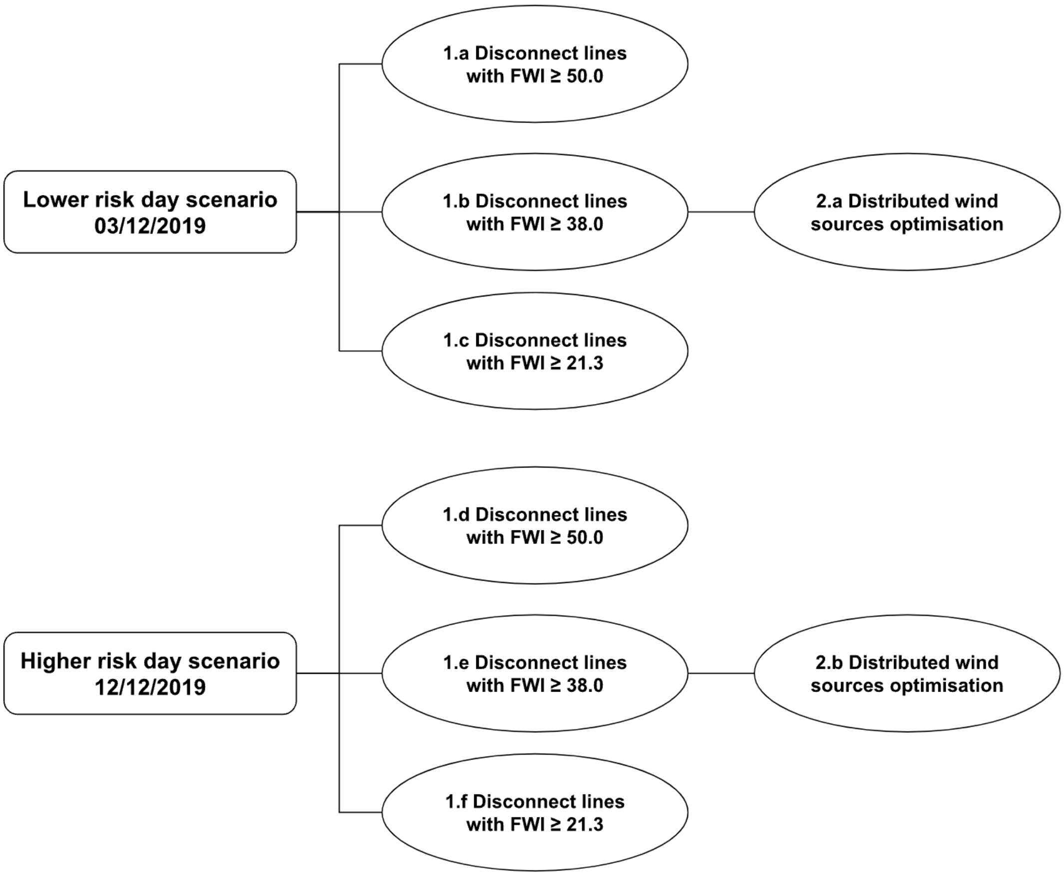

Figure 3.9: Scenario designs for Chapter III - representative worst case grid operation studies during wildfire seasons

3.1).

As the main objective, distributed generation solutions were applied to mitigate the system burden during the wildfire season. In Scenario 2, strategies to prevent blackouts under wildfire conditions were examined. Two operating cases were developed based on Scenario 1.b and Scenario 1.e, where lines were disconnected once the FWI exceeded the "very high" risk threshold (38.0). Wind generators were installed at nodes experiencing load shedding, with capacities incrementally increased to eliminate load shedding across the grid. The outage and DG costs were analysed and compared in the cost-benefit analysis, following the result discussion for two scenarios.

3.4 Results and discussion

The results are analysed through technical, economic, and environmental aspects for each scenario. As mentioned in Table 3.2, performance indices are obtained and assessed in each scenario, including system line loading percentages, load shedding rates, system operating costs and emission factors.

There were different operating cases defined for each scenario. In Scenario 1, six operating cases were selected for different days with various preset FWI thresholds, representing different system fire risk control levels. Two operating cases were set up in Scenario 2 to study the effectiveness and feasibility of DG deployment.

3.4.1 Scenario 1 FWI line disconnection threshold

Among the six operating cases in Scenario 1, different numbers of lines were disconnected due to variations in fire risk levels, system demand, and fire management measures (FWI thresholds). As shown in Figures 3.6 and 3.8, overall system fire risks on 3rd December were lower than those on 12th December. In terms of total system demand, Victoria recorded 4,565 MW and 4,575 MW at 4 p.m. on 3rd and 12th December, respectively, indicating similar levels of demand. In general, the system was under greater stress on 12th December at the peak burning period (4 p.m.). Table 3.3 presents the line disconnection statistics for all operating cases. Notably, more lines were disconnected in the 12th December cases when the FWI thresholds were the same, further indicating greater system stress on that day. Scenarios 2.a and 2.b exhibited the same number of line disconnections as Scenarios 1.b and 1.e, respectively, as the FWI threshold (38.0) remained unchanged. In Scenarios 2.a and 2.b, wind generators were installed to prevent the load shedding observed in Scenarios 1.b and 1.e.

According to the evaluation metrics in Table 3.2, the performance results for six operating cases in Scenario 1 are recorded in Table 3.4. The results will be

Table 3.3: Line disconnection numbers due to fire risks (122 transmission lines in Victoria)

Dates	Scenarios	Thresholds	Line disconnection numbers
3rd	1.a	50.0	0
3rd	1.b	38.0	5
3rd	1.c	21.3	36
12th	1.d	50.0	7
12th	1.e	38.0	20
12th	1.f	21.3	53
3rd	2.a	38.0	5
12th	2.b	38.0	20

discussed following the order in Table 3.4.

Table 3.4: Scenario 1: grid resilience performances for peak burning conditions on 3rd & 12th December 2019 in Victoria, Australia

Metrics	**1.a**	**1.b**	**1.c**	**1.d**	**1.e**	**1.f**	**Unit**
Thresholds	**50.0**	**38.0**	**21.3**	**50.0**	**38.0**	**21.3**	**N/A**
Dates	3rd	3rd	3rd	12th	12th	12th	**N/A**
LL_{grid}^{ave}	46.15	40.73	33.68	40.60	37.23	30.11	%
LS_{grid}	0	699.26	1,642.36	718.88	1,483.80	1,693.16	MWh
$LS_{grid}^{percent}$	0	15.32	35.98	15.71	34.01	37.01	%
C_{grid}	283,832	290,825	300,253	291,022	298,661	300,765	AU$
C_{grid}^{ave}	62.21	75.23	102.72	75.51	103.72	104.49	$AU\$$ /MWh
E_{grid}	269,812	270,210	275,210	270,599	275,502	281,235	kg
E_{grid}^{ave}	59.11	71.20	94.18	71.36	95.58	98.23	kgCO_{2eq} /MWh

With regard to technical metrics, line loading and load shedding were evaluated to provide deeper insight into the distribution of system burden. The average grid line loading (LL_{grid}^{ave}) progressively decreased as the FWI thresholds became more strict on both selected dates. For a given FWI threshold, LL_{grid}^{ave} on 12 December was consistently lower than on 3 December, as the higher fire risk levels on 12 December resulted in more line disconnections according to Table 3.3. Detailed line loading maps for all operating cases are presented in Figure 3.10. Lines disconnected due to violations of the preset FWI thresholds are highlighted in dark purple, aligning with the high fire risk regions depicted in Figures 3.6 and 3.8. Notably, lines in the southwest and southeast of Victoria operated at relatively higher loading levels on both days.

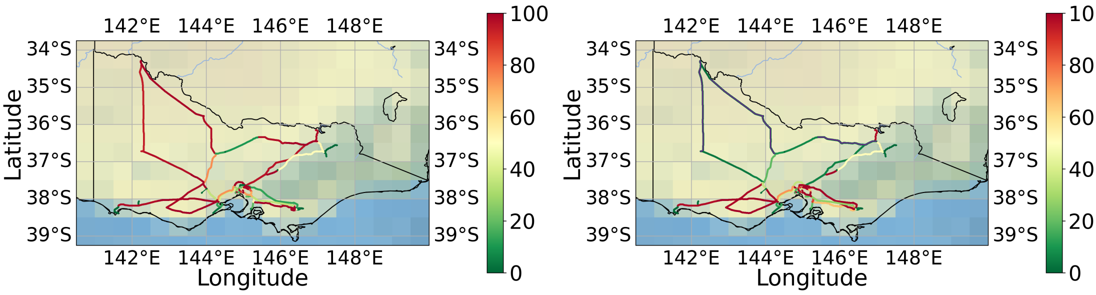

(a) Scenario 1.a (threshold = 50.0)

(b) Scenario 1.b (threshold = 38.0)

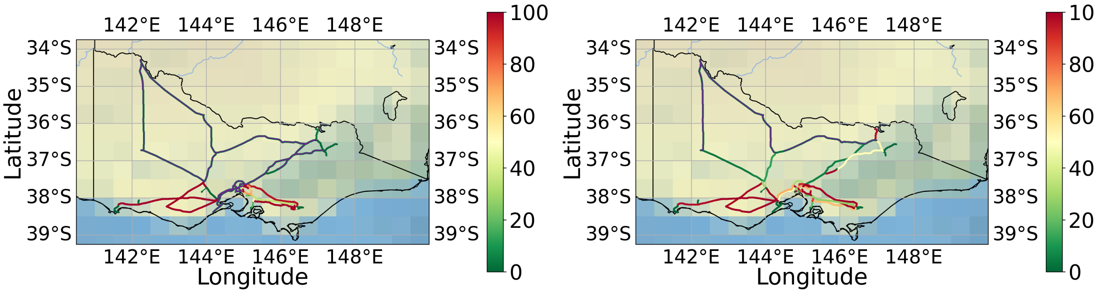

(c) Scenario 1.c (threshold = 21.3)

(d) Scenario 1.d (threshold = 50.0)

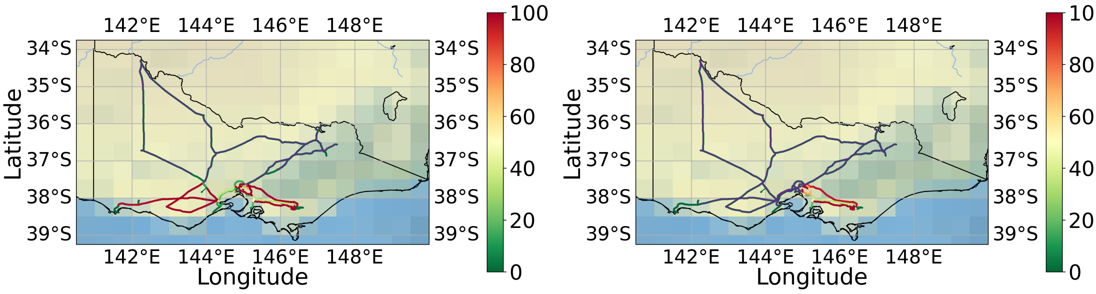

(e) Scenario 1.e (threshold = 38.0)

(f) Scenario 1.f (threshold = 21.3)

Figure 3.10: Line loading maps for transmission networks with different FWI line disconnection thresholds in Victoria, Australia. Scenarios 1.a-c are based on 3rd Dec 2019 cases, and Scenarios 1.d-f are based on 12th Dec 2019 cases (lines pre-disconnected due to the violation of the preset FWI risk thresholds are marked in dark purple)

With regard to load shedding (LS_{grid}), greater amounts of load were curtailed as the FWI thresholds were lowered on both days. Notably, LS_{grid} was consistently higher on 12 December, reflecting the larger number of lines pre-emptively disconnected under the defined risk thresholds. In the strictest operating cases (Scenarios 1.c and 1.f), 35.98% and 37.01% of system demand were shed at the peak burning period, potentially leading to significant economic and social impacts. The detailed distributions of load shedding percentages are presented in Figure 3.11.

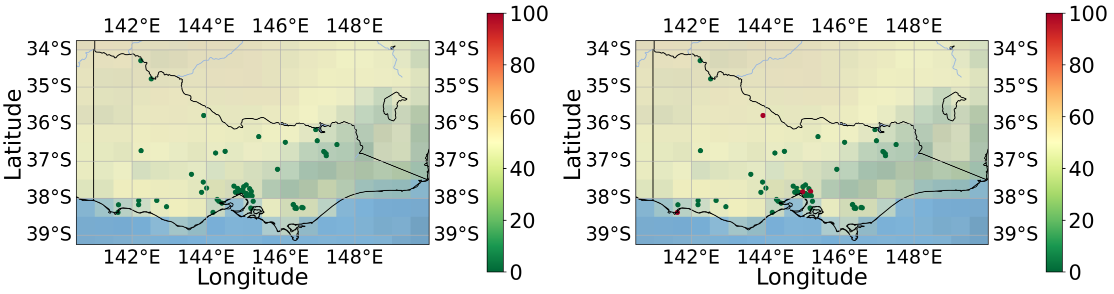

(a) Scenario 1.a (threshold = 50.0) **(b)** Scenario 1.b (threshold = 38.0)

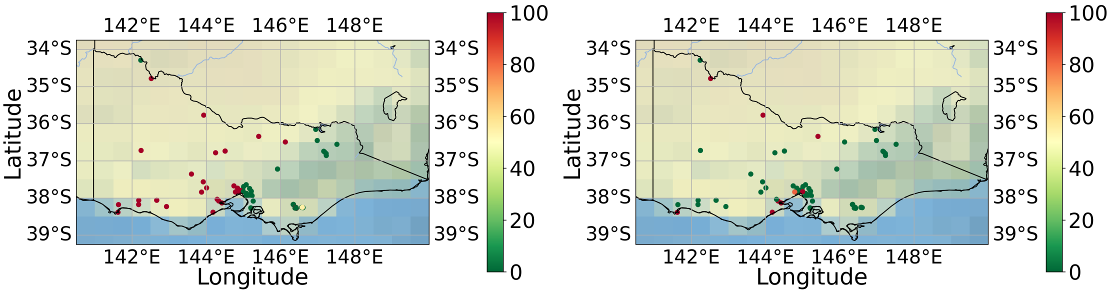

(c) Scenario 1.c (threshold = 21.3) **(d)** Scenario 1.d (threshold = 50.0)

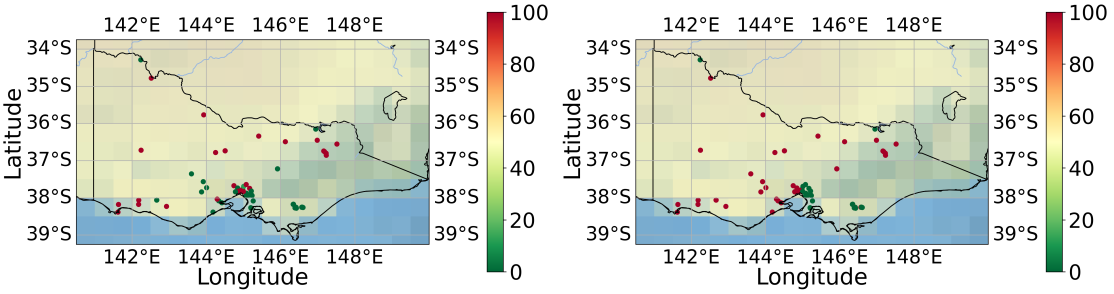

(e) Scenario 1.e (threshold = 38.0) **(f)** Scenario 1.f (threshold = 21.3)

Figure 3.11: Load shed percentage maps for transmission networks with different FWI line disconnection thresholds in Victoria, Australia. Scenarios 1.a-c are based on 3rd Dec 2019 cases, and Scenarios 1.d-f are based on 12th Dec 2019 cases

With regard to economic metrics, the total system cost (C_{grid}) and unit cost (C_{grid}^{ave}) were compared and analysed. In both cases, total system operating costs increased progressively as the FWI thresholds became stricter, rising by AU$16,421 and AU$9,743 on 3 and 12 December, respectively. The rate of increase in unit cost was more pronounced, as lower FWI thresholds resulted in reduced demand satisfaction. On 3 and 12 December 2019, unit costs rose by 65.12% and 38.38%, respectively, as the FWI threshold decreased from 50.0 to 21.3.

Regarding the total system emissions, operating cases in both two representative days increased as the threshold decreased. The unit carbon emission became higher as the actual served demand decreased from the loose fire control operating case (with the FWI threshold of 50.0) to the strict one (with the FWI threshold of 21.3). The consistent trend across both days indicates that the grid becomes less environmentally friendly as the FWI threshold is set at a stricter level.

The specific FWI threshold should be determined based on actual wildfire control requirements. Where stricter wildfire control is necessary, demand-side response (DSR) services should be integrated to ensure that 100% of the load is met. In Scenario 2, solutions to prevent load shedding during the fire season are explored by considering the deployment of DGs at nodes experiencing load curtailment.

3.4.2 Scenario 2 Distributed generation solutions

Scenario 2 comprises two operating cases, which explore methods to recover the load shedding observed in Scenarios 1.b and 1.e, where the FWI disconnection threshold was set at 38.0. Scenario 2.a builds on Scenario 1.b (3 December 2019), in which five lines were pre-emptively disconnected, resulting in 15.32% load shedding. Scenario 2.b is based on Scenario 1.e, where 20 lines were disconnected, leading to 36.86% load shedding. Similar to Scenario 1, the resilience metrics are presented in Table 3.5.

Table 3.5: Scenario 2: grid resilience performances for peak burning conditions on 3rd & 12th December 2019 in Victoria, Australia

Metrics	**2.a**	**2.b**	**Unit**
LL_{grid}^{ave}	41.67	35.58	%
LS_{grid}	0	0	MWh
$LS_{grid}^{percent}$	0	0	%
C_{grid}	829,114	1,893,388	AU$
C_{grid}^{ave}	181.64	413.83	$AU\$/MWh$
E_{grid}	270,210	275,502	kg
E_{grid}^{ave}	60.29	72.31	kgCO_{2eq}/MWh

In terms of technical metrics, no load shedding occurred in either Scenario 2.a or 2.b, as wind generators were installed at the nodes where load shedding had been recorded in Scenarios 1.b and 1.e. Specifically, the capacities of the newly installed wind generators were determined based on the amount of load shed at each node. For nodes that continued to experience load shedding after an initial installation matching the original shed amount, additional wind generation was iteratively added until load shedding was fully eliminated across the system. Details of the new wind generation capacities installed at each node for both scenarios are provided in Table 3.6 (detailed node location information can be obtained by following the methods in [151]). It is noticeable that more wind generation capacities were added in Scenario 2.b than in Scenario 2.a as more than double the amount of load shed occurred on 12 December than on 3 December. Line loading results in Scenarios 2.a and 2.b showed little variation from those in Scenarios 1.b and 1.e, as the recovered loads were largely supplied by local wind distributed generators rather than through transmission from neighbouring nodes. Detailed line loading maps are presented in Figure 3.12. In real operation, line loading results can be referred by system operators to take additional reinforcement actions on lines with continuous high loading levels to enhance grid resilience.

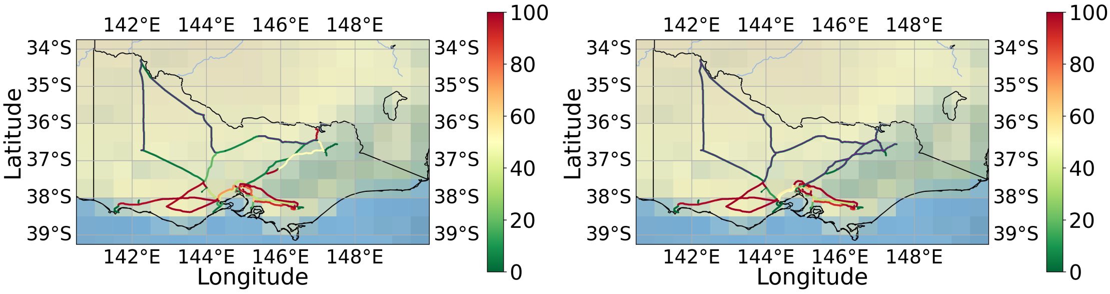

(a) Scenario 2.a **(b)** Scenario 2.b

Figure 3.12: Line loading maps for transmission networks with distributed wind generation in Victoria, Australia (FWI line disconnection threshold = 38.0). Scenario 2.a is based on 3rd Dec 2019 case, and Scenario 2.b is based on 12th Dec 2019 case (lines pre-disconnected due to the violation of the preset FWI risk thresholds are marked in dark purple)

In terms of economic metrics, both the total system cost and the unit cost increased significantly due to the additional wind generation. Compared to Scenario 1, the total system operating cost rose sharply from AU$290,825 and AU$298,661 to AU$829,114 and AU$1,893,388 for the 3 December and 12 December cases, respectively. However, as load shedding was mitigated through the integration of wind generation, the economic assessment of the proposed DG solutions should also account for the avoided economic and social losses in Scenario 2. A more detailed cost-benefit analysis is presented in Section 3.4.3.

Compared to the carbon emission metrics in Scenarios 1.b and 1.e, total carbon emissions remained unchanged, as wind generation is assumed to be a zero-carbon technology in this study. As shown in Table 3.5, unit carbon emissions decreased by 15.32% and 24.35% following the deployment of DGs in the 3 December and 12 December cases, respectively.

Table 3.6: Scenario 2: newly added wind generation for 3rd & 12th December 2019 in Victoria, Australia

2.a (3rd)		**2.b (12th)**					
Node	**Wind (MW)**	**Node**	**Wind (MW)**	**Node**	**Wind (MW)**	**Node**	**Wind (MW)**
2	8.54	1	4.52	19	162.12	55	2.39
6	42.72	2	25.28	25	140.74	56	0.04
11	53.70	3	16.97	38	15.10	57	0.23
17	301.00	4	11.11	39	31.74	58	0.17
44	19.72	6	83.66	44	39.52	59	3.07
65	273.59	8	227.29	46	16.38	60	24.87
N/A	N/A	10	6.60	47	10.78	65	535.75
N/A	N/A	11	123.76	49	11.76	67	17.92
N/A	N/A	13	125.58	50	12.34	68	74.68
N/A	N/A	14	27.55	51	96.00	69	67.44
N/A	N/A	16	159.94	53	9.50	70	108.32
N/A	N/A	18	27.36	54	30.00	71	25.82

3.4.3 Cost-benefit analysis for distributed generation solutions

There are various natural resources for renewable energy in Victoria, including wind, hydro, solar, and bioenergy. The existing widely distributed onshore wind farms and ongoing offshore wind farm projects have proved the feasibility of wind power utilisation in Victoria [180]. Victoria is an excellent site for wind power generation with an average wind speed measured at $6.5ms^{-1}$ [181].

In this chapter, we propose hypothetical planning of renewable utilisation in Victoria. Both wind and solar resources are abundant in Victoria. A demonstration of renewable resource distribution in Victoria is shown in Figure 3.13. Referring to the Victorian transmission network in Figure 3.3 and the FWI maps in Figure 3.6, wind resource distribution is highly colocated with both the fire risk and the network distribution than solar power. Furthermore, there is a positive correlation between wind speed and wildfire spread [60], i.e., fire-prone areas are likely to have greater wind power potential. There is a relatively high coincident distribution between the wind abundance and the severe fire risk. In addition, wind power operates more reliably diurnally than solar power. As mentioned in Section 1, wildfire smoke can negatively affect solar generation efficiency. Therefore, we would select wind as the DG source as an example here [182], [183].

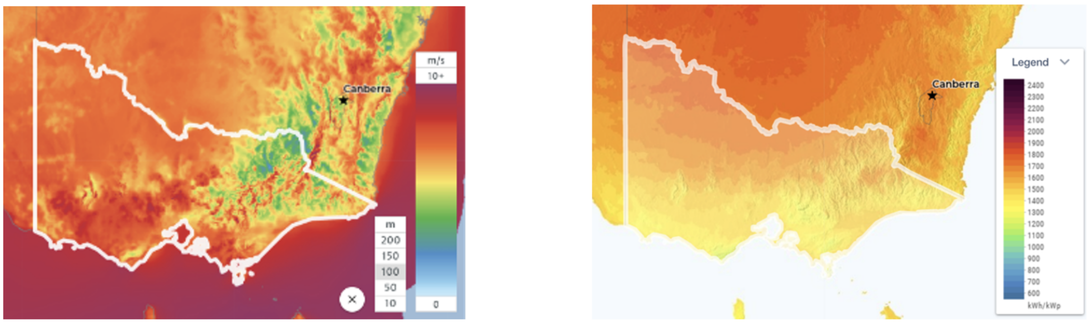

Figure 3.13: Distribution maps of renewable resources in Victoria, Australia. Left: mean wind speed (ms^{-1}) [182]. Right: mean PV power output (kWh/ kWp) [183]

The system costs before and after the DG installation were compared based on Equation (3.15).

$$SO_{cost} = TS_{cost} + VoLL \tag{3.15}$$

Where SO_{cost} represents the overall cost of the Test System, and TS_{cost} denotes the total system cost obtained from the OPF. VoLL captures the economic impact of load shedding by multiplying the unit VoLL cost by the shed load. There are three main metrics commonly used to evaluate electricity prices. The Levelised Cost of Electricity (LCOE) assesses the generation cost of a generator over its lifespan, incorporating both capital and operation and maintenance (O&M) costs [184]. Short-Run Marginal Cost (SRMC) and Long-Run Marginal Cost (LRMC) measure the cost of producing an additional unit of electricity under different conditions. SRMC focuses on short-term operational costs within a fixed network configuration, whereas LRMC reflects the cost of meeting incremental demand changes, assuming all production factors are variable [185]. As noted in Section 3.2.5, LRMC has been selected as the appropriate metric for incorporating DG costs in the OPF calculation in this chapter (already embedded in SO_{cost}). Thus, SO_{cost} is calculated by combining TS_{cost} and the VoLL cost.

According to the Australian Energy Regulator [186], the average electricity price for the Victoria network was AU$84/MWh in 2019. Referring to the latest 2021 economic analysis report about power grids in the NEM, the NEM's Market Price Cap (MPC) of AU$15,000/MWh is almost the highest in the world [187]. In the UK, Ofgem and the National Grid regularly update and determine VoLL through customer surveys and economic modelling [188]. Similarly, in Australia, AEMO and AER (the system operator and regulator) determine VoLL using comparable methods. In Australia, VoLL is commonly represented by MPC, which reflects the maximum price that can be charged in the wholesale electricity market during scarcity events and captures the economic value of unserved energy. As of 2020, the MPC was approximately AUD 15,000/MWh [189]. Thus, we assume the VoLL induced by outages in the scenario without DGs amounted to AU$15,000/MWh as an upper limit here.

Table 3.7 presents the comparative cost–benefit analysis results for operating cases with and without wind DG support. While the proposed DG solutions increased grid operational costs (TS_{cost}), the overall system cost (SO_{cost}) decreased sharply in the latter two operating cases, since significant proportions of load were recovered, reducing VoLL costs. With load effectively restored through wind DG installation in Scenario 2, the overall system costs were substantially reduced by 92.31% and 91.99% for the 3 and 12 December cases, respectively.

Table 3.7: Cost-benefit analysis for peak burning conditions on 3rd & 12th December 2019 in Victoria, Australia

Scenarios	TS_{cost} $AU\$$	Load shed MWh	VoLL $AU\$$	SO_{cost} $AU\$$
1.b (3rd)	290,825	700	10,490,370	10,781,195
1.e (12th)	298,661	1,556	23,339,363	23,638,024
2.a (3rd)	829,114	0	0	829,114
2.b (12th)	1,893,388	0	0	1,893,388

As VoLL was set as the MPC to estimate the overall economic and social losses, this reflects extreme cases where blackout-affected infrastructure, such as hospitals and transport systems, is of critical priority to society. According to Table 3.7, the breakeven point of VoLL can be computed to determine the minimum unit VoLL cost at which investment in wind generation becomes economically justified. The method for calculating this breakeven point is provided in Equation 3.16, where SO_{cost}^{ori} represents the overall system cost without wind DG, SO_{cost}^{wind} is the system cost with wind DG installed, and LS denotes the load shed. The breakeven unit VoLL ($VoLL_{unit}$) is calculated separately for the 3 and 12 December cases, yielding AU$14,217/MWh and AU$13,974/MWh, respectively. In other words, if the unit VoLL exceeds these two thresholds, investment in wind DG to recover load shed becomes economically and socially beneficial. In real-world operations, the cost–benefit of investing in renewable DG at various locations with differing criticality should be assessed against the venue-specific VoLL at the relevant times.

$$VoLL_{unit} = \frac{SO_{cost}^{ori} - SO_{cost}^{wind}}{LS} \tag{3.16}$$

3.5 Conclusion and future work

This chapter has proposed the use of DGs as a novel strategy to mitigate powerline fire risks without the need for blackouts. The power system resilience performance was assessed in high wildfire risk regions. Victoria, Australia, in December 2019 was selected as an example case study. This chapter was driven by the practical need to protect power systems and reduce economic and social loss during a high wildfire risk period. The results obtained from the simulations have shown how can intentional power shut offs and DGs enhance power system resilience in a financially feasible way. The validated FWI was first utilised in a weather-affected power system, which improved the spatial and temporal resolution of wildfire risk positioning in power grids.

Methodologies to assess grid resilience and to build the weather-affected energy system were introduced and discussed. The controllable power line switch played the role of the bridge between the Wildfire Index and the Grid Model, which was automatically disconnected as the line FWI exceeded the preset thresholds under different fire control conditions. The methodology does not exclusively apply to the Test System in Victoria but can be adjusted to other fire-prone regions, supporting the use of the applied methods across various wildfire-prone grids.

The results demonstrated that overall system stress increased with higher fire risk or stricter fire control levels (i.e., lower FWI line-disconnection thresholds), leading to greater load curtailment, higher unit operational costs, and elevated unit carbon emissions. These trends were consistently observed on the two representative days selected from the 2019–2020 wildfire season.

This chapter examined methods for installing wind-based DGs at vulnerable nodes — those experiencing load shedding due to severe fire risks. Although the deployment of wind DGs incurred higher operational costs, the overall system costs were substantially reduced, as the significant VoLL-related costs were avoided in cases where DGs were added. Given that VoLL varies considerably depending on blackout locations and timing, breakeven points were calculated to identify the VoLL levels at which DG investment becomes economically viable.

As FWI data are currently measured daily at noon local standard time worldwide, this chapter evaluated only the peak burning conditions on two representative days. However, power systems are typically assessed on an hourly basis. More accurate modelling could be achieved with higher temporal resolution weather data. An FWI curve with hourly resolution can be approximated based on FWI-related parameter curves. At present, the system models only instantaneous, static peak operations; more frequent monitoring of grid operations is therefore desirable. Further scenarios will be explored in a continuous-time model in Chapter 6, where energy flows — rather than just instantaneous power flows — are considered, including cases involving energy storage.

4

Phase II: Multi-factor deep learning-based load forecasting tool with climate resilience

Contents

With the increasing incidence of power blackouts attributed to climate change, climate-resilient load forecasting is increasingly necessary to enable timely network reconfiguration during extreme weather events. Phase II aims to develop an intelligent load forecasting model with climate resilience, e.g., incorporating climate variables like temperature and fire risks in the forecasting model to improve forecasting performance during wildfire seasons. It is demonstrated that the load forecasting is more difficult during extreme stress than usual. The significance of applying the proposed model has been proved through multiple experiments, enhancing the forecast accuracy and stability substantially.

There are two papers published as the outcome of this Chapter. The conference paper: "Optimising multi-factor assistance in a deep learning-based electricity forecasting model with climate resilience: an Australian case study" was accepted by IEEE PES Innovative Smart Grid Technologies Conference Europe 2023 [2]. Three distribution networks in Victoria, Australia were tested to develop a basic load forecasting tool considering multiple factors. Deep learning methods that particularly appropriate for time series tasks, i.e., LSTM and GRU, were selected as the fundamental forecasting structures.

As this is a co-authored paper, a detailed description of each author's contribution should be provided for this conference paper. Weijia Yang: Methodology, Software, Writing – original draft, Writing – review & editing. Sarah N. Sparrow: Writing – review & editing, Methodology, Supervision. David C.H. Wallom: Writing – review & editing, Methodology, Supervision.

In addition, the journal paper: "A comparative climate-resilient energy design: Wildfire Resilient Load Forecasting Model using multi-factor deep learning methods" was accepted by Applied Energy. Compared to the conference paper, a more comprehensive review of recent trending machine learning methods were conducted, the climate resilient load forecasting tool was improved both in the model novelty and complexity, and the categories of potentially affected factors.

As this is a co-authored journal paper, a detailed description of each author's contribution should be provided. Weijia Yang: Writing – original draft, Software, Methodology, Writing – review & editing. Sarah N. Sparrow: Methodology, Supervision, Writing – review & editing. David C.H. Wallom: Writing – review & editing, Supervision, Conceptualization.

This chapter will present a detailed discussion of the two papers, with more extensive results provided in two separate sections. Some parts of literature reviews have been omitted if they are already covered in Chapter 2. The conference paper will be discussed first, as it addresses the research question in a more general context, followed by a deeper and more specific case study presented in the subsequent journal paper.

4.1 Optimising multi-factor assistance in a deep learning-based electricity forecasting model with climate resilience: an Australian case study

4.1.1 Introduction

Whilst completing the energy systems transition to a zero or low carbon future, the power system faces significant uncertainty due to generation source diversification and demand electrification. Meanwhile, increasing climate risks pose substantial challenges to reliable and resilient energy system operation, with extreme weather events resulting in emergent and unintentional power blackouts. For example, the 2020 Australian Wildfire Season led to thousands of households being disconnected from the power system in New South Wales [1]. Therefore, a pressing need exists to develop intelligent and climate-resilient load forecasting tools to reconfigure power networks and recover load during extreme weather events in a timely manner.

There are two main types of load forecasting method: traditional statistical methods based on time series analysis and Artificial Intelligence (AI) [109] based methods. In [110], several widely used statistical forecasting techniques were discussed, including Multiple Linear Regression (MLR), Semi-parametric Additive Models (SAM), Autoregressive Integrated Moving Average (ARIMA), and Exponential Smoothing Models (ESM). Statistical forecasting methods are the most frequently employed tools currently. However, these methods may struggle to capture demand fluctuations induced by extreme weather events due to the implicit non-linear characteristics. Therefore, data-driven methods such as Neural Networks (NN) have emerged as a promising solution to load forecasting problems in recent research. Of all the NN-based models, Recurrent Neural Networks (RNNs) have been shown to be particularly effective in handling time-series datasets [114]. Consequently, our study selected two RNN-derived methods, Long Short-Term Memory (LSTM) and Gated Recurrent Unit (GRU), as the primary structures.

In our study, we have optimised the use of metadata as input factors, including input structures, calendar labels, and climate factors, to enhance their contributions. While most existing research has considered daily mean or instantaneous temperature as an auxiliary input without justification [190], [125], we introduce flexible temperature demand relationships to enhance their contribution.

This paper proposes a novel Deep Learning (DL) based climate-resilient electricity forecast model incorporating the flexible use of calendar and climate factors. The model is applied to three real Distribution Networks (DNs) in Victoria, Australia, during wildfire seasons in 2015-2020. Our results demonstrate that the proposed method can achieve an average Mean Absolute Percentage Error (MAPE) of 2.95% and reduce the MAPE by 30.73% compared to using instantaneous temperature alone. The remaining paper is structured as follows. Section II outlines the research methodology, while Section III provides information on the case study background and available data sources. Section IV discusses the performance results. Finally, Section V concludes the paper by summarising the main findings and highlighting potential areas for future work.

4.1.2 Methodology

4.1.2.1 Multi-factor deep learning forecast model structure

Figure 4.1 illustrates the pre-processing steps to generate the input matrix and the DL model mechanism to output the load forecast. The model takes historical load and temperature datasets of DNs (temperature data at each selected distribution network) as input. The pre-processing steps are illustrated in the three boxes on the left-hand side of Figure 4.1. Firstly, the load data are varied to determine the appropriate input sequence length n that balances accuracy and computational efficiency. A One-hot encoder is used to extract the calendar feature and convert categorical features to numeric variables [191]. Calendar information is classified into m types and arranged as an $m \times n$ matrix in the middle of the input matrix. Temperature datasets are processed through a dynamic correlation analysis to find the flexible instantaneous, maximum, or average temperature conditions strongly correlated with the load within specific preceding hours, placed in the last row.

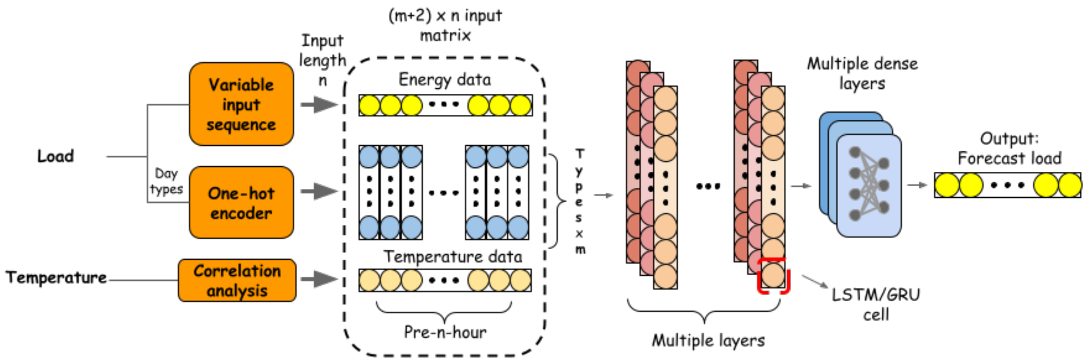

Figure 4.1: Climate resilient multi-factor deep learning load forecast model - the main structure

A multi-layer DL model based on LSTM or GRU is utilised to extract the non-linear relationships and forecast load [192]. Both methods comprise different gates, helping determine which information is valuable and should be retained to produce the next memory cell [109]. The two structures have unique advantages in certain scenarios. GRU has a simplified gate structure using less memory and is faster than LSTM. The GRU structure is also more resistant to gradient exploding and vanishing issues [193]. However, for complex sequences, LSTM has demonstrated superior performance in forecasting [194]. As a result, our paper compares and tests both LSTM and GRU structures, expecting that there will be different scenarios where each performs best, for which we will identify underlying causes.

In general, the optimal number of layers and nodes in a neural network cannot be determined analytically. There is a trade-off between forecast accuracy and computational efficiency, and each dataset has its ideal architecture. Referring to [195] and [196], we use three LSTM/GRU layers with either 32 or 64 neurons to balance the trade-off. Two dense layers with 16 and 1 neurons are then connected to output the forecast load as a sequence.

4.1.2.2 Forecast evaluation metrics

Our study calculates the loss at each epoch using Mean Squared Error (MSE) to adjust the training direction [197]. Two main metrics are employed to evaluate the forecast performance: MSE and MAPE. While MSE, (4.1), is a scale-based metric, the MAPE, (4.2), is expressed as a percentage, allowing it to be compared across datasets with different units and scales.

$$MSE = \frac{1}{n}\sum_{i=1}^{n}(y_i - \hat{y}_i)^2 \tag{4.1}$$

$$MAPE = \frac{1}{n}\sum_{i=1}^{n}\left|\frac{(y_i - \hat{y}_i)}{y_i}\right| \tag{4.2}$$

where: y is the actual value, $\hat{y}$ is the predicted value, and n is the number of data points.

The daily error variance σ^2, (4.3), is computed to assess the fluctuation in the forecast performance within a day.

$$\sigma^2 = \frac{\Sigma(X - \mu)^2}{N} \tag{4.3}$$

where: X is the average half-hourly error, μ is the mean of the average half-hourly error over a day, and N is the total sampling points for a day.

4.1.3 Case study

4.1.3.1 Background and overview

To develop a load forecasting tool resilient to extreme climate conditions, it is preferable to focus on regions that experience such conditions frequently. Therefore, we study DNs in Victoria, Australia, which face annual extreme wildfire seasons. Among the DNs in Victoria, Horsham is selected as the first to study due to its central location and good data availability. The electricity demand data for Horsham is publicly available from Powercor, the distribution company that operates throughout western Victoria and the western suburbs of Melbourne. Wildfire seasons (Oct-Mar) during the years 2015-2020 are chosen to train and test model performance, with the first three seasons considered as the training dataset and the remaining two seasons used as the testing dataset. A six-year dataset of hourly records is an appropriate duration for developing a load forecasting model under fire risk conditions because: (1) it adequately captures seasonal patterns; (2) the period from 2015 to 2020 includes most major fires, while 2014 is a relatively inactive fire year; and (3) existing load forecasting research demonstrates that a training dataset of 2–3 years is sufficient to prevent overfitting and enhance model generalisation [110, 116].

The analysis to develop the forecast model consists of three main steps as follows. (1) Determine the optimal input sequence length for both LSTM and GRU models and test their performance. (2) Evaluate the impact of using different calendar label classification methods on forecast accuracy. (3) Use a flexible temperature correlation analysis to investigate the relationship between different types of leading temperatures and load behaviour and then input them into the DL model to enhance the forecast performance.

4.1.3.2 Energy and climate dataset acquisition and processing

POWERCOR is a major energy distribution network operator covering western and central Victoria, Australia. Due to the higher risk of summer wildfires in the west, we focus on the POWERCOR coverage area in our research [23], for which the energy consumption dataset is downloaded from [198] with a 30min temporal resolution.

For temperature data, ERA5 (ECMWF Reanalysis v5) data are sourced from the Copernicus Climate data store [177] at an hourly temporal resolution and 0.25°×0.25° spatial resolution. Since the load dataset is half-hourly, the temperature dataset is temporally interpolated to half-hourly to maintain consistency. As the temperature is a relatively smoothly evolving field, this approach is reasonable, whereas other climate variables may not be suitable for temporal interpolation methods. To better pinpoint the DN's location, the temperature dataset is also spatially interpolated (linear) into a 0.01°×0.01° resolution.

In this case, temperature data at 0.25° (~25 km) resolution is interpolated to 0.01°. As a result, the temperature data may not exhibit substantial variation across several tens of grid boxes in the interpolated grid. Therefore, although transmission line positions are available at a finer spatial scale (~km), it is unnecessary to expect temperature data to reflect variations at this resolution, and doing so may increase computational cost. In future work, the appropriate spatial resolution of weather datasets should be determined according to the model inputs required. For example, a 0.25° temperature dataset may already be sufficient, whereas more intermittent variables such as wind speed and wind direction may justify using finer resolutions, depending on dataset availability.

4.1.4 Results and discussion

4.1.4.1 Step 1: Determining the optimal data input length

In the first step, we feed the sequential energy consumption dataset into LSTM and GRU models separately. By varying the input data length, we can observe the change in forecast accuracy and identify the optimal input length.

Figure 4.2 shows that MSE and MAPE decrease as the input length increases and reach a stable level when the input is around 16 hours for both models. Initially, the MSE on LSTM is lower than that on GRU. However, as the length of input increases, the MSE on GRU is becoming slightly lower than LSTM. For the MAPE, GRU constantly outperforms LSTM for various input lengths. A GRU might produce forecasts that, on average, deviate by a smaller percentage of the true value (hence a lower MAPE) but still incur some large absolute errors on high-value observations—those large errors inflate the MSE. Conversely, an LSTM could make slightly larger relative errors on low-volume periods (giving a higher MAPE) but avoid extreme absolute miss-predictions on peak loads, resulting in a lower MSE. As the MSE performances for LSTM and GRU are similar, we select the better model by MAPE in this case. At the selected stable point (when the previous 16 hours of information is considered), our results demonstrate that the GRU-based model outperforms the LSTM-based model on MSE and MAPE by 8.18% and 22.81%, respectively. Thus, we further develop our model with the GRU structure and 32 sampling points as input length.

4.1.4.2 Step 2: Testing impact of various calendar factor uses

In this step, three operating conditions are tested: no-calendar-label, three-calendar-label, and eight-calendar-label. For the three-calendar-label conditions, the labels are classified into weekday, weekend, and holiday. The eight-calendar-label conditions are classified into Monday to Sunday plus a holiday label. The no-calendar-label condition is included as a control group.

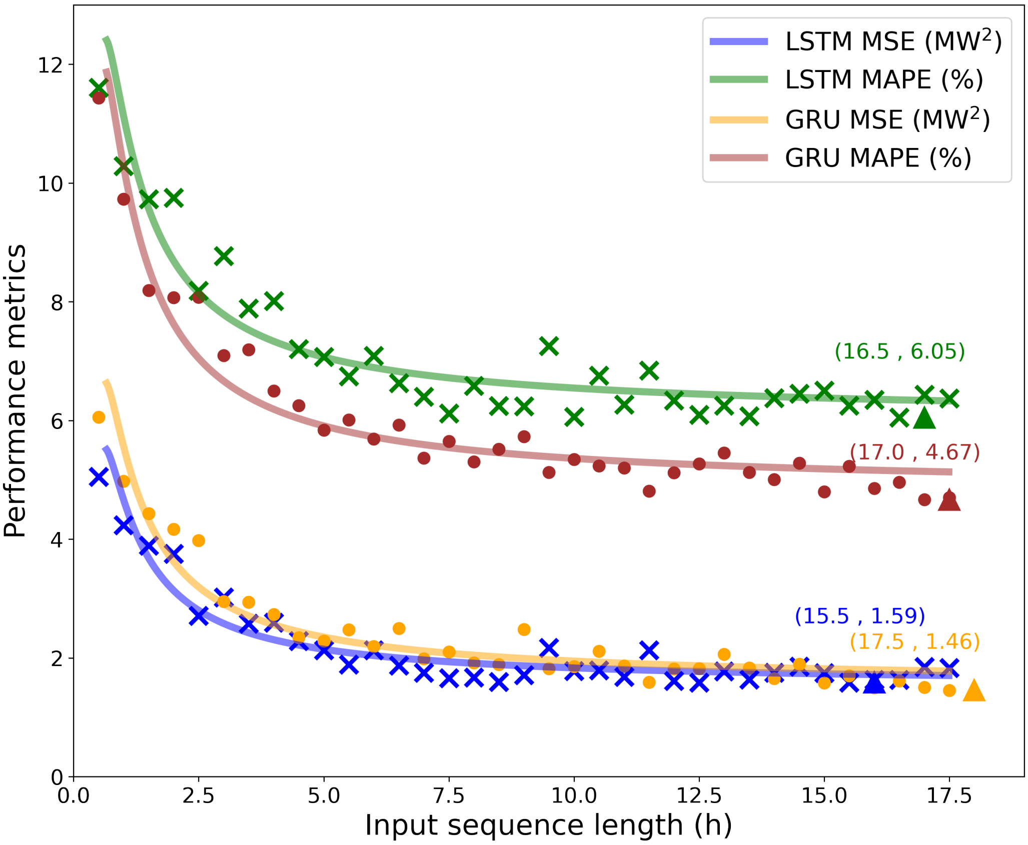

Figure 4.2: Step 1 various input sequence lengths and deep learning methods effects on forecast performance. Triangles represent the lowest error points

Figure 4.3a indicates that all three forecast powers strongly correlate with the real power. The two cases with calendar labels perform better than the one without calendar tags, particularly at energy consumption peaks. The Probability Density Function (PDF) and Cumulative Distribution Function (CDF) plots with MAPEs of the three forecast cases are displayed in Figure 4.3b and Figure 4.3c, respectively. The MAPE of the eight-calendar-label case is 4.23% lower than the case without calendar-label and 1.01% lower than the three-calendar-label case. Most error points for the eight-calendar-label case gather at a lower value than the other two cases in the PDF and CDF plots. Therefore, we choose the eight-calendar-label method to consider the day effect in the following steps.

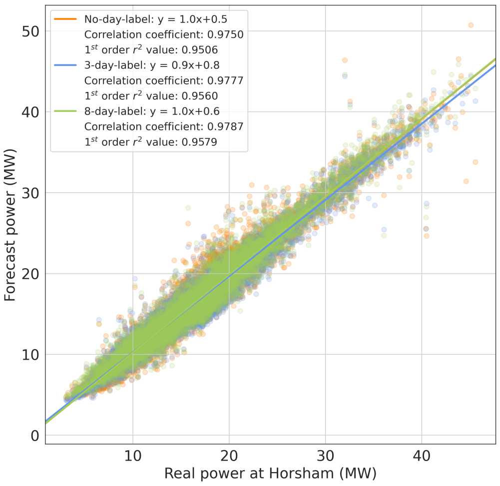

(a) Real power vs forecast power

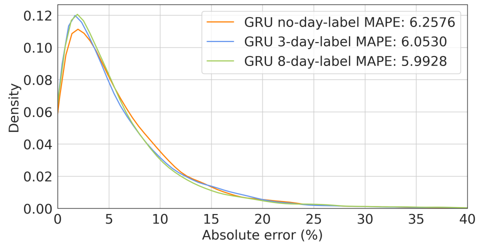

(b) Probability Density Function

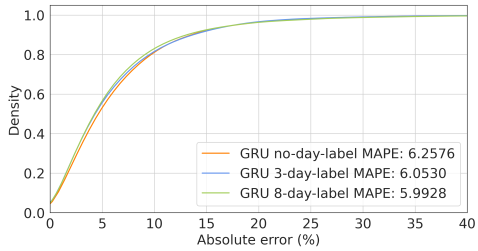

(c) Cumulative Distribution Function

Figure 4.3: Step 2 different calendar labels impact on GRU load forecast performance: no-calendar-labels vs three-calendar-labels vs eight-calendar-labels. (a) Regression plots for the real and forecast powers (b) Probability Density Functions for forecast errors (c) Cumulative Distribution Functions for forecast errors

4.1.4.3 Step 3: Shaping a flexible leading temperature conditions

Our paper conducts a correlation analysis between energy consumption and pre-n-hour instantaneous, maximum and average temperature, ranging from 0.5 to 24 hours ahead. To clarify, the maximum and average temperature conditions are calculated as the maximum and average temperature in the preceding n hours (within the timescale from instantaneous time to the previous n hours). The correlation coefficient, the 1^{st} order r^2 value, and the 2^{nd} order r^2 value are plotted in Figure 4.4. The load is highly correlated with the preceding temperature, with the highest correlation coefficient exceeding 0.7 for different lead times of instantaneous and average temperatures. The 2^{nd} order r^2 value curve peaks at 0.647 under the pre-7-hour average temperature condition. Table 4.1 records the conditions that lead to the best correlation and 2^{nd} order r^2 value.

The six flexible temperature conditions recorded in Table 4.1 are then used as input for our load forecast model. We also test the model without temperature input and the model using simultaneous temperature as benchmarks. In Figure 4.5a,

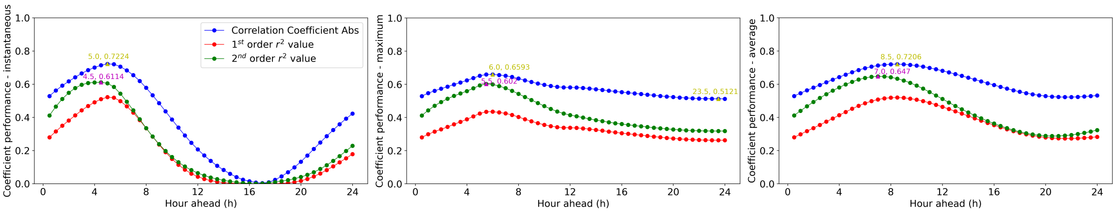

(a) Instantaneous temperature **(b)** Maximum temperature **(c)** Average temperature

Figure 4.4: Step 3 correlation analysis for load and various preceding temperatures. (a) Instantaneous temperature from 0.5 to 24 hours ahead (b) Maximum temperature within the preceding 0.5 to 24 hours (c) Average temperature within the preceding 0.5 to 24 hours

Table 4.1: Selected instantaneous, maximum, and average temperatures showing strong correlation with load in Horsham, Victoria, Australia (the wildfire seasons in 2015-2020)

Conditions	**Instantaneous temperature**		**Maximum temperature**		**Average temperature**	
Metrics	Hour	Value	Hour	Value	Hour	Value
Correlation coefficient	5hr lead	0.7224	6hr lead	0.6593	8.5hr lead	0.7206
2^{nd} **order** r^2 **value**	4.5hr lead	0.6114	5.5hr lead	0.602	7hr lead	0.647

the bold blue line represents the observed daily mean load, while the bold green line represents the 5-hour-ahead instantaneous temperature case since it performs the best among all. Noticeably, there is a timing mismatch between the real load curve and the two forecast lines that do not use the proposed preceding temperature conditions. This mismatch is corrected by applying conditions from Table 4.1, with forecast lines shifting later to better match the real load curve.

Figure 4.5b quantifies the daily forecast performance with three evaluation metrics. The blue line shows the real daily load of Horsham, and the grey area surrounded by the blue dotted line represents the 5th to 95th percentile interval. The six lines using our proposed methods mostly control the half-hourly error within 5%, while the two comparison cases demonstrate errors of up to 20%. The 5-hour-ahead instantaneous temperature line is marked bold green to highlight the best performance condition: the σ^2 is $2.79MW^2$, MSE is $0.62MW^2$, and MAPE is 3.81%. Compared to the simultaneous-temperature-load and no-temperature methods, our proposed method reduces the MAPE by 30.73% and 36.39%, respectively.

4.1.5 Conclusion and future work

This paper presents a robust multi-factor deep learning-based load forecast model to predict short-term electricity consumption in DNs in Victoria, Australia, during extreme wildfire seasons from 2015 to 2020. We have analysed and optimised factors that affect load forecast accuracy, including input data structures, calendar labels, and the flexible use of preceding temperatures. Our model has been tested on three DNs in Victoria and achieved good and stable performance, with an average MAPE of 2.95% over two five-month wildfire season test datasets from 2018 to 2020. The novel input feature selection decreases the MAPE by 36.39% and 30.73%, compared to using no-temperature and simultaneous temperature alone, respectively. Our standardised load forecast method can be applied to other regions facing extreme weather conditions in the future, given its climate robustness and accurate performance.

4.2 A comparative climate-resilient energy design: Wildfire Resilient Load Forecasting Model using multi-factor deep learning methods

4.2.1 Introduction

On the path to Net Zero, power systems face significantly growing uncertainty due to generation diversification and demand electrification. Furthermore, the escalating incidence of extreme weather events poses substantial challenges to the reliable and resilient operation of energy systems. In the case of generation, not only does the output of all types of renewable generators become increasingly intermittent, but conventional power generation may also experience substantial change. Fossil fuel and nuclear-based power stations are affected due to shortages and higher

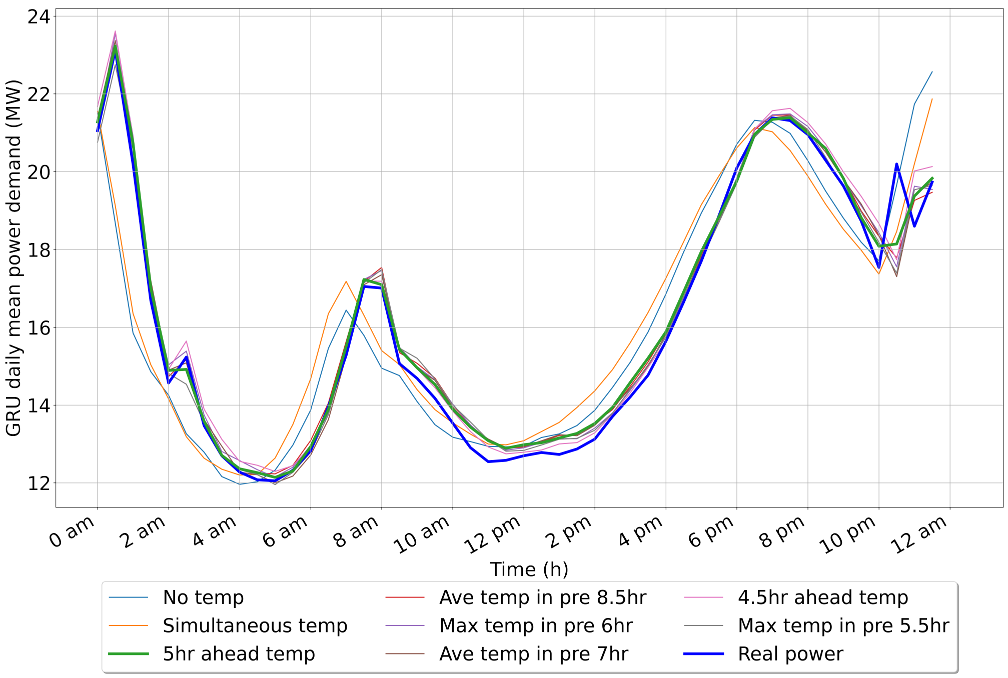

(a) Daily mean load & forecast load

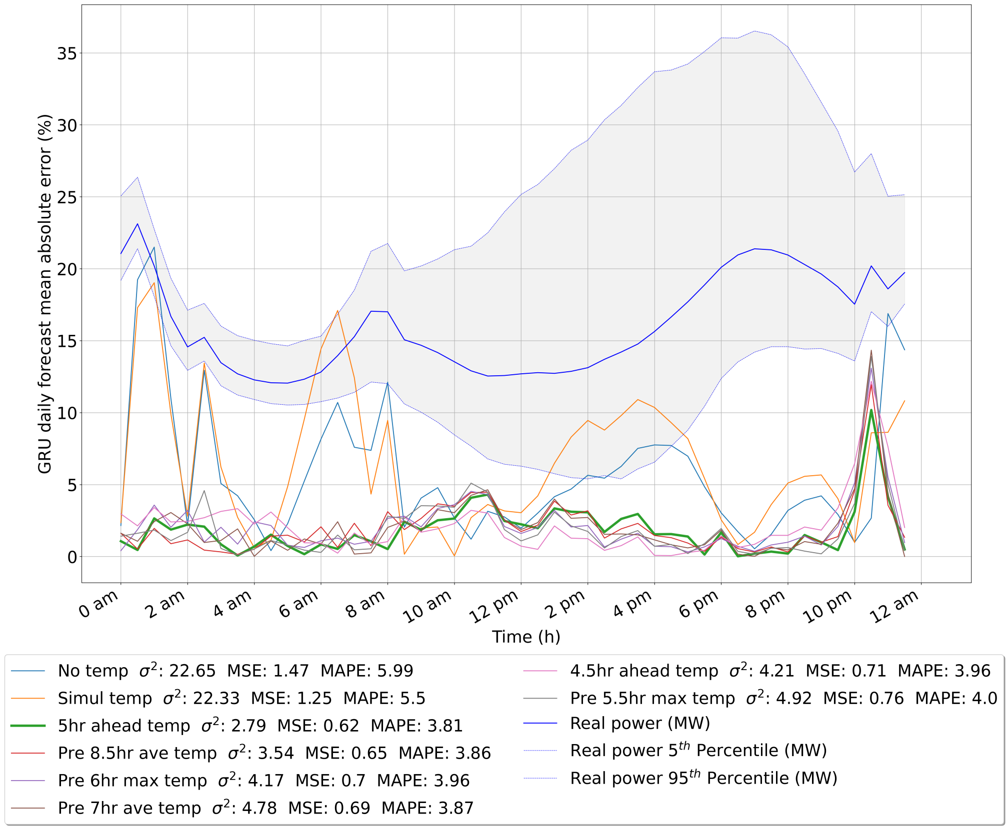

(b) Daily forecast mean errors with different temperature uses

Figure 4.5: Step 3 load forecast performance comparison using flexible temperature conditions. (a) The real and forecast daily mean loads (b) The daily mean absolute errors for 8 forecast methods and the real daily load dispersion (The uptick in consumption observed around 1 am is attributed to dedicated loads from off-peak electrical hot water systems)

temperatures of water supplies used in cooling. For example, the frequency of climate-related nuclear plant outages has increased nearly eightfold since the 1990s, as reported by the American Nuclear Society [199]. On the consumer side, demand surges during periods of extreme weather, particularly for cooling and heating applications. For instance, it is projected that the peak electricity demand in the U.S. will increase by 7.2% by the end of this century due to increasing extreme temperature events [200]. Therefore, a pressing need exists to develop intelligent and climate-resilient energy forecasting tools to help local energy operators properly dispatch power in advance or swiftly restore power connections when facing extreme weather.

With the combined risks from climate change and the ageing power systems, extreme weather events increasingly cause unintentional blackouts, resulting in significant economic and social costs. Among these consequences, power grid damage due to wildfire has become a growing concern, e.g., reduced line capacity, conductor line sag, and physical infrastructure damage. For example, Australia faces annual wildfire seasons from November to March. During the 2019-2020 wildfire season, numerous wildfires erupted in Australia, with a notable impact in Victoria State, leading to 33 fatalities and 19 million hectares of land destruction [201]. Furthermore, during the New Year Period in New South Wales, over 20,000 households experienced power outages [1].

As extreme wildfire risks are characterised by high temperature, low humidity and high wind conditions, our study picks multi-year wildfire seasons in Australia as a case study, aiming to develop the Wildfire Resilient Load Forecasting Model (hereafter the WRLFM) at the Distribution Network (DN) level. In terms of extreme weather, it is a regional and short-term phenomenon rather than a large-area and long-term climate pattern. Therefore, load forecasting at the transmission network or higher national level is out of scope.

In our paper, we develop the WRLFM through a two-stage approach. First, we assess, compare, and adapt trending load forecasting models to identify the most effective ones. Subsequently, we incorporate multiple factors into the model, updating some previously employed variables to enhance flexibility. Additionally, we introduce the Canadian Forest Service Fire Weather Index Rating System (FWI), which improves the overall load forecast accuracy and resilience.

There are two primary categories of load forecasting methods: traditional statistical methods and Artificial Intelligence (AI) based methods. Commonly used statistical techniques include Multiple Linear Regression (MLR), Autoregressive Integrated Moving Average (ARIMA), Semi-parametric Additive Model (SAM), and Exponential Smoothing Model (ESM) [110], [111]. However, these methods face challenges capturing demand fluctuations induced by non-linear characteristics during extreme weather events. To address non-linearity, data-driven methods such as shallow Machine Learning (ML) and Deep Learning (DL) have emerged in recent research. Common shallow ML methods encompass Support Vector Machine (SVM), Random Forest (RF) and Extreme Gradient Boosting (XGB) [112]. DL methods have further evolved in two main directions: Recurrent Neural Network (RNN) specialised in handling sequential data and Convolutional Neural Network (CNN) proficient in capturing spatial data features, such as image recognition [114], [109].

In addition to comparing and adapting various forecast models, the inclusion of multiple factors is crucial for enhancing forecast accuracy. Few studies have investigated the internal relationship between various factors and load behaviours before incorporating them as model inputs. For example, prior studies [119] and [120] typically used 24-hour ahead load data as the default input due to its daily periodicity but had yet to explore the optimised design of input structures. Calendar effects were applied to load forecasting studies in different classification ways, such as working and non-working day characteristics in [121]. While most studies adopt a specific method for calendar effects, there is room to explore and compare various approaches. Furthermore, multiple climate-related factors, such as temperature, humidity, wind speed, and precipitation, have been considered before. Daily mean or instantaneous temperature was commonly used [122], [123], [124], [125]. However, the relationship between load and temperature varies by region, necessitating a thorough investigation into the efficient utilisation of temperature and its temporal dynamics. Our paper comprehensively evaluates and compares existing approaches to incorporate multi-factors, including input sequence lengths, calendar effects, and temperatures. We aim to optimise the utilisation of each factor. Additionally, we introduce the use of the FWI, a factor calculated based on temperature, relative humidity, wind, and rainfall, to enhance the performance of the WRLFM during extreme wildfire seasons [202].

This paper introduces a novel climate-resilient multi-factor load forecasting model, known as the WRLFM, based on RNN and CNN-derived methods. The WRLFM has been developed using operational data from a DN in Victoria, Australia, during the wildfire seasons in 2015-2020. Initially, we compare and adapt 13 contemporary ML and DL models to identify the most effective ones with suitable input structures. Subsequently, we explore the internal relationship between energy consumption behaviours and various factors. Each factor's contribution is optimised, including the input matrix structure, calendar effects, correlation-based preceding temperature conditions, and the innovative inclusion of a high-resolution factor: the Fire Weather Index. Finally, the generalised WRLFM is further evaluated using the wildfire and non-wildfire datasets. This evaluation underscores the challenges associated with load forecasting during extreme stress periods and the significance of our work.

The rest of this paper is organised as follows. Section 4.2.2 presents the core methodology used to develop the WRLFM, including pre-processing steps to generate the input matrix and an in-depth discussion of how each factor contributes to improved forecast performance. Additionally, we review the mechanisms of each ML/DL method and the metrics used for performance evaluation. Section 4.2.3 introduces the background and data acquisition methods for our case study. Our model's generalisation is outlined in Section 4.2.4 through five key steps based on the performance enhancements. Section 4.2.5 summarises the key findings and advises future work.

4.2.2 Methodology

In Figure 4.6, the main steps to develop the WRLFM are described in a flow chart on the left-hand side, with the detail of how each factor contributes to the model resilience and accuracy improvement shown on the right. The pre-processing methods for each factor and details to generate the input matrix are explained in Section 4.2.2.1. Then, the input matrix is fed into various trending ML/DL methods to forecast sequential electricity demand. The mechanism of each forecast structure is reviewed in detail in Section 4.2.2.2. Finally, the metrics used for performance evaluation are discussed in Section 4.2.2.3.

4.2.2.1 Pre-processing steps to generate the multi-factor input matrix

As displayed in Figure 4.6, the input matrix is created through four stages: input structure selection, classification of calendar effects, consideration of flexible preceding temperature conditions, and introduction of the Fire Weather Index. In Step 5, the final generalised model is tested with datasets corresponding to wildfire and non-wildfire seasons to ascertain the effectiveness and significance of applying the proposed methods during periods of extreme weather.

Step 1 Input sequence structure

Step 1 comprises two distinct functions: comparing 13 trending methods and selecting the appropriate input sequence length for each method. The structure and mechanism of each AI-based forecasting model will be discussed in Section 4.2.2.2. In a sequential forecasting scenario, historical data with a fixed length must be

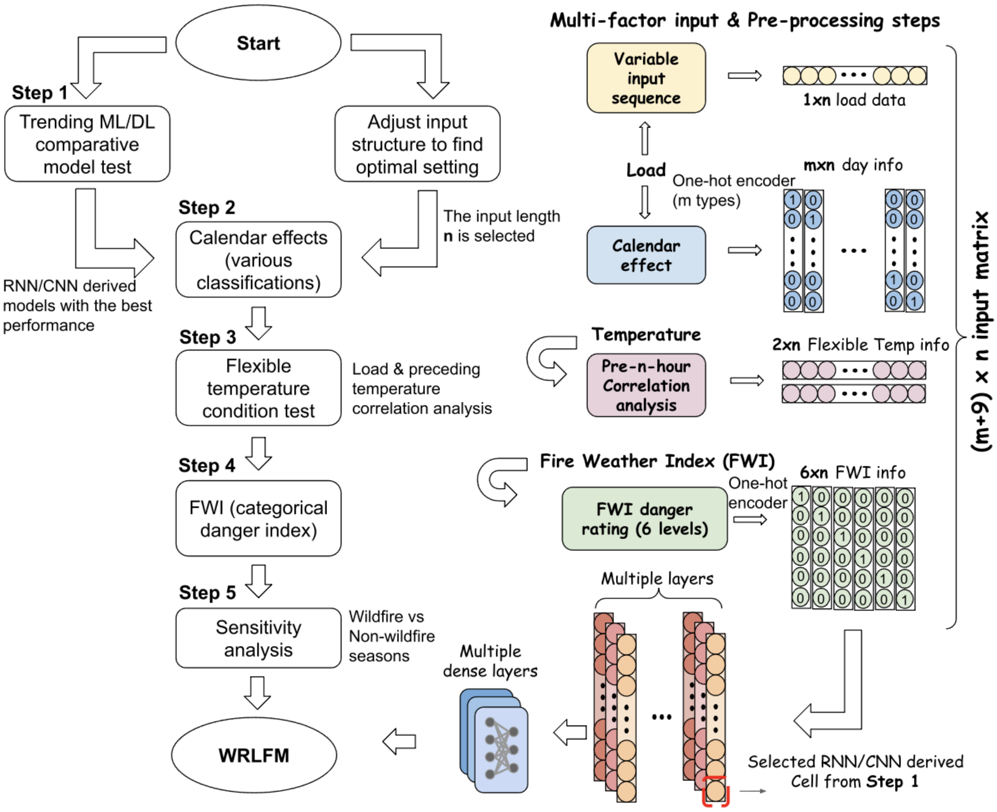

Figure 4.6: Main structures of the Wildfire Resilient Load Forecasting Model (WRLFM)

defined to predict the next one or several data points. In Step 1, we exponentially vary the input sequence length to identify the optimal input length n, ensuring both high accuracy and an acceptable computational burden. The column number of the input matrix is then determined by the input sequence length, set as n columns.

Step 2 Calendar effect

In Step 2, calendar information is categorised into m types using a One-hot encoder, which converts categorical day-type features into numeric variables [191]. The principle of One-hot encoding is as follows: a categorical variable $\mathbf{x}$ with n discrete values is expressed as $x_1, x_2, ..., x_n$. Each category is transformed into a vector $\mathbf{v}$, where every element of the vector is zero except for the i^{th}, which has a value of 1. For each sampling point, the calendar vector is transposed into a column vector according to its category, arranged as an $m \times n$ matrix, and placed in the middle of the input matrix.

Step 3 Flexible preceding correlation based temperature

As depicted in Figure 4.6, temperature information occupies two rows within the input matrix. The first row comprises a sequence of the preceding n temperature data, akin to extracting the $1 \times n$ load data in Step 1. The second row is organised based on flexible preceding temperature conditions determined through dynamic correlation analyses. Recognising that temperature changes may induce fluctuations in energy demand, we perform correlation analyses involving preceding instantaneous, maximum, and average temperatures with energy consumption. These analyses sort out the potential flexible temperature conditions to improve the WRLFM performance.

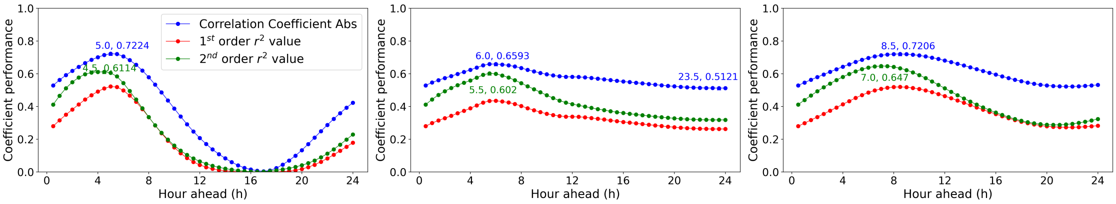

(a) Instantaneous temperature **(b)** Maximum temperature **(c)** Average temperature

Figure 4.7: Correlation analyses for load and various preceding temperatures of Horsham, Victoria, Australia during wildfire seasons in 2015-2020. (a) Instantaneous temperatures from 0.5 to 24 hours ahead (b) Maximum temperatures within the preceding 0.5 to 24 hours (c) Average temperatures within the preceding 0.5 to 24 hours

Figure 4.7 illustrates the results of a flexible correlation analysis between energy demand and various preceding temperatures, using operational data from the Horsham DN in Victoria, Australia, during the wildfire seasons in 2015-2020. The analysis considers the instantaneous temperatures at different hours ahead, the maximum and the average temperatures over various preceding hours, with increments of 0.5 hours, ranging from 0.5 to 24 hours ahead. Correlation coefficients, the 1^{st} order r^2 value, and the 2^{nd} order r^2 value are plotted for load and temperature. Some correlation coefficients exceed 0.7 for various instantaneous and average temperature lead times. The 2^{nd} order r^2 value curves follow a similar trend to the correlation coefficient, peaking at 0.64 under the pre-7-hour average temperature condition. The temperature condition leading to the strongest correlation among the three temperature types is identified and selected as the method for processing temperature information, placing it in the second row to potentially enhance its contribution to forecast performance.

Step 4 High-resolution Fire Weather Index

As our case study aims to design a load forecasting tool resilient to wildfire risks, we introduce a novel feature, the Fire Weather Index (FWI), to aid the WRLFM. The FWI is a meteorological index designed to estimate the risk of fire globally. It encompasses the effects of fuel moisture and wind impact on wildfire spread. A higher FWI indicates a greater likelihood of fire initiation and a more intense fire risk. Illustrated in Figure 4.8, FWI calculation necessitates five climate variables as initial inputs for subsequent computation of moisture codes and fire behaviour indices. These variables include temperature, 10m wind speed (u direction), 10m wind speed (v direction), total precipitation, and relative humidity.

The off-the-shelf FWI is available with a daily temporal resolution and a spatial resolution of 0.25°×0.25° from the European Centre for Medium-Range Weather Forecasts (ECMWF) Copernicus database [203]. However, these resolutions are inconsistent with energy load requirements; higher temporal and spatial resolutions are needed for the load forecasting tool. The procedures for calculating the high-resolution FWI are detailed in Figure 4.8. Firstly, NetCDF files for five climate variables are obtained from the ECMWF Reanalysis v5 (ERA5) hourly databases on single and pressure levels. Subsequently, each variable is refined with a 15-minute temporal resolution and a 0.01°×0.01° spatial resolution using the interpolation tool of the Climate Data Operator [204]. As the data are in NetCDF format, they are then transformed into CSV format, facilitating subsequent calculations. A unit conversion procedure is carried out since the original units for variables differ from the unit requirements in the primary FWI calculation process.

As shown at the bottom of Figure 4.8, the primary FWI calculation process consists of three stages. Firstly, four fire observational variables are required, each with specific units. Subsequently, moisture codes are computed based on various combinations of these observational variables. Moisture codes serve as numeric ratings for the moisture content of the forest floor and other deceased organic matter, with values increasing as moisture content decreases. The Fine Fuel Moisture Code (FFMC), the Duff Moisture Code (DMC), and the Drought Code (DC) indicate the moisture levels of litter and other fine fuels, loosely compacted organic layers of moderate depth, and deep, compact organic layers, respectively. The remaining three fire behaviour indices are the Initial Spread Index (ISI), the Buildup Index (BUI), and the Fire Weather Index (FWI), signifying the rate of fire spread, the fuel available for combustion, and the frontal fire intensity, respectively. Detailed calculation methods for generating FWI can be found in [205] and [206].

To validate the effectiveness of our methods in generating high-resolution FWI, we compared the daily FWI downloaded directly with the 15-minute resolution FWI curves we calculated. The daily FWI, available for download, aims to capture the peak burning condition of a day, typically around 16:00 local standard time (LST) [78]. Figure 4.9 illustrates the results of the Quantile-Quantile (Q-Q) comparative plots for the downloaded daily FWI and the calculated FWI at 4 pm, as well as the calculated daily peak FWI. Figure 4.9a demonstrates that the calculated FWIs at 4 pm do not align well with the distribution of downloaded daily FWI. This discrepancy arises because peak burning conditions may occur at times different from 16:00 LST. In Figure 4.9b, the distribution of the calculated peak daily FWI fits very well with the downloaded daily FWI (peak burning condition), proving the effectiveness and reliability of using our methods to generate high-resolution FWI curves. Figure 4.10 depicts the distribution and variability of the calculated high-resolution FWI by plotting the mean FWI curve and percentile lines. The

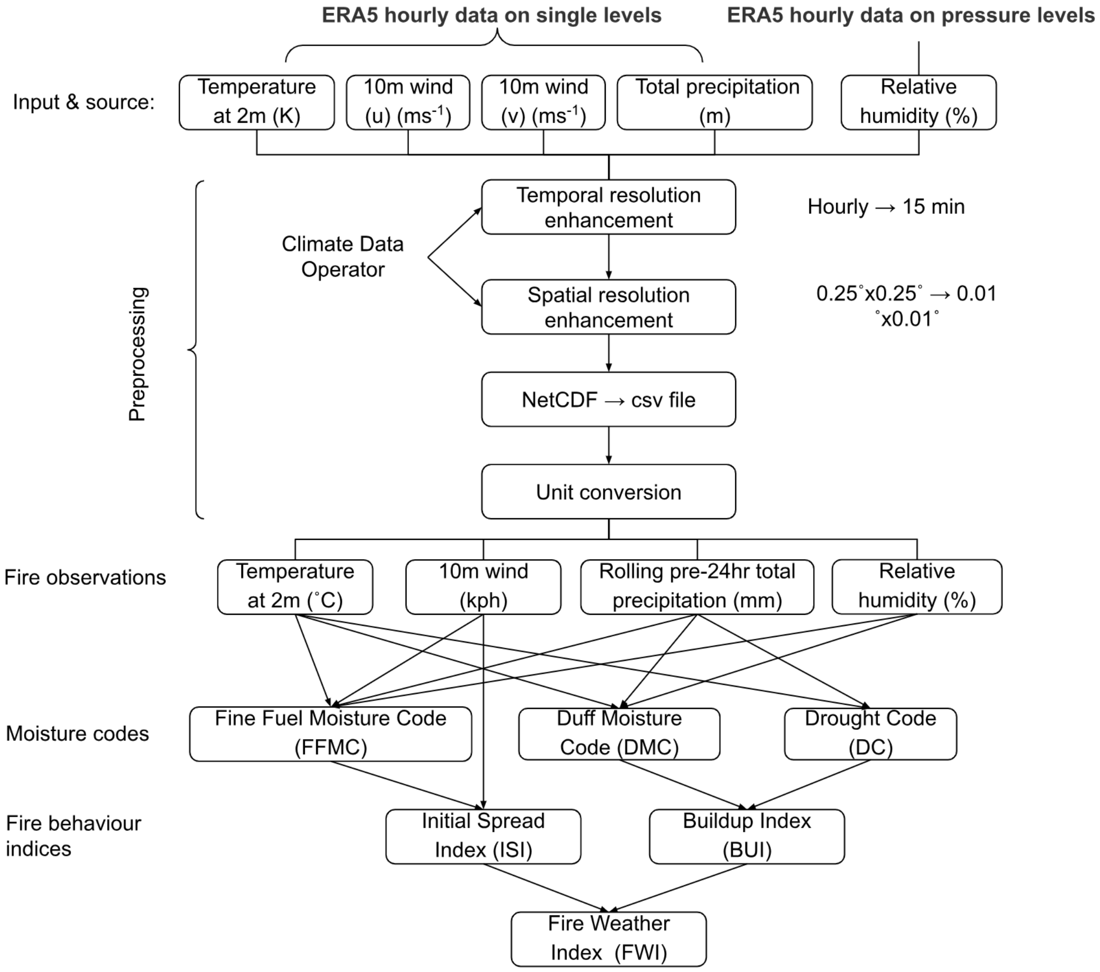

Figure 4.8: Methodology to generate Fire Weather Index (FWI) data with high spatial and temporal resolutions

blue rug plot at the bottom demonstrates the density distribution of the peak FWI times, indicating that FWIs are most likely to peak around 6 pm. Again, this underscores the importance of using high-resolution FWI to represent the fire risk trend within a day rather than directly using the fixed daily FWI value.

While the FWI is a numeric index, the FWI Danger Rating (DR) is classified into six levels, as illustrated in Table 4.2. Similar to calendar effects, FWI information is integrated into the input matrix using a One-hot encoder. The categorical FWI information is transformed into a $6 \times n$ matrix, positioned at the bottom of the input matrix.

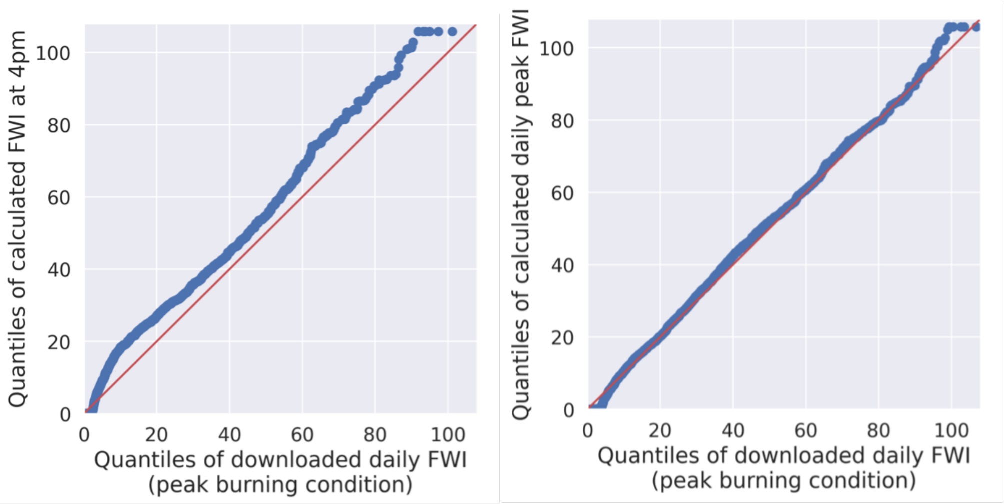

(a) Q-Q plot for calculated FWI at 4 pm & downloaded daily FWI

(b) Q-Q plot for calculated daily peak & downloaded daily FWI

Figure 4.9: Comparison between the downloaded daily FWI and the calculated FWI at 4 pm & the calculated daily peak FWI, based on operational data of Horsham, Victoria, Australia, from 2015 to 2020

Table 4.2: FWI Danger Rating levels (upper bound excluded)

Danger Rating	FWI range
Very low	(0, 5.2)
Low	(5.2, 11.2)
Moderate	(11.2, 21.3)
High	(21.3, 38.0)
Very high	(38.0, 50.0)
Extreme	(50.0, $+\infty$)

Finally, the input matrix, with a size of $(m + 9) \times n$, is composed, where m represents the category number of calendar effects, and n denotes the optimal length of historical input (look_back). The comprehensive input matrix is then fed into the selected multi-layer RNN-derived or CNN-related forecast structures to generate the load forecast.

4.2.2.2 Trending ML/DL based forecast methods

This section reviews the mechanisms of trending AI-based methods designed for addressing sequential data forecasting tasks. The description will be expanded in

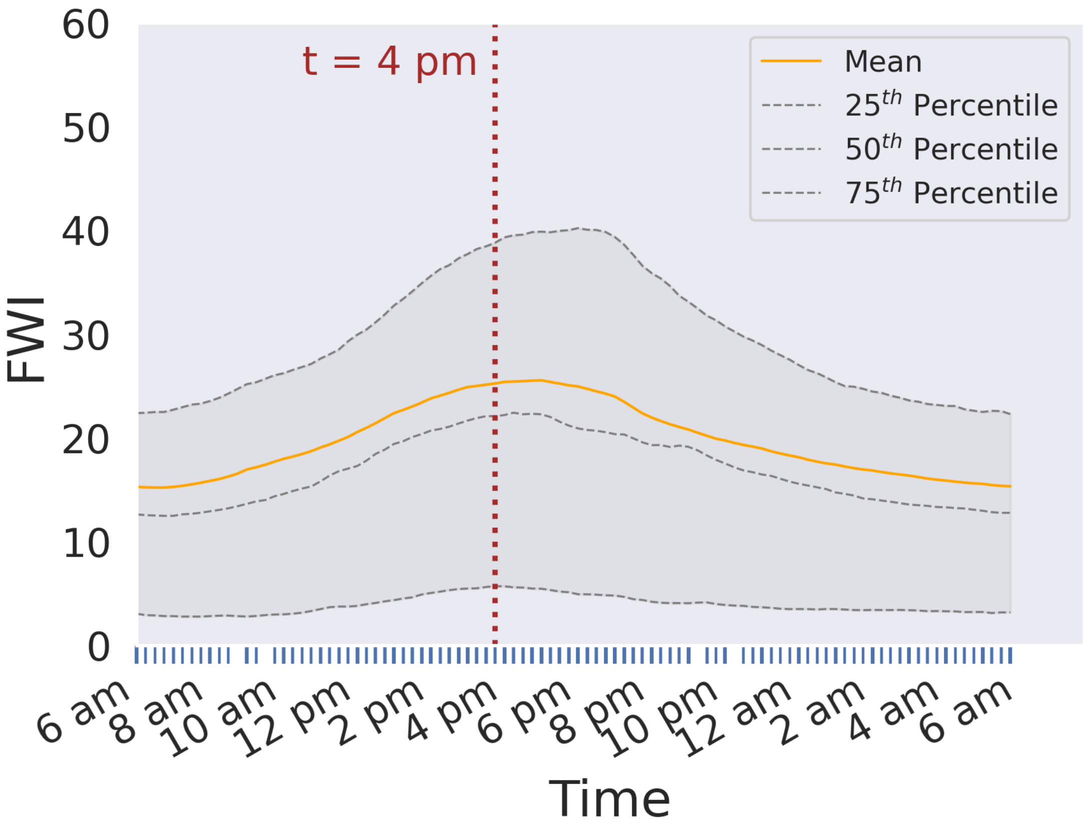

Figure 4.10: The distribution of the calculated daily 15-min resolution FWI curves, based on operational data of Horsham, Victoria, Australia, from 2015 to 2020. The 25^{th}, 50^{th}, 75^{th} percentile lines and the daily mean FWI curve are plotted to show variability of distribution

detail, commencing with shallow ML methods, progressing to basic DL methods, and then further exploring RNN-derived and CNN-related methods.

Shallow machine learning: SVM

The Support Vector Machine (SVM) was first proposed by Vapnik [207]. This technique involves mapping the data into an N-dimensional space (N features) and constructing an optimal separating hyperplane to classify all data points. The optimal hyperplane is selected to be the one with the maximum margin, meaning the distance between the hyperplane and each data group is maximised. Hinge loss is employed as the loss function to aid in maximising the margin. The kernels (linear, polynomial, radial basis function) and parameters (regularisation, gamma, degree) should be adjusted in different cases [208].

Shallow machine learning: RF

Random Forest (RF) is an ensemble learning method that combines the predictions of multiple decision trees to enhance overall performance and reduce overfitting. Each decision tree in the forest is trained on a random subset of the data and a random subset of features at each split. This approach enhances the diversity of the systems and improves classification performance. For the RF model, three parameters need adjustment and selection: the input feature period, the ratio of randomly selected features, and the number of predictors [209].

Shallow machine learning: XGB

Extreme Gradient Boosting (XGB) is widely employed for classification and regression tasks. Operating on the gradient boosting framework, it is renowned for its efficiency and effectiveness in generating accurate predictions. XGB sequentially builds a series of decision trees, introducing a new tree in each iteration to minimise the loss function, with each tree correcting the errors of its predecessors. Parameters, including the learning rate, maximum depth of trees, and regularisation terms, can be tuned to enhance forecast performance [210].

DL basis: MLP

A Multilayer Perceptron (MLP) is a category of artificial neural networks characterised by a minimum of three layers of nodes: an input layer, one or more hidden layers, and an output layer. Neurons serve as the fundamental computational units within each layer. Each neuron receives input, processes it utilising weights adjusted during training, applies an activation function, and generates an output. The activation function introduces non-linearity into the network, with common activation functions encompassing the sigmoid, Hyperbolic Tangent (tanh), and Rectified Linear Unit (ReLU). The loss function gauges the disparity between the predicted output and the actual target. Throughout the training process, the objective is to minimise this loss by iteratively adjusting the weights through optimisation algorithms such as gradient descent. The fine-tuning of activation functions, hidden layer numbers, and the quantity of neurons in each layer is imperative for effectively addressing diverse datasets [113].

RNN-derived methods

Recurrent Neural Network (RNN) constitutes a category of DL methods that have demonstrated notable effectiveness in tasks dealing with sequences, such as natural language processing, time series analysis, and speech recognition [211]. Let x_t, h_t, y_t denote the input, hidden state and the output at time step t. The hidden state at each time step is calculated as a function of the input and the preceding hidden state:

$$h_t = f(W_{hh} * h_{t-1} + W_{xh} * x_t + b_h) \tag{4.4}$$

, where W_{hh} represents the weight matrix for recurrent connections, W_{xh} is the weight matrix for input connections, b_h denotes the bias term, and f stands for the activation function. The current state output y_t is subsequently computed based on the current hidden state:

$$y_t = W_{yh} * h_t + b_y \tag{4.5}$$

, where W_{yh} is the weight matrix for output connections and the b_y denotes the bias term.

Traditional RNNs face challenges in capturing long-range dependencies due to the vanishing or exploding gradient problem. More advanced architectures, such as Long Short-Term Memory (LSTM) networks and Gated Recurrent Unit (GRU) networks, have been introduced. These architectures incorporate gating mechanisms that help control the flow of information through the network, allowing for more effective handling of long sequences and mitigating gradient-related problems. Both methods comprise different gates, helping determine which information is valuable and should be retained to produce the next memory cell. LSTM has three gates to control the memory cell state s_t, including the input gate Ψ_{it}, the forget gate Ψ_{ft}, and the output gate Ψ_{ot}, following the formulae (4.6), (4.7), (4.8), (4.9), (4.10) and (4.11) [109].

$$\Psi_{ft} = sigmoid(w_{fx}x_t + w_{fh}h_{t-1} + b_f) \tag{4.6}$$

$$\Psi_{it} = sigmoid(w_{ix}x_t + w_{ih}h_{t-1} + b_i) \tag{4.7}$$

$$\Psi_{gt} = tanh(w_{gx}x_t + w_{gh}h_{t-1} + b_g) \tag{4.8}$$

$$\Psi_{ot} = sigmoid(w_{ox}x_t + w_{oh}h_{t-1} + b_o) \tag{4.9}$$

$$s_t = \Psi_{gt} * \Psi_{it} + s_{t-1} * \Psi_{ft} \tag{4.10}$$

$$h_t = tanh(s_t) * \Psi_{ot} \tag{4.11}$$

, where Ψ_{gt} is the input node, w and b represent the corresponding connection weight and bias matrices.

The GRU was proposed by [212] in 2014 to address deficiencies found in traditional RNNs, including the vanishing gradient problem and the overhead reduction in the LSTM architecture. To diminish computational complexity, the GRU employs two gates to propagate the information flow: the update gate Ψ_{zt} and the reset gate Ψ_{rt}. The computation of each GRU cell can be expressed using Equations (4.12), (4.13), (4.14) and (4.15).

$$\Psi_{zt} = sigmoid(W_z \cdot [h_{t-1}, x_t]) \tag{4.12}$$

$$\Psi_{rt} = sigmoid(W_r \cdot [h_{t-1}, x_t]) \tag{4.13}$$

$$\hat{h_t} = tanh(W \cdot [\Psi_{rt} * h_{t-1}, x_t]) \tag{4.14}$$

$$h_t = (1 - \Psi_{zt}) * h_{t-1} + \Psi_{zt} * \hat{h_t} \tag{4.15}$$

, where W represents the corresponding weight matrices.

Further details of functional equations and weight matrices for LSTM and GRU can be found in [109] and [213]. While both LSTM and GRU belong to the RNN category, they exhibit advantages over each other in specific cases. GRU, a more recent invention than LSTM, features a simplified gate structure that utilises less memory and is faster. Additionally, it has been demonstrated that GRU is more resilient to gradient exploding and vanishing issues [193]. However, for datasets with long and high-complexity sequences, LSTM has exhibited superior forecast performance [194]. Consequently, both structures are tested and compared based on the WRLFM.

While RNN, LSTM and GRU models are tested, their corresponding bi-directional structures are also introduced and compared. Bi-directional RNN (Bi-RNN), Bi-directional LSTM (Bi-LSTM), and Bi-directional GRU (Bi-GRU) process sequential data in both forward and backward directions to comprehend the context from both past and future. Combining information from the two hidden layers (forward and backward) effectively captures long-term dependencies in sequences [214].

CNN-related methods

Given that the load forecast is calculated based on historical load and other features, the generated multi-factor matrix can be processed using deep learning methods designed for image feature extraction. Convolutional Neural Network (CNN), Temporal Convolutional Network (TCN), and Vision Transformer (ViT) are tested in our paper to understand the multi-factor input and predict future electricity demand.

CNN is designed to process structured grid data, such as images, specialising in extracting spatial features in datasets [215]. Convolutional layers consist of filters (also known as kernels) that slide across the input data, capturing local patterns. Pooling layers are then utilised to decrease spatial dimensions, retaining important information.

TCN is an extension of CNN designed for sequential data, making it suitable for time series tasks. It maintains the convolutional architecture but is adapted for 1D input sequences. In addition to the normal CNN structure, dilated convolutions allow TCN to capture various dependencies across different time scales. Skip connections help address the vanishing gradient problem and facilitate the flow of information [216].

ViT represents a novel approach to addressing image processing and multivariate time series forecasting tasks [217]. It leverages the transformer architecture, originally designed for sequence-to-sequence tasks in natural language processing, for image classification. ViT divides the input into fixed-size, non-overlapping patches, treating each patch as a token. These patches are linearly embedded and fed into the transformer encoder, which uses self-attention mechanisms to capture global contextual information in parallel. Positional encoding is used to record spatial information [218]. The self-attention mechanism allows the model to weigh various parts of the input sequence differently, capturing dependencies and relationships between elements. The attention mechanism is computed using three sets of vectors: Query (Q), Key (K), and Value (V), as expressed in Equation (4.16), (4.17) and (4.18).

$$Attention(Q, K, V) = softmax(\frac{QK^T}{\sqrt{d_k}})V \tag{4.16}$$

$$MultiHead(Q, K, V) = Concat(head_1, ..., head_h)W^o \tag{4.17}$$

$$head_i = Attention(QW_i^Q, KW_i^K, VW_i^V),\ i \in 1, 2, 3, ..., h \tag{4.18}$$

d_k is the dimensionality of the Query and Key vectors. Softmax is a mathematical function used for normalisation by converting raw scores into probabilities. Multi-head attention comprises multiple sets of Q, K, and V. Each head operates in parallel, and their results are concatenated to obtain the final output of the attention mechanism. The motivation behind using multiple heads is to enable the model to attend to different parts of the input sequence simultaneously, capturing diverse patterns and relationships. W^o is the output weight matrix after multi-head attention splicing. Function *Concat* concatenates the attention output from each head. W_i^Q, W_i^K and W_i^V are the weight parameter matrices for model training.

4.2.2.3 Evaluation methods

In our paper, Mean Squared Error (MSE) calculates the loss at each epoch to adjust the DL model training direction [218]. Additionally, MSE serves as one metric to evaluate the forecast performance. Another commonly used metric for assessing forecast accuracy is the Mean Absolute Percentage Error (MAPE) [219]. While MSE is a scale-based metric, the unit of MAPE is percentages, rendering it comparable among datasets with different units and scales.

$$MSE = \frac{1}{n}\sum_{i=1}^{n}(y_i - \hat{y}_i)^2 \tag{4.19}$$

$$MAPE = \frac{1}{n}\sum_{i=1}^{n}|\frac{(y_i - \hat{y}_i)}{y_i}| \tag{4.20}$$

where: y is the actual value, $\hat{y}$ is the predicted value, and n is the number of data points.

MSE and MAPE calculate the average error over the entire testing period. To evaluate the daily forecast performance, the daily mean error plots with the temporal resolution of 30 minutes are discussed in Section 4.2.4. The daily error variance is computed to assess the fluctuation in forecast performance within a day. The error variance σ^2 is calculated using the formula (4.21):

$$\sigma^2 = \frac{\Sigma(X-\mu)^2}{N} \tag{4.21}$$

where σ^2 is the error variance, X is the average half-hourly error, μ is the mean of the average half-hourly error over a day, and N is the total sampling points for a day. The smaller the daily error variance σ^2, the better robustness and stability of the forecast model [220]. Studying the stability of forecast accuracy within a day is valuable for identifying daily weak points and enhancing performance by addressing hard-to-predict periods.

4.2.3 Case study

To validate and demonstrate the development of the WRLFM, we selected the Horsham Distribution Network, located in the centre of Victoria, as the case study region. Five wildfire seasons (Nov-Mar) from 2015 to 2020 were chosen to train and assess model performance. The first three wildfire seasons (2015-2018) were selected as training datasets, while the last two were used as testing datasets. This section reviews the five main steps in developing the WRLFM, providing a detailed explanation of relevant data sources.

Overview of the case study

As depicted in Figure 4.6, the development of the WRLFM comprises five main steps: (1) Compare and identify the optimal input structures for 13 recently trending ML/DL methods. (2) Test the effect of applying different calendar classification methods. (3) Conduct a correlation analysis to elucidate the internal relationship between various preceding temperatures and load, selecting highly correlated temperature conditions to enhance forecast performance. (4) Apply categorical FWI features to the WRLFM. (5) Conduct sensitivity analysis on wildfire and non-wildfire periods to substantiate the effectiveness and resilience of

Table 4.3: Original data formats and sources. N/A represents non-applicable

Name	Spatial resolution	Temporal resolution	Unit	Source
Energy demand	N/A	30min	MW	Powercor [198]
Calendar data	N/A	30min	day-month-year	Powercor [198]
Temperature at 2m	0.25°×0.25°	hourly	K	ERA5 single level[177]
10m wind speed (u)	0.25°×0.25°	hourly	$m \cdot s^{-1}$	ERA5 single level [177]
10m wind speed (v)	0.25°×0.25°	hourly	$m \cdot s^{-1}$	ERA5 single level [177]
Total precipitation	0.25°×0.25°	hourly	m	ERA5 single level [177]
Relative humidity	0.25°×0.25°	hourly	%	ERA5 pressure level [178]
Fire Weather Index	0.25°×0.25°	daily	unit-less	Copernicus Database [143]

the WRLFM against extreme wildfire risks.

Original dataset acquisition and processing

The original data sources required to construct the WRLFM encompass historical energy demand data, calendar data, temperature, and FWI data (derived from temperature, wind speed, pre-24-hour total precipitation, and relative humidity). To consolidate all data into a unified input matrix, preprocessing steps are essential to ensure consistent resolutions. The preprocessing methods for generating the input matrix have been comprehensively discussed in Section 4.2.2.1. Table 4.3 details all datasets' sources and formats.

Powercor is one of the five primary energy distributors in Victoria, Australia, covering western and central Victoria. The energy consumption dataset is obtained from the Powercor Zone Substation Reports [198], with a temporal resolution of 30 minutes. Following the pre-processing steps, the temporal resolutions of all datasets are standardised to 30 minutes. For improved location accuracy of the DN, all climate datasets are spatially interpolated with a spatial resolution of 0.01°×0.01° using CDO.

4.2.4 Results and discussion

This section assesses and discusses the results, following the steps described in Figure 4.6. With each factor added, the improvement in load forecasting accuracy is evaluated to determine the appropriate method of embedding various factors into the input. After completing the four steps, a sensitivity analysis is conducted to compare the model's performance during wildfire and non-wildfire seasons, demonstrating the greater difficulty of load forecasting during extreme weather events and highlighting the significance of employing our proposed method to contribute to a more resilient and accurate load forecasting during wildfire seasons.

4.2.4.1 Step 1 Comparative analyses of trending ML techniques and corresponding optimal input structures

Following the description of Step 1 in Section 4.2.2.1, the MSE and MAPE based on 13 trending ML methods were plotted and compared in Figure 4.11. In each subplot, the input length was exponentially raised from 1 to 64 to determine the appropriate input sequence size with both good accuracy and acceptable computational burden. Overall, DL methods outperformed shallow ML methods (SVM, RF, and XGB) in terms of both MSE and MAPE.

Within the DL methods, as covered in Section 4.2.2.2, Bi-GRU exhibited the lowest error among all RNN-derived techniques, with an MAPE of 3.16% and an MSE of 0.44 MW^2. Concerning CNN-related methods, the ViT demonstrated the best performance with an MAPE of 3.20% and an MSE of 0.45 MW^2. Consequently, we selected the top-performing models from RNN-derived (Bi-GRU) and CNN-related (ViT) categories as the foundational forecasting structures for the WRLFM in the following steps.

Errors decreased as the input length increased and reached a stable level when the input length was approximately 16 hours. Although several models achieved their minimum error with an input sequence length of 64, the errors were close between the 32-lookback and 64-lookback operating cases. Therefore, the pre-16-hour period (lookback = 32) was determined as the optimal input sequence length for subsequent steps, i.e., setting the column number of the input matrix to 32.

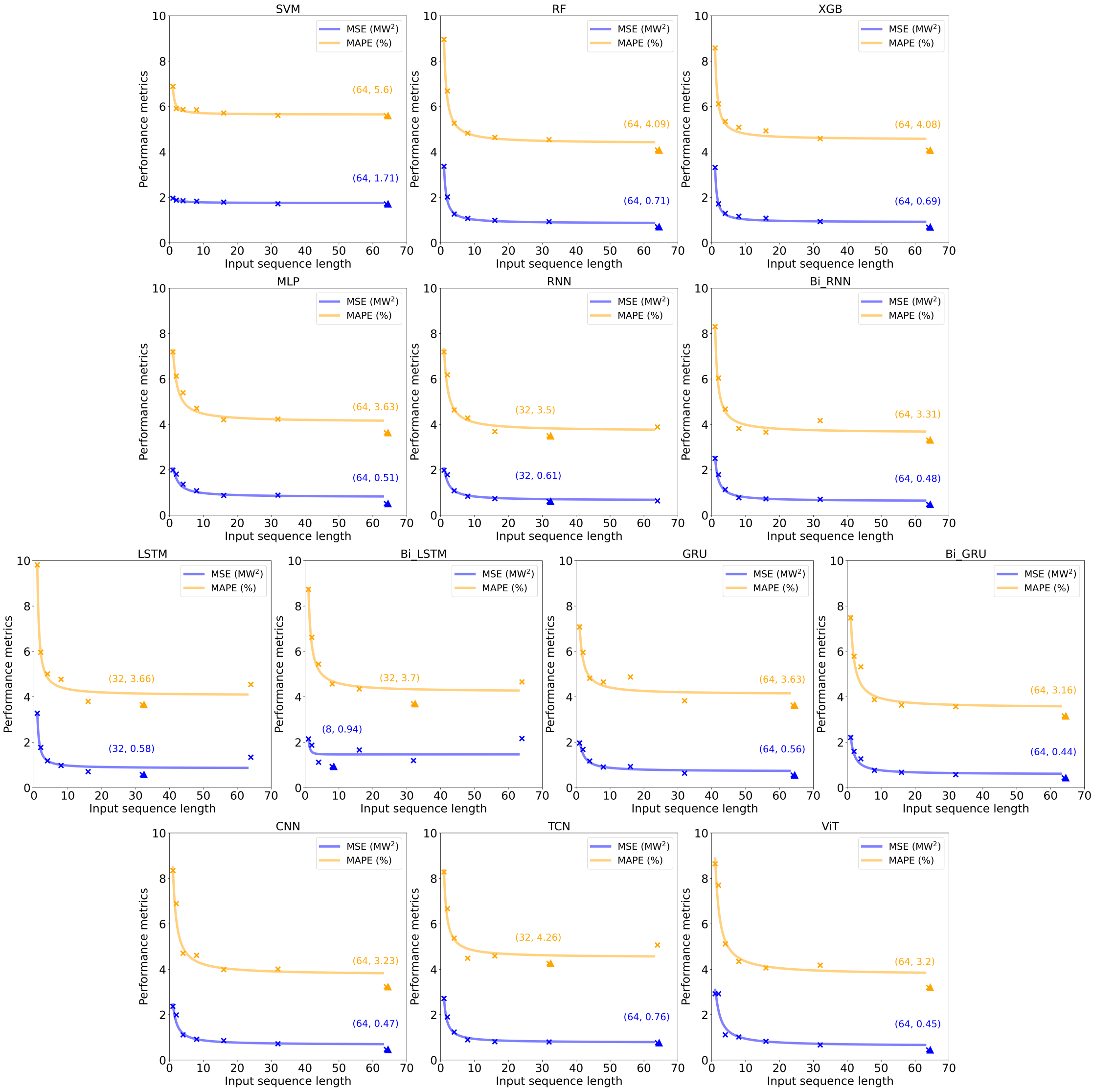

Figure 4.11: Horsham electricity load forecasting performances using the state-of-the-art ML methods and various lengths of historical data as input. The input length was raised exponentially from 1-64 to find the lowest error point. (the lowest error points are marked with triangles)

4.2.4.2 Step 2 Calendar information impact on forecast accuracy

In Step 2, two distinct approaches for assessing calendar effects on load forecasting were juxtaposed with the scenario lacking calendar information. The initial operational scenario categorised day types into three groups: weekdays, weekends, and holidays. The alternative method under consideration further refined the classification, encompassing each day of the week from Monday to Sunday, along with a separate category for holidays (comprising a total of eight types).

To evaluate performance, Probability Density Function (PDF) and Cumulative Distribution Function (CDF) plots, along with MAPEs and MSEs for all operational scenarios, are presented in Figure 4.12. Bi-GRU and ViT, identified as the top performers in Step 1, were both subjected to testing. It is evident that the incorporation of calendar information significantly enhanced forecast accuracy, as the error points in the case without calendar information accrued at higher values for both forecasting structures. Furthermore, the three-category calendar classification method surpassed the eight-category calendar classification method. Upon applying the three-category calendar classification method, the MSE decreased by 8.1% and 18.8%, and the MAPE decreased by 5.3% and 15.4% for the Bi-GRU and ViT models, respectively, compared to the original case without considering calendar information in the input.

4.2.4.3 Step 3 Adopt flexible temperature conditions based on correlation analysis

In Step 3, our proposed flexible temperature conditions based on correlations were compared with typical temperature applications in existing load forecasting methods. The assessments were conducted using the best-performing conditions identified in the first two steps: Bi-GRU and ViT forecast models with three-calendar classification methods. Load forecasting performances were evaluated under various temperature conditions, including scenarios with no temperature, simultaneous temperature conditions, previous 24-hour mean temperature conditions, and flexible correlation-based temperature conditions. For our case study, we identified the temperature condition exhibiting the strongest correlation coefficient with the load as a novel and flexible condition. In Figure 4.7, the instantaneous temperature five hours ahead of the load demonstrates the most robust relationship, with a correlation coefficient of 0.7224. Consequently, the five-hour-ahead instantaneous temperature condition was selected for comparison with three alternative methods.

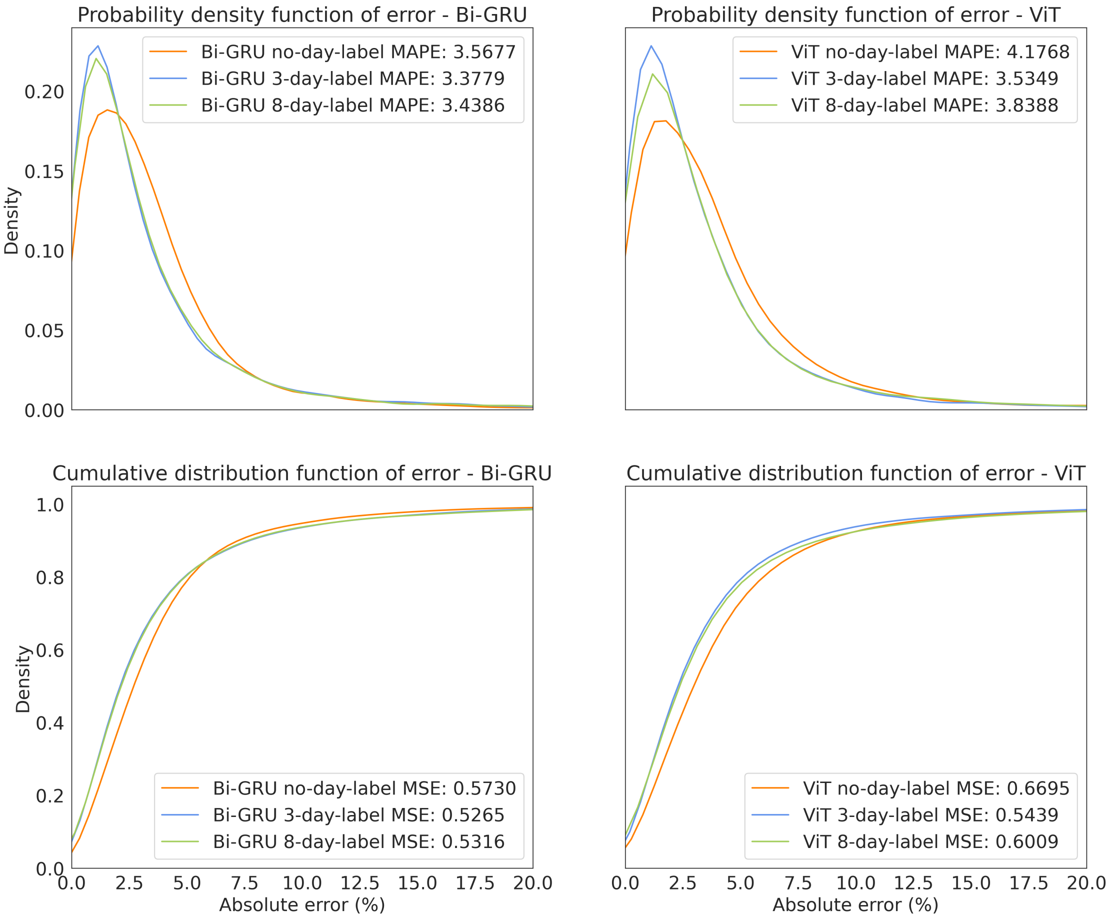

Figure 4.12: Impact of applying various calendar classification methods on load forecasting performance. Probability density functions and Cumulative distribution functions for forecast errors, based on Bi-GRU and ViT structures

Figure 4.13 illustrates the comparative daily mean absolute error curves for Bi-GRU and ViT-based models. The bold blue lines depict Horsham's real power curve, while the shaded area surrounded by blue dotted lines represents the 5^{th} to 95^{th} percentile interval of the daily load, indicating the change in dispersion level. The additional uptick in consumption observed between 10:30 pm and 1:30 am is attributed to dedicated loads from off-peak electrical hot water systems [221]. It is noticeable that the proposed best correlation temperature conditions yielded optimal performance in terms of MSE and MAPE for both Bi-GRU and ViT models. Compared to the no-temperature operating cases, our suggested best correlation temperature conditions contributed 9.4% & 5.6% of reductions in MSEs and 7.4% & 3.7% of decreases in MAPEs for the Bi-GRU and ViT-based models, respectively.

While our proposed methods, utilising the best correlation temperature conditions, demonstrated superior performance in terms of the two error evaluation metrics, the 24-hour mean temperature methods exhibited slightly better results with regard to daily error variation. Specifically, in Figure 4.13b, the error variance of our proposed method is twice as high as that of the 24-hour mean temperature condition. One potential explanation could be the influence of loads from the off-peak electrical hot water systems. Given that we selected the previous five-hour instantaneous temperature as the flexible condition, it posed a challenge to adequately capture the relationship between load and temperature during manually controlled large-scale heating periods. Future work is required to explore methods to mitigate error variance without compromising accuracy.

4.2.4.4 Step 4 Upgrade load forecasting with categorical Fire Weather Index

As described in Section 4.2.2.1, high-resolution FWI curves were generated to contribute to the inaugural WRLFM. According to Table 4.2, FWI Danger Ratings are classified into six levels. The One-hot encoder was employed to convert the categorical wildfire risks into a $6 \times n$ matrix, thereby incorporating wildfire effects into load forecasting. Step 4 confirmed that the inclusion of high-resolution FWI contributed to an enhancement in forecast performance.

Figure 4.14 demonstrates the comparative outcomes for Bi-GRU and ViT models. Applying our proposed categorical FWI resulted in reductions across all three evaluation metrics. For the Bi-GRU-based model, MSE, MAPE, and error variance were decreased by 4.2%, 2.2%, and 24.6% following the incorporation of FWI. In the case of the ViT-based model, the introduction of FWI led to reductions of 3.9%, 2.9%, and 59.4% in MSE, MAPE, and error variance, respectively. While the decreases in MSE and MAPE were more modest, the use of categorical FWI notably diminished error variances, thereby enhancing the stability and reliability of forecasting results.

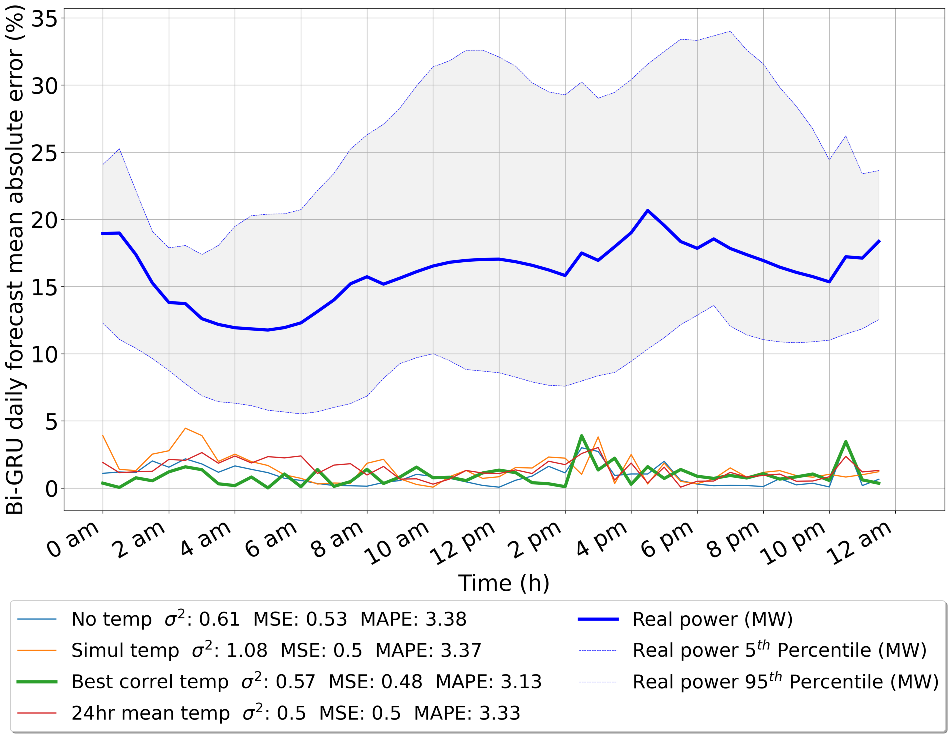

(a) Bi-GRU based model

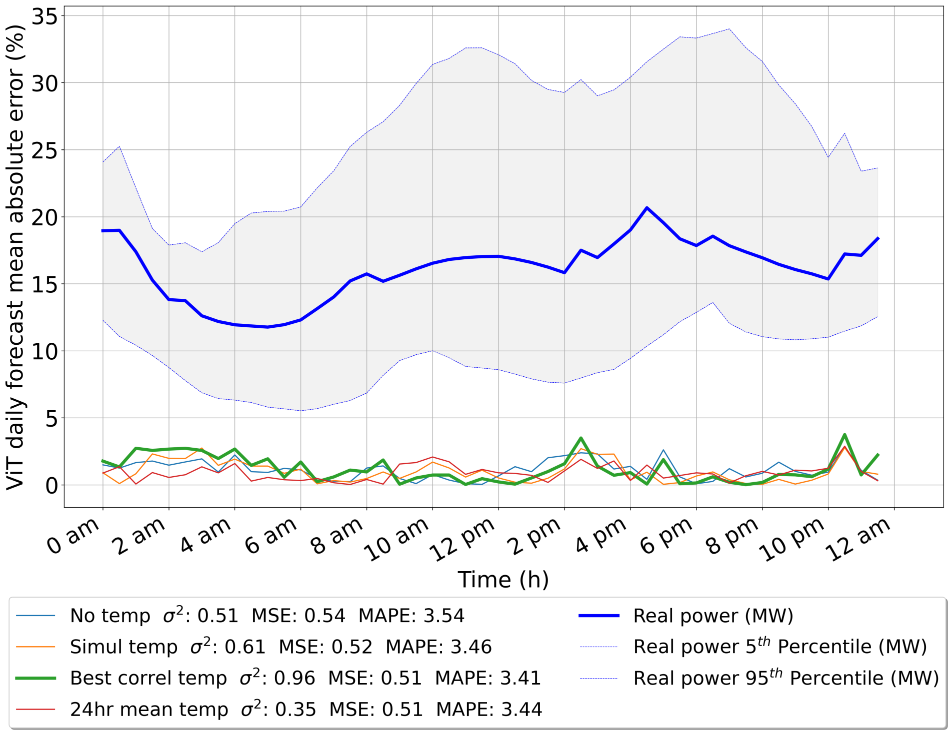

(b) ViT based model

Figure 4.13: Impact assessment of various temperature conditions on load forecasting performances. Daily forecast mean absolute error curves, along with MSEs, MAPEs, and error variances, are presented in each subfigure (Bi-GRU & ViT). The analysis utilises operational data from Horsham, Victoria, Australia, during the wildfire seasons in 2015-2020 (The uptick in consumption observed around 1 am is attributed to dedicated loads from off-peak electrical hot water systems)

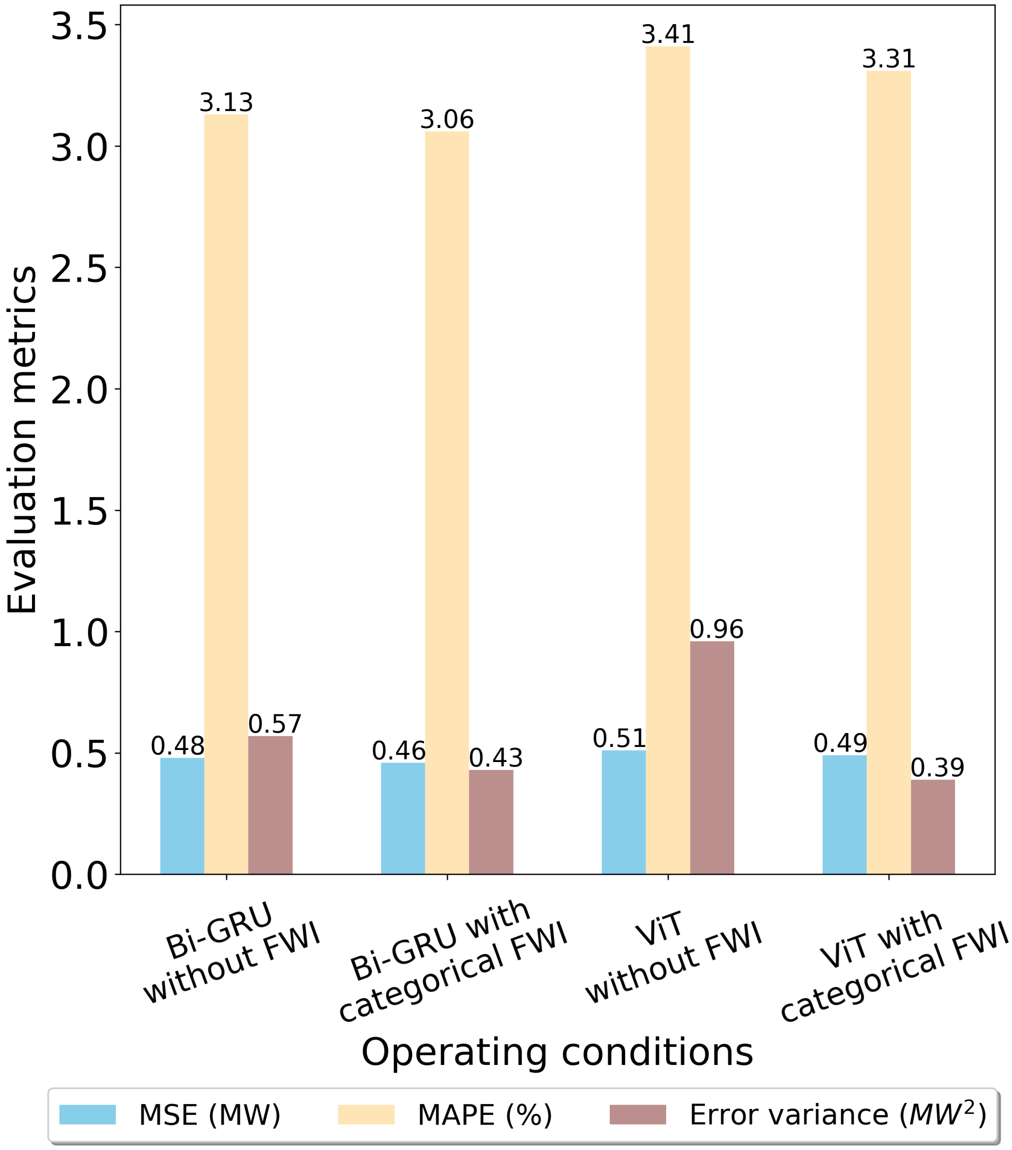

Figure 4.14: Impact of considering categorical Fire Weather Index on load forecasting performance

4.2.4.5 Step 5 Sensitivity analysis: data patterns and forecast performances during wildfire & non-wildfire seasons

Drawing conclusions from the four aforementioned steps, the optimal configuration for the WRLFM model can be summarised as follows.

(1) Configuring the input sequence length as 32 historical data points.

(2) Implementing the three-calendar classification method.

(3) Choosing the best correlation-based temperature condition.

(4) Incorporating high-resolution categorical FWI as an input.

The subsequent Step 5 is to assess the performance of the WRLFM during both wildfire and non-wildfire seasons, aiming to enhance our understanding of the importance of focusing on load forecasting amidst extreme weather events.

Before evaluating changes in forecast performances, it is essential to analyse the inherent characteristics of the datasets. As depicted in Figure 4.15, the relationship between power and temperature is assessed and compared based on various classification standards. The distributions of points exhibit distinctive features, with datasets having higher FWI values or occurring during wildfire seasons demonstrating greater absolute values of correlation coefficients compared to those with lower FWI values or during non-wildfire seasons. This suggests a potential closer relationship between climate factors and demand behaviour during wildfire seasons.

In Step 5, the original power-only forecast model from Step 1 and the ultimately best-performing WRLFM from Step 4 were applied to datasets corresponding to wildfire and non-wildfire seasons. Given that the annual wildfire season spans five months, we selected a comparable duration of non-wildfire seasons for testing. The comparative results are presented in Table 4.4. Notably, as indicated in the last column of Table 4.4, regardless of the DL structures and factor settings employed, load forecasting accuracy during non-wildfire periods consistently surpasses that during wildfire seasons under equivalent conditions. These results underscore the increased difficulty of load forecasting during extreme weather periods.

Additionally, we gauged the enhancements in forecast performance achieved by employing our proposed novel feature selection methods for both the Bi-GRU and ViT models. In the case of Bi-GRU, MAPEs were reduced by 14.37% and 2.8% when applying the WRLFM based on wildfire and non-wildfire season datasets, respectively. Similarly, the MAPE reductions from using the WRLFM were 20.86% and 14.01% during wildfire and non-wildfire seasons, respectively, for operating cases

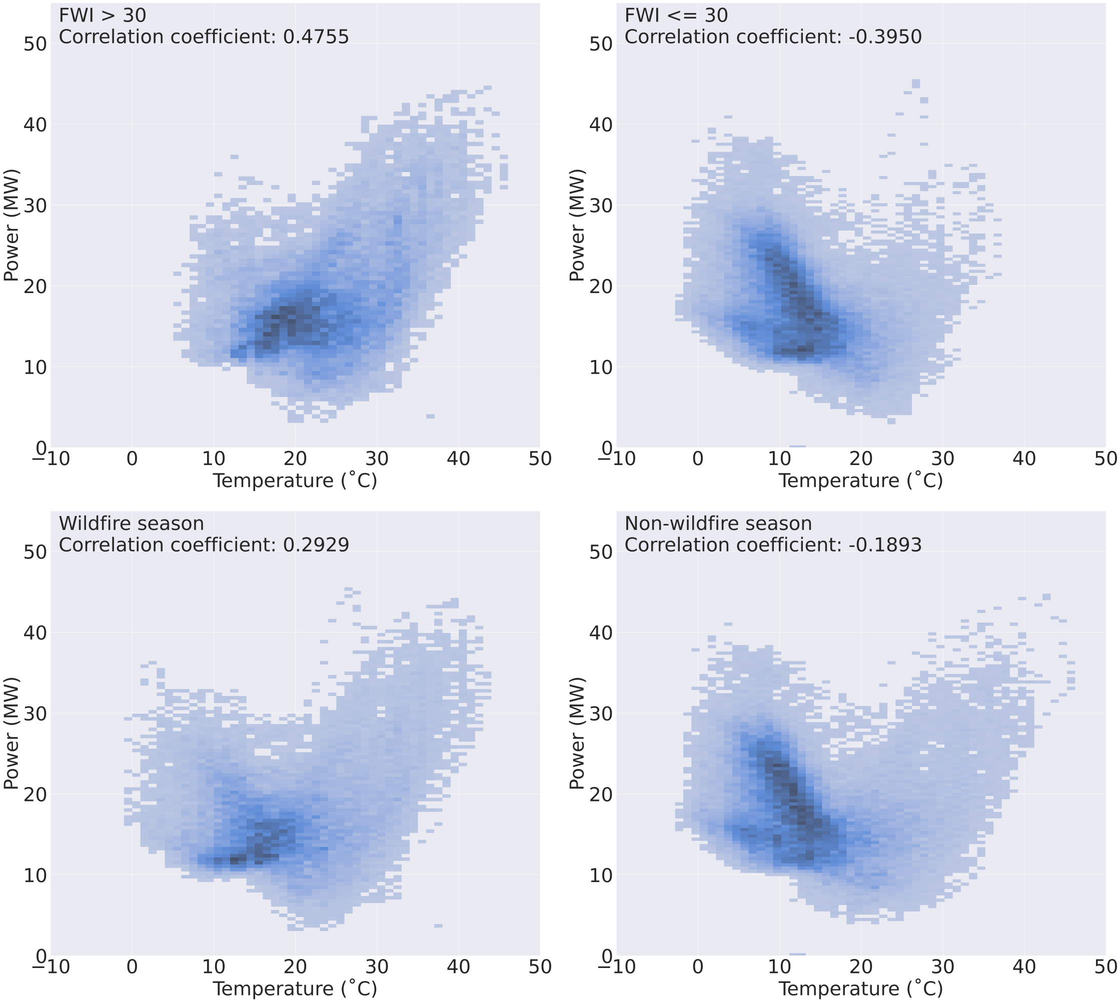

Figure 4.15: Different patterns of power-temperature relationships during wildfire and non-wildfire seasons – Horsham, Victoria, Australia, 2015-2020, grouped by operating periods and FWI values

based on the ViT structure. The more pronounced improvement in forecast accuracy during wildfire season scenarios underscores the effectiveness and robustness of employing our proposed WRLFM for predicting electricity load during extreme wildfire seasons.

In Table 4.4, the superiority of the WRLFM during wildfire seasons is demonstrated. Since the wildfire season in Victoria State is defined from October to March, not all testing points necessarily fall under high fire risk conditions. Therefore, we further compare the prediction performance at specific testing points with high fire risk versus those without risk during the wildfire seasons. Of the two five-month

Table 4.4: The load forecasting performance comparison between the proposed WRLFM and the original setting during wildfire and non-wildfire seasons - based on Bi-GRU and ViT structures

Model	Factor setting	dataset period	MSE (MW^2)	MAPE (%)
Bi-GRU	Original	Wildfire	0.5730	3.5677
		Non-Wildfire	0.6232	2.9154
	WRLFM	Wildfire	0.4639	3.0551
		Non-Wildfire	0.5812	2.8337
ViT	Original	Wildfire	0.6695	4.1768
		Non-Wildfire	0.6773	3.7878
	WRLFM	Wildfire	0.4924	3.3057
		Non-Wildfire	0.6465	3.2571

Table 4.5: The load forecasting performance comparison between the proposed WRLFM and the original setting for testing points with various FWI risk levels - based on Bi-GRU and ViT structures

Model MAPE (%)	Factor setting	FWI ≥30	FWI <30	Overall fire season
Bi-GRU	Original	3.1394	3.9195	3.5677
	WRLFM	2.6616	3.3782	3.0551
ViT	Original	3.7004	4.5680	4.1768
	WRLFM	2.7914	3.7280	3.3057

wildfire season testing datasets, 44.89% of the testing points have an FWI over 30, while the remaining 55.11% have an FWI below 30. Detailed predictions for datasets with FWI over and below 30 are provided in Table 4.5. Notably, the prediction accuracy for the dataset with an FWI over 30 consistently outperforms that with a lower FWI during wildfire seasons. In addition, the relative improvement, i.e., the accuracy improvement from the case with FWI below 30 to that with FWI over 30, is greater when using the WRLFM than the original model, demonstrating that the proposed WRLFM further enhances forecasting accuracy under high fire risk conditions.

4.2.5 Conclusion and future work

This paper has developed the Wildfire Resilient Load Forecasting Model (WRLFM) through a series of comprehensive comparative analyses based on operational data from a distribution network in Australia from 2015 to 2020. Visual interpretation of the datasets has demonstrated that load forecasting under wildfire risks is more challenging than during normal times, and there exists a closer relationship between load behaviour and climate variables during wildfire seasons. Therefore, we tested and optimised multiple forecast structures and factors, enhancing load forecasting performance during wildfire seasons.

In the beginning, 13 recently trending ML-based forecast models were compared to identify the best performers with appropriate input sequence structures. Bi-GRU and ViT emerged as the top performers among RNN-derived and CNN-related methods, respectively, with 32 historical data points selected as the optimal input sequence lengths for subsequent steps.

After determining appropriate forecast structures, multiple factors were incorporated into the input matrix to enhance forecast performance. Concerning calendar information, classifying days into three types (weekdays, weekends, and holidays) outperformed other common methods, resulting in an average reduction of 13.5% in MSE and 10.4% in MAPE, compared to the scenario without calendar information.

Furthermore, various temperature applications in load forecasting were tested, demonstrating that our proposed best correlation-based temperature conditions yielded optimal performances. The average reductions in MSE and MAPE were 7.5% and 5.6%, respectively, compared to the previous step.

Lastly, we introduced the novel use of the categorical high-resolution FWI as a factor to enhance the robustness and accuracy of load forecasting in the face of high wildfire risks. As the original FWI dataset is generated daily, detailed methods to generate half-hourly FWI curves were provided to align with the electricity data resolution in our paper. Categorical FWI information was embedded in the input using a One-hot encoder, leading to significant reductions in all three error metrics: 4% in MSE, 2.6% in MAPE, and 42% in daily error variance. To clarify, all error reductions calculated in this paragraph are the averages of the Bi-GRU and ViT results.

The final optimised setting of the WRLFM was identified as the Bi-GRU/ViT-based model with (1) an input sequence length of 32, (2) a three-calendar classification method, (3) a best-correlation-based temperature, and (4) categorical high-resolution FWIs. The optimised WRLFM reduced the MAPE of load forecasting during wildfire seasons by 14.37% and 20.86% for the Bi-GRU and ViT-based models, respectively. In contrast, the improvement rate of load forecasting performance during non-wildfire seasons was more than two times less, indicating the significance of applying the WRLFM, particularly to operational data during wildfire seasons.

Although our proposed best-correlation-based temperature conditions performed well in both MSE and MAPE, the stability of the forecasting was somewhat inferior compared to the use of pre-24-hour mean temperature conditions. One possible explanation discussed is that the load from large-scale off-peak electrical hot water systems might affect the best-correlation temperature conditions (the previous five-hour instantaneous temperature), capturing the relationship between load and temperature around midnight. Future work is needed to explore methods to enhance forecast stability by considering additional factors, such as large-scale, manually controlled load signals.

While we assessed five annual wildfire seasons in our paper, a more extended period of datasets can be utilised to enhance forecast robustness and reliability. When employing datasets spanning longer than a decade, certain long-term effects, such as the impact of El Niño-Southern Oscillation (ENSO) on load forecasting, should be further considered to fortify model robustness [222].

In conclusion, our paper proposes a deep learning-based multi-factor WRLFM to address the challenges of predicting load under extreme wildfire risks. A comparative analysis was conducted to determine the most effective deep learning forecast structures among recently trending methods. Relationships between load behaviours and multiple factors were discussed to identify the optimal way to incorporate variables into the input of the WRLFM. High-resolution FWI was generated and applied in load forecasting for the first time, improving overall forecast accuracy during wildfire seasons and significantly enhancing performance stability. Compared to original load forecasting without multi-factor application, the MSEs were reduced by 19.04% and 26.45%, and the MAPEs were reduced by 14.37% and 20.86%, for Bi-GRU and ViT-based models, respectively, after using the proposed WRLFM in our paper. While the distribution network load has been assessed, the WRLFM can be further applied to residential load forecasting. Additionally, the generalised WRLFM can be adjusted to incorporate other extreme weather risk indicators, contributing to a more resilient and accurate load forecasting performance in regions facing various types of extreme weather events.

5

Phase III: The generalised Wildfire Energy Model: a theoretical IEEE case

Contents

In this chapter, a generalised and dynamic Wildfire Energy Model (WEM) is developed, building upon the work conducted in the previous two phases. The initial phase focuses on worst-case power system resilience analysis, while the third phase extends the WEM's operational period, incorporating both temporal and spatial dynamics. The Wildfire Resilient Load Forecasting Model (WRLFM) proposed in the second phase is upgraded and integrated into the third phase of the WEM by including a net demand forecast function. Given that deterministic solutions are impractical for real-world energy system optimisation, uncertainty analysis is a critical component of the third phase of the WEM, managing various levels of resilience risk. This chapter provides a detailed discussion on the development of temporal dynamic functions, net demand forecasts, and the estimation of uncertain resilience risks.

To construct the WEM, the initial development is based on a theoretical power grid model to evaluate its performance and establish a generalised methodology. This methodology is then applied to a real-world power grid case study in Australia to further demonstrate its feasibility and efficacy in the next chapter. This chapter is divided into two primary sections: (1) main methodologies to build the WEM based on the IEEE 24-Bus Reliability Test System (RTS), and (2) results and discussion of the WEM performance based on this theoretical case.

This section provides detailed information on the modified IEEE 24-Bus RTS, which serves as the theoretical case study for developing the dynamic WEM. Following the introduction of the case grid, the principal methodologies for integrating dynamic fire risks, net demand forecasting functions, and uncertain resilience risk levels into the WEM are elaborated upon. The methods to calculate optimal power flow have been discussed in detail in Chapter 3, thus not repeated in this chapter. Preceding the analysis of results, the operational scenarios and multifaceted evaluation metrics are discussed. Finally, Section 5.6 offers a summary of this section, including remarks and challenges.

5.1 The modified IEEE 24-Bus RTS: grid structure, operational information and sources

The IEEE 24-Bus Reliability Test System was first proposed by the IEEE reliability subcommittee in 1979 as a benchmark for implementing power system reliability analysis [26]. With the development of power grid reliability and resilience studies, many modified and updated versions of the IEEE 24-Bus RTS have been developed to fit various test scenarios [223], [224].

To carry out a grid resilience study with climate risks, a modified IEEE 24-Bus RTS was designed in our research, with detailed information about the system elaborated in this section (generators, demand, bus voltage, and lines). In Figure 5.1, the basic structure of the modified IEEE 24-Bus RTS system is displayed, with generation types and capacities marked in detail. The grid is divided into two regions with different voltage levels, 138 kV and 230 kV, connected by five transformers. 24 buses are connected through 34 lines. Although the original grid has no renewable generation or battery storage, some wind turbines and storage are integrated into the grid in several operational scenarios in our study to recover load shed due to weather risks.

Generator information

The fundamental information about the types, capacities, and numbers of conventional generators at corresponding buses is listed in Table 5.1. To configure the generators' operational modes at each operating time, technical parameters should be set as model constraints to ensure generators operate within safety boundaries. The maximum generation capacity, minimum generation capacity, ramp-up rate, and ramp-down rate for each generator type are recorded in Table 5.2.

As cost-effectiveness and environmental impact are considered in model performance assessment, economic and environmental parameters for each generator type are discussed in this paragraph. According to [226], the generators' operational cost

Table 5.1: Conventional generator information: number, location, capacity, and type [26]

Number	Bus	Capacity (MW)	Type
1	1	152	Coal
2	2	152	Coal
3	7	300	Oil
4	7	50	Hydro
5	13	591	Oil
6	15	155	Coal
7	15	180	Oil
8	16	155	Coal
9	18	400	Nuclear
10	21	600	Nuclear
11	22	300	Hydro
12	23	310	Coal
13	23	350	Coal
Total	N/A	3695	N/A

Table 5.2: Technical parameters for conventional generators [225]

Gen cap (MW)	**Type**	**Max gen cap (MW)**	**Min gen cap (MW)**	**Uphill rate (MW/h)**	**Downhill rate (MW/h)**
152	Coal	152	30.4	14	14
155	Coal	155	54.25	21	21
310	Coal	310	108.5	21	21
350	Coal	350	140	28	28
180	Oil	180	36	21	21
300	Oil	300	75	42	42
591	Oil	591	206.85	21	21
50	Hydro	50	0	6	6
300	Hydro	300	0	35	35
400	Nuclear	400	100	47	47
600	Nuclear	600	150	70.5	70.5

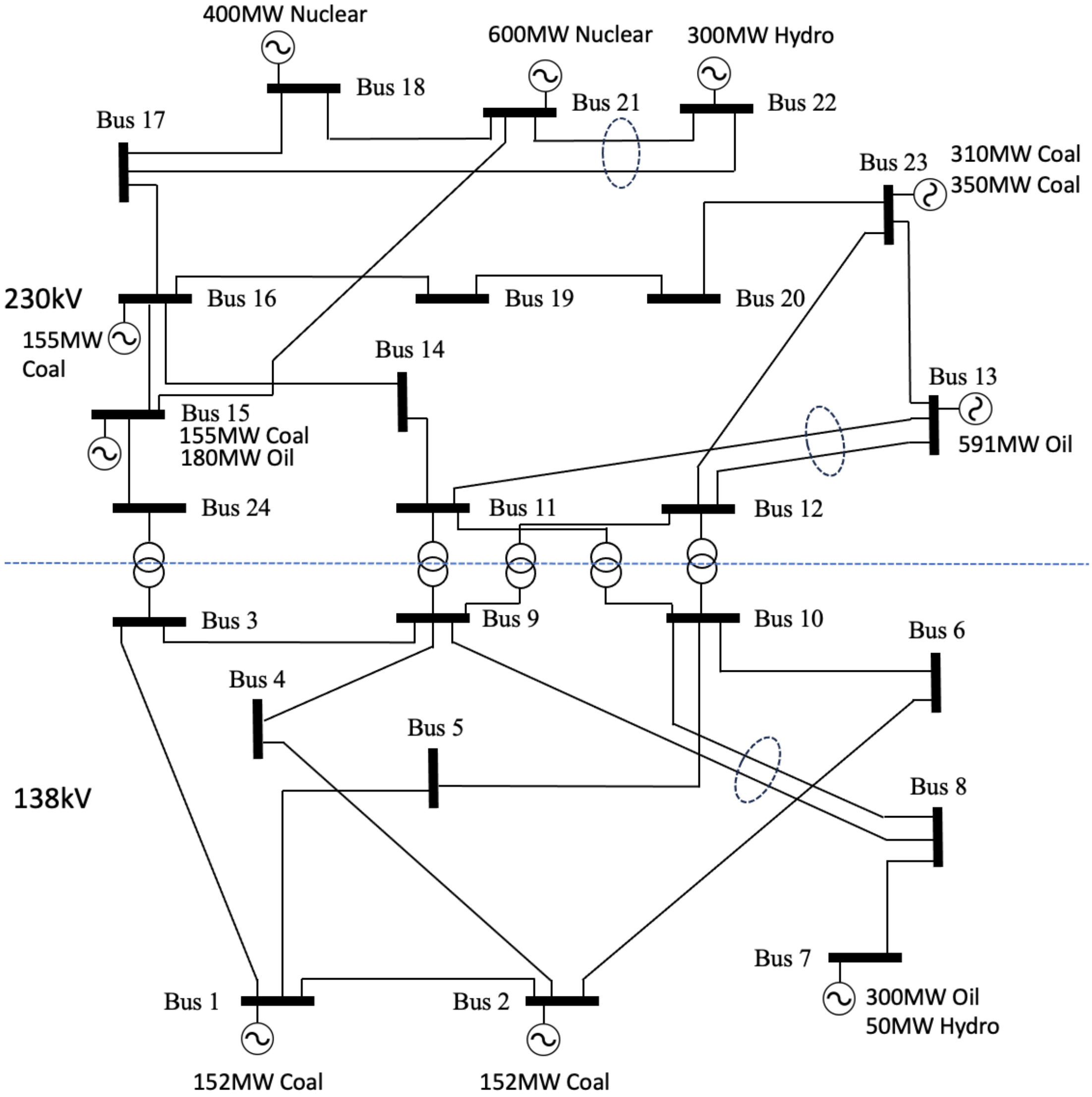

Figure 5.1: The modified IEEE 24-bus Reliability Test System Diagram

can be depicted using a quadratic function. The expression of the fuel cost is shown in (5.1), where $F_i(P_{gi})$ represents the fuel cost for the i^{th} generator, P_{gi} stands for the power output for the i^{th} generator and a&b&c are the three cost coefficients.

$$F_i(P_{gi}) = a_i P_{gi}^2 + b_i P_{gi} + c_i \tag{5.1}$$

The generator cost coefficients data are collated from a study at the Georgia Tech Power Systems Control and Automation Laboratory [225]. According to [227], the unit carbon emissions are calculated from both the constructional and

Table 5.3: Economic and environmental parameters for conventional generators [225], [227]

Generation Capacity (MW)	**Type**	**Cost coef - a** ($\$/MWh^2$)	**Cost coef - b** ($\$/MWh$)	**Cost coef - c** ($)	**Carbon emission coef - d** ($kgCO_2eq/MWh$)
76	Coal	0.014142	16.0811	212.3076	900
155	Coal	0.008342	12.3883	382.2391	900
350	Coal	0.004895	11.8495	665.1094	900
12	Oil	0.328412	56.5640	86.3852	650
100	Oil	0.052672	43.6615	781.5210	650
197	Oil	0.00717	48.5804	832.7575	650
50	Hydro	0	0.0010	0.0010	20
400	Nuclear	0.000213	4.4231	395.3749	5
600	Nuclear	0.000213	4.4231	395.3749	5

operational processes for specific generation sources. The cost coefficient and unit carbon emission for each type of generator are recorded in Table 5.3.

Demand information

The electricity load at each bus is also essential information for system operation and control. The peak demand and voltage boundaries at each bus are recorded in Table 5.4. In the original IEEE 24-Bus RTS, different demand curves are designed for various situations. The demand percentages with regard to the peak load are differentiated based on the seasons, week number, weekday, and hours [26]. To build a temporal and spatial dynamic WEM, one specific 24-hour load curve is selected for the modified IEEE 24-Bus RTS in our study, as displayed in Figure 5.2.

Line information

As depicted in Figure 5.1, there are 34 lines in the system, connecting the 24 buses. To carry out the dynamic optimal power flow analysis, the connection methods and technical parameters for all lines should be clarified. Table 5.5 provides information about the lines, including the starting points, ending points, reactances,

Table 5.4: Bus and demand information: peak demand and voltage limitations at each bus for the modified IEEE 24-Bus RTS [26]. Voltage limits are the per unit values

Bus number	**Peak load (MW)**	V_{min}	V_{max}
1	108	0.95	1.05
2	97	0.95	1.1
3	180	0.95	1.05
4	74	0.95	1.05
5	71	0.95	1.1
6	136	0.95	1.05
7	125	0.95	1.05
8	171	0.95	1.1
9	175	0.95	1.05
10	195	0.95	1.05
11	0	0.95	1.1
12	0	0.95	1.05
13	265	0.95	1.1
14	194	0.95	1.05
15	317	0.95	1.05
16	100	0.95	1.05
17	0	0.95	1.05
18	333	0.95	1.05
19	181	0.95	1.05
20	128	0.95	1.05
21	0	0.95	1.05
22	0	0.95	1.05
23	0	0.95	1.05
24	0	0.95	1.05

and transmission power limits.

5.2 Fire Weather Index and resilient threshold design

To optimise power grid operation during wildfire seasons, it is important to establish a relationship between quantified fire risks and the safety boundaries of grid equipment. In the first phase of the DPhil work, we considered fixed fire risk thresholds for lines operating in fire-prone regions. According to the Danger Rating

Table 5.5: Line information: locations, reactance and power limits [26]

From bus	**To bus**	**Reactance X (p.u.)**	**Power limit (MW)**
1	2	0.0139	175
1	3	0.2112	175
1	5	0.0845	175
2	4	0.1267	175
2	6	0.1920	175
3	9	0.1190	175
3	24	0.0839	400
4	9	0.1037	175
5	10	0.0883	175
6	10	0.0605	175
7	8	0.0614	175
8	9	0.1651	175
8	10	0.1651	175
9	11	0.0839	400
9	12	0.0839	400
10	11	0.0839	400
10	12	0.0839	400
11	13	0.0476	500
11	14	0.0418	500
12	13	0.0476	500
12	23	0.0966	500
13	23	0.0865	500
14	16	0.0389	500
15	16	0.0173	500
15	21	0.0245	1000
15	24	0.0519	500
16	17	0.0259	500
16	19	0.0231	500
17	18	0.0144	500
17	22	0.1053	500
18	21	0.01295	1000
19	20	0.0198	1000
20	23	0.0108	1000
21	22	0.0678	500

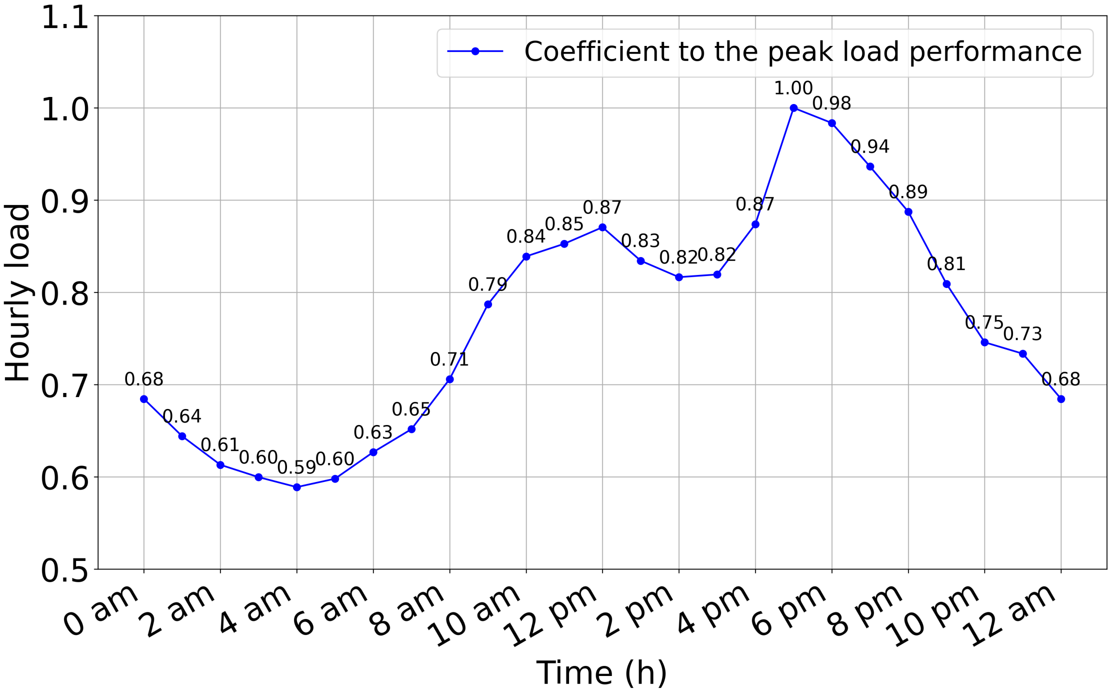

Figure 5.2: Daily load curve for the modified IEEE 24-Bus RTS, representing the percentage of peak demand [26]

Classification Table, the FWI thresholds were set at extreme (50.0), very high (38.0), and high (21.3) for three operating cases, serving as signals to disconnect lines under high risks. If the maximum FWI of all sampling points on a line exceeded the preset FWI threshold, the line was disconnected to prevent fire-related power faults. In the worst-case scenario (Phase I work), it is demonstrated that the stricter the threshold, the greater the load shedding would occur. The integration of DGs is needed under some strict fire risk control situations to satisfy 100% of the load. Proper FWI thresholds should be set based on the required local fire risk control level.

In Phase III, a more dynamic relationship between the FWI and power system operation is developed to better reflect practical scenarios. Compared to the fixed risk thresholds used in Phase I, a continuous and dynamic relationship between fire risks and the capacity limits of power lines is discussed and tested. As shown in Figure 5.3, a hypothesised relationship between FWI and line capacity limits is proposed.

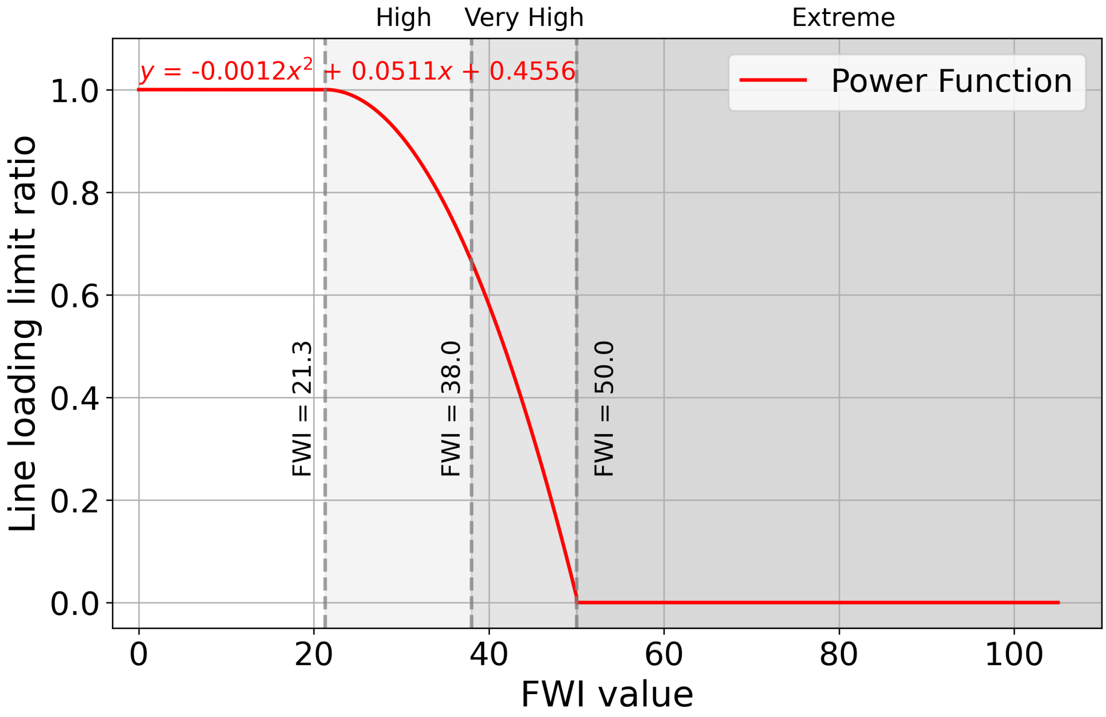

Figure 5.3: The hypothesised relationship between Fire Weather Index and line loading limit

This power function is selected to describe a hypothesised relationship between the line loading limit and the FWI value in Figure 5.3. With increasing negative slopes, this relationship assumes that the impact of fire risk on power lines becomes increasingly severe as the regional FWI risk rises. According to the Danger Rating Classification Table, it is assumed that the line can operate safely when the FWI is lower than 21.3 (moderate risk). When the FWI of a line is greater than or equal to 50.0 (extreme risk), the line needs to be fully de-energised to avoid a chain of regional blackouts. Based on these two hypotheses, the power function relationship is developed and shown in (5.2), where y is the line loading limit ratio, and x is the maximum FWI value of the line.

$$y = \begin{cases} 1.0 & x < 21.3 \\ -0.0012x^2 + 0.0511x + 0.4556 & 21.3 \leq x < 50.0 \\ 0.0 & x \geq 50.0 \end{cases} \tag{5.2}$$

Rationales of derating lines to reduce fire impact

Derating line capacity can protect power lines from safety issues caused by high temperatures during wildfire seasons. Figure 5.4 illustrates the rationale behind derating lines to mitigate fire risk. By limiting current, conductor temperature decreases, reducing line sag and the risk of vegetation contact faults, especially in windy and extreme heat conditions. The temperature reduction also lessens the mechanical tension on the lines, alleviating stress and preventing permanent damage, such as the annealing of metal components. Additionally, lower temperatures result in a higher breakdown voltage, increasing the difficulty of air ionisation and reducing the likelihood of corona effects and flashover.

The appropriate derating factors for lines under wildfire risk vary by location and can change in real time due to various factors, including ambient temperature, wind speed, wind direction, fire intensity, topography, line material, and conductor age. As noted in [228], the safety line capacity becomes increasingly constrained as the fire approaches. The derating rate is not linear: it accelerates as the fire nears the line. Consequently, the power function derating relationship proposed in Figure 5.3 is a reasonable assumption. In the future, real-time dynamic line ratings considering fire risks can be calculated using detailed ambient and technical datasets, employing the heat balance equation. Equation (5.3) provides a possible method for quantifying the safety line rating under fire risk, where I represents the line rating, R is the conductor resistance, Q_s is the heat gain from solar irradiation, Q_{rf} is the radiative heat gain from the fire, Q_{cf} is the convective heat gain from the fire, Q_r is the radiative heat dissipation, and Q_c is the convective heat dissipation.

$$I^2R + Q_s + Q_{rf} + Q_{cf} = Q_r + Q_c \tag{5.3}$$

5.3 Grid reserve analysis: "N-1" vs "LOLP" methods

Grid reserve is crucial for ensuring resilient operation during extreme events. This chapter evaluates and compares both the traditional and the proposed Loss of Load

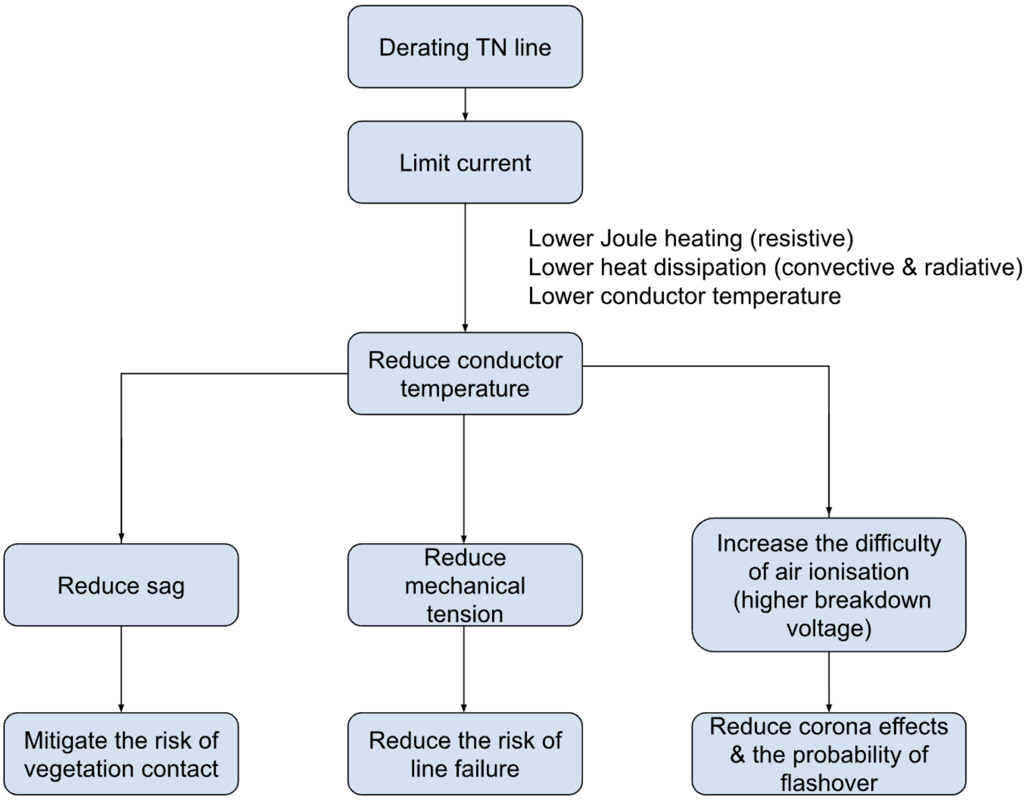

Figure 5.4: The rationale of derating lines for grid protection under fire risks

Probability (LOLP) based methods to determine the required grid reserve under wildfire risks. LOLP quantifies the probability of insufficient generation to meet total system demand at a given operational time [229]. As the traditional "N-1" method has been reviewed in Section 2.4.3, it is not repeated here. This section focuses on explaining the estimation of grid reserve using the LOLP method in two steps: net demand forecasting and probabilistic distribution based on various risk tolerance levels.

5.3.1 Step 1: Net demand forecasting

As grid reserve seeks to prevent insufficient generation under stress, the accuracy of net demand forecasting is crucial for determining the required reserve. For example, the operator predicts the generation and the demand for the next 24 hr. Then, the net demand can be calculated to help the operator prepare and dispatch to meet the net demand. But there will be an error between the forecast value and the real value, the difference here is the net demand error. Figure 5.5 presents flowcharts illustrating the calculation of net demand error over the next 24 hours.

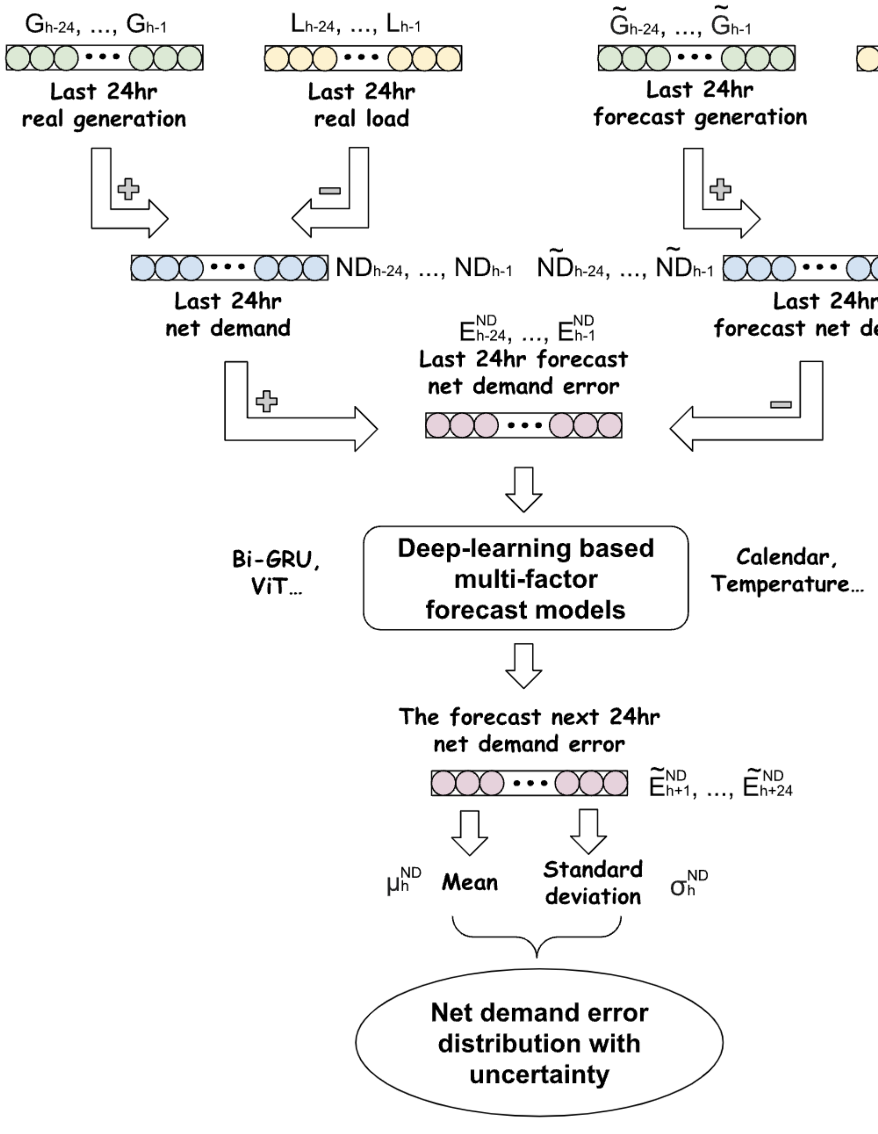

Figure 5.5: Flow chart to forecast and assess the next 24-hour net demand error

As shown in Figure 5.5, the real net demand for the previous 24 hours (ND_{h-24}, ..., ND_{h-1}) is calculated as the difference between the real generation over the last

24 hours (G_{h-24}, ..., G_{h-1}) and the real demand over the same period (L_{h-24}, ..., L_{h-1}). Then, the forecast net demand ($\tilde{ND}_{h-24}$, ..., $\tilde{ND}_{h-1}$) for the last 24 hours is computed by subtracting the forecast load ($\tilde{L}_{h-24}$, ..., $\tilde{L}_{h-1}$) from the forecast generation ($\tilde{G}_{h-24}$, ..., $\tilde{G}_{h-1}$) over the last 24 hours. Here, the forecast value for the previous 24 hours can be regarded as the hindcast value. Hindcast refers to methods commonly used in meteorology, which use historical information and known conditions to simulate what would happen in the past [230]. This technique is suitable for validating and improving forecasting models as the hindcast results can be compared with real historical data. By comparing the real net demand of the last 24 hours to the hindcast net demand, the net demand error for the last 24 hours (E^{ND}_{h-24}, ..., E^{ND}_{h-1}) is obtained and fed into multi-factor deep learning based load forecasting models. The output of the forecast model (next 24-hour net demand error) can then be described by a normal distribution with specific parameters (mean: μ^{ND}_h, standard deviation: σ^{ND}_h,). The net demand calculation excludes transmission losses, as DCOPF is applied to the high-voltage transmission network, where such losses can be omitted for computational efficiency. With the probabilistic distribution of the next 24-hour net demand, the grid reserve can be calculated based on various risk tolerance levels, i.e., different LOLPs. An example of creating a distribution of net demand error with relative parameters and evaluating grid reserve required under different LOLP requirements will be discussed in Section 5.3.2.

5.3.2 Step 2: Probabilistic distribution considering various resilience risk tolerance levels

This section discusses methods to depict the distribution of net demand error based on the sequential forecast results generated in Section 5.3.1. Additionally, the procedures for computing power grid capacity and electricity reserves under various resilience risk tolerance levels are explained in detail.

The mean μ^{ND}_h and the standard deviation σ^{ND}_h are calculated from the predicted next 24-hour net demand error for each sampling point. As the normal distribution is a typical way to describe error dispersion in most forecasting models, it has been selected to describe grid-related forecast errors in many studies [231], [232] and [233]. Thus, the Probability Density Function (PDF) is built using the normal or Gaussian distribution, as shown in (5.4).

$$f(x) = \frac{1}{\sigma_h^{ND}\sqrt{2\pi}} e^{-\frac{1}{2}\left(\frac{x-\mu_h^{ND}}{\sigma_h^{ND}}\right)^2} \tag{5.4}$$

Figure 5.6 displays an example of the normal distribution of net demand error with various risk levels. The risk levels refer to the LOLP. In the real electricity trading market in the UK, LOLP is used as a metric to help assess the Reserve Scarcity Prices (RSC) by the Balancing Mechanism Reporting Agent (BMRA) and Settlement Administration Agent (SAA) [229].

The histogram in Figure 5.6 illustrates the probability of the system experiencing various net demand errors. A negative value signifies that generation exceeds demand. The frequency distributions of deficit generation to varying extents are depicted to the right of the vertical grey dotted line. To determine the insufficient power capacity at different LOLPs, the reserve capacity is calculated as the distance between zero and the respective percentile points of the PDF. The differences between the zero point and the 90^{th}, 95^{th}, and 99^{th} percentile points represent the required grid capacity reserve (R) for 10%, 5%, and 1% LOLPs, respectively. For example, the power reserve capacity at a 10% LOLP is indicated by the bold green line in Figure 5.6. In other words, R MW of additional capacity is required to ensure safe system operation with a tolerance of 10% of LOLP. With a tighter tolerant resilience risk, the R needs to increase to fulfil the shortage, i.e., the R is larger in the case under a 5% resilience risk (LOLP) than in the one with a 10% risk (LOLP).

The traditional "N-1" method determines the required power reserve by calculating the additional capacity needed to maintain system operation in the event of a single equipment failure. However, as demand variability increases due to more

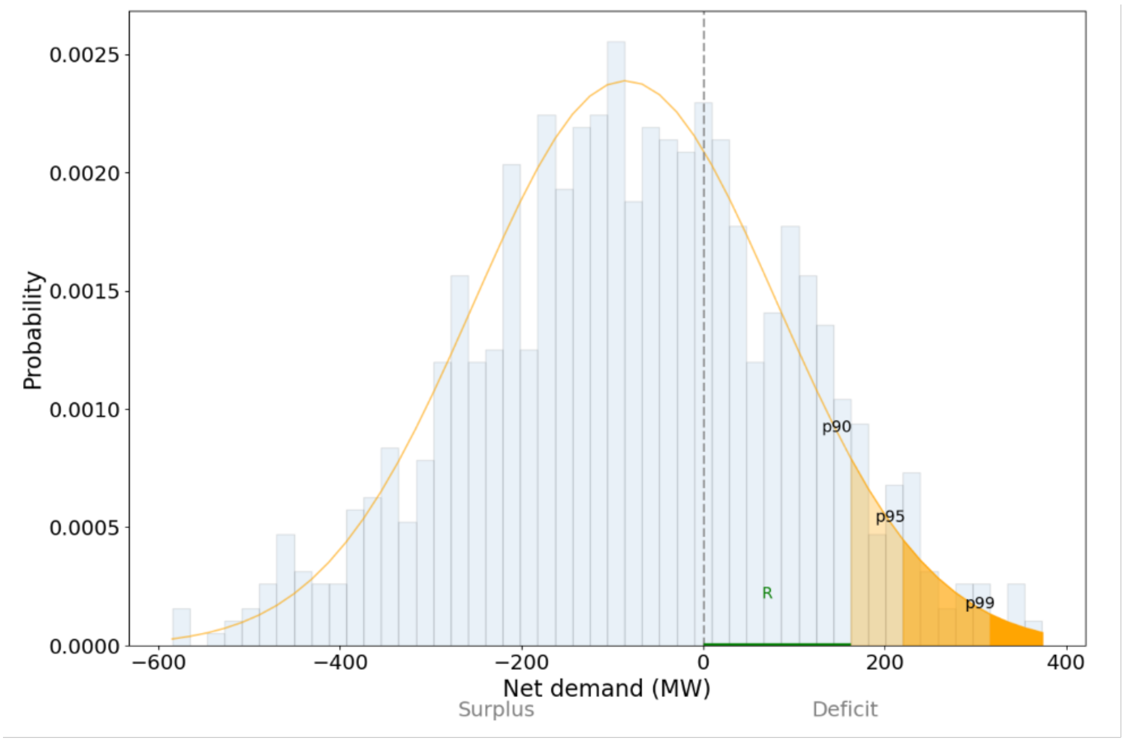

Figure 5.6: Probabilistic distribution of net demand error under various resilience risk levels to assess power grid reserves

frequent extreme events, the "N-1" method may no longer provide a reliable solution to prevent unintentional blackouts. In contrast, the LOLP method is data-driven and accounts for system-wide uncertainties by incorporating net demand forecast accuracy. These two methods are applied to both the theoretical IEEE network in this chapter and a real grid case in Chapter 6 to develop cost-effective and reliable reserve calculation strategies under wildfire risks.

5.4 Scenario settings

In this section, the settings of various operational scenarios are discussed in detail, demonstrating the development of the generalised WEM step by step. Compared to static peak burning condition OPF analysis in Chapter 3, this chapter conducts a time series OPF for a day during wildfire seasons with an hourly resolution. The operational scenarios, with sub-scenarios for each step, are illustrated in Figure 5.7. As the starting point, the DCOPF for the original grid is built and analysed in Scenario 1.a as the baseline case. Subsequently, the operational cases where four lines are considered at risk in the 138 kV and the 230 kV sub-regions, respectively, are tested and compared to to assess the impact of regional fire risk on power grid operation. As mentioned in Figure 5.3, the proposed power function is tested in Scenario 1.b and Scenario 1.c to integrate fire risk impact into grid operations. The details about lines at risk in Scenarios 1 and 2 are provided in Table 5.6. As Scenario 3 focuses on power reserve analysis and is developed based on Scenario 2.b, lines at risk in Scenario 3 are not provided in Table 5.6.

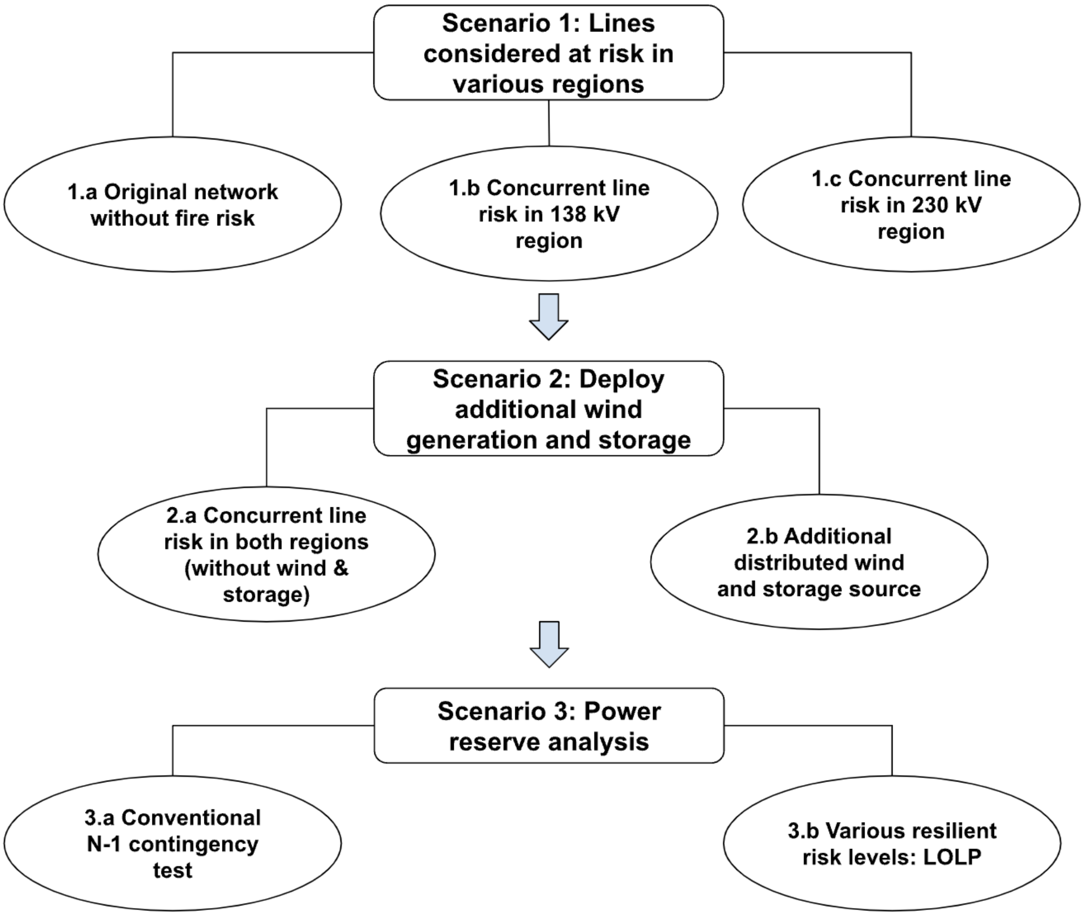

Figure 5.7: Scenario designs for developing the generalised Wildfire Energy Model (WEM) besed on the modified IEEE 24-Bus Reliability Test System

Scenario 2 seeks to recover load shedding caused by fire risks in the sub-regions identified in Scenario 1. In Scenario 2.a, the four lines at risk in the 138 kV region

Table 5.6: Lines at fire risk in Scenarios 1 & 2

Case	Line ID	Number	Region
1.a	N/A	0	N/A
1.b	Bus 2 - 6, Bus 5 - 10, Bus 8 - 9, Bus 8 - 10	4	138 kV
1.c	Bus 14 - 16, Bus 15 - 21, Bus 16 - 19, Bus 17 - 22	4	230 kV
2.a	Bus 2 - 6, Bus 5 - 10, Bus 8 - 9, Bus 8 - 10 Bus 14 - 16, Bus 15 - 21, Bus 16 - 19, Bus 17 - 22	8	both
2.b	Bus 2 - 6, Bus 5 - 10, Bus 8 - 9, Bus 8 - 10 Bus 14 - 16, Bus 15 - 21, Bus 16 - 19, Bus 17 - 22	8	both

(Scenario 1.b) and the four lines at risk in the 230 kV region (Scenario 1.c) are both treated as at risk, thereby extending the fire-impact areas. DGs and energy storage are then installed at nodes with significant load shedding to ensure demand is met. The deployment methods follow those described in Chapter 3. The benefits of using renewable DGs to reduce load shedding are evaluated in terms of both cost and environmental impact.

Finally, the analysis of power grid reserves is conducted using two methods. In Scenario 3.a, the conventional "N-1" contingency test is implemented. The "N-1" criterion stipulates that the grid should be able to continue operating normally following the disconnection of any single component, including generators, transmission lines, and transformers [234]. The power reserve capacity required for the grid is estimated by deactivating each component individually and determining the maximum load shed across all scenarios. However, the "N-1" contingency test may not adequately capture the practical risks of grid operation in modern contexts, as multiple failures can occur simultaneously due to ageing infrastructure and extreme weather risks. To consider the system uncertainty holistically, a novel power reserve analysis method based on various levels of resilience risk tolerance is proposed and tested in Scenario 3.b. This approach accounts for the intermittency of generation, demand, and weather simultaneously using advanced machine-learning-based forecasting methods.

5.5 Results and discussion

This section develops the generalised WEM through three operational scenarios, following the flow chart in Figure 5.7. For each scenario, the grid performance is analysed from various perspectives using technical, economic, and environmental metrics. Evaluation metrics have been discussed in Table 3.2 in Chapter 3, thus not repeated here.

5.5.1 Scenario 1: The impact of concurrent lines at risk in various sub-regions

Scenario 1 assessed how multiple line risks occurred in different regions, affected grid resilience. The hourly FWI curve used for the IEEE 24-Bus RTS test was assumed and calculated based on the FWI conditions during the Black Summer in Victoria, Australia, on 3^{rd} December 2019, as shown in Figure 5.8 [143]. This representative day was selected since it was a day with mid-risk across the 2019-2020 wildfire season. In the following four scenarios, all selected lines with fire risks were assumed to follow this FWI risk curve throughout the 24 operational hours. As Figure 5.3 shows, lines are fully de-energised when the FWI exceeds 50. On the selected day (Figure 5.8), no line reaches this threshold; therefore, no line is fully disconnected in this chapter.

Table 5.7 presents the evaluation results for the three operating cases in Scenario 1. No fire risk was considered in Scenario 1.a, whereas four lines in the 138 kV and 230 kV regions were designated as at risk in Scenarios 1.b and 1.c, respectively. With respect to technical metrics, average line loading decreased by 26.02%, while overall load shed increased by 1.86% from Scenario 1.a to 1.c. Notably, fire risks in the higher-voltage (230 kV) region imposed greater system stress than risks in the lower-voltage (138 kV) region. Detailed maps of average maximum line

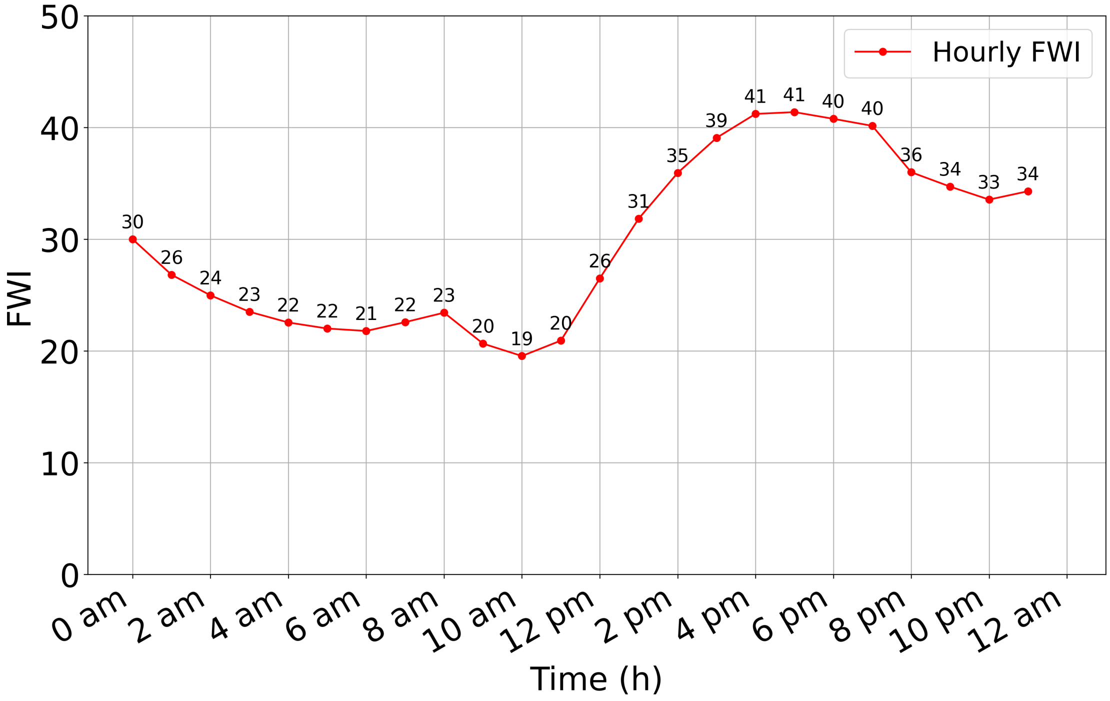

Figure 5.8: Hourly Fire Weather Index (FWI) curve for the IEEE 24-Bus RTS. A representative mid-risk FWI curve for Victoria, Australia on 3^{rd} December 2019

loading over 24 hours for Scenarios 1.a–c are provided in Figures 5.9–5.11. These maps illustrate that, although original loading was higher in the 230 kV network, stress shifted to the 138 kV network in the latter two cases. In particular, the maximum loading on the Line between Buses 7 and 8 reached 99% and 100% in Scenarios 1.b and 1.c, respectively. This reflects that Bus 7 lies at the terminus of a regional network and can receive power only locally or via a single connecting line; hence, DGs should be deployed at such isolated nodes under extreme conditions.

To assess lines operating at high loading levels, the 24-hour loading curves for lines exceeding 70% maximum loading are plotted in Figure 5.12. These high-loading events occurred predominantly in the afternoon, when both fire risk and demand peaked. Optimised generator outputs are shown in Figure 5.13. Nuclear generation (green lines) remained constant, as it was non-dispatchable. Coal and hydro served as the primary sources for system balancing in Scenario 1. In practice, these optimal dispatch profiles can be provided to the system operator to ensure

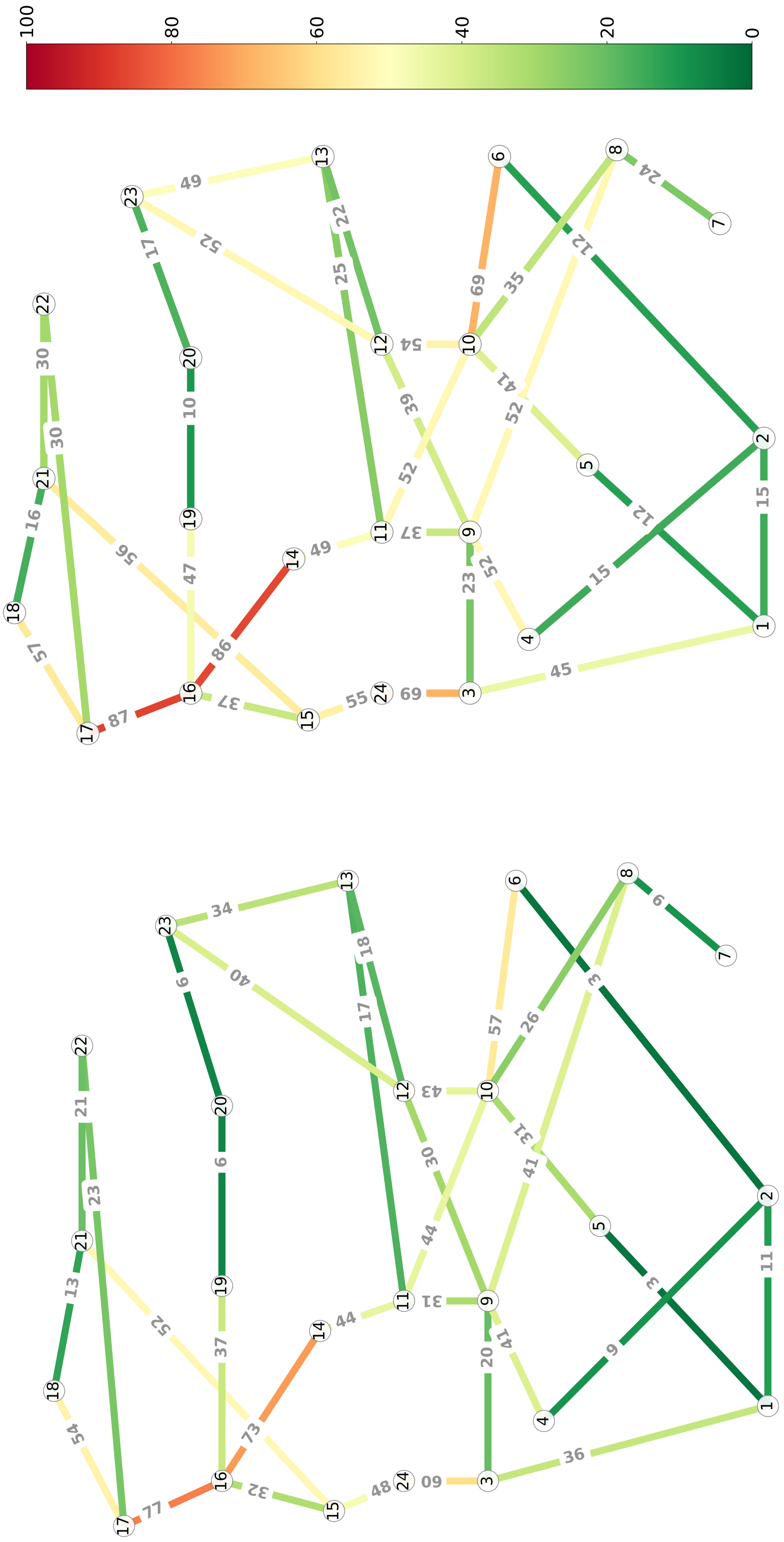

(a) The average line loading map

(b) The maximum line loading map

Figure 5.9: Scenario 1.a: Line loading map for the original IEEE 24-Bus RTS

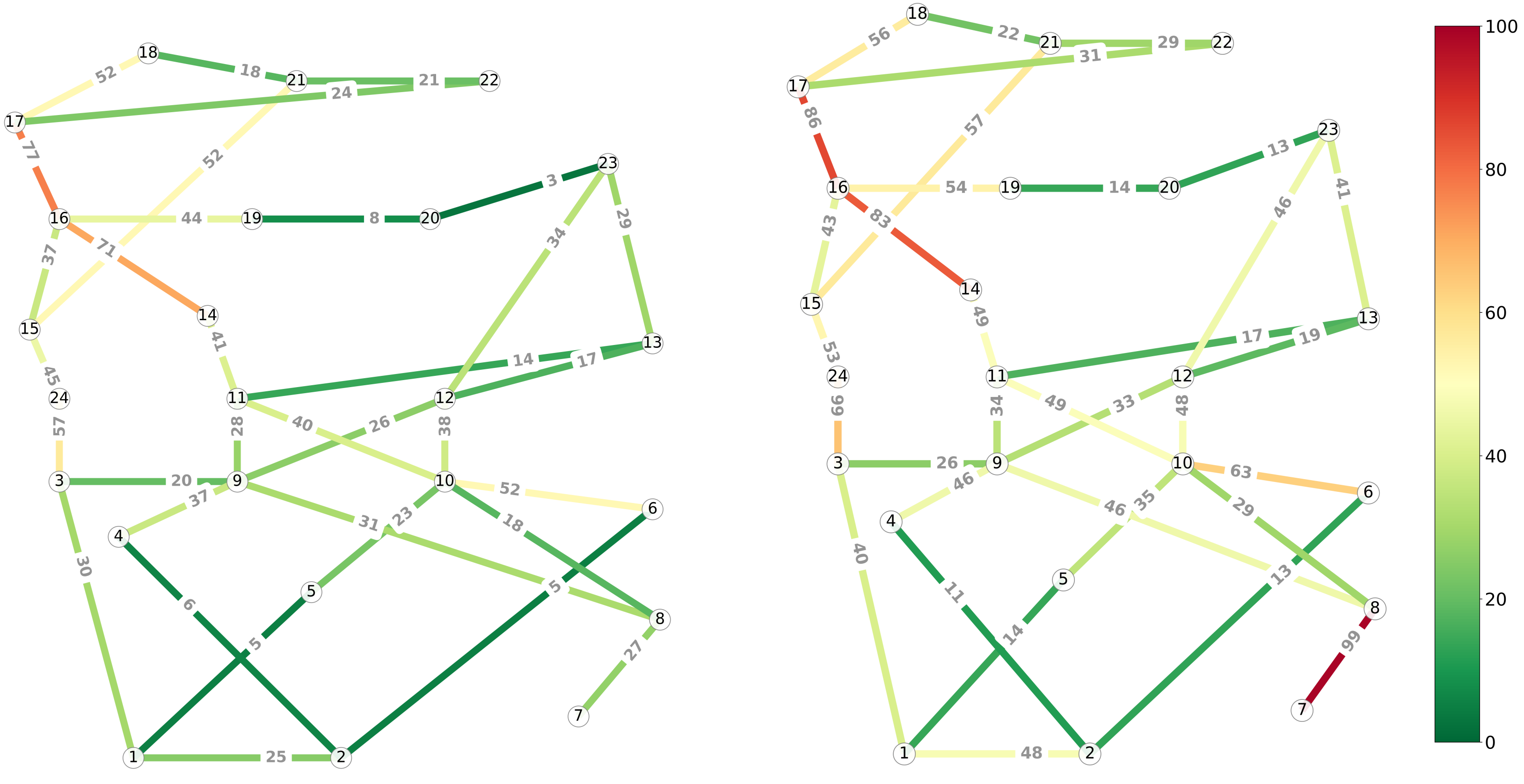

(a) The average line loading map

(b) The maximum line loading map

Figure 5.10: Scenario 1.b: Line loading map when four lines are at risk in the 138 kV region

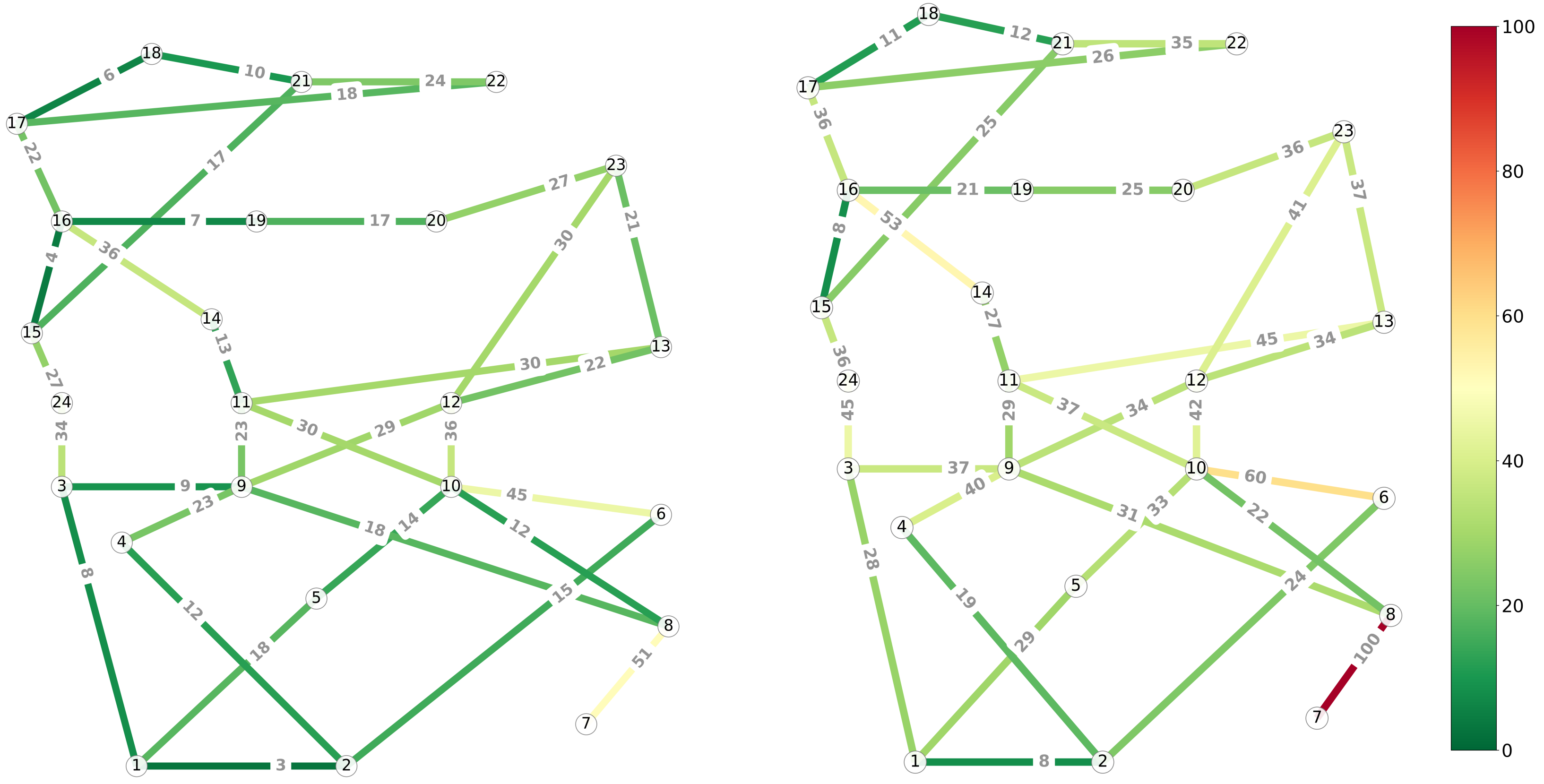

(a) The average line loading map

(b) The maximum line loading map

Figure 5.11: Scenario 1.c: Line loading map when four lines are at risk in the 230 kV region

Table 5.7: Scenario 1: grid resilience performances for multiple fire occurrences in various regions

Metrics	**1.a**	**1.b**	**1.c**	**Unit**
LL_{grid}^{ave}	32.01	28.26	23.68	%
LS_{grid}	0	362.66	979.79	MWh
$LS_{grid}^{percent}$	0	0.69	1.86	%
C_{grid}	12,028,835	15,678,736	22,163,521	AU$
C_{grid}^{ave}	228.11	299.39	428.26	$AU\$$ /MWh
E_{grid}	19,963,145	24,573,255	30,564,686	kg
E_{grid}^{ave}	378.58	469.23	590.59	kgCO_{2eq} /MWh

secure grid operation.

In terms of economic performance, both total and unit grid operating costs increased when multiple lines were set at risk. Specifically, unit grid cost rose by 31.25% and 87.74% in the 138 kV and 230 kV concurrent-risk cases, respectively, compared with the baseline case without fire risk. Similarly, grid emissions increased when fire risk affected different regions. Notably, the impact on carbon emissions was greater when the risk occurred in the higher-voltage network (Scenario 1.c) than in the 138 kV region (Scenario 1.b). Relative to the baseline, unit emissions per kWh increased by 19.32% and 45.18% in Scenarios 1.b and 1.c, respectively.

5.5.2 Scenario 2: Flexible dispatch with renewable generation and storage

There are two operating cases in Scenario 2. Scenario 2.a combines Scenarios 1.b and 1.c, in which eight lines were deemed at risk. In Scenario 2.b, DG and energy storage were installed at nodes experiencing load shedding to assess the feasibility

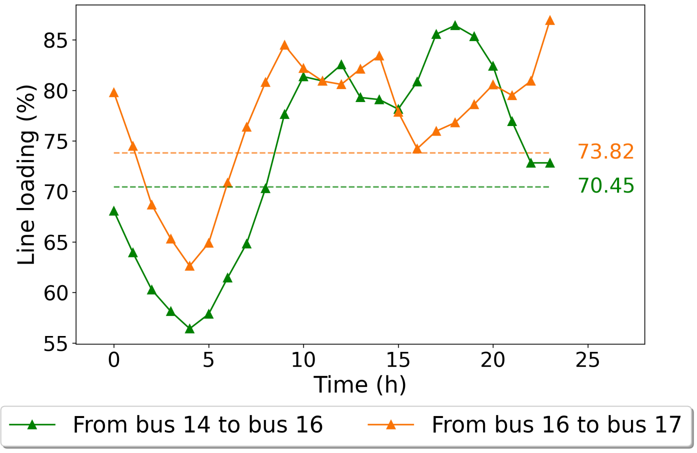

(a) Scenario 1.a: The original grid test

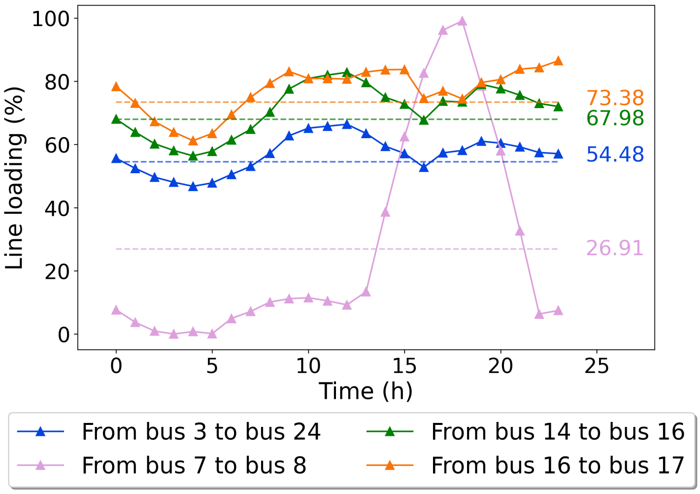

(b) Scenario 1.b: Four lines at risk in the 138 kV region

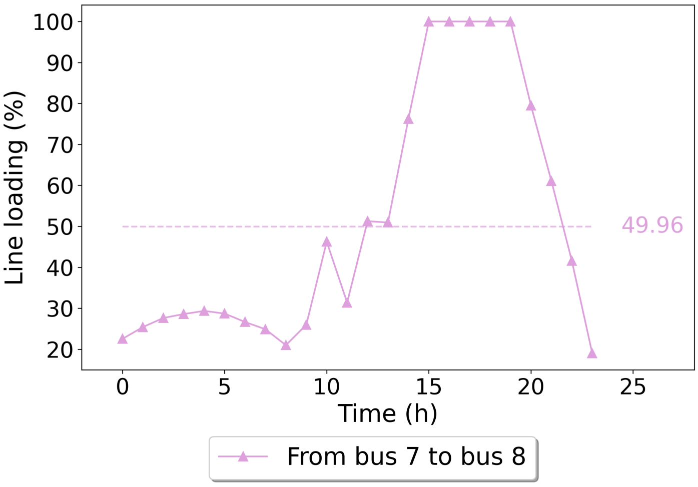

(c) Scenario 1.c: Four lines at risk in the 230 kV region

Figure 5.12: Line loading curves for lines with the maximum loading over 70% in Scenario 1

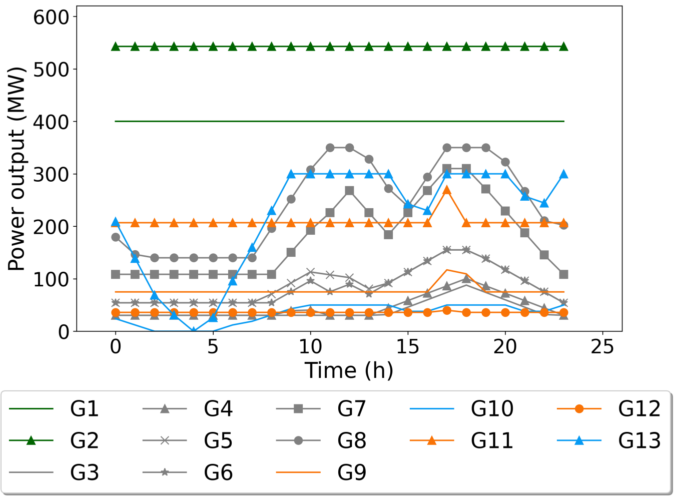

(a) Scenario 1.a: The original grid test

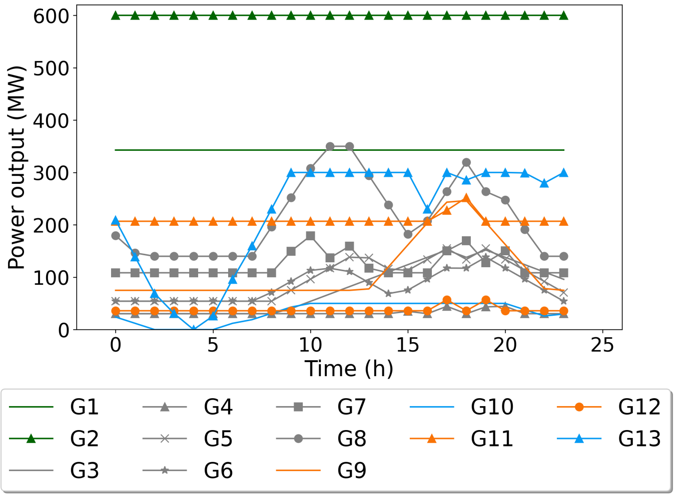

(b) Scenario 1.b: Four lines at risk in the 138 kV region

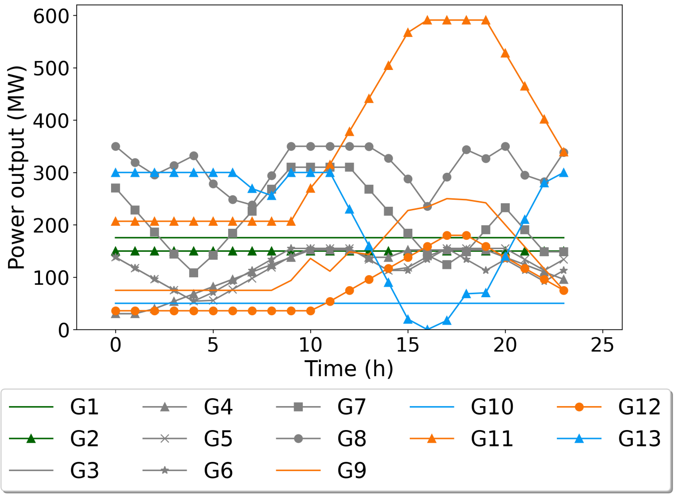

(c) Scenario 1.c: Four lines at risk in the 230 kV region

Figure 5.13: Generator power output curves for Scenario 1. Green lines represent nuclear generation, grey lines denote coal generation, orange lines are oil generation and blue lines stand for hydro generation

of preventing blackouts using sustainable solutions. The method of deploying wind generators follows that described in Chapter 3 and is not repeated here.

Energy storage systems were also installed at selected nodes to support wind-turbine operation. Battery capacity requirements vary by case, but a common design target is 1–4 hours of the wind farm's average power output [235]. For a 100 MW wind farm, this corresponds to 100–400 MWh of storage, which effectively smooths short-term variability and provides grid support. Gholami et al. [236] found that optimal battery size is approximately 1–2 times the average power output, accounting for turbulence, wake effects, and spatial smoothing. Accordingly, we initially assumed storage capacity equal to twice the peak-hour average wind output and subsequently adjusted capacities in light of operational experience, reducing storage where its use was uneconomical relative to alternative energy sources.

Table 5.8 presents the evaluation results for the two operating cases in Scenario 2. Following the deployment of wind DG and storage, the 24-hour load shed of 1,129 kWh in Scenario 2.a was fully recovered. Average line loading increased slightly from 26.83% in Scenario 2.a to 27.61% in Scenario 2.b. Detailed average and maximum line-loading distributions for Scenarios 2.a and 2.b are shown in Figures 5.14 and 5.15, respectively. The similarity of the line-loading distributions between the two cases reflects that load recovery was achieved primarily through the newly installed local DG.

To further interpret the loading distribution, the line with the highest loading—Line (Bus 7–8)—is examined. It was the only line to exceed 70% loading in both Scenarios 2.a and 2.b. The 24-hour loading profile for this line is shown in Figure 5.16. Although its maximum loading reached 100% in both cases, Figure 5.16 shows that the deployment of DG and storage significantly reduced system stress: the number of time steps at full loading fell from four in Scenario 2.a to one in Scenario 2.b. Optimised generator outputs, presented in Figure 5.17, illustrate

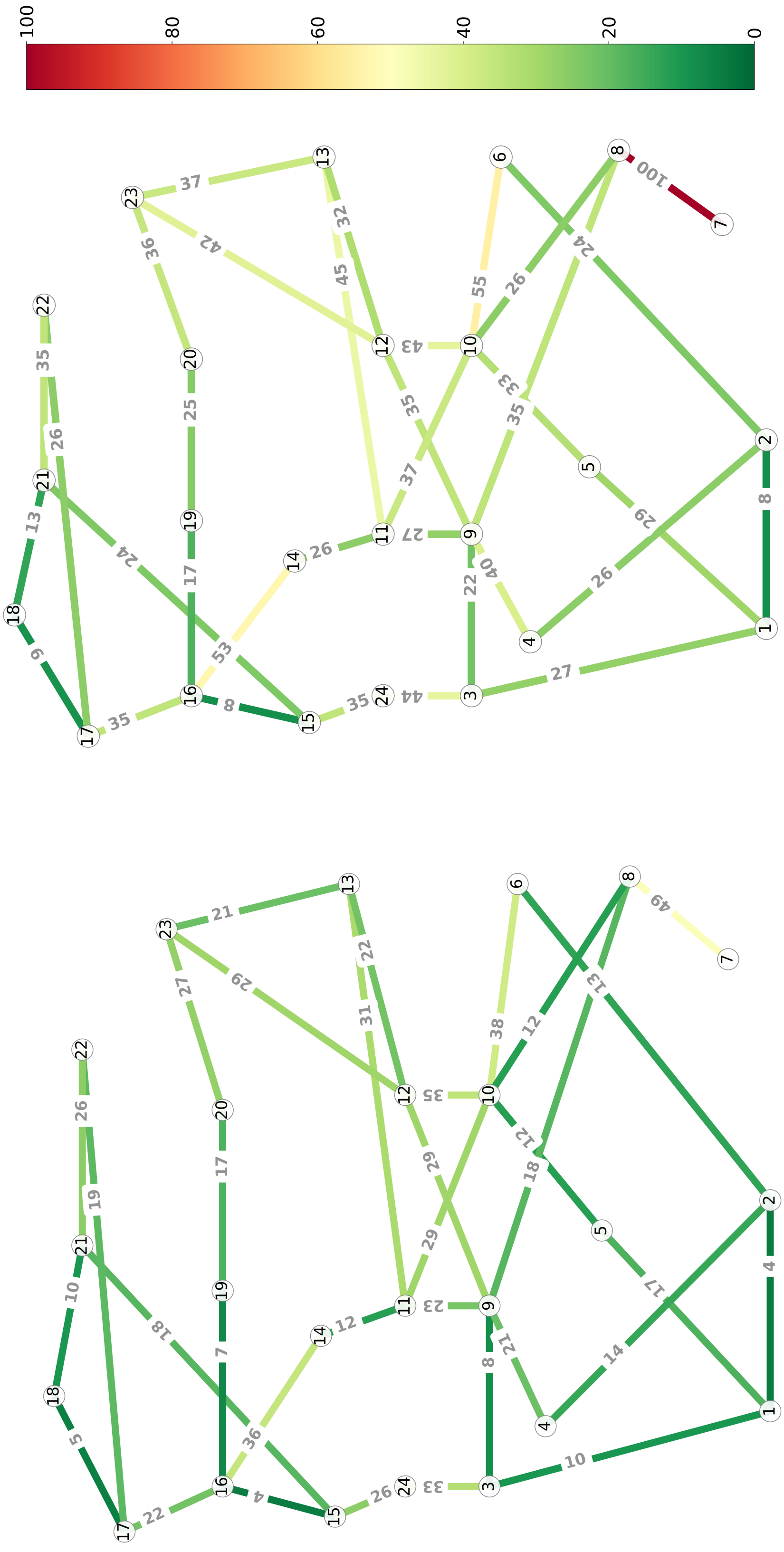

(a) The average line loading map

(b) The maximum line loading map

Figure 5.14: Scenario 2.a: Line loading maps when 8 lines are considered at risk

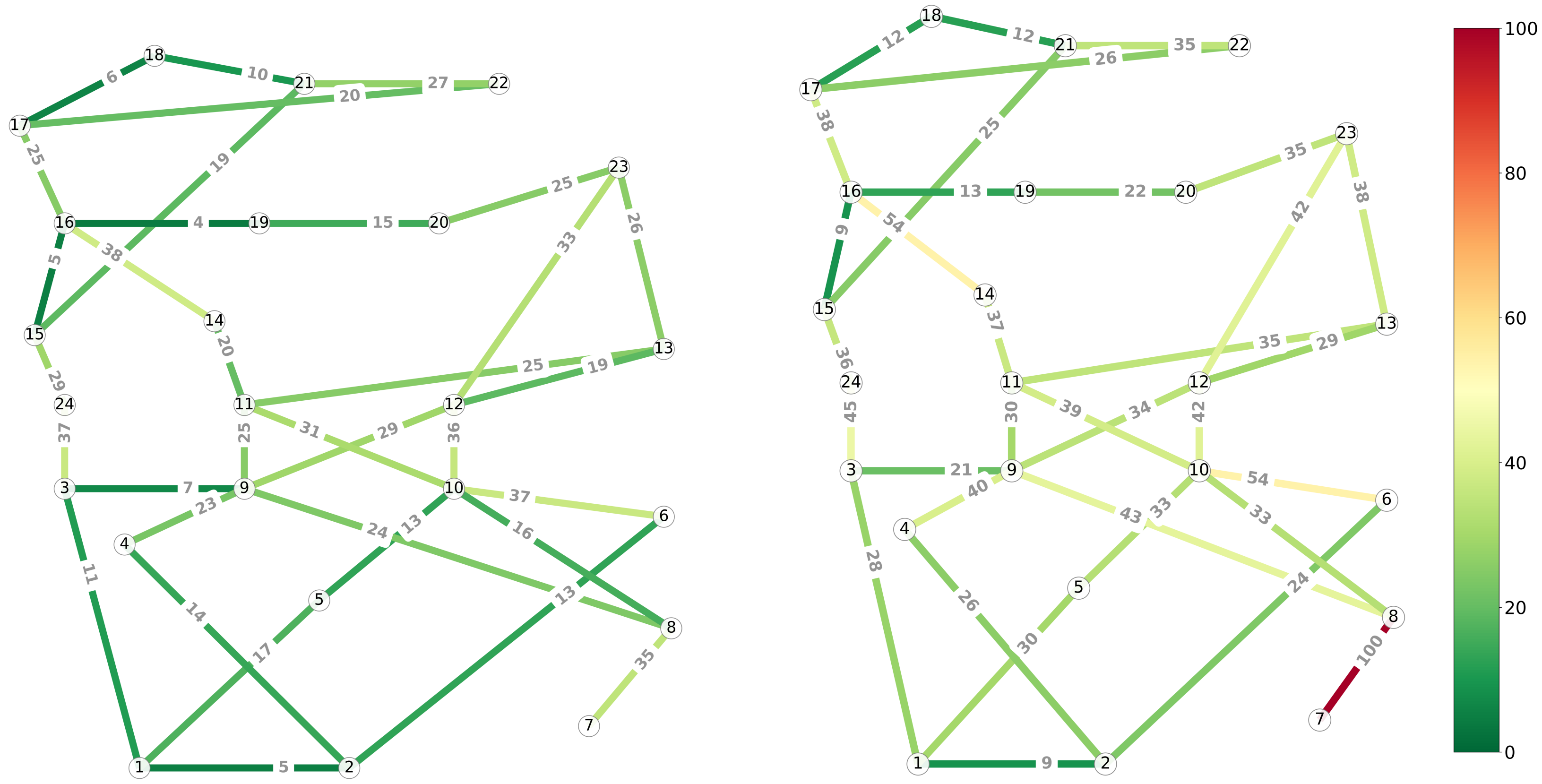

(a) The average line loading map

(b) The maximum line loading map

Figure 5.15: Scenario 2.b: Line loading map when 8 lines are considered at risk with flexible DG and storage solutions

Table 5.8: Scenario 2: grid resilience performances: without vs with flexible DG & storage

Metrics	**2.a**	**2.b**	**Unit**
LL_{grid}^{ave}	26.83	27.61	%
LS_{grid}	1,129.21	0	MWh
$LS_{grid}^{percent}$	2.14	0	%
C_{grid}	23,651,595	12,808,499	AU$
C_{grid}^{ave}	458.33	242.90	*AU$* /MWh
E_{grid}	30,448,507	29,538,481	kg
E_{grid}^{ave}	590.06	560.16	kgCO_{2eq} /MWh

the most economical dispatch strategy.

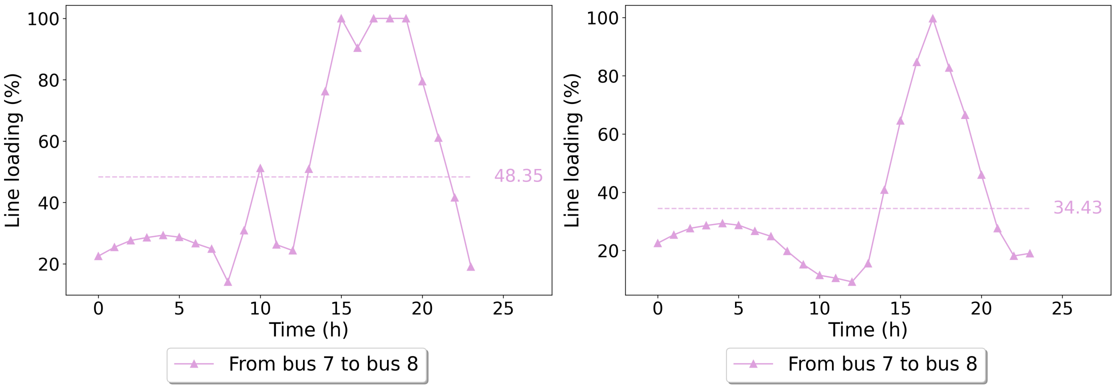

(a) Scenario 2.a: 8 lines considered at risk **(b)** Scenario 2.b: Flexible DG solution

Figure 5.16: Line loading curves for lines with the maximum loading over 70% in Scenario 2

Integration of DG and storage markedly alleviated system stress in both economic and environmental terms. Total and unit grid operating costs were reduced by 84.66% and 47.00%, respectively, following deployment of flexible DG and storage. Total and unit grid carbon emissions decreased by 2.99% and 5.07%, respectively.

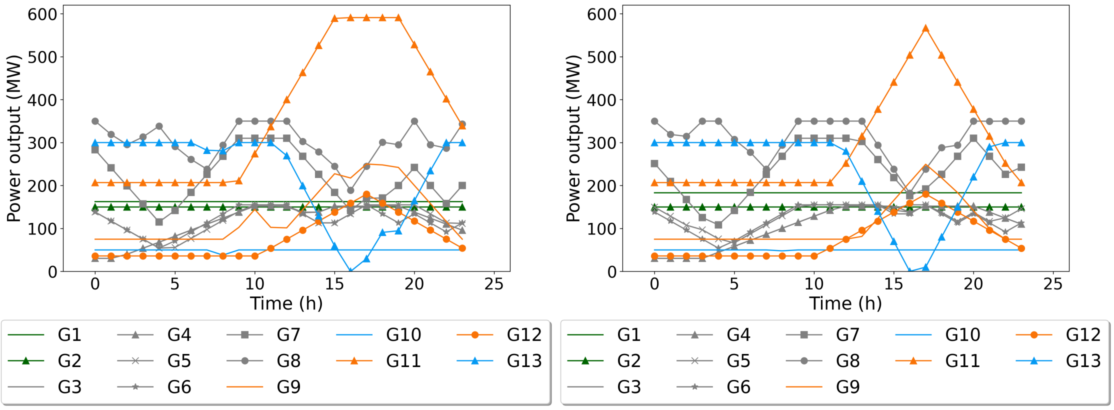

(a) Scenario 2.a: 8 lines considered at risk **(b)** Scenario 2.b: Flexible DG solution

Figure 5.17: Generator power output curves for Scenario 2. Green lines represent nuclear generation, grey lines denote coal generation, orange lines are oil generation and blue lines stand for hydro generation

These findings demonstrate that the proposed DG deployment methods can restore system load sustainably. In addition, it should be noted that the total system operational cost in this chapter includes VoLL attributed to load shedding, with a unit VoLL of AU$10,000 assumed for the theoretical grid case. This accounts for the substantial cost reduction observed from Scenario 2.a to 2.b, due to DG deployment and load recovery. By contrast, Chapters 3 and 6 excluded VoLL from the objective function and instead incorporated it separately in the cost–benefit analysis to determine the break-even VoLL that would justify DG investment in real grid applications.

In addition to resilience metrics, the optimised outputs of wind generators and storage are shown in Figures 5.18 and 5.19. In Scenario 2.b, these assets were sited at nodes that experienced load shedding in Scenario 2.a. For reference, the detailed load-shedding results from Scenario 2.a are provided in Table 5.9.

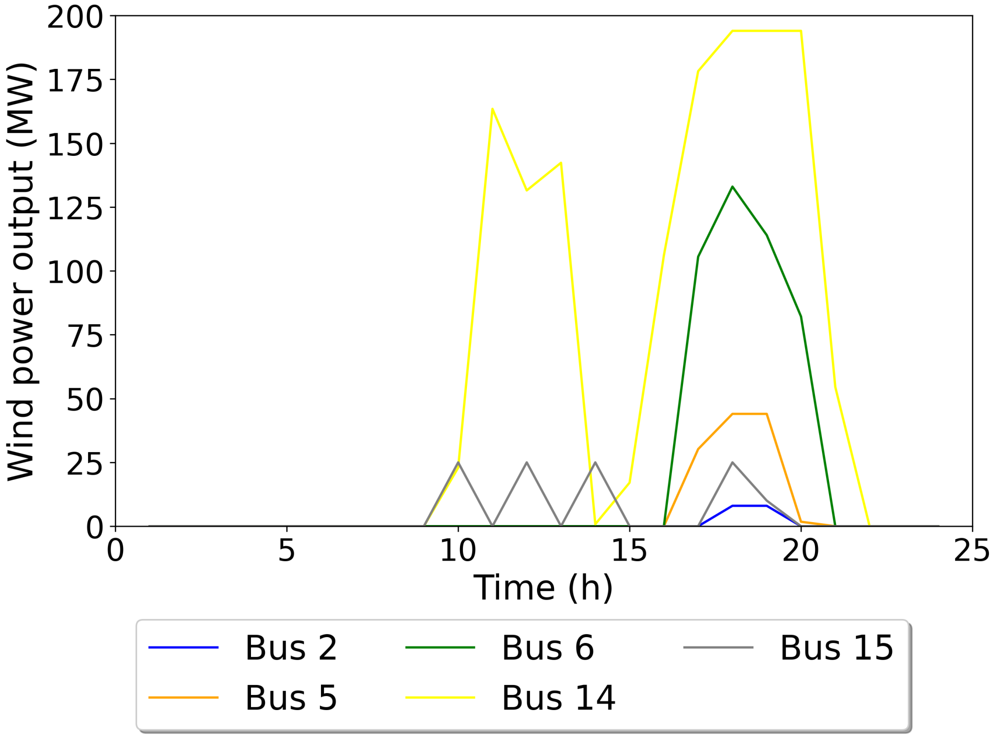

(a) The optimised power output results for wind generators

Figure 5.18: Scenario 2.b: the optimised power output results for wind generation

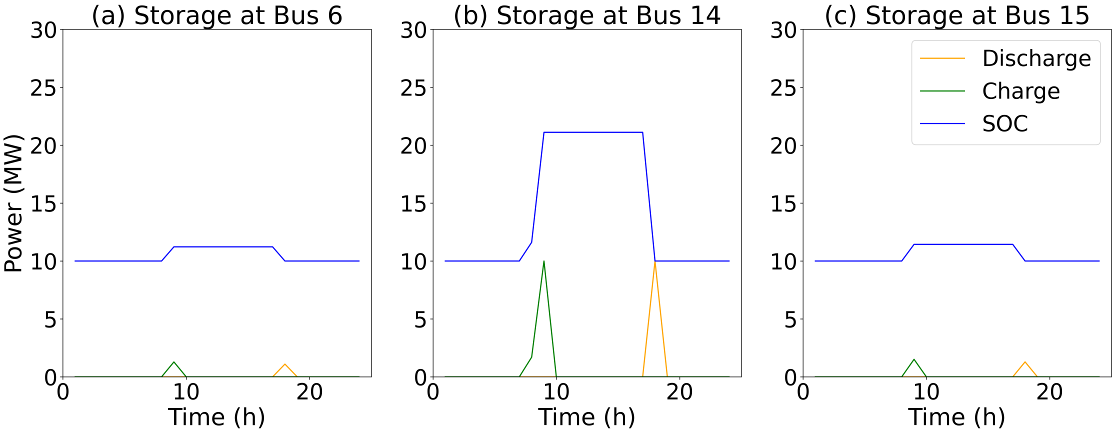

Figure 5.19: Scenario 2.b: the optimised operational results for storage systems

5.5.3 Scenario 3: Power system reserve analyses - "N-1" contingency test & LOLP uncertainty test

To ensure safe and resilient power grid operations, accurate power reserves are crucial for addressing unexpected load deficiencies. In Scenario 3, the power system reserve was calculated using two methods: the conventional "N-1" contingency test and

Table 5.9: Detailed load shed for the IEEE 24-Bus RTS in Scenario 2.a, where eight lines were considered with fire risks

NO.	Bus	Time point	Load shed (MWh)
1	5	17	21.44
2	6	17	118.86
3	14	17	121.34
4	2	18	7.64
5	5	18	43.79
6	6	18	133.33
7	9	18	3.72
8	14	18	194.0
9	15	18	24.78
10	5	19	30.60
11	6	19	86.87
12	14	19	169.54
13	5	20	7.58
14	6	20	47.36
15	14	20	118.35
Total	N/A	N/A	1129.21

the LOLP-based test, which accounts for systematic uncertainty. The comparative results were analysed, presenting a comprehensive and reliable approach to assessing grid reserves under extreme weather risks.

3.a Conventional "N-1" security rule to calculate the grid reserve

In Scenario 3.a, each grid component was turned off one by one, and the power reserve capacity needed was determined as the maximum system load shed across all DCOPF cases. For Scenario 3, the main components consisted of 34 lines, 13 generators, 5 wind generators, and 3 storage systems. The maximum load shed occurred when the Line (Bus 12-13) was turned offline. Among all "N-1" tests, the 191.8 MW of load curtailed at Bus 10 at the 17:00 was the maximum load shed point. Thus, 191.8 MW was determined as the proper grid power reserve capacity for the IEEE 24-Bus RTS model.

3.b Different LOLP risk levels: 1%, 5%, 10% to estimate the grid reserve

Following the methodologies discussed in Section 5.3.2, the power reserve was calculated based on different risk tolerance levels. As the IEEE 24-Bus RTS model is a theoretical case study, no real net demand forecast error data is available. Therefore, some assumptions were made to calculate the power reserve in Scenario 3.b. In the second phase of the DPhil study, the WRLFM was developed to forecast energy demand at distribution levels in Horsham, Victoria, Australia. The MAPE and the error variance calculated for the best-performing case were 3% and 0.43 MW^2 for a grid with a load around 20 MW. According to the forecast performance of the Horsham case study, the mean and standard deviation of the forecast next 24-hour net demand error can be assumed and scaled accordingly. In other words, the mean net demand error (μ_h^{ND}) was assumed to be 3% of the peak load at each operational time point. The standard deviation of the net demand error (σ_h^{ND}) was scaled up by the load difference between the Horsham case (20 MW+) and the IEEE 24-Bus RTS (2000 MW+). With the μ_h^{ND} and σ_h^{ND} values computed for each time point, the power reserve considering various levels of resilience risks was plotted as probabilistic distribution plots for 24 operational time points.

The power reserve capacities at each time point were calculated for the three cases with 1%, 5%, and 10% of LOLP risk levels in Scenario 3.b. Figure 5.20 displays the probabilistic power reserve results for the 18^{th} time point (17:00) since the power reserve peaked at this time point for all three LOLP levels. Table 5.10

records the calculated power reserve and 24-hour electricity reserve for safe grid operation under three LOLP risk levels. Compared to the results in Scenario 3.a, power reserve capacities for the three LOLP risk levels were all lower. Even for the strictest case (1% risk level), the power reserve needed was lower than the "N-1" contingency case, indicating a lower requirement for additional renewable generation capacities can still satisfy a low-risk requirement (1% risk of lost load).

Both the "N-1" contingency test and the LOLP-based uncertainty estimation methods have pros and cons. The conventional "N-1" method can identify the most critical grid component and vulnerable buses that tend to have significant load shed during high-stress periods. However, it only considers one element offline at a time, which may not be sufficient to model the current power grid with multiple simultaneous risk sources. In contrast, the proposed LOLP-based method considers systematic risks based on numerous factors, calculating power reserve more comprehensively. In addition, the power reserve capacity of the 1% LOLP case in Scenario 3.b is 30.79% lower than in Scenario 3.a, indicating that the LOLP-based method is an economical, comprehensive risk-considered, and resilient approach to estimating power reserve. Therefore, the LOLP-based method is recommended for calculating power reserve under different risk tolerance requirements, while the conventional "N-1" contingency test is still suggested to assist in identifying critical and vulnerable components of power systems.

5.6 Remark, limitation and summary

In this chapter, the general methodologies for developing a temporally dynamic WEM were discussed in detail based on the IEEE 24-Bus RTS. First, grid information for the IEEE-24 bus RTS was reviewed to build the basic network model using the MILP-based DCOPF model. The relationship between the FWI risk and the control strategy for transmission lines was then tested and established: a properly hypothesised power function relationship was determined. Since part of the grid

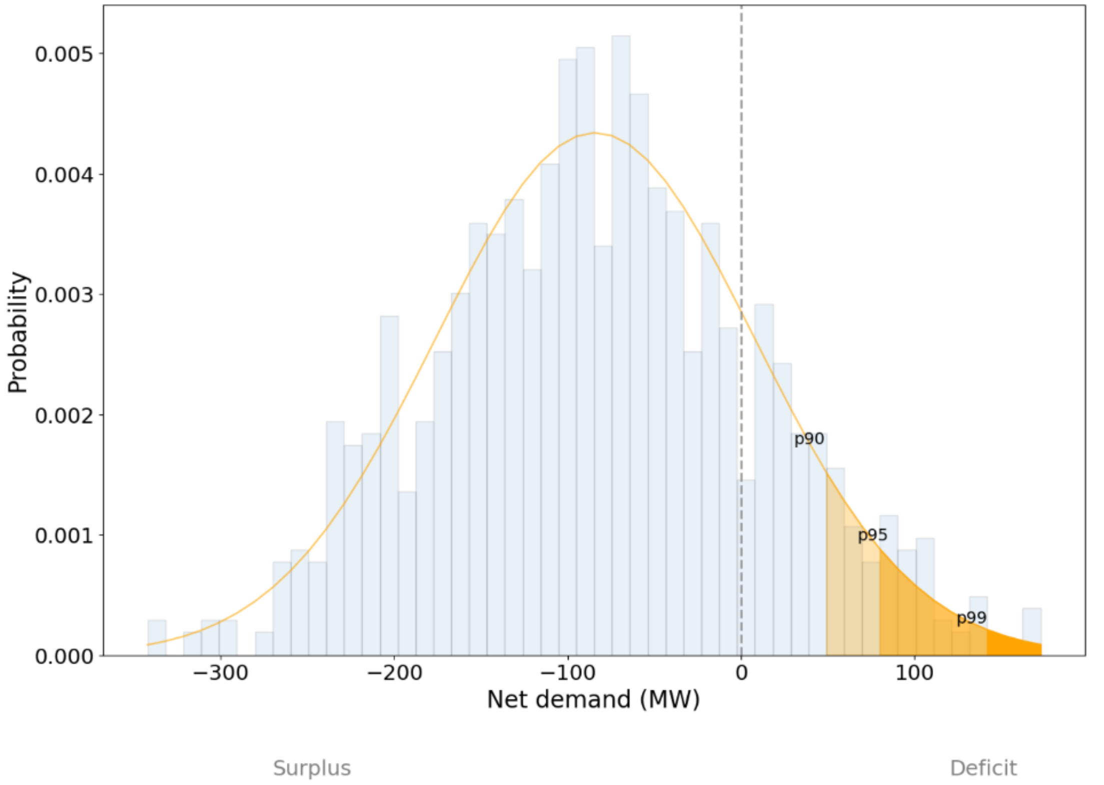

Figure 5.20: Scenario 3.b: power reserve probabilistic distribution based on different resilience risk levels at 17:00. (1%, 5%, and 10% of LOLP)

Table 5.10: Scenario 3.b: power reserve capacity and 24-hour electricity reserve for 1%, 5%, and 10% LOLP cases

LOLP level	**Time point**	**Maximum power reserve (MW)**	**Electricity reserve for 24 hours (MWh)**
1%	18	132.74	2384.63
5%	18	76.01	1272.18
10%	18	39.46	632.94

load was curtailed after incorporating fire risks, various scales of DGs and storage were added to vulnerable nodes of the grid to support local supply. In addition, the traditional "N-1" security rule and the proposed LOLP-based method were compared to calculate power reserve capacity during extreme wildfire periods.

Through the three scenarios, several remarks can be made based on the technical, economic, and environmental evaluations. Key conclusions include: (1) Power grid operational performance was constrained in all aspects after integrating fire risk into the DCOPF. (2) The relationship between the FWI and line operational limit can be described by a power function, with the function parameters adjustable to meet different risk control requirements in various cases. (3) The impact of fire on power grids was more significant when the risk occurred in the higher high voltage region than in the lower high voltage region. (4) DG solutions can recuperate all load shed caused by fire risks in a financially viable and environmentally friendly manner: the unit operational cost and the unit carbon emission became 47.00% and 5.07% lower, respectively, after applying flexible DG methods. (5) The "LOLP-based" method was proposed to assess grid reserve by considering systematic risks to estimate grid power reserve capacity in the face of multi-source uncertainties, demonstrating a safe and resilient grid design at a relatively lower cost than the conventional method. Nevertheless, the conventional "N-1" security rule is still recommended to help determine critical grid components.

Though some conclusions have been drawn from this theoretical case, several limitations need to be addressed in future work to generalise the model. Various uncertain factors were accumulated in the IEEE 24-Bus RTS, attributed to multiple hypotheses. (1) The hourly FWI risk curve was assumed based on a calculated FWI curve for a representative day during wildfire season in Victoria. No corresponding climate datasets were available to compute fire risk curves for the theoretical case. (2) Lines selected at risk were assumed to have the same hourly FWI curve, whereas they should differ from line to line in actual cases. (3) In the worst-risk scenario (Scenario

2.a), 8 out of 34 lines were considered at risk to study the impact. However, the specific FWI risk for all lines should be considered simultaneously for real grid cases. These issues will be addressed in Chapter 6 by validating the WEM based on real FWI and grid datasets in Victoria, Australia, aiming to develop a high-fidelity model.

6

Phase IV: The generalised Wildfire Energy Model: a Victoria grid case

Contents

In this chapter, the generalised continuous Wildfire-Energy Model, developed based on the theoretical IEEE 24-Bus RTS in Chapter 5, is further validated through an analysis of a real power grid. Victoria, Australia, is chosen as the case study region to maintain consistency with the region examined in Chapter 3, where the static worst-case scenario was assessed. Given that the related introduction and methodology have been comprehensively detailed in Chapters 3 and 5, this chapter proceeds directly to the background of the case study, providing an evaluation and summary of the performance results.

6.1 Case study briefing

To be consistent with the worst-case study of Chapter 3, 3 December 2019 and 12 December 2019 were also selected as representative test days in this chapter. On 3 December, fire risks were more geographically dispersed with a lower mean value, whereas on 12 December, they were more severe and concentrated in specific regions. The methodology for deriving fire-risk maps from fundamental climate variables for the two selected days is detailed in Section 3.3.1 of Chapter 3 and is not repeated here. This chapter evaluates dynamic power-system operational performance under these varied fire-risk patterns and develops feasible methods to ensure system security.

Figure 6.1 outlines the four scenarios considered in this chapter. Scenario 1 investigates the effect of varying fire-control management strengths by disconnecting lines at different fire-danger thresholds. In Scenario 2, flexible DG and storage are deployed at vulnerable nodes to restore load shed. Similar to Chapter 3, a cost–benefit analysis follows Scenario 2 to evaluate the trade-off between DG investment and VoLL savings. Scenarios 3 and 4 compare two approaches to calculating grid reserves: the traditional "N-1" contingency method and an LOLP-based method. Notably, Scenario 3 also includes a comparison of reserve requirements with and without consideration of fire risk.

The actual load curves for Victoria are shown in Figure 6.2. Notably, both days exhibit two demand peaks: one around 08:00 and another at 20:00. On 3 December, the morning peak was higher, whereas on 12 December the evening peak was greater.

6.2 Results and discussion

In this section, the dynamic Victoria WEM case study is evaluated from technical, economic, and environmental perspectives. The performance metrics, which have been thoroughly explained in Chapter 3, will not be repeated here.

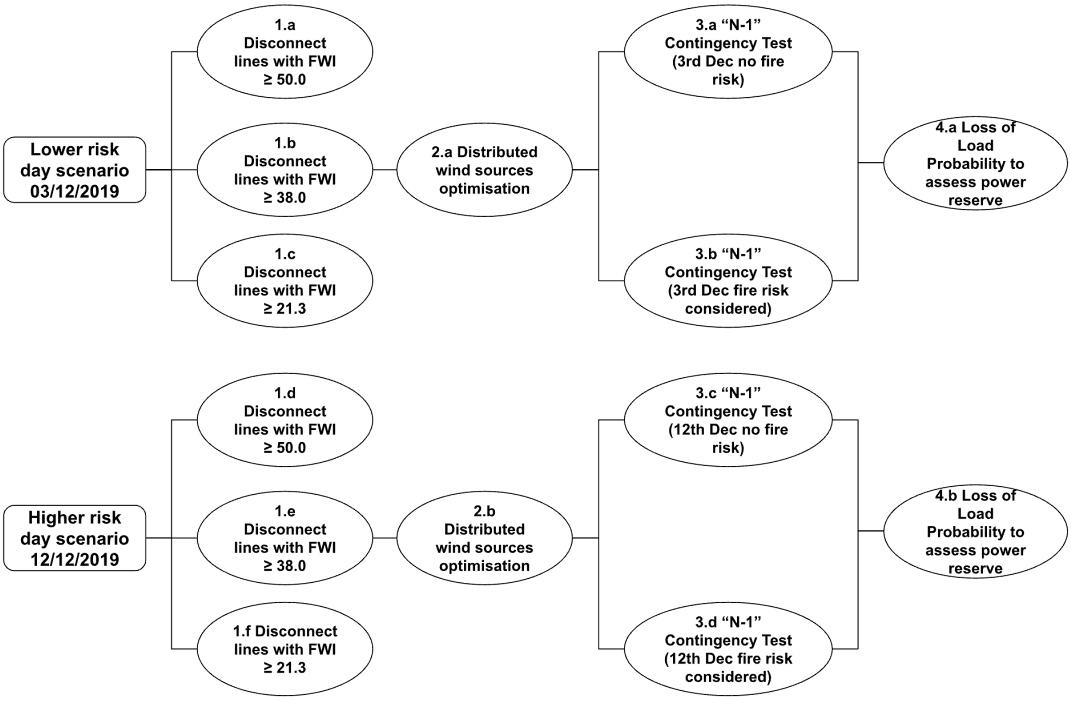

Figure 6.1: Scenario settings for the dynamic Victoria WEM case study

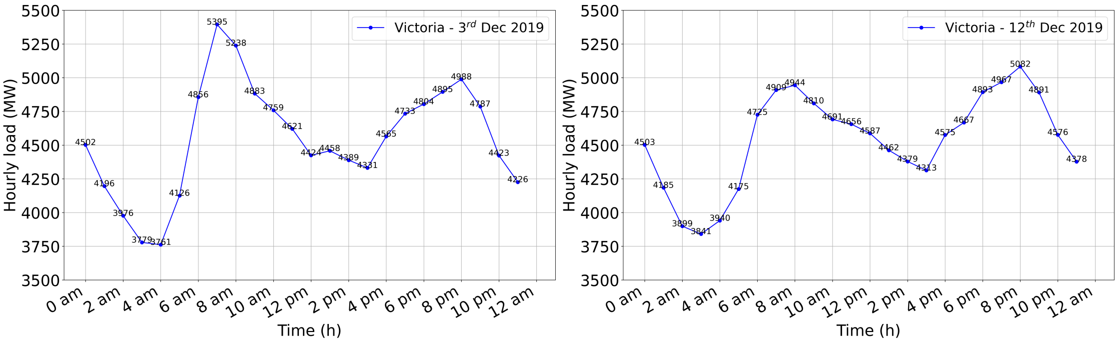

(a) 3 December 2019 **(b)** 12 December 2019

Figure 6.2: Hourly load curves on 3 & 12 December 2019 in Victoria, Australia

6.2.1 Scenario 1: All lines considered with dynamic FWI risk with various FWI-Line control strategies

In Scenario 1, the same three FWI disconnection thresholds (21.3, 38.0 & 50.0) tested in Chapter 3 were applied to the full 24-hour simulations of 3 and 12 December 2019. Whereas Chapter 3 considered only the peak burning condition, continuous operation was modelled to capture optimal energy flows in this chapter. Variations in fire-risk impacts on lines are illustrated in Figures 6.3 and 6.4. Fire risks on

3 December were lower but more widely dispersed. On 12 December, peak FWI values were higher, although the affected areas were smaller than on 3 December. These two days therefore exhibited distinct fire-risk patterns.

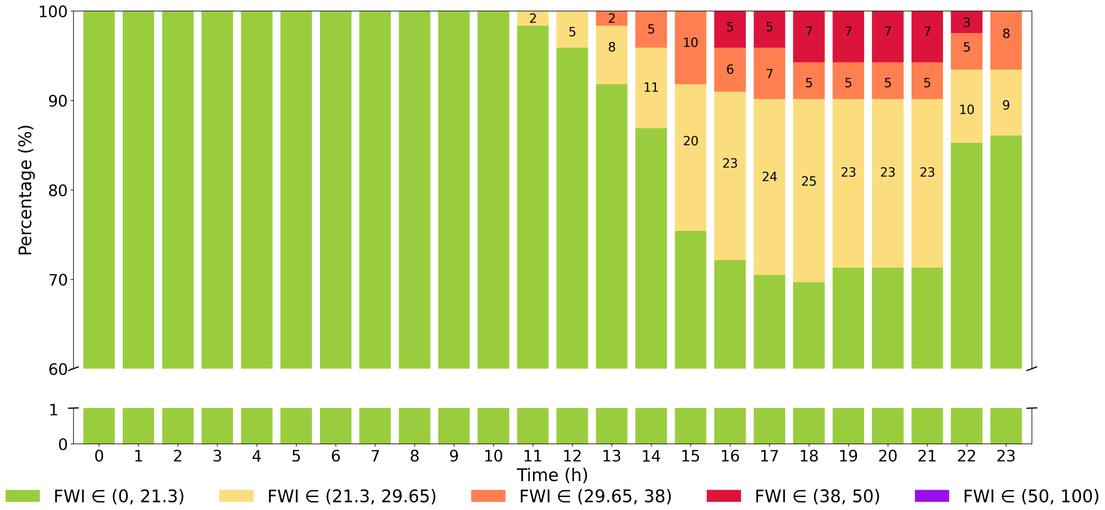

Figure 6.3: Percentage of lines having max FWI in each danger range on 3 December 2019

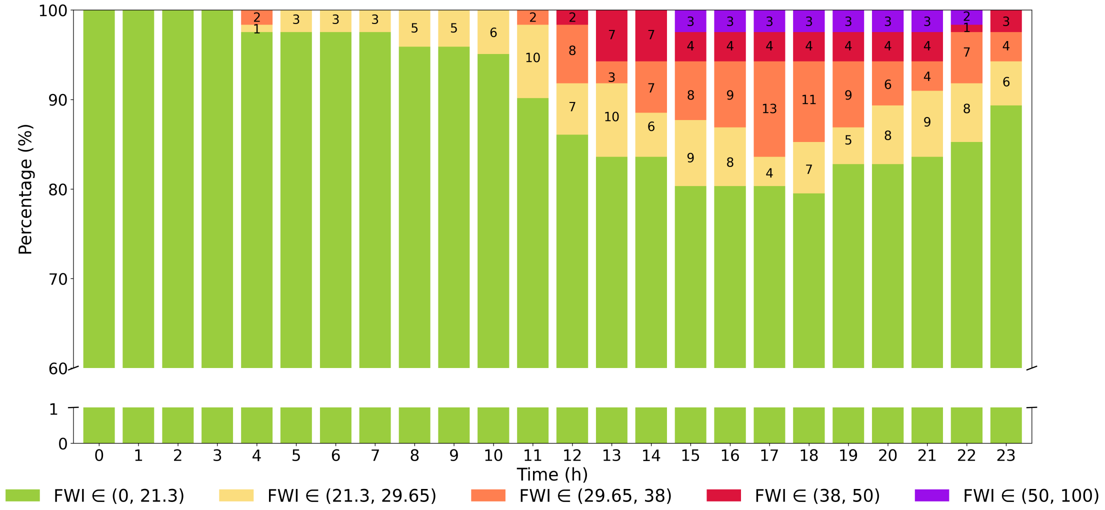

Figure 6.4: Percentage of lines having max FWI in each danger range on 12 December 2019

According to the evaluation metrics in Table 3.2, the performance results for six operating cases in Scenario 1 are recorded in Table 6.1. The results will be discussed following the order in Table 6.1.

Table 6.1: Scenario 1: daily grid resilience performances with different line disconnection thresholds on 3$^{\text{rd}}$ & 12$^{\text{th}}$ December 2019 in Victoria, Australia

Metrics	**1.a**	**1.b**	**1.c**	**1.d**	**1.e**	**1.f**	**Unit**
Thresholds	**50.0**	**38.0**	**21.3**	**50.0**	**38.0**	**21.3**	**N/A**
Dates	3^{rd}	3^{rd}	3^{rd}	12^{th}	12^{th}	12^{th}	**N/A**
LL_{grid}^{ave}	45.89	44.36	40.10	44.75	43.28	40.39	%
LS_{grid}	0	529.99	17,926.14	65.39	951.97	9,084.47	MWh
$LS_{grid}^{percent}$	0	0.49	16.43	0.06	0.87	8.33	%
C_{grid}	6,811,832	6,817,132	6,991,094	6,812,486	6,821,352	6,902,677	AU$
C_{grid}^{ave}	62.43	62.78	76.66	62.51	63.10	69.05	$AU\$$ /MWh
E_{grid}	6,339,449	6,349,253	6,349,357	6,342,019	6,349,618	6,350,068	kg
E_{grid}^{ave}	58.09	58.47	69.63	58.19	58.74	63.52	kgCO_{2eq} /MWh

In terms of technical metrics, average grid loading decreased as the FWI threshold became more stringent on both dates, falling by 12.62% on 3 December and 9.74% on 12 December. Figure 6.5 illustrates the average line-loading distributions for the six operating cases in Scenario 1. Notably, the region around Melbourne consistently experienced higher loading stress. In operating cases 1.c and 1.f, the north-west regions exhibited lower loading, since most lines there were pre-disconnected to mitigate elevated fire-risk levels.

The line-FWI maps and the lines disconnected by the preset thresholds are shown in Figure 6.6; these indicate that the north and north-west of Victoria faced more severe fire risks than the southern areas. The distribution of load shedding, presented in Figure 6.7, increased progressively as FWI thresholds were reduced from 50.0 to 21.3, resulting in the load shed increments of 16.43% and 8.33% on 3 and 12 December, respectively. Load curtailment occurred predominantly in the north and north-west regions, consistent with the spatial fire-risk pattern. During actual operations in the 2018–2019 wildfire season, the maximum load shed in Victoria reached 272 MW on 25 January 2019 [237]. Assuming this level persisted for 24 hours, the estimated energy shed would be 6,528 MWh. Compared to the load shed in Scenarios 1.c and 1.f, the theoretical and observed 24-hour load sheds are of a similar order of magnitude.

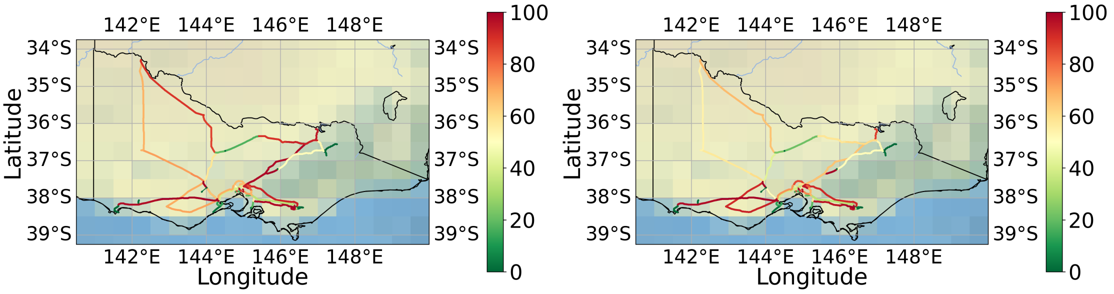

(a) Scenario 1.a (threshold = 50.0) **(b)** Scenario 1.b (threshold = 38.0)

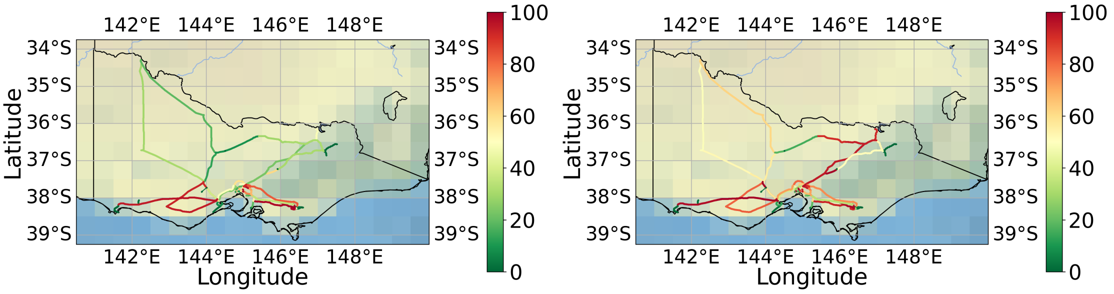

(c) Scenario 1.c (threshold = 21.3) **(d)** Scenario 1.d (threshold = 50.0)

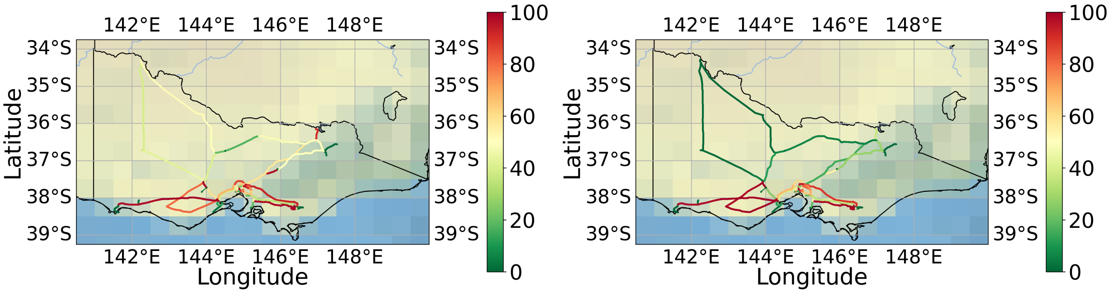

(e) Scenario 1.e (threshold = 38.0) **(f)** Scenario 1.f (threshold = 21.3)

Figure 6.5: Average line loading maps for transmission networks with different FWI line disconnection thresholds in Victoria, Australia. Scenarios 1.a-c are based on 3rd Dec 2019 cases, and Scenarios 1.d-f are based on 12th Dec 2019 cases

From economic and environmental perspectives, overall grid stress increased as the line FWI thresholds became stricter on both representative days. The unit grid operational cost rose by 18.56% and 9.47% on 3 and 12 December, respectively, as the disconnection thresholds were tightened from 50.0 to 21.3. Electricity generation also became more carbon-intensive under stricter thresholds, with unit carbon

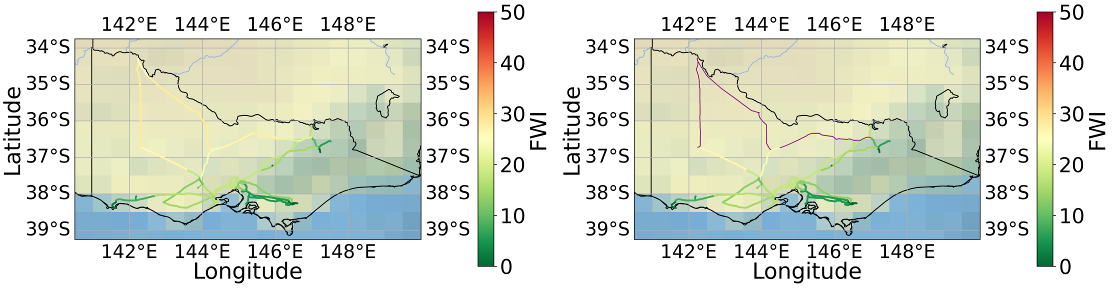

(a) Scenario 1.a (threshold = 50.0) **(b)** Scenario 1.b (threshold = 38.0)

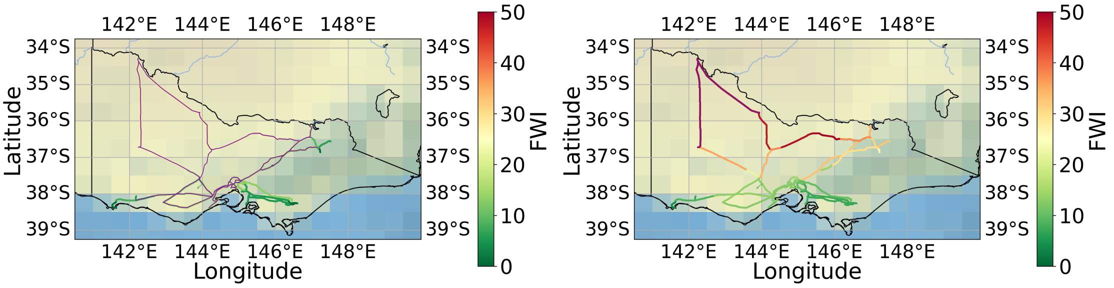

(c) Scenario 1.c (threshold = 21.3) **(d)** Scenario 1.d (threshold = 50.0)

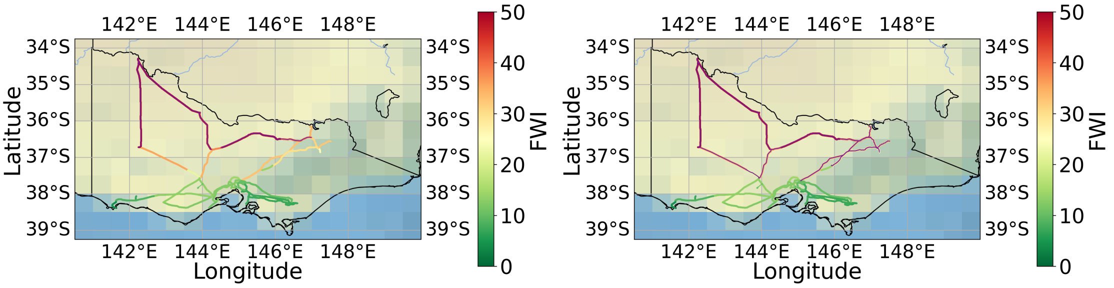

(e) Scenario 1.e (threshold = 38.0) **(f)** Scenario 1.f (threshold = 21.3)

Figure 6.6: Average line-fire risk maps for transmission networks with different FWI line disconnection thresholds in Victoria, Australia. Scenarios 1.a-c are based on 3rd Dec 2019 cases, and Scenarios 1.d-f are based on 12th Dec 2019 cases (lines pre-disconnected due to the violation of the preset FWI risk thresholds are marked in dark purple)

emissions increasing by 16.57% and 8.39% on the two days, respectively. In practice, the appropriate FWI threshold for disconnecting or derating lines during wildfire seasons should be determined based on real-time fire management needs, balancing effective fire mitigation with reliable grid operation. In comparison to the actual electricity cost in Victoria, the average price was reported to be AU$150/MWh in 2019 [238]. This total comprises wholesale costs (40%), network charges (40%), retail costs (10%), environmental levies (5%), and regulatory costs (5%). This study

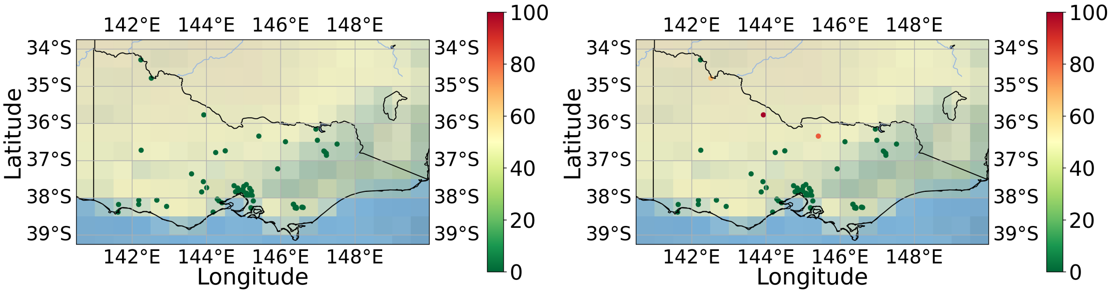

(a) Scenario 1.a (threshold = 50.0) **(b)** Scenario 1.b (threshold = 38.0)

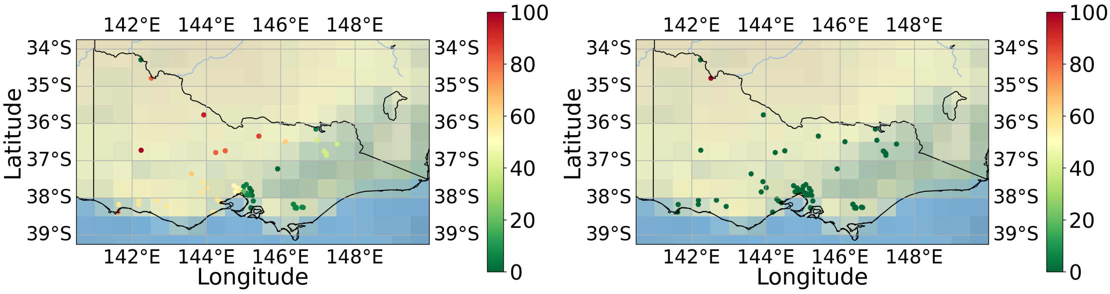

(c) Scenario 1.c (threshold = 21.3) **(d)** Scenario 1.d (threshold = 50.0)

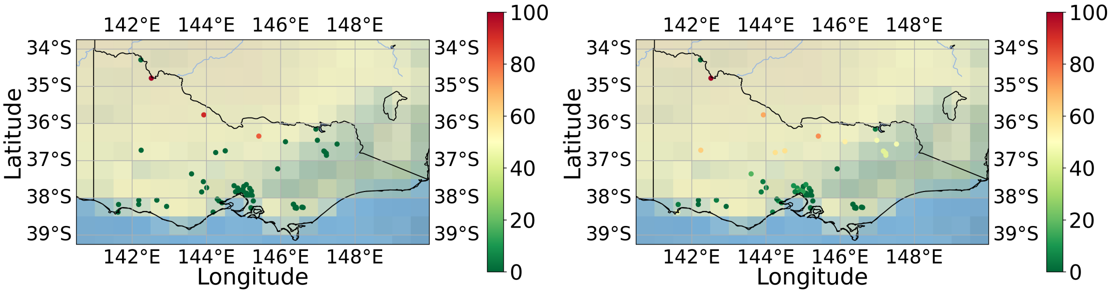

(e) Scenario 1.e (threshold = 38.0) **(f)** Scenario 1.f (threshold = 21.3)

Figure 6.7: Average load shed maps for transmission networks with different FWI line disconnection thresholds in Victoria, Australia. Scenarios 1.a-c are based on 3rd Dec 2019 cases, and Scenarios 1.d-f are based on 12th Dec 2019 cases

assesses costs at the transmission network level, focusing primarily on the wholesale component. The average wholesale electricity price, therefore, is approximately AU\$60/MWh (40% of the AU\$150/MWh) — comparable to the estimated unit grid operational costs of AU\$62-77/MWh presented in Table 6.1. This suggests that the estimation reasonably reflects real-world operational conditions.

6.2.2 Scenario 2: Flexible DG solutions to reinforce power networks during wildfire seasons

In Scenario 2, DGs and storage were deployed to recover the load shed observed in Scenarios 1.b and 1.e on the two selected days. Line-disconnection thresholds were set at 38.0 (very high), consistent with Scenario 2 in Chapter 3. Wind DGs and storage were installed at nodes experiencing load curtailment in Scenarios 1.b and 1.e to meet 100% of demand in Scenarios 2.a and 2.b. The grid-resilience results for Scenario 2 are presented in Table 6.2.

Table 6.2: Scenario 2: grid resilience performances with flexible DG and storage deployment on 3^{rd} & 12^{th} December 2019 in Victoria, Australia

Metrics	**2.a**	**2.b**	**Unit**
Thresholds	**38.0**	**38.0**	**N/A**
Dates	3^{rd}	12^{th}	**N/A**
LL_{grid}^{ave}	44.22	42.93	%
LS_{grid}	0	0	MWh
$LS_{grid}^{percent}$	0	0	%
C_{grid}	8,400,123	8,458,192	AU$
C_{grid}^{ave}	76.98	77.56	$AU\$$ /MWh
E_{grid}	6,349,253	6,349,618	kg
E_{grid}^{ave}	58.19	58.23	kgCO_{2eq} /MWh

Based on the load shedding observed in Scenarios 1.b and 1.e, wind DG and storage were installed at nodes 25, 44, and 67 for both dates. In Scenario 2.a, additional wind capacity of 80 MW, 25 MW, and 15 MW was assigned to nodes 25, 44, and 67, respectively; in Scenario 2.b, the capacities were 80 MW, 25 MW, and 10 MW. Storage capacities were determined according to the criteria described in Chapter 5. Figure 6.8 highlights the locations of the newly deployed wind generators in Scenario 2. Storage was deployed according to the strategy proposed in Chapter 5. However, it was found that storage was unnecessary for these two representative operating days, owing to the cost difference between wind generation and storage.

Storage may become financially attractive over longer operational periods, which could be explored in future work.

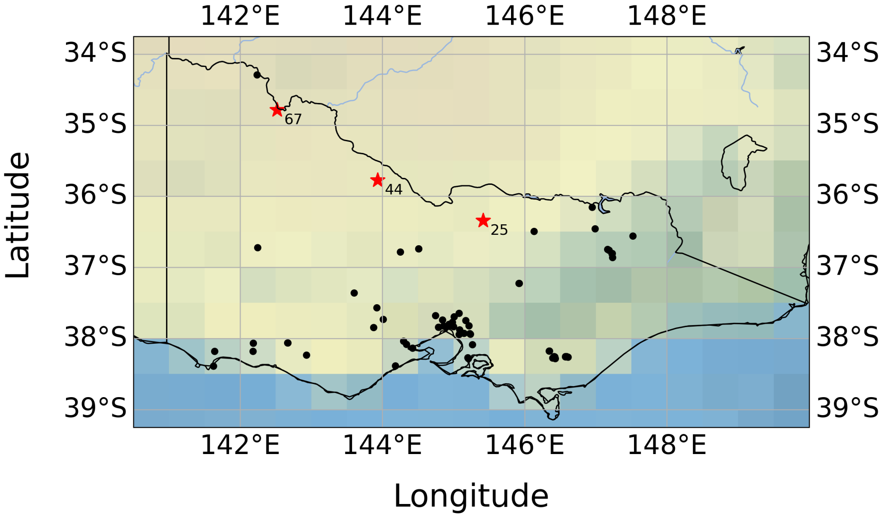

Figure 6.8: Scenario 2: locations of the newly deployed wind generation

Compared with Scenarios 1.b and 1.e, the system average line loading in Scenario 2 fell slightly—by 0.32% on 3 December and 0.81% on 12 December—owing to local DG support. Line-loading patterns remained largely unchanged, as the previously shed demand was met locally rather than via neighbouring nodes. Detailed line-loading maps for Scenario 2 are shown in Figure 6.9. Notably, the southern Victoria region (around Melbourne) consistently experienced higher loading levels on both dates. In practice, these high-loading areas would warrant more frequent inspections and stricter fire-management measures during wildfire seasons, such as reduced vegetation-clearance distances.

In terms of economic performance, the introduction of DGs increased operational costs: unit costs rose by 22.62% and 22.92% on 3 and 12 December, respectively. Environmentally, total emissions remained unchanged after DG deployment on both days, since wind turbines were assumed to produce zero operational carbon. Consequently, unit carbon emissions decreased by 0.48% and 0.87% on 3 and 12

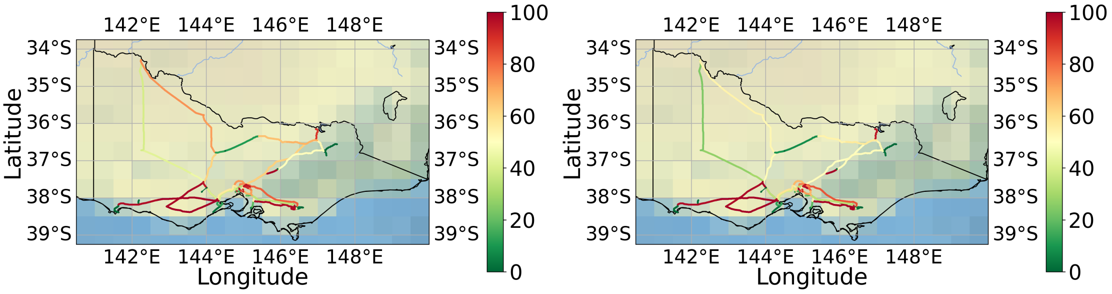

(a) 3 December 2019 **(b)** 12 December 2019

Figure 6.9: Scenario 2: with DG and storage solutions - average line loading maps on 3 & 12 December 2019 in Victoria, Australia

December, respectively, as curtailed load was recovered by local DGs.

Although operational costs rose after deploying DGs, total system benefits should account for VoLL savings. Using the cost–benefit methodology of Section 3.4.3, Table 6.3 presents the evaluation of DG investment to avert blackouts. The overall system cost decreased on both operating days following the implementation of wind DGs, falling by 43.12% on 3 December and 59.92% on 12 December. This demonstrates that the proposed DG solution can prevent blackouts in a financially advantageous manner. A VoLL of AU\$15,000/MWh was used in Table 6.3 according to the AEMO's guidance. For our specific cases, the breakeven VoLLs, calculated via Equation 3.16, are AU\$12,013/MWh and AU\$13,281/MWh for 3 December and 12 December, respectively. Thus, if actual VoLLs exceed these values, DG deployment is justified to prevent power outages during wildfire seasons.

The cost-effectiveness of the proposed DG solution is closely linked to the calculated breakeven VoLL. A VoLL of AU\$15,000/MWh is adopted in this thesis, reflecting the 2020 benchmark used by the National Electricity Market in Australia. In Chapters 3 and 6, the calculated average breakeven VoLLs are AU\$14,096/MWh (static peak fire scenario) and AU\$12,647/MWh (24-hour continuous scenario), both lower than AU\$15,000/MWh, thereby supporting the effectiveness of the proposed DG solutions. Notably, the average breakeven VoLL decreases from

Table 6.3: Cost-benefit analysis 3rd & 12th December 2019 in Victoria, Australia

Scenarios	TS_{cost} $AU\$$	Load shed MWh	VoLL $AU\$$	SO_{cost} $AU\$$
1.b (3rd)	6,817,132	529.99	7,949,850	14,766,982
1.e (12th)	6,821,352	951.97	14,279,550	21,100,902
2.a (3rd)	8,400,123	0	0	8,400,123
2.b (12th)	8,458,192	0	0	8,458,192

Chapter 3 to Chapter 6 as the operational period is extended, with the breakeven VoLL peaking when fire risk and system stress peak. This suggests that the breakeven VoLL would fall further if extended to entire wildfire seasons spanning several months. In 2020, the VoLL determined by AEMO was already above the calculated breakeven values, at AU$15,000/MWh. Looking ahead, VoLL is expected to rise further: according to AEMO, it increased from AU$16,600/MWh in 2023 to AU$17,500/MWh in 2024 [239]. Consequently, the proposed DG solutions will become increasingly practical and cost-effective.

6.2.3 Scenario 3: Fire risk impact on "N-1" contingency test

In this scenario, "N–1" contingency tests were conducted both with and without consideration of fire risk. Four operating cases were examined: the 3 December 2019 day case without fire risk; the 3 December day case with fire risk; the 12 December 2019 day case without fire risk; and the 12 December day case with fire risk. This scenario aims to assess the importance of incorporating fire risk when evaluating grid reserves.

Table 6.4 summarises the maximum reserve requirements for the four operating cases in Scenario 3, along with the components whose disconnection triggered maximum load shedding and the associated load-shedding incidences. Notably, integrating fire risk increased reserve needs by 12.77% on 3 December and 14.93% on

Table 6.4: Fire impact on "N-1" contingency tests on 3rd & 12th December 2019 in Victoria, Australia

Scenarios	**Fire risk**	**Power reserve (MW)**	**Triggering component**	**Energy reserve (MWh)**	**Shed bus**	**Shed time**
3.a (3rd)	No	329	Gen at Bus 8	13,599	Bus 18	20:00
3.b (3rd)	Yes	371	Gen at Bus 8	30,973	Bus 41	19:00
3.c (12th)	No	335	Gen at Bus 8	13,368	Bus 18	20:00
3.d (12th)	Yes	385	Gen at Bus 8	41,730	Bus 41	20:00

12 December. In all cases, the disconnection of the generator at Bus 8 — a 212 MW wind farm near Melbourne — caused the greatest load shedding. The fifth column of Table 6.4 reports the total 24-hour energy curtailed following this disconnection, demonstrating that considering fire risk also raises energy curtailment. The final two columns list the location and timing of the peak load shed; in three of the four cases this occurred at 20:00, and in one at 19:00, indicating that system stress peaked in the evening. Figure 6.10 maps the critical component and the nodes experiencing maximum load shedding in Scenario 3: the red marker indicates the wind farm at Bus 8, and the blue markers denote the vulnerable load-shedding nodes, all situated around Melbourne, the principal demand centre of Victoria.

6.2.4 Scenario 4: data-driven "LOLP" based method to assess grid reserve

The "LOLP" - based methods described in Section 5.3 were applied to estimate grid reserves for the two selected days in Scenario 4. Table 6.5 records the required power reserve and 24-hour energy reserve under various risk tolerance levels. To limit the probability of lost load to 1%, reserves of 333 MW and 381 MW are required for the 3 and 12 December cases, respectively. These figures are of the same order of magnitude as the "N–1" reserves in Table 6.4; the LOLP-based power reserves

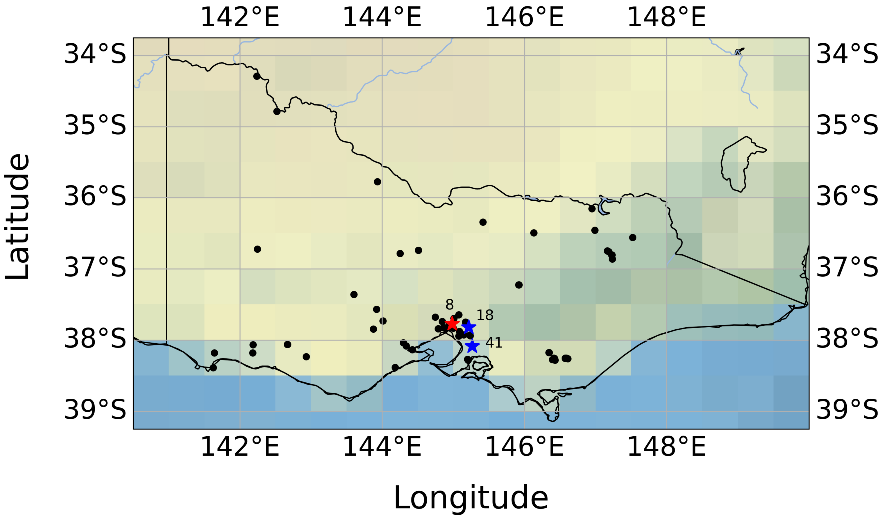

Figure 6.10: Scenario 3: critical nodes. The red scatter represents the critical wind generation site that leads to the maximum load shed in the "N-1" contingency test. The blue scatters stand for the vulnerable nodes with the biggest load shed

are 10.24% and 1.04% lower than the "N–1" values for the 3 and 12 December cases, respectively. Regarding the timing of maximum load shedding, the "N–1" scenario peaked at 19:00 or 20:00, whereas the "LOLP" method identifies the worst forecasting hours — 22:00 on 3 December and 18:00 on 12 December — as the critical points. This shift reflects the data-driven nature of the "LOLP" approach, which depends on the accuracy of real-time forecasts. Figure 6.11 illustrates the risk distribution of load shedding at these peak times.

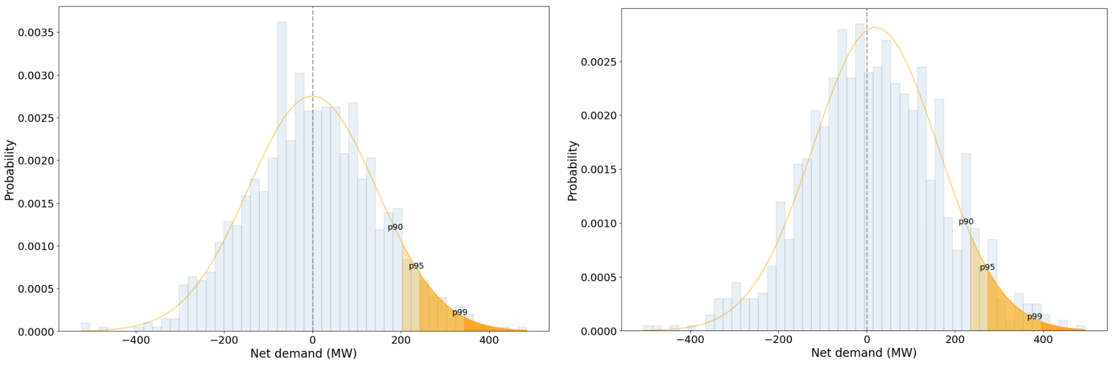

(a) 22:00 - 3 December 2019

(b) 18:00 - 12 December 2019

Figure 6.11: Scenario 4 - power reserve probabilistic distribution based on different resilience risk levels - 1%, 5%, and 10% of Lost of Load Probabilities (LOLPs) - at the maximum load shed time. (Victoria, Australia)

Table 6.5: Scenario 4: power reserve capacity and 24-hour electricity reserve for 1%, 5%, and 10% LOLP cases. (3^{rd} and 12^{th} Dec 2019 in Victoria, Australia)

Date Date	LOLP level	Time point	Maximum power reserve (MW)	Electricity reserve for 24 hours (MWh)
3^{rd}	1%	22	333	5086.31
3^{rd}	5%	22	235	3,545.05
3^{rd}	10%	22	205	2,702.65
12^{th}	1%	18	381	7,660.96
12^{th}	5%	18	274	5,581.44
12^{th}	10%	18	225	4,424.01

Both the "N–1" contingency test and LOLP-based uncertainty estimation have distinct advantages and limitations when assessing power reserve requirements. The traditional "N–1" method effectively identifies critical grid components and vulnerable buses — such as the wind generation site at Bus 8, and Buses 18 and 41 highlighted in Section 6.2.3. However, it evaluates only one component at a time, which may be inadequate for modern grids facing multiple concurrent risks. In contrast, the LOLP-based approach addresses systemic risk by estimating power reserves through comprehensive, data-driven analysis. Notably, the 1% LOLP reserve in Scenario 4 was 6% lower than the "N–1" reserve in Scenario 3, demonstrating that LOLP can provide an economical and resilient estimate of required reserves. Therefore, while the "N–1" test remains valuable for pinpointing critical components, the LOLP-based method is recommended as a flexible method to determine overall reserve levels under varying risk tolerance requirements.

6.3 Summary and suggestions

This chapter extends the time-series Wildfire Energy Model (WEM), originally developed on the theoretical IEEE 24-bus RTS, to a real-world grid in Victoria, Australia. By comparing results from the theoretical and Victorian cases, we validate the WEM's general applicability for simulating network operations under extreme wildfire conditions. The findings show that properly implemented DG methods can fully offset load curtailed by severe fire events. In Victoria, the proposed flexible DG approach reduces overall system cost by 43.12% and 59.92% on two representative risk days, primarily through VoLL savings associated with avoided outages.

For future research, the Victoria WEM could be adapted to other fire-prone regions, such as the western United States, Canada and Brazil. Extending the analysis beyond the two selected 2019–2020 risk days would assess their representativeness. Moreover, the model's framework can accommodate other extreme weather scenarios by substituting appropriate climate datasets to evaluate grid resilience under diverse hazards.

This chapter addresses the main research question of this DPhil study. We have developed a high-resolution temporal and spatial WEM, using real grid data and observed weather-risk information for Victoria, to assess grid resilience under fire threats. The results confirm that flexible DG deployments can ensure reliable operation during high-stress periods, delivering resilience, economic benefit and decarbonisation, while mitigating potential wildfire risks from electrical faults. Chapter 7 will summarise these key findings across all four phases and provide an integrative discussion.

7

Conclusion and outlook

Contents

This chapter summarises the key findings of the thesis. The critical insights are discussed in relation to the research questions presented in Section 1.2.1. Finally, the limitations of this thesis are outlined, and recommendations for future work are provided.

7.1 Conclusion and insight

This section goes over the research questions of this thesis, discussing the general insights and main contributions from each question, supported by key findings as evidence. The three research questions are considered first, followed by a concluding discussion that answers the overarching research question of the thesis.

7.1.1 Answering research question I: How is grid resilience affected by wildfire risks under selected peak fire conditions?

This thesis demonstrates that power grid resilience is substantially reduced during peak fire conditions across three main dimensions: technical, economic, and environmental. From a technical perspective, considerable load curtailment is required due to wildfire risks, leading to large-scale power outages. Economically, both overall system costs and unit electricity prices increase significantly under wildfire conditions. The rise in system costs is primarily driven by the VoLL associated with curtailed demand. Such cost increases place considerable financial pressure on power utilities and local governments. In some severe cases, utilities may face legal action if a wildfire is caused by electrical faults. From an environmental perspective, unit carbon emissions increase markedly under fire risks. Elevated carbon emissions may further accelerate climate change, with consequent impacts on weather patterns, sea levels, and ecosystems.

More specifically, the impact of wildfire risks on power grid resilience is quantified in Phase I (Section 3.4.1), through testing peak fire scenarios using the proposed WEM. When high fire risks are taken into account, resilience declines markedly across all three dimensions: 36.50% of power system is blackout under peak-fire conditions, the unit operational cost rises by 51.75%, and the unit carbon emission increases by 48.49% in Victoria.

In addressing the first research question, the main contribution of this section is the development of the WEM, which combines the FWI and OPF to quantify power grid resilience under peak wildfire conditions across technical, economic, and environmental dimensions.

7.1.2 Answering research question II: How can electricity demand be accurately predicted during wildfire seasons?

The second research question arises from the observation that forecasting electricity demand during wildfire seasons is more challenging than during non-wildfire periods. This is due to the greater variability in demand patterns under wildfire risks. Inaccurate forecasts during such periods increase the likelihood of inappropriate power dispatch, which may result in unintentional blackouts. Most existing power utilities rely on traditional statistical tools to forecast electricity demand; however, these methods are insufficient to capture demand patterns under wildfire risks. Therefore, more advanced machine learning-based approaches, incorporating relevant risk factors such as temperature and the FWI are developed to improve forecast accuracy under heightened uncertainty.

In Phase II, a climate-resilient load forecasting model (WRLFM) is developed to predict electricity demand during extreme wildfire seasons. As shown in Table 4.4, forecasting electricity demand in Australia is more challenging during wildfire seasons, with errors increasing by 10.49% compared with non-wildfire periods. To improve accuracy under wildfire risks, the WRLFM incorporates architectural innovations and carefully selected risk factors. For instance, certain factors exhibit stronger correlations with electricity demand during wildfire conditions; for example, as illustrated in Figure 4.15, the correlation coefficient between the FWI and electricity demand is 20.38% higher on high fire-risk days than on normal days. Other variables, such as temperature, also display stronger correlations with demand under wildfire risks. Accordingly, these input risk factors are integrated into the WRLFM. Furthermore, state-of-the-art deep learning architectures, such as Bi-GRU and ViT, are employed to enhance forecasting performance. The proposed WRLFM achieves an accuracy exceeding 97% in predicting electricity demand during wildfire seasons in Australia.

The main contribution to knowledge from the second research question is that, for the first time, a deep learning-based electricity load forecasting model has been developed specifically for extreme wildfire conditions. By incorporating relevant risk factors and leveraging advanced AI architectures, the proposed WRLFM achieves an accuracy exceeding 97%.

7.1.3 Answering research question III: How can the resilience of wildfire-affected power grids be continuously assessed and enhanced in both theoretical and real-world case studies?

The initial WEM developed in Phase I is built at a daily peak resolution, as most fire risk products are only available at daily scales. However, since power systems are typically simulated on an hourly basis in practice, this motivated the third research question. In Phases III and IV, an hourly FWI is derived from fundamental meteorological observations to extend the WEM with time-series assessment capabilities. The continuous modelling demonstrates that power grid resilience is significantly reduced on high fire-risk days across technical, economic, and environmental dimensions. Consistent with the findings in Phase I, load shedding, total network costs, and unit carbon emissions all increase markedly once wildfire risks are incorporated, but here they are analysed at an hourly rather than daily resolution. To mitigate these impacts and enhance grid resilience, DG and storage are deployed near vulnerable nodes. The results show that renewable DG combined with storage has the potential to alleviate load shedding sustainably. In addition to fully recovering power outages caused by wildfire risks, the proposed strategy substantially reduces overall power system costs and slightly lowers carbon emissions. In the cost-benefit analysis, we figure out that the substantial saving in overall system cost is primarily driven by VoLL savings from avoided outages. To justify investment in DG and storage for resilience enhancement, it is recommended that a VoLL analysis be conducted, comparing the breakeven VoLL with the market

VoLL to assess the economic viability of the investment.

In addition to the power flow optimisation function of the proposed WEM, this section also examines the reserve requirements of the power grid during wildfire seasons. It is observed that greater reserves are needed to ensure reliable grid operation under fire risks. Without sufficient reserves, the power system faces a heightened risk of blackouts during peak wildfire conditions or peak demand periods, resulting in a significant loss of resilience. To address this, we propose an integrated grid reserve assessment tool that combines the traditional ‘N-1’ contingency test with a data-driven LOLP-based method to estimate the required reserves under fire risks. While the traditional ‘N-1’ test identifies vulnerable points in the grid, the proposed data-driven reserve analysis incorporates systemic risks to forecast reserve needs. Together, these methods provide a more robust framework for assessing grid reserve requirements under wildfire risks.

Using the derived hourly FWI from fundamental climate variables, power grid resilience is simulated at an hourly resolution in the upgraded WEM. The updated model is applied to both a theoretical case (IEEE 24-Bus RTS) in Phase III and a real-world case (the Australian grid) in Phase IV. On representative high-risk days in Australia, resilience is shown to be noticeably degraded, with up to 16.43% of grid load curtailed. The deployment of DG and storage near vulnerable nodes effectively restores curtailed load in a sustainable manner: the unit grid cost decreases by 22.77% and the total system cost by 51.52%, as shown in Table 6.1 and Table 6.2. In the cost–benefit analysis, the breakeven VoLL is calculated and compared with the market VoLL. For the Victorian grid case, the breakeven VoLL is AU$12,647, which is lower than the value set by the market operator (AEMO), indicating the effectiveness of the proposed DG and storage strategy. Regarding grid reserve requirements, it is observed that 13.85% more reserve capacity is needed during wildfire seasons than in non-wildfire periods (Table 6.4). To assess reserve needs under wildfire risks, both the traditional ‘N-1’ contingency method and the proposed data-driven LOLP-based method are employed. While both approaches yield results of a similar magnitude, the ‘N-1’ test remains useful for identifying critical components, whereas the LOLP-based method is recommended as a more flexible tool for determining overall reserve requirements under varying risk tolerance levels.

The main contribution from addressing this research question is the development of a high spatio-temporal resolution WEM to quantify power grid resilience under wildfire risks. Furthermore, resilience is enhanced through the deployment of DG and storage, alongside the introduction of a robust data-driven tool for power grid reserve analysis.

7.1.4 Answering the main research question: How can power system resilience be assessed and enhanced under extreme wildfire risks?

The main research question is addressed following the discussion of the three research questions. Using the proposed WEM, the degradation of power grid resilience due to wildfire risks is assessed across technical, economic, and environmental dimensions. The findings demonstrate that wildfire risk is a critical factor for power utilities, as grid resilience is substantially reduced during wildfire seasons. To mitigate these impacts, DG and storage are deployed across the network, effectively recovering shed load while delivering positive economic and environmental outcomes. Furthermore, the WRLFM is developed to enhance the forecasting of electricity demand during wildfire seasons, thereby enabling more timely power dispatch that accounts for wildfire risks and reduces the likelihood of wildfire-induced blackouts. Finally, an integrated grid reserve assessment method is proposed to more accurately determine the reserve capacity required to prevent blackouts under wildfire conditions and to further strengthen grid resilience.

Using the WEM, resilience degradation is quantified for Victoria, Australia, on representative wildfire-season days: system load curtailment increases by 12.38%, the unit cost of electricity by 14.02%, and the unit carbon emission by 12.48%. To mitigate these impacts and enhance grid resilience, DG and storage are deployed across the network to recover curtailed load. The results demonstrate that DG and storage substantially improve resilience, enabling full recovery from wildfire-induced curtailment and reducing overall system costs by 51.52%. The finalised WEM contributes to resilience enhancement under wildfire risks by facilitating the cost-effective deployment of DG and storage, improving electricity demand forecasting, and providing a robust estimation of reserve requirements. The proposed framework holds significant practical relevance for local authorities, utilities, businesses, and communities, as grid resilience is essential for regional prosperity and welfare.

7.2 Future work

The generalised WEM developed in the final phase was tested on selected risk days in Victoria during the 2019-2020 wildfire season. To validate the typicality of these days, a more extended testing period should be considered, such as a month or the entire wildfire season. In terms of geographical coverage, the WEM can be applied across Australia, as wildfire risks are not confined to Victoria; New South Wales and Queensland are also high-risk regions. Additionally, the WEM can be adapted for other regions experiencing extreme wildfire seasons, such as Brazil, Greece, Canada, and the western United States.

The FWI was used to simulate general fire risks, and several hypothesised FWI-line control strategies were proposed in this thesis. However, determining a clear relationship between fire risk levels and their adverse impact on grid operations remains challenging. Future research could focus on quantifying the impact of fire risks on grid operations under different circumstances.

While we considered FWI risks on grid transmission infrastructures, particularly the line loading limits for safe operation, it is also essential to consider variations in generation and demand patterns during wildfire seasons. For instance, the capacity factors of solar generators may decrease due to wildfire smoke, and demand may rise in urban areas due to higher temperatures and increased use of air conditioning. Future work should account for the impact on both generation and demand when analysing grid resilience.

In terms of the LOLP-based power reserve analysis, the probabilistic power reserve was estimated using the forecasting results from the WRLFM case study in Phase II. This was necessitated by the temporary unavailability of net demand error data for real grid operations in Victoria, Australia. As the net demand forecast error will vary depending on the forecasting tools used by grid operators, future research could obtain more detailed and accurate net demand error data through collaborated research with local grid companies.

This thesis specifically examined the impact of wildfires on transmission networks, as it has been proven that wildfire-related damages in high-voltage systems tend to be much more severe than in medium- or low-voltage regions. Nevertheless, the majority of electrical faults in actual grid operations occur within distribution networks. The generalised WEM can be further developed to mitigate wildfire risks and prevent electrical faults in distribution networks through the application of smart solutions.

In this thesis, the generalised WEM was developed, focusing on grid resilience under wildfire risks. The standardised methodology can be readily adapted to reinforce grid operations in the face of other extreme weather events, such as floods, hurricanes, and snowstorms in the future.

References

[1] Weijia Yang et al. “Resilient by design: Preventing wildfires and blackouts with microgrids”. In: *Applied Energy* 313 (2022), p. 118793.

[2] Weijia Yang, Sarah N Sparrow, and David CH Wallom. “Optimising multi-factor assistance in a deep learning-based electricity forecasting model with climate resilience: an australian case study”. In: *2023 IEEE PES Innovative Smart Grid Technologies Europe (ISGT EUROPE)*. IEEE. 2023, pp. 1–5.

[3] Weijia Yang, Sarah N Sparrow, and David CH Wallom. “A comparative climate-resilient energy design: Wildfire Resilient Load Forecasting Model using multi-factor deep learning methods”. In: *Applied Energy* 368 (2024), p. 123365.

[4] Weijia Yang, Pu Yang, and Stephanie Hirmer. “Building the Resilience of Local Power Systems Against Climate Change”. In: *Digitalisation of Local Energy Systems*. Ed. by Weiqi Hua, Xiao-Ping Zhang, and David C.H. Wallom. Cham: Springer Nature Switzerland, 2025, pp. 219–245. DOI: `10.1007/978-3-031-77833-9_7`. URL: `https://doi.org/10.1007/978-3-031-77833-9_7`.

[5] Enerdata. *Share of electricity in total final energy consumption*. Tech. rep. World Energy & Climate Statistics – Yearbook 2024, 2024.

[6] IEA. *Tracking Clean Energy Progress 2023*. Tech. rep. IEA, 2023.

[7] Weiqi Li et al. “Extreme weather impact on carbon-neutral power system operation schemes: A case study of 2060 Sichuan Province”. In: *Energy* 313 (2024), p. 133677.

[8] Ofgem. *RIIO-ET3: Economic Lives of Electricity Transmission Network Assets*. Tech. rep. Ofgem, 2024.

[9] Javier Farfan and Christian Breyer. “Aging of European power plant infrastructure as an opportunity to evolve towards sustainability”. In: *International Journal of Hydrogen Energy* 42.28 (2017), pp. 18081–18091.

[10] Michael Goss et al. “Climate change is increasing the likelihood of extreme autumn wildfire conditions across California”. In: *Environmental Research Letters* 15.9 (2020), p. 094016.

[11] David Ribeiro et al. “Enhancing community resilience through energy efficiency”. In: American Council for an Energy-Efficient Economy Washington. 2015.

[12] Melissa Dumas, Binita Kc, and Colin I Cunliff. *Extreme weather and climate vulnerabilities of the electric grid: A summary of environmental sensitivity quantification methods*. Tech. rep. Oak Ridge National Lab.(ORNL), Oak Ridge, TN (United States), 2019.

[13] CDP. *2019-2020 Australian Bushfires.* `https://disasterphilanthropy.org/disasters/2019-australian-wildfires/`. 2020.

[14] Endeavour Energy. *Cost pass through application 2019-20 Bushfire disaster event.* Tech. rep. Endeavour Energy, 2020.

[15] PG&E. *Company information - PG&E's profile, policies, goals and values.* `https://www.pge.com/en/about/company-information.html`. 2021.

[16] Mark Murphy and Juan Diaz. *THE CAMP FIRE PUBLIC REPORT - A SUMMARY OF THE CAMP FIRE INVESTIGATION.* Tech. rep. Butte County District Attorney, 2020.

[17] Ivan Penn and Peter Eavis. *PG&E Pleads Guilty to 84 Counts of Manslaughter in Camp Fire Case.* `https://www.nytimes.com/2020/06/16/business/energy-environment/pge-camp-fire-california-wildfires.html`. 2020.

[18] Zhaohong Bie et al. "Battling the extreme: A study on the power system resilience". In: *Proceedings of the IEEE* 105.7 (2017), pp. 1253–1266.

[19] UNCC. *The Paris Agreement.* `https://unfccc.int/process-and-meetings/the-paris-agreement/the-paris-agreement`. 2022.

[20] Johnny Wood. *The world added 50% more renewable capacity last year than in 2022.* `https://www.weforum.org/agenda/2024/02/renewables-energy-capacity-demand-growth/`. 2024.

[21] IEA 50. *Coal.* `https://www.iea.org/energy-system/fossil-fuels/coal`. 2024.

[22] Francesca Di Giuseppe et al. *Copernicus fire danger forecast goes online.* `https://www.ecmwf.int/en/newsletter/151/news/copernicus-fire-danger-forecast-goes-online`. 2017.

[23] Australian Government. *Forest Fire Danger Index (FFDI).* `http://www.bom.gov.au/climate/maps/averages/ffdi/`. 2022.

[24] Joe H Scott, Matthew P Thompson, and David E Calkin. "A wildfire risk assessment framework for land and resource management". In: (2013).

[25] Noah Rhodes, Lewis Ntaimo, and Line Roald. "Balancing wildfire risk and power outages through optimized power shut-offs". In: *IEEE Transactions on Power Systems* 36.4 (2020), pp. 3118–3128.

[26] Probability Methods Subcommittee. "IEEE reliability test system". In: *IEEE Transactions on power apparatus and systems* 6 (1979), pp. 2047–2054.

[27] Pedro HJ Nardelli et al. "Models for the modern power grid". In: *The European Physical Journal Special Topics* 223.12 (2014), pp. 2423–2437.

[28] Eleftherios Tsampasis et al. "Communication challenges in smart grid". In: *MATEC web of conferences.* Vol. 41. EDP Sciences. 2016, p. 01004.

[29] Abdul Ahad Jhumka et al. "Swing equation in power systems: approximate analytical solution for the dynamics of the system inertia". In: *IET Conference Proceedings CP822.* Vol. 2022. 27. IET. 2022, pp. 36–41.

[30] Kim Hanh Nguyen and Makoto Kakinaka. “Renewable energy consumption, carbon emissions, and development stages: Some evidence from panel cointegration analysis”. In: *Renewable energy* 132 (2019), pp. 1049–1057.

[31] IRENA. *Renewable electricity.* Tech. rep. IRENA, 2021.

[32] MR Elkadeem et al. “A systematic decision-making approach for planning and assessment of hybrid renewable energy-based microgrid with techno-economic optimization: A case study on an urban community in Egypt”. In: *Sustainable Cities and Society* 54 (2020), p. 102013.

[33] Makbul AM Ramli, Ayong Hiendro, and Yusuf A Al-Turki. “Techno-economic energy analysis of wind/solar hybrid system: Case study for western coastal area of Saudi Arabia”. In: *Renewable energy* 91 (2016), pp. 374–385.

[34] S Bahramara, M Parsa Moghaddam, and MR Haghifam. “Optimal planning of hybrid renewable energy systems using HOMER: A review”. In: *Renewable and Sustainable Energy Reviews* 62 (2016), pp. 609–620.

[35] Office of ELECTRICITY. *Grid Systems.* Tech. rep. U.S. Department of Energy, 2020.

[36] Aaron Clark-Ginsberg. “What’s the Difference between Reliability and Resilience”. In: *Department of Homeland Security. March* (2016), pp. 1932–4537.

[37] Chen-Ching Liu. “Distribution systems: reliable but not resilient?[In My View]”. In: *IEEE Power and Energy Magazine* 13.3 (2015), pp. 93–96.

[38] Mathaios Panteli et al. “Metrics and quantification of operational and infrastructure resilience in power systems”. In: *IEEE Transactions on Power Systems* 32.6 (2017), pp. 4732–4742.

[39] Paul J Maliszewski and Charles Perrings. “Factors in the resilience of electrical power distribution infrastructures”. In: *Applied Geography* 32.2 (2012), pp. 668–679.

[40] The World Bank. *Getting electricity: System average interruption duration index (SAIDI) (DB16-20 methodology).* `https://datacatalog.worldbank.org/getting-electricity-system-average-interruption-duration-index-saidi-db16-20-methodology`. 2019.

[41] Mathaios Panteli and Pierluigi Mancarella. “Influence of extreme weather and climate change on the resilience of power systems: Impacts and possible mitigation strategies”. In: *Electric Power Systems Research* 127 (2015), pp. 259–270.

[42] Eduardo Ibanez and Michael Milligan. “Comparing resource adequacy metrics and their influence on capacity value”. In: *2014 International Conference on Probabilistic Methods Applied to Power Systems (PMAPS).* IEEE. 2014, pp. 1–6.

[43] Abdrabbi Bourezg and H Meglouli. “Reliability assessment of power distribution systems using disjoint path-set algorithm”. In: *Journal of industrial engineering international* 11.1 (2015), pp. 45–57.

[44] Eklas Hossain et al. “Metrics and enhancement strategies for grid resilience and reliability during natural disasters”. In: *Applied energy* 290 (2021), p. 116709.

[45] Jean-Paul Watson et al. “Conceptual framework for developing resilience metrics for the electricity oil and gas sectors in the United States”. In: *Sandia national laboratories, albuquerque, nm (united states), tech. rep* (2014).

[46] Michel Bruneau et al. “A framework to quantitatively assess and enhance the seismic resilience of communities”. In: *Earthquake spectra* 19.4 (2003), pp. 733–752.

[47] Baoping Cai et al. “Availability-based engineering resilience metric and its corresponding evaluation methodology”. In: *Reliability Engineering & System Safety* 172 (2018), pp. 216–224.

[48] Masanubu Shinozuka et al. “Resilience of integrated power and water systems”. In: (2004).

[49] Sayonsom Chanda and Anurag K Srivastava. “Defining and enabling resiliency of electric distribution systems with multiple microgrids”. In: *IEEE Transactions on Smart Grid* 7.6 (2016), pp. 2859–2868.

[50] John C Whitson and Jose Emmanuel Ramirez-Marquez. “Resiliency as a component importance measure in network reliability”. In: *Reliability Engineering & System Safety* 94.10 (2009), pp. 1685–1693.

[51] Yanling Lin, Zhaohong Bie, and Aici Qiu. “A review of key strategies in realizing power system resilience”. In: *Global Energy Interconnection* 1.1 (2018), pp. 70–78.

[52] Feng Wang et al. “A multi-stage restoration method for medium-voltage distribution system with DGs”. In: *IEEE transactions on smart grid* 8.6 (2016), pp. 2627–2636.

[53] Juan Li et al. “Distribution system restoration with microgrids using spanning tree search”. In: *IEEE Transactions on Power Systems* 29.6 (2014), pp. 3021–3029.

[54] Mingrui Zhang and Jie Chen. “Islanding and scheduling of power distribution systems with distributed generation”. In: *IEEE Transactions on Power Systems* 30.6 (2014), pp. 3120–3129.

[55] Chen Chen et al. “Resilient distribution system by microgrids formation after natural disasters”. In: *IEEE Transactions on smart grid* 7.2 (2015), pp. 958–966.

[56] Tao Ding et al. “A new model for resilient distribution systems by microgrids formation”. In: *IEEE Transactions on Power Systems* 32.5 (2017), pp. 4145–4147.

[57] Saeed Jazebi, Francisco De Leon, and Albert Nelson. “Review of wildfire management techniques—Part II: Urgent call for investment in research and development of preventative solutions”. In: *IEEE Transactions on Power Delivery* 35.1 (2019), pp. 440–450.

[58] Ken Pimlott, John Laird, and Edmund G Brown Jr. “Wildfire activity statistics”. In: *California Department of Forestry and Fire Protection Office of the StateFire Marshal* (2015), pp. 1–45.

[59] Joseph W Mitchell. “Power line failures and catastrophic wildfires under extreme weather conditions”. In: *Engineering Failure Analysis* 35 (2013), pp. 726–735.

[60] John W Muhs et al. “Characterizing probability of wildfire ignition caused by power distribution lines”. In: *IEEE Transactions on Power Delivery* 36.6 (2020), pp. 3681–3688.

[61] Jayant Sathaye et al. “Estimating risk to California energy infrastructure from projected climate change”. In: (2012).

[62] POWERLINK Queensland. *Fire and high voltage transmission line safety - information sheet.* Tech. rep. POWERLINK Queensland, 2015.

[63] Reddit. *Transformer explosion leads to forest fire, leading to evacuation (Utah Valley, June 28th, 2020).* `https://www.reddit.com/r/CatastrophicFailure/comments/hhav43/transformer_explosion_leads_to_forest_fire/`. 2020.

[64] Adam Voiland. *A New Global Fire Atlas.* `https://earthobservatory.nasa.gov/images/145417/a-new-global-fire-atlas`. 2019.

[65] Jeff Masters. "Reviewing the horrid global 2020 wildfire season» Yale Climate Connections". In: *Yale Climate Connections* (2021).

[66] Copernicus. *How wildfires in the Americas and tropical Africa in 2020 compared to previous years.* `https://atmosphere.copernicus.eu/how-wildfires-americas-and-tropical-africa-2020-compared-previous-years`. 2020.

[67] Meg A Krawchuk et al. "Global pyrogeography: the current and future distribution of wildfire". In: *PloS one* 4.4 (2009), e5102.

[68] National Park Service. *Wildfire Causes and Evaluations.* `https://www.nps.gov/articles/wildfire-causes-and-evaluation.htm`. 2020.

[69] Hamish Clarke et al. "Developing and testing models of the drivers of anthropogenic and lightning-caused wildfire ignitions in south-eastern Australia". In: *Journal of environmental management* 235 (2019), pp. 34–41.

[70] Alexandra D Syphard and Jon E Keeley. "Location, timing and extent of wildfire vary by cause of ignition". In: *International Journal of Wildland Fire* 24.1 (2015), pp. 37–47.

[71] Zhangwen Su et al. "Using GIS and Random Forests to identify fire drivers in a forest city, Yichun, China". In: *Geomatics, Natural Hazards and Risk* 9.1 (2018), pp. 1207–1229.

[72] Natural Resources Canada. *Canadian National Fire Database (CNFDB).* `https://cwfis.cfs.nrcan.gc.ca/ha/nfdb`. 2020.

[73] Jessie Yeung. "Blame humans for starting the Amazon fires, environmentalists say". In: *CNN. Retrieved* 26 (2019).

[74] Sally Archibald. "Managing the human component of fire regimes: lessons from Africa". In: *Philosophical Transactions of the Royal Society B: Biological Sciences* 371.1696 (2016), p. 20150346.

[75] Tara Law. "About 2.5 Million Acres in Alaska Have Burned. The State's Fire Seasons Are Getting Worse, Experts Say". In: *Time, August* 20 (2019).

[76] DARIA LITVINOVA and VLADIMIR ISACHENKOV. *EXPLAINER: What's fueling Russia's 'unprecedented' fires?* `https://apnews.com/article/europe-business-russia-environment-and-nature-climate-change-9f08b16cc35f773d27ce6b2746b410cd`. 2021.

[77] US Forest Service. *Pacific Southwest Research Station. Fire in chaparral ecosystems.* `https://www.fs.fed.us/psw/topics/fire_science/ecosystems/chaparral.shtml`. 2012.

[78] W.J. de Groot. *Interpreting the Canadian Forest Fire Weather Index (FWI) System.* Tech. rep. Northern Forestry Centre, 1987.

[79] Francesca Di Giuseppe. *Fire Index User Guide.* `https://confluence.ecmwf.int/display/CEMS/Fire+danger+indices+historical+data+from+the+Copernicus+Emergency+Management+Service`. 2023.

[80] Paul Schlobohm and Jim Brain. “Gaining an understanding of the national fire danger rating system”. In: *National wildfire coordinating group, PMS* 932 (2002).

[81] Andrew James Dowdy et al. “Australian fire weather as represented by the McArthur forest fire danger index and the Canadian forest fire weather index”. In: (2009).

[82] Stephen W Taylor and Martin E Alexander. “Science, technology, and human factors in fire danger rating: the Canadian experience.” In: *International Journal of Wildland Fire* 15.1 (2006), pp. 121–135.

[83] D Xavier Viegas et al. “Comparative study of various methods of fire danger evaluation in southern Europe”. In: *International Journal of wildland fire* 9.4 (1999), pp. 235–246.

[84] Andrew J Dowdy et al. “Index sensitivity analysis applied to the Canadian forest fire weather index and the McArthur forest fire danger index”. In: *Meteorological Applications* 17.3 (2010), pp. 298–312.

[85] Met Office. *England and Wales Fire Severity Index.* `https://www.metoffice.gov.uk/public/weather/fire-severity-index/#?tab=map&fcTime=1627988400&zoom=5]&lon=-4.00&lat=55.74`. 2021.

[86] Vivian Do et al. “Spatiotemporal distribution of power outages with climate events and social vulnerability in the USA”. In: *Nature communications* 14.1 (2023), p. 2470.

[87] Fiona Harvey. *Power cuts caused by flooding ’major danger’ to British lives, engineers warn.* `https://www.theguardian.com/environment/2016/may/11/power-cuts-caused-by-flooding-major-danger-to-british-lives-engineers-warn#:~:text=news-,Share,-Reuse%20this%20content`. 2016.

[88] M Kendon. *Storms Dudley, Eunice and Franklin February 2022.* Tech. rep. Technical Report. Met Office, 2022.

[89] Le Xie et al. *What Went Wrong With Texas’ Power Failure And How To Fix It.* `https://today.tamu.edu/2021/02/20/what-went-wrong-with-texas-power-failure-and-how-to-fix-it/`. 2021.

[90] Zihao Chen and Shuo Gao. *From Sichuan to California, Extreme Heat Is Pushing the Grid to Its Limit.* `https://rmi.org/from-sichuan-to-california-extreme-heat-is-pushing-the-grid-to-its-limit/`. 2022.

[91] Minghao Qiu et al. “Drought impacts on the electricity system, emissions, and air quality in the western United States”. In: *Proceedings of the National Academy of Sciences* 120.28 (2023), e2300395120.

[92] Bananeh Ansari and Salman Mohagheghi. "Optimal energy dispatch of the power distribution network during the course of a progressing wildfire". In: *International Transactions on Electrical Energy Systems* 25.12 (2015), pp. 3422–3438.

[93] Salman Mohagheghi and Steffen Rebennack. "Optimal resilient power grid operation during the course of a progressing wildfire". In: *International Journal of Electrical Power & Energy Systems* 73 (2015), pp. 843–852.

[94] Dimitris N Trakas and Nikos D Hatziargyriou. "Optimal distribution system operation for enhancing resilience against wildfires". In: *IEEE Transactions on Power Systems* 33.2 (2017), pp. 2260–2271.

[95] Fei Teng. *Enhancing power distribution grid resilience against massive wildfires.* The George Washington University, 2020.

[96] Meng Zhao and Masoud Barati. "A real-time fault localization in power distribution grid for wildfire detection through deep convolutional neural networks". In: *IEEE Transactions on Industry Applications* 57.4 (2021), pp. 4316–4326.

[97] Reza Bayani and Saeed D Manshadi. "Resilient expansion planning of electricity grid under prolonged wildfire risk". In: *IEEE Transactions on Smart Grid* 14.5 (2023), pp. 3719–3731.

[98] Mark Specht. *Why Did My Power Go Out? Four Ways the Grid Can Fail and Cause an Outage.* `https://blog.ucsusa.org/mark-specht/why-did-my-power-go-out-four-ways-the-grid-can-fail-and-cause-an-outage/`. 2020.

[99] Tomás Tapia et al. "A robust decision-support method based on optimization and simulation for wildfire resilience in highly renewable power systems". In: *European Journal of Operational Research* 294.2 (2021), pp. 723–733.

[100] Anthony L Westerling and Benjamin P Bryant. "Climate change and wildfire in California". In: *Climatic Change* 87.Suppl 1 (2008), pp. 231–249.

[101] Anthony Leroy Westerling et al. *Wildfire Simulations for California's Fourth Climate Change Assessment: Projecting Changes in Extreme Wildfire Events with a Warming Climate: a Report for California's Fourth Climate Change Assessment.* California Energy Commission Sacramento, CA, 2018.

[102] Larry Dale et al. "Assessing the impact of wildfires on the California electricity grid". In: *Lawrence Berkeley National Laboratory* (2018).

[103] Hanbin Yang et al. "Multi-period power system risk minimization under wildfire disruptions". In: *IEEE Transactions on Power Systems* 39.5 (2024), pp. 6305–6318.

[104] Gary Davis, Aaron F Snyder, and James Mader. "The future of distribution system resiliency". In: *2014 Clemson University power systems conference.* IEEE. 2014, pp. 1–8.

[105] Edison Electric Institute. *Before And After: The Storm A compilation of recent studies, programs, and policies related to storm hardening and resiliency.* Tech. rep. Edison Electric Institute, 2014.

[106] David R. Baker. *Underground power lines don't cause wildfires. But they're really expensive.* `https://www.sfchronicle.com/bayarea/article/Underground-power-lines-don-t-cause-wildfires-12295031.php`. 2017.

[107] B Don Russell, Carl L Benner, and Jeffrey A Wischkaemper. "Distribution feeder caused wildfires: Mechanisms and prevention". In: *2012 65th Annual Conference for Protective Relay Engineers*. IEEE. 2012, pp. 43–51.

[108] Patrick Murphy. "Preventing wildfires with power outages: The growing impacts of California's public safety power shutoffs". In: *Energy and Environment Program* (2021).

[109] Hosein Eskandari, Maryam Imani, and Mohsen Parsa Moghaddam. "Convolutional and recurrent neural network based model for short-term load forecasting". In: *Electric Power Systems Research* 195 (2021), p. 107173.

[110] Tao Hong and Shu Fan. "Probabilistic electric load forecasting: A tutorial review". In: *International Journal of Forecasting* 32.3 (2016), pp. 914–938.

[111] Juyong Lee and Youngsang Cho. "National-scale electricity peak load forecasting: Traditional, machine learning, or hybrid model?" In: *Energy* 239 (2022), p. 122366.

[112] IH Sarker. *Machine learning: algorithms, real-world applications and research directions. SN Comput Sci 2: 160*. 2021.

[113] JH Kim, BS Lee, and CH Kim. "A Study on the development of long-term hybrid electrical load forecasting model based on MLP and statistics using massive actual data considering field applications". In: *Electric Power Systems Research* 221 (2023), p. 109415.

[114] Hao Xiao et al. "A novel deep learning based probabilistic power flow method for Multi-Microgrids distribution system with incomplete network information". In: *Applied Energy* 335 (2023), p. 120716.

[115] Yun Bai et al. "Regression modeling for enterprise electricity consumption: A comparison of recurrent neural network and its variants". In: *International Journal of Electrical Power & Energy Systems* 126 (2021), p. 106612.

[116] Ahmad O Aseeri. "Effective RNN-based forecasting methodology design for improving short-term power load forecasts: Application to large-scale power-grid time series". In: *Journal of Computational Science* 68 (2023), p. 101984.

[117] Rodney Rick and Lilian Berton. "Energy forecasting model based on CNN-LSTM-AE for many time series with unequal lengths". In: *Engineering Applications of Artificial Intelligence* 113 (2022), p. 104998.

[118] Chuang Li et al. "A multi-energy load forecasting method based on parallel architecture CNN-GRU and transfer learning for data deficient integrated energy systems". In: *Energy* 259 (2022), p. 124967.

[119] Sumit Kumar et al. "Energy load forecasting using deep learning approach-LSTM and GRU in spark cluster". In: *2018 fifth international conference on emerging applications of information technology (EAIT)*. IEEE. 2018, pp. 1–4.

[120] Binbin Yu et al. "A novel short-term electrical load forecasting framework with intelligent feature engineering". In: *Applied Energy* 327 (2022), p. 120089.

[121] Hu Xiaoyan et al. “A novel forecasting method for short-term load based on TCN-GRU model”. In: *2021 IEEE international conference on energy internet (ICEI)*. IEEE. 2021, pp. 79–83.

[122] Belgin Emre Türkay and Dilara Demren. “Electrical load forecasting using support vector machines”. In: *2011 7th International Conference on Electrical and Electronics Engineering (ELECO)*. IEEE. 2011, pp. I–49.

[123] Jieyang Peng et al. “Dual-stage attention-based long-short-term memory neural networks for energy demand prediction”. In: *Energy and Buildings* 249 (2021), p. 111211.

[124] Sebastian Maldonado, Agustin Gonzalez, and Sven Crone. “Automatic time series analysis for electric load forecasting via support vector regression”. In: *Applied Soft Computing* 83 (2019), p. 105616.

[125] Yuanyuan Wang et al. “Short-term load forecasting for industrial customers based on TCN-LightGBM”. In: *IEEE transactions on power systems* 36.3 (2020), pp. 1984–1997.

[126] AEMO. *Forecasting increasingly critical to harnessing wind and solar for power systems.* `https://www.aemo.com.au/newsroom/news-updates/forecasting-increasingly-critical-to-harnessing-wind-and-solar-for-power-systems`. 2023.

[127] RTE. *Consumption forecast.* `https://www.services-rte.com/en/view-data-published-by-rte/consumption-forecast.html`. 2025.

[128] NGED. *Climate Change Adaptation Report Round 4 (ARP4).* Tech. rep. National Grid Electricity Distribution, 2024.

[129] Natinoal Grid. *Clarification of the applicability of the N-1-1 Criterion.* Tech. rep. Natinoal Grid, 2018.

[130] Powerlink Queensland. *2023-27 Powerlink Queensland Revenue Proposal.* Tech. rep. Powerlink Queensland, 2021.

[131] Amin Shokri Gazafroudi, Fabian Neumann, and Tom Brown. “Topology-based approximations for N- 1 contingency constraints in power transmission networks”. In: *International Journal of Electrical Power & Energy Systems* 137 (2022), p. 107702.

[132] Mojdeh Abdi-Khorsand, Mostafa Sahraei-Ardakani, and Yousef M Al-Abdullah. “Corrective transmission switching for N-1-1 contingency analysis”. In: *IEEE Transactions on Power Systems* 32.2 (2016), pp. 1606–1615.

[133] O Alizadeh Mousavi, R Cherkaoui, and Mokthar Bozorg. “Blackouts risk evaluation by Monte Carlo Simulation regarding cascading outages and system frequency deviation”. In: *Electric Power Systems Research* 89 (2012), pp. 157–164.

[134] Christos K Simoglou et al. “Probabilistic evaluation of the long-term power system resource adequacy: The Greek case”. In: *Energy Policy* 117 (2018), pp. 295–306.

[135] Konstantinos F Krommydas et al. “Flexibility study of the Greek power system using a stochastic programming approach for estimating reserve requirements”. In: *Electric Power Systems Research* 213 (2022), p. 108620.

[136] Tiantian Qian et al. “N-1 static security assessment method for power grids with high penetration rate of renewable energy generation”. In: *Electric Power Systems Research* 211 (2022), p. 108200.

[137] Matthew Perry and Alberto Troccoli. “Impact of a fire burn on solar irradiance and PV power”. In: *Solar Energy* 114 (2015), pp. 167–173.

[138] S York. “Smoke from California wildfires decreases solar generation in CAISO”. In: *US Energy Information Administration* (2020).

[139] M Effendy Ya’acob et al. “Decreasing of grid-tied PV power output due to thick haze phenomena in Malaysia”. In: *2014 Saudi Arabia Smart Grid Conference (SASG)*. IEEE. 2014, pp. 1–5.

[140] Miguel G Cruz and Martin E Alexander. “The 10% wind speed rule of thumb for estimating a wildfire’s forward rate of spread in forests and shrublands”. In: *Annals of Forest Science* 76.2 (2019), p. 44.

[141] Paul Duginski. *Strong winds and high fire danger expected in Northern California this weekend.* `https://www.latimes.com/california/story/2019-10-25/strong-winds-and-high-fire-danger-expected-in-northern-california-this-weekend`. 2019.

[142] National Wildfire Coordinating Group. *Fire Weather Index (FWI) System.* `https://www.nwcg.gov/publications/pms437/cffdrs/fire-weather-index-system`. 2021.

[143] Copernicus Emergency Management Service. *Fire danger indices historical data from the Copernicus Emergency Management Service.* `https://cds.climate.copernicus.eu/cdsapp#!/dataset/cems-fire-historical-v1?tab=overview`. 2023.

[144] netCDF4 API. *netCDF4 API documentation.* Tech. rep. netCDF4, 2019.

[145] Yiqi Luo and Xuhui Zhou. “Temporal and spatial variations in soil respiration”. In: *Soil respiration and the environment* (2006), pp. 107–131.

[146] Geert Jan Van Oldenborgh et al. “Attribution of the Australian bushfire risk to anthropogenic climate change”. In: *Natural Hazards and Earth System Sciences Discussions* 2020 (2020), pp. 1–46.

[147] Andrea Camia and Giuseppe Amatulli. “Weather factors and fire danger in the Mediterranean”. In: *Earth observation of wildland fires in Mediterranean ecosystems*. Springer, 2009, pp. 71–82.

[148] AP Dimitrakopoulos, AM Bemmerzouk, and ID Mitsopoulos. “Evaluation of the Canadian fire weather index system in an eastern Mediterranean environment”. In: *Meteorological Applications* 18.1 (2011), pp. 83–93.

[149] Gutemberg Borges França et al. “A fire-risk-breakdown system for electrical power lines in the North of Brazil”. In: *Journal of Applied Meteorology and Climatology* 53.4 (2014), pp. 813–823.

[150] Google Developers. *Keyhole Markup Language.* `https://developers.google.com/kml`. 2021.

[151] Aleksis Xenophon and David Hill. “Open grid model of Australia’s National Electricity Market allowing backtesting against historic data”. In: *Scientific data* 5.1 (2018), pp. 1–21.

[152] Australian Bureau of Statistics. *Australian Statistical Geography Standard (ASGS): Volume 5—Remoteness Structure.* 2016.

[153] Australian Bureau of Statistics. *Regional Population Growth, Australia.* Tech. rep. Australian Bureau of Statistics, 2016.

[154] Lili Ju, Todd Ringler, and Max Gunzburger. “Voronoi tessellations and their application to climate and global modeling”. In: *Numerical techniques for global atmospheric models.* Springer, 2011, pp. 313–342.

[155] AEMO. *The National Electricity Market FACT SHEET.* Tech. rep. Australian Energy Market Operator, 2021.

[156] Peyman Khezr and Rabindra Nepal. “On the viability of energy-capacity markets under decreasing marginal costs”. In: *Energy Economics* 96 (2021), p. 105157.

[157] K. Orr and B. Allan. *Electricity Transmission Lines.* Tech. rep. Geoscience Australia, 2014.

[158] Christopher Arderne et al. “Predictive mapping of the global power system using open data”. In: *Scientific data* 7.1 (2020), p. 19.

[159] Yong Liu and Chanan Singh. “A methodology for evaluation of hurricane impact on composite power system reliability”. In: *IEEE Transactions on Power Systems* 26.1 (2010), pp. 145–152.

[160] Government of South Australia. *Identifying powerlines.* Tech. rep. Government of South Australia, 2017.

[161] Eaton. *Recloser Technical Data.* Tech. rep. Eaton, 2017.

[162] Leon Thurner et al. “pandapower—an open-source python tool for convenient modeling, analysis, and optimization of electric power systems”. In: *IEEE Transactions on Power Systems* 33.6 (2018), pp. 6510–6521.

[163] National Grid. *Guidance for UK Fire and Rescue Services.* Tech. rep. National Grid, 2018.

[164] Gerald B. Sheble and Gerald B. Sheble. *Module E3 Economic Dispatch Calculation.* `https://home.engineering.iastate.edu/~jdm/ee458/EE.PSE.E3.pdf`. 2019.

[165] Junjie Sun and Leigh Tesfatsion. “DC optimal power flow formulation and solution using QuadProgJ”. In: (2010).

[166] PA Trodden et al. “MILP formulation for controlled islanding of power networks”. In: *International Journal of Electrical Power & Energy Systems* 45.1 (2013), pp. 501–508.

[167] Jan Kronqvist et al. “A review and comparison of solvers for convex MINLP”. In: *Optimization and Engineering* 20.2 (2019), pp. 397–455.

[168] Deepesh Sharma et al. “Comparative analysis of ACOPF and DCOPF based LMP simulation with distributed loss model”. In: *2016 International Conference on Control, Computing, Communication and Materials (ICCCCM).* IEEE. 2016, pp. 1–6.

[169] London Economics. "The value of lost load (VoLL) for electricity in Great Britain". In: *Final report for OFGEM and DECC* (2013).

[170] Oscar E Rojas and Muhammad A Khan. "A review on electrical and mechanical performance parameters in lithium-ion battery packs". In: *Journal of Cleaner Production* 378 (2022), p. 134381.

[171] Szymon Potrykus et al. "Advanced lithium-ion battery model for power system performance analysis". In: *Energies* 13.10 (2020), p. 2411.

[172] K. Orr and B. Allan. *Electricity Transmission Substations.* Tech. rep. Geoscience Australia, 2019.

[173] K. Orr and N. Skeers. *Power Stations.* Tech. rep. Geoscience Australia, 2019.

[174] AEMO. *Market Data NEMWEB.* `https://www.aemo.com.au/energy-systems/electricity/national-electricity-market-nem/data-nem/market-data-nemweb#mms-data-model`. 2020.

[175] AEMO. *NTNDP database.* `https://www.aemo.com.au/energy-systems/major-publications/integrated-system-plan-isp/national-transmission-network-development-plan-ntndp/ntndp-database`. 2020.

[176] AEMO. *Guide to Generator Exemptions and Classification of Generating Units.* `https://www.aemo.com.au/-/media/Files/Electricity/NEM/Participant_Information/New-Participants/Generator-Exemption-and-Classification-Guide.docx`. 2022.

[177] ECMWF. *ERA5 hourly data on single levels from 1940 to present.* `https://cds.climate.copernicus.eu/cdsapp#!/dataset/reanalysis-era5-single-levels?tab=overview`. 2023.

[178] ECMWF. *ERA5 hourly data on pressure levels from 1940 to present.* `https://cds.climate.copernicus.eu/cdsapp#!/dataset/reanalysis-era5-pressure-levels?tab=overview`. 2023.

[179] USGS. *How much distance does a degree, minute, and second cover on your maps?* `https://www.usgs.gov/faqs/how-much-distance-does-a-degree-minute-and-second-cover-your-maps?qt-news_science_products=0#qt-news_science_products`. 2018.

[180] Victoria State Government. *Renewable Energy Action Plan.* Tech. rep. Victoria State Government, 2017.

[181] Geoscience Australia. *Wind Energy | Geoscience Australia.* `https://www.ga.gov.au/scientific-topics/energy/resources/other-renewable-energy-resources/wind-energy`. 2020.

[182] Global Wind Atlas. *Energy Data Info.* `https://globalwindatlas.info/`. 2020.

[183] Global Solar Atlas. *Energy data info.* `https://globalsolaratlas.info/map?c=-35.201256,144.148881,6&r=AUS:AUS.10_1`. 2020.

[184] U.S. Energy Information Administration. *Levelized Costs of New Generation Resources in the Annual Energy Outlook 2022.* Tech. rep. U.S. Energy Information Administration, 2022.

[185] Australian Energy Regulator. *Approach to electricity wholesale market performance monitoring.* `https://www.aer.gov.au/system/files/Discussion%20paper%20-%20Approach%20to%20electricity%20wholesale%20market%20performance%20monitoring.DOCX`. 2017.

[186] Wholesale statistics. *Australian Energy Regulator.* `https://www.aer.gov.au/wholesale-markets/wholesale-statistics`. 2021.

[187] Paul Simshauser. “Rooftop solar PV and the peak load problem in the NEM’s Queensland region”. In: *Energy Economics* 109 (2022), p. 106002.

[188] London Economics. “The value of lost load (VoLL) for electricity in Great Britain”. In: *Final report for OFGEM and DECC* (2013).

[189] AEMC. *2024-25 market price cap now available.* `https://www.aemc.gov.au/news-centre/media-releases/2024-25-market-price-cap-now-available`. 2024.

[190] Pan Zeng and Min Jin. “Peak load forecasting based on multi-source data and day-to-day topological network”. In: *IET Generation, Transmission & Distribution* 12.6 (2018), pp. 1374–1381.

[191] John T Hancock and Taghi M Khoshgoftaar. “Survey on categorical data for neural networks”. In: *Journal of big data* 7.1 (2020), p. 28.

[192] Ouya Wang, Jiabao Gao, and Geoffrey Ye Li. “Learn to adapt to new environments from past experience and few pilot blocks”. In: *IEEE Transactions on Cognitive Communications and Networking* 9.2 (2022), pp. 373–385.

[193] Balduíno César Mateus et al. “Comparing LSTM and GRU models to predict the condition of a pulp paper press”. In: *Energies* 14.21 (2021), p. 6958.

[194] Roberto Cahuantzi, Xinye Chen, and Stefan Güttel. “A comparison of LSTM and GRU networks for learning symbolic sequences”. In: *Science and information conference.* Springer. 2023, pp. 771–785.

[195] B Rizk et al. “Meniscal lesion detection and characterization in adult knee MRI: a deep learning model approach with external validation”. In: *Physica Medica* 83 (2021), pp. 64–71.

[196] Jianxi Yang et al. “A hierarchical deep convolutional neural network and gated recurrent unit framework for structural damage detection”. In: *Information Sciences* 540 (2020), pp. 117–130.

[197] Qingyong Zhang et al. “TransformGraph: A novel short-term electricity net load forecasting model”. In: *Energy Reports* 9 (2023), pp. 2705–2717.

[198] POWERCOR. *Powercor Zone Substation Reports.* `https://www.powercor.com.au/industry-partners/renewable-generation/powercor-zone-substation-reports/`. 2022.

[199] American Nuclear Society. *Report: Extreme weather is affecting nuclear power’s reliability.* Tech. rep. American Nuclear Society, 2021.

[200] Maximilian Auffhammer, Patrick Baylis, and Catherine H Hausman. “Climate change is projected to have severe impacts on the frequency and intensity of peak electricity demand across the United States”. In: *Proceedings of the National Academy of Sciences* 114.8 (2017), pp. 1886–1891.

[201] Alexander I Filkov et al. “Impact of Australia’s catastrophic 2019/20 bushfire season on communities and environment. Retrospective analysis and current trends”. In: *Journal of safety science and resilience* 1.1 (2020), pp. 44–56.

[202] Natural Resources Canada. *Canadian Forest Fire Weather Index (FWI) System.* `https://cwfis.cfs.nrcan.gc.ca/background/summary/fwi`. 2018.

[203] Christos Giannakopoulo. *Fire Weather Index (FWI) – Dataset Description.* `https://confluence.ecmwf.int/pages/viewpage.action?pageId=283569774`. 2023.

[204] Max Planck Institute. *Climate Data Operators - Tutorials.* `https://code.mpimet.mpg.de/projects/cdo/wiki/Tutorial#Interpolation`. 2021.

[205] Natural Resource Canada. *Canadian Fire Weather Index Calculator.* `https://code.google.com/archive/p/pyfwi/`. 2012.

[206] CE van Wagner. *Development and structure of the Canadian forest fire weather index system.* 35. 1987.

[207] Vladimir Vapnik. *The nature of statistical learning theory.* Springer science & business media, 2013.

[208] Shuzhan Fan. *Understanding the mathematics behind Support Vector Machines.* `https://shuzhanfan.github.io/2018/05/understanding-mathematics-behind-support-vector-machines/`. 2018.

[209] Ying-Ying Cheng, Patrick PK Chan, and Zhi-Wei Qiu. “Random forest based ensemble system for short term load forecasting”. In: *2012 international conference on machine learning and cybernetics.* Vol. 1. IEEE. 2012, pp. 52–56.

[210] Shafiul Hasan Rafi, Mohammad Mahruf Mahdi, et al. “A short-term load forecasting technique using extreme gradient boosting algorithm”. In: *2021 IEEE PES Innovative Smart Grid Technologies-Asia (ISGT Asia).* IEEE. 2021, pp. 1–5.

[211] Heng Shi, Minghao Xu, and Ran Li. “Deep learning for household load forecasting—A novel pooling deep RNN”. In: *IEEE transactions on smart grid* 9.5 (2017), pp. 5271–5280.

[212] Kyunghyun Cho et al. “Learning phrase representations using RNN encoder-decoder for statistical machine translation”. In: *arXiv preprint arXiv:1406.1078* (2014).

[213] Christian Versloot. *ReLU, Sigmoid and Tanh: today’s most used activation functions.* `https://github.com/christianversloot/machine-learning-articles/blob/main/relu-sigmoid-and-tanh-todays-most-used-activation-functions.md`. 2019.

[214] Nada Mounir, Hamid Ouadi, and Ismael Jrhilifa. “Short-term electric load forecasting using an EMD-BI-LSTM approach for smart grid energy management system”. In: *Energy and Buildings* 288 (2023), p. 113022.

[215] Xiangya Bu et al. “Hybrid short-term load forecasting using CGAN with CNN and semi-supervised regression”. In: *Applied Energy* 338 (2023), p. 120920.

[216] Abdul Khalique Shaikh et al. “A new approach to seasonal energy consumption forecasting using temporal convolutional networks”. In: *Results in Engineering* 19 (2023), p. 101296.

[217] Yuqi Nie et al. "A time series is worth 64 words: Long-term forecasting with transformers". In: *arXiv preprint arXiv:2211.14730* (2022).

[218] Zhang Qingyong et al. "TransformGraph: A novel short-term electricity net load forecasting model [J]". In: *Energy Reports* 9 (2023), pp. 2705–2717.

[219] Tingze Zhang et al. "Highly accurate peak and valley prediction short-term net load forecasting approach based on decomposition for power systems with high PV penetration". In: *Applied Energy* 333 (2023), p. 120641.

[220] Dehua Zheng et al. "Short-term wind power forecasting using a double-stage hierarchical ANFIS approach for energy management in microgrids". In: *Protection and Control of Modern Power Systems* 2 (2017), pp. 1–10.

[221] Victoria Gov. *Electric hot water systems.* `https://www.sustainability.vic.gov.au/energy-efficiency-and-reducing-emissions/save-energy-in-the-home/water-heating/choose-the-right-hot-water-system/electric-hot-water-systems`. 2022.

[222] Christopher Goddard. *ENSO impacts on Europe.* `https://confluence.ecmwf.int/display/COPSRV/ENSO+impacts+on+Europe`. 2023.

[223] Shahab Dehghan, Nima Amjady, and Antonio J Conejo. "Reliability-constrained robust power system expansion planning". In: *IEEE Transactions on Power Systems* 31.3 (2015), pp. 2383–2392.

[224] Clayton Barrows et al. "The IEEE reliability test system: A proposed 2019 update". In: *IEEE Transactions on Power Systems* 35.1 (2019), pp. 119–127.

[225] Georgia Tech Power Systems Control and Automation Laboratory. *case24_ieee_rts.* `https://matpower.org/docs/ref/matpower5.0/case24_ieee_rts.html`. 2015.

[226] Dieu Ngoc Vo, Tri Phuoc Nguyen, and Khoa Dang Nguyen. "Multi-objective security constrained optimal active and reactive power dispatch using hybrid particle swarm optimization and differential evolution". In: *GMSARN International Journal* 12 (2018), pp. 84–117.

[227] RenSMART Open Forum. *CO2 calculator.* `https://www.rensmart.com/Calculators/KWH-to-CO2`. 2020.

[228] Moein Choobineh, Bananeh Ansari, and Salman Mohagheghi. "Vulnerability assessment of the power grid against progressing wildfires". In: *Fire Safety Journal* 73 (2015), pp. 20–28.

[229] Elexon. *Loss of Load Probability Calculation Methodology Statement.* Tech. rep. Elexon, 2019.

[230] Jonathan D Black and William LW Henson. "Hierarchical load hindcasting using reanalysis weather". In: *IEEE Transactions on Smart Grid* 5.1 (2013), pp. 447–455.

[231] Hossein Shahinzadeh et al. "Unit commitment in smart grids with wind farms using virus colony search algorithm and considering adopted bidding strategy". In: *2017 Smart Grid Conference (SGC).* IEEE. 2017, pp. 1–9.

[232] Xingyu Yan, Dhaker Abbes, and Bruno Francois. “Uncertainty analysis for day ahead power reserve quantification in an urban microgrid including PV generators”. In: *Renewable Energy* 106 (2017), pp. 288–297.

[233] Ivalin Petkov and Paolo Gabrielli. “Power-to-hydrogen as seasonal energy storage: an uncertainty analysis for optimal design of low-carbon multi-energy systems”. In: *Applied Energy* 274 (2020), p. 115197.

[234] Hassan Heidari, Mehrdad Tarafdar Hagh, and Pedram Salehpoor. “Accurate, simultaneous and Real-Time screening of N-1, Nk, and N-1-1 contingencies”. In: *International Journal of Electrical Power & Energy Systems* 136 (2022), p. 107592.

[235] Guido Francesco Frate et al. “Techno-economic sizing of a battery energy storage coupled to a wind farm: an Italian case study”. In: *Energy Procedia* 148 (2018), pp. 447–454.

[236] Mehrdad Gholami et al. “Optimum storage sizing in a hybrid wind-battery energy system considering power fluctuation characteristics”. In: *Journal of Energy Storage* 52 (2022), p. 104634.

[237] AEMO. *Load Shedding in Victoria on 24 and 25 January 2019.* Tech. rep. Australia Energy Market Operator, 2019.

[238] AEMC. *RESIDENTIAL ELECTRICITY PRICE TRENDS 2019.* Tech. rep. Australian Energy Market Commission, 2019.

[239] AEMC. *2024-25 market price cap now available.* Tech. rep. Australian Energy Market Commission, 2024.